Multiwavelength Study of Active Galaxies

A thesis

submitted for the degree of

Doctor of Philosophy

In

The Faculty of Science

University of Calicut, Calicut

by

Veeresh Singh

Indian Institute of Astrophysics

Bangalore 560 034, INDIA

August 2010

To

My Parents

(*Smt. Subhadra Devi & Shri Fateh Bahadur Singh*)

and

All My Teachers

DECLARATION

I hereby declare that the matter contained in this thesis is the result of research work carried out by me at the Indian Institute of Astrophysics, Bangalore, under the supervision of Prof. Prajval Shastri. This thesis has not been submitted for the award of any degree, diploma, associateship, fellowship etc. of any university or institute.

Prof. Prajval Shastri   Veeresh Singh

(Ph.D. Thesis Supervisor)   (Ph.D. Candidate)

Indian Institute of Astrophysics

Bangalore - 560034, INDIA

August, 2010

CERTIFICATE

This is to certify that the thesis entitled **"Multiwavelength Study of Active Galaxies"** submitted to the University of Calicut by Mr. Veeresh Singh for the award of the degree of Doctor of Philosophy in the faculty of Science, is based on the results of the research work carried out by him under my supervision and guidance, at the Indian Institute of Astrophysics, Bangalore. This thesis has not been submitted for the award of any degree, diploma, associateship, fellowship etc. of any university or institute.

Prof. Prajval Shastri

(Ph. D. Thesis Supervisor)

Indian Institute of Astrophysics

Bangalore - 560034, INDIA

August, 2010

ACKNOWLEDGMENTS

mission at the Calicut University.

When it comes to acknowledge the friends, it appears to me like solving a many-body problem! long list of friends, so many interactions and indeed unimaginative life without them. I am grateful to all my friends over the years at IIA - Abhay, Alkendra, Alvin, Amit Kumar, Amit Pathak, Amit Shukla, Anant, Bharat, Blesson, Chandrashekhar, Chiranjib, Girjesh, Jay Kumar, Krishna, Madhulita, Malay, Nagaraju, Nataraj, Ramya S., Rumpa, Shivani, Sreeja, Siddhu, Sashi, Tapan, Uday, Vigeesh and many more; and my seniors - Bijay, Gajendra, Jayendra, Kathiravan, Latha, Maheshwar, Malay Nayak, Manoj, Preeti, Raj Lakhsmi, Rezi Mathew, Ravinder, Rajguru, Shalima, Shanmuga, Suresh; and my Juniors - Anantha, Arun, Arya Dhar, Avijeet, Dinesh, Drisya, Hema, Indu, Laxmi Pradeep, Manpreet, Prasanth, Ramya P., Ramesh, Rathna, Sagar, Sajal, Samyaday, Shashi Kumar, Shubham, Sindhuja, Smitha S., Subharathi, Sudhakar, Suresh, Vineeth and many more. I rejoiced my early days during my course-work with Blesson, Nataraj, Uday and Vigeesh and often long discussions with Nataraj. Over all these years I enjoyed playing Badminton, Cricket more than my school and college days and would like to thank all those friends who have been enthusiastically participating.

The pages would never be sufficient to appreciate the contribution and cooperation of all of my teachers and friends outside IIA, nonetheless, I must remember my Mathematics and Physics teachers Sarabjeet Singh and Inder Singh at my intermediate college, who created a seed of passion in me to study Mathematics and Physics, which ultimately destined me to pursue Ph.D. in Astrophysics. I am indebted to my parents and all the family members for their encouragement, blessings and everlasting heartily support, which is beyond the words.

LIST OF PUBLICATIONS

1. Testing Seyfert unification at low-frequency radio regime, *Singh V., Shastri P. & Athreya R.*, 2011, (*in preparation*)

2. Suzaku X-ray spectral properties of Compton-thick Seyfert galaxy NGC 5135, *Singh V., Risaliti G., Braito V. & Shastri P.*, 2011, MNRAS (*submitted*)

3. X-ray spectral properties of Seyfert galaxies and the unification scheme, *Singh V., Shastri P. & Risaliti G.*, 2011, A&A (*in press*)

4. Radio and X-ray emission from low-luminosity AGNs: testing unification hypothesis, *Singh V., Shastri P., Risaliti G., Athreya R.*, 2010, ASPC 427

5. Radio emission from Seyfert galaxies, *Singh V., Shastri P. & Athreya R.*, 2009, Bull. Astr. Soc. India (*in press*)

6. Low-frequency radio emission from Seyfert galaxies, *Singh V., Shastri P. & Athreya R.*, 2009, ASPC 407 173S

7. X-ray emission from Seyfert galaxies: surroundings of their supermassive black holes, *Singh V. & Shastri P.*, 2008, AIPC 1053 51S

Table of Contents

List of Tables

List of Figures

ABSTRACT

Seyfert galaxies are categorized as nearby, low luminosity ($M_B \leq$ -23), radio-quiet ($\frac{F_{5\ GHz}}{F_{B-band}} < 10$) Active Galactic Nuclei (AGN) hosted in spiral or lenticular galaxies. Demographically, Seyfert galaxies may account for $\sim 10\%$ of the entire population of active galaxies in the nearby universe. Seyfert galaxies are classified mainly into two subclasses named as 'type 1' and 'type 2' Seyfert galaxies, based on the presence and absence of broad permitted emission lines in their optical spectra, respectively. Spectropolarimetric observations of Seyfert type 2s laid the foundation of the Seyfert unification scheme, which hypothesizes that Seyfert type 1s and type 2s belong to the same parent population and appear different solely due to the differing orientations of the obscuring material having a torus-like geometry around the AGN (Antonucci and Miller 1985; Antonucci 1993).

The primary objective of this thesis work is to examine the validity and limitations of the orientation and obscuration based Seyfert unification scheme using multiwavelength (mainly X-ray and radio) observations. The key issue in testing the Seyfert unification scheme is acquiring a rigorously selected Seyfert sample such that the two Seyfert subtypes are intrinsically similar within the framework of the unification scheme. I study two samples of Seyfert galaxies which are rigorously selected on the basis of the orientation-independent properties of AGN as well as the host galaxy. In our sample we ensure the intrinsic similarity of the two subtypes in cosmological redshift, [OIII] λ5007Å emission line luminosity, absolute bulge magnitude, absolute stellar magnitude of the host galaxy and the Hubble stage of the host galaxy. Our sample selection criteria also mitigates the biases generally inherent in most of the Seyfert samples derived from flux limited surveys at different wavelengths.

The obscuring material supposedly having a torus-like geometry is optically

thick for optical, UV and soft X-ray wavelengths. However, X-ray and radio studies are advantageous since X-ray spectral analysis enables to estimate the absorbing column density and radio emission is optically thin to the obscuring torus. I study the X-ray and radio properties of the Seyfert galaxies of our samples to test the predictions of the Seyfert unification scheme. To derive the X-ray spectral properties I model the *XMM-Newton* pn X-ray spectra of our sample Seyfert galaxies. I perform statistical comparison of the X-ray spectral properties (*i.e.*, X-ray luminosities, absorbing column densities, hard X-ray spectral shapes, equivalent widths of Fe Kα line, soft excess, reflection components etc.) of the two Seyfert subtypes in the framework of unification. I also attempt to unveil the nature of obscuring material around a Compton-thick Seyfert galaxy NGC 5135 using *Suzaku* broadband X-ray spectral analysis. The correlations of the nuclear hard X-ray luminosity to the pc-scale and kpc-scale radio luminosities are also investigated for the two Seyfert subtypes.

To test the predictions of the Seyfert unification in the radio regime, I study the radio properties of Seyfert galaxies using Giant Meterwave Radio Telescope (GMRT) observations carried out at 240 MHz and 610 MHz, and NRAO VLA Sky Survey observations at 1.4 GHz and VLA 5 GHz observations from the literature. The radio luminosities and spectra are found to be similar for the Seyfert type 1s and type 2s. I also investigated radio - IR luminosity correlations and find that for both the Seyfert subtypes, the total 610 MHz and 240 MHz radio luminosities are moderately correlated with near-IR, mid-IR luminosities while the correlation becomes poorer with far-IR luminosities. Furthermore, the 12 μm, 25 μm, 60 μm and 100 μm IR luminosity distributions are not statistically different for the Seyfert type 1s and type 2s. I conclude that the X-ray, radio and IR properties of the Seyfert galaxies of our rigorously selected samples are consistent with the unification scheme.

Multiwavelength Study of Active Galaxies

Chapter 1

Introduction

1.1 Active galaxies

Galaxies are gravitationally bound systems of 10^9 - 10^{11} stars and radiate by the combined output of their stars and can have spiral, elliptical and irregular morphologies. A small fraction of galaxies ($\sim 10\%$) have highly luminous nuclei visible in nearly all electromagnetic wavelengths ranging from radio to X-rays and sometimes the highly luminous nucleus outshines the host galaxy. These galaxies often have emission-line spectra with a wide range of ionization and many of these show variable output on different time scales, over entire electromagnetic spectrum. The spectral continuum emission coming from the nuclei of these galaxies is characterized as non-thermal. These galaxies are known as 'active galaxies' and the nuclei as 'Active Galactic Nuclei' (AGN). Some of active galaxies also show collimated relativistic jets emanating from the nucleus and extending to hundreds of kiloparsecs and sometimes even a mega-parsec. The origin of the non-stellar nuclear emission can be explained by accretion of surrounding material on to a supermassive black hole (SMBH) of mass $\sim 10^6$ - 10^9 $M_\odot$ residing at the center of galaxy (Peterson 1997) (p.32). The energy which drives the nuclear activity is believed to come from the release of gravitational potential energy of surrounding material falling on to SMBH via an accretion disk which radiates powerfully across much of the electromagnetic spectrum. The accretion of material forms a disk which may span from a few Schwarzschild radii to a few thousand Schwarzschild radii (Krolik

1

1999) (p.97) with X-rays coming from the innermost part of the accretion disk, UV and optical from outer region (Peterson 1997) (p.118-122). Therefore, a complete picture of AGN can be obtained only by observing it at multiwavelengths of the electromagnetic spectrum.

1.2 Fundamental components of AGN

In following sections I give the brief details of the fundamental components of an AGN. Figure 1.1 depicts the different components of an AGN.

1.2.1 Supermassive black holes

Recent studies reveal that a supermassive black hole ($M_{BH} \simeq 10^6$ - 10^9 $M_\odot$) resides at the center of almost every galaxy (Kormendy and Richstone 1995; Magorrian *et al.* 1998). It has been found that the mass of SMBH scales linearly with the luminosity (or mass) of the bulge of host galaxy (Ho 1999; Kormendy 2001) and the stellar velocity dispersion (Ferrarese and Merritt 2000; Gebhardt *et al.* 2000). The luminosity - M_{SMBH} relation for active and non-active (normal) galaxies suggests that activity of AGN decreases smoothly towards non-active state (Ho 2008). Ho, Filippenko, and Sargent (1997) carried out a detailed optical spectroscopic survey of a large number of nearby galaxies and found that between a third and a half of their sample galaxies show active galactic nuclei (AGN) like spectra, albeit of low luminosity, thus confirming that SMBHs are not only present in galaxies, but they are also active (atleast at some level). The accretion of surrounding matter onto SMBH determine the nature of galaxy, *i.e.*, 'active' or 'non-active'.

1.2.2 The accretion disc

The friction between gas layers/clouds of different relative velocities in the ambiance of SMBH will lead to the formation of a rotating disk of matter called

'accretion disk' (Shlosman, Begelman, and Frank 1990). Accreting matter transfers angular momentum and dissipates binding energy via magneto-rotational instabilities and produces a magnetically active corona. The accretion disk, heated by magnetic and/or viscous processes, radiates in much of the electromagnetic spectrum ranging from optical to soft X-rays. There may be different kinds of accretion flows depending on the accretion rate ($\dot{m}$) and viscosity (α) of the matter being accreted (Chen 1995). For low accretion rates, different kinds of accretion flows have been suggested, *i.e.*, optically-thin 'Advection-Dominated Accretion flow' (ADAF) (Narayan and Yi 1994), Advection-Dominated Inflows - Outflows solutions (ADIOs) (Blandford and Begelman 1999) and Convection-Dominated Accretion Flow (CDAF) (Narayan, Igumenshchev, and Abramowicz 2000; Quataert and Gruzinov 2000). When $\alpha^2 < \dot{m} < 1$, the disk has the standard optically-thick geometrically-thin structure (Shakura and Sunyaev 1973).

1.2.3 The Broad Line Region (BLR)

The IR, optical and UV spectra of AGNs show broad permitted emission lines (FWHM $\sim$ few thousand $\mathrm{km\,s^{-1}}$) with a wide range of ionization and the prominent broad emission lines comprise of the Lyman, Balmer, Paschen and Bracket series lines of atomic Hydrogen (*i.e.*, Ly_α, H_α, H_β, Pa_α, Pa_β), Helium (HeII $\lambda 4686\text{Å}$, HeI $\lambda 5876\text{Å}$), Carbon (*i.e.*, CIII] $\lambda 1909\text{Å}$, CIV $\lambda\lambda$ 1548Å, 1551Å), Nitrogen (NV $\lambda\lambda$ 1239Å, 1243Å), Oxygen (*i.e.*, OVI $\lambda\lambda$ 1032Å, 1038Å), Silicon (*i.e.*, SiIV $\lambda\lambda$ 1394Å, 1403Å), Magnesium (MgII $\lambda\lambda$ 2796Å, 2804Å) and multiplets of Iron (FeII) (Krolik (1999), p. 309). The line strengths, their widths and shapes are powerful diagnostics tools to understand the emitting gas region of an AGN. The classical and more recent studies point toward photoionization as the main heating source for the BLR emitting gas (see, *e.g.*, Kwan and Krolik (1981); Osterbrock (1989); Baldwin *et al.* (1995, 1996); Krolik (1999)). The BLR contains high velocity ($\sim$ 3000 - 5000 $\mathrm{km\,s^{-1}}$), dense ($\sim 10^{10} \mathrm{cm^{-3}}$) gas clouds located at $\sim$ 0.001 - 0.1 pc from

the SMBH. The cloud system is bound to the gravitational potential of SMBH, as black hole gravity dominates over the AGN radiation pressure force. The presence of semi-forbidden CIII] line and the absence of [OIII] doublet, suggest that the electron density in the BLR is $\sim 10^8$ - 10^9 cm^{-3}. The fraction of thermal disk emission reprocessed by BLR clouds is roughly equal to the cloud covering factor (0.1) and because of the small covering factor absorption lines are predicted to be extremely weak (*e.g.*, Netzer and Maoz (1990)).

1.2.4   The Narrow Line Region (NLR)

The narrow emission lines (FWHM $\sim$ few hundred km s^{-1}) are believed to originate from low density (n$_e$ $\sim 10^3$ - 10^6 cm^{-3}) gas clouds relatively far (*i.e.*, few pc to few hundreds of pc) from the nucleus, which are ionized either by photoionization from the nuclear source (Koski 1978; Ferland and Netzer 1983; Stasińska 1984) or by shock excitation from the radio jets emanating from the nucleus (Dopita and Sutherland 1995). The optical spectra of a subclass of active galaxies show only narrow permitted emission lines, *e.g.*, HI, HeI and HeII, and narrow forbidden emission lines among which the strongest are [OIII] λ λ 4959, 5007Å, [OII] λ3727Å, [NII] λ λ 6548, 6583Å. Unlike HII regions, in active galaxies [OIII] λ5007 is usually the strongest line overall except Lyα. Because of the collimated radiation field, NLR often appears elongated or even biconical with axis perpendicular to the postulated torus (Pogge 1989).

1.2.5   The obscuring torus

The central region (SMBH, accretion disk and BLR) of AGN is believed to be surrounded by an optically-thick dusty torus which hides the AGN when line-of-sight passes through it (Rowan-Robinson 1977; Antonucci and Miller 1985; Urry *et al.* 1995), however, it is debated if torus exists in all AGNs. The obscuring torus around the central engine may extend from few parsec to a few hundred parsec,

having density of 10^4 - 10^6 cm^{-3} and equivalent hydrogen column density of 10^{22} - 10^{25} H atoms cm^{-2} and even larger. The torus is optically-thick for optical, UV and soft X-ray photons and due to the large column density only the hard X-ray photons can penetrate the torus and even these photons are limited to a few Compton depths. From the dust sublimation temperature argument, the inner scale of the torus is thought to be of order 1 pc (*e.g.*, Krolik and Begelman (1988); Gallimore *et al.* (1999); Ulvestad *et al.* (1999); Jaffe *et al.* (2004)) but other properties are poorly constrained owing to angular resolution limitations. The torus is thought to comprise high-density gas/clouds, in which dust and molecules co-exist. The gas/clouds in the inner part of the torus may lose sufficient angular momentum by collisional friction and fall onto the SMBH via accretion disk formation (Krolik and Begelman 1988; Tacconi *et al.* 1994). The torus itself is thought to be fed by incoming gas from kpc scales (Shlosman, Begelman, and Frank 1990; Friedli and Martinet 1993; Wilson and Tsvetanov 1994; Maiolino and Rieke 1995) in the host galaxy.

1.2.6 Relativistic and sub-relativistic jets

In AGNs, jets originate in the vicinity of a supermassive black hole and transport energy, momentum and angular momentum over large distances ranging from few hundreds of pc to a few megaparsec (*e.g.*, Marscher (2009) and references therein). The wide variety of AGN is reflected in the diversity of their jets too and jets range from relatively slow, weak, and poorly collimated flows (*e.g.*, in Seyfert galaxies; Ulvestad *et al.* (1999)) to strong jets with relativistic speeds (*e.g.*, in FR I radio galaxies and radio-loud quasars) to most luminous, highly focused, and relativistic beams (in FR II radio galaxies and BL Lac objects) (Urry *et al.* 1995). There is observational evidence that some jets have relativistic velocities, *i.e.*, VLBI observations show superluminal motions of bright radio knots emanating from the AGN and moving away from the core (*e.g.*, Shen *et al.* (2001); Giovannini *et al.*

(1999)). In superluminal motion, the apparent velocity of plasma blob is faster than the velocity of light (c) because the emitting plasma blob approaches us with the velocity close to c and making a small angle $\sim 5°$ *w.r.t.* to the line-of-sight.

AGN jets radiate profusely from radio to γ-ray wavelengths and the jet emission can also be prominent in optical and X-ray wavelengths even at distances of hundreds of kiloparsecs from the nucleus (see, *e.g.*, Stawarz *et al.* (2004)). Synchrotron emission from the extended jets/lobes dominates at the lower radio wavelengths, while synchrotron radiation from the compact jets supplies most of the flux from GHz to optical wavelengths. Synchrotron as well as inverse Compton emission mechanisms are attributed to produce most of the X-ray photons at > 1 keV and γ rays at < 100 GeV energies in the compact jet (*e.g.*, in 3C 273, Marscher (2009)).

Jets are believed to be launched by magneto-hydrodynamic processes at the inner regions of the accreting SMBH (Blandford and Payne 1982; Begelman, Blandford, and Rees 1984; Koide, Shibata, and Kudoh 1999). Magnetic launching is considered to be the driving force behind most of the relativistic jets in AGN. It has been proposed that the energy extraction from the spin of the SMBH (Blandford and Znajek 1977) and the energy extraction from a accretion disk wind (Blandford and Payne 1982) possibly play a key role in the formation of jets in AGNs. The details of the formation of inner jets that connect the nucleus to the observed radio jets, their acceleration close to the speed of light and the strong collimation remain poorly understood (Marscher 1995; Begelman 1995; Marscher 2009).
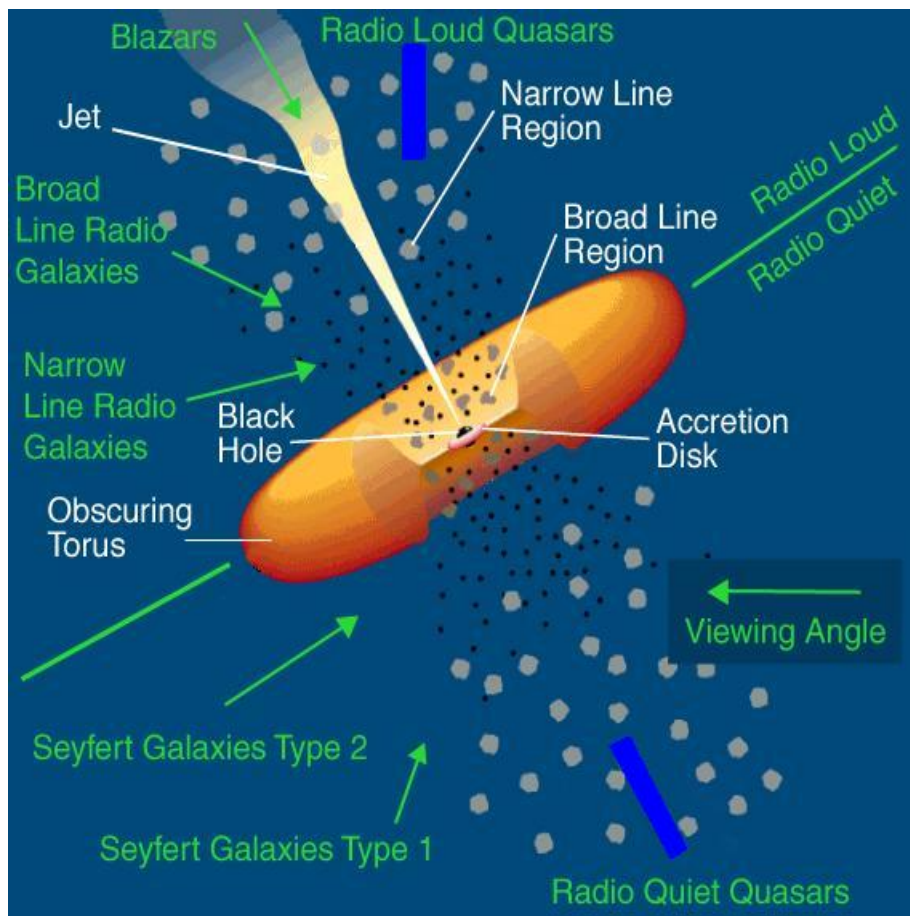
Figure 1.1: An artistic illustration depicting various components of an AGN and the unification scheme. Green arrows indicate the AGN type that is seen from a certain viewing angle according to the unification scheme.

1.3   Active Galactic Nuclei taxonomy

AGNs are broadly classified into two categories, on the basis of the ratio of their radio to optical flux density, named as radio-loud ($\frac{F_{5\ GHz}}{F_{B-band}} \geq 10$) and radio-quiet ($\frac{F_{5\ GHz}}{F_{B-band}} < 10$) (Kellermann *et al.* 1989). A small fraction of AGNs are radio-loud according to the above criterion. Radio-loud objects are further classified into Fanaroff-Riley type I (FR I) and Fanaroff-Riley type II (FR II) on the basis of their radio morphology (Fanaroff and Riley 1974). AGNs with relativistic jets and spectacular big lobes fall into radio-loud category and often reside in elliptical host galaxies, while most of the radio-quiet AGNs are hosted in spiral or lenticular galaxies (Antonucci 1993). Radio-quiet quasars and Seyfert galaxies having similar optical spectra are distinguished by luminosity limit, *i.e.*, quasars are more luminous ($M_B \leq$ -23) than Seyfert galaxies (Urry *et al.* 1995). Figure 1.2 shows the AGN classification scheme and parent populations of different AGNs.

Among the radio-loud population, FR I radio galaxies and BL Lacertae objects are believed to come from the same parent population with FR Is oriented at large angle *wrt* line-of-sight, while in BL Lacertae objects the jet is pointed towards the observer. FR II radio galaxies and radio-loud quasars are believed to belong to the same parent population with core-dominated radio quasars are thought to be oriented at relatively small angles w.r.t. the line-of-sight ($\theta \leq 15°$), while lobe-dominated radio quasars are thought to be at the angles intermediate between those of core-dominated radio quasars and FR II radio galaxies (Urry *et al.* 1995).
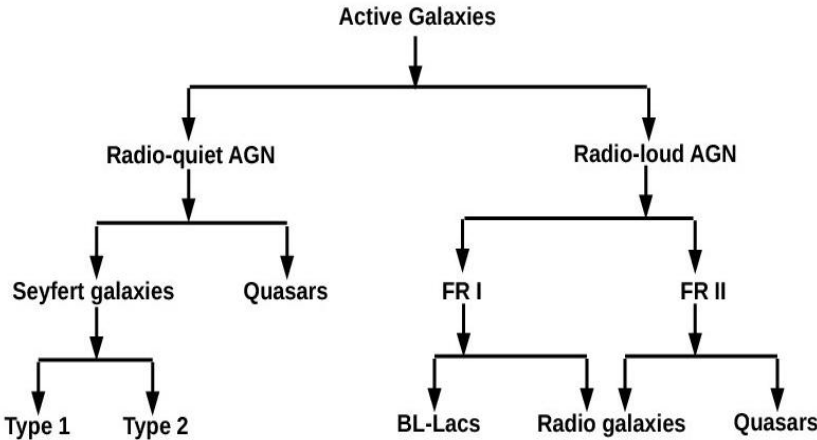
Figure 1.2: A tree-chart depicting AGN classification.

1.4 Seyfert galaxies: a subclass of active galaxies

Seyfert galaxies were discovered by Carl Seyfert (see, Seyfert (1943)), with the aim to study the optical spectra of a group of galaxies selected on the basis of high central surface brightness, *i.e.*, stellar-appearing cores and found that the optical spectra of several of these galaxies (*e.g.*, NGC 1068, NGC 1275, NGC 3516, NGC 4051, NGC 4151, and NGC 7469) were dominated by high-excitation nuclear emission lines with typical width of $\sim$ few thousand km s^{-1}. Woltjer (1959) made the first attempt to understand the physics of Seyfert galaxies and concluded that the size of Seyfert nuclei is less than 100 pc, with mass in the range M $\simeq 10^{9\pm1}$ M$_\odot$ and nuclear emission may last for more than 10^8 years.

Seyfert galaxies contain an AGN that is evident from the non-thermal continuum and emission line (with a wide range of ionization) dominated optical spectra of the nucleus. Also, the nuclei are associated with jets which extends from pc-scale to a few kpc-scale and are seen radio or optical (Cecil, Wilson, and Tully 1992; Thean *et al.* 2000; Lal, Shastri, and Gabuzda 2004). Seyfert galaxies may account for $\sim$ 10% of the entire AGN population (Maiolino and Rieke 1995; Ho, Filippenko, and Sargent 1997). Seyfert galaxies are categorized as low luminosity (M$_{\rm B} \leq$ -23) (Schmidt and Green 1983), radio quiet ($\frac{\rm F_{5~GHz}}{\rm F_{B-band}} < 10$) (Kellermann *et al.* 1989) AGNs hosted in spiral or lenticular galaxies (Weedman 1977).

1.4.1 Classification of Seyfert galaxies

1.4.1.1 Seyfert 'type 1s' and 'type 2s'

Seyfert galaxies are classified mainly into two classes named as 'type 1' and 'type 2' Seyfert galaxies, based on the presence and absence of broad permitted emission lines in their optical spectra, respectively (Khachikian and Weedman 1974; Antonucci 1993). In type 2s, both permitted and forbidden emission lines present in the optical spectra are of equal widths ($\sim$ few hundred km s^{-1}), while in type 1s,

broad permitted emission lines are also seen which have widths (FWHM $\sim$ few thousands km s^{-1}) much larger than typical widths of narrow permitted as well as forbidden emission lines. The optical spectra of Seyfert type 2s show narrow permitted emission lines of HI, HeI and HeII, and narrow forbidden emission lines among which the strongest are [OIII] $\lambda\lambda$ 4959, 5007Å, [NII] $\lambda\lambda$ 6548, 6583Å. Other forbidden emission lines include [OI] $\lambda\lambda$ 6300, 6364Å, [SII] $\lambda\lambda$ 6716, 6731Å, often [FeVII] λ6087Å, and in many cases [FeX] λ6375Å. The nuclear spectra of type 1s include all these 'narrow' permitted emission lines as well as much broader emission lines of HI, HeI, HeII and FeII, of typical width FWHM $\sim$ few thousand km s^{-1}.

The narrow emission lines are emitted from a 'narrow-line region' (NLR) in which the velocity field ranges up to a few hundreds of km s^{-1}, and the broad emission lines are emitted from a 'broad-line region' (BLR) in which the velocity field ranges up to as high as few thousand km s^{-1}. The absence of forbidden emission lines (which originate via collisional de-excitation) from the BLR implies that the electron density throughout BLR region is much higher than the critical densities for collisional de-excitation of all the strong forbidden lines observed from the NLR (*e.g.*, Osterbrock (1989)). From the known transition probabilities and strengths of collisional excitation for the forbidden lines of the abundant ions, the critical electron density limit is n$_{\mathrm{e}}$ $\sim$ 10^8 cm^{-3}.

1.4.1.2 Seyfert galaxies of intermediate types

Seyfert galaxies are further sub-classified into intermediate types based on the strength of the broad H$_\beta$ component relative to the narrow H$_\beta$ component, *i.e.*, type 1.5 Seyferts when the broad and narrow components of the H$_\beta$ lines are comparable, type 1.8 Seyferts when the broad components are weak but nonetheless detectable in Hα and H$_\beta$, type 1.9 Seyferts when the broad component can only be detected in the Hα line (Osterbrock 1981). The 12th edition catalog of AGN
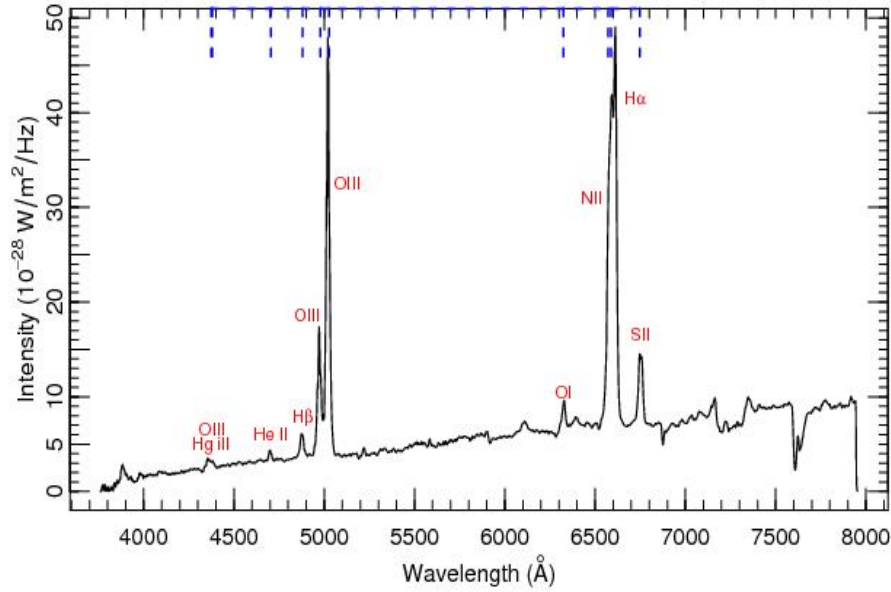
Figure 1.3: Optical spectrum of NGC 1068, a type 2 Seyfert galaxy.

and quasars (Véron-Cetty and Véron 2006) followed a more quantitative Seyfert classification introduced by Winkler (1992) :

For Seyfert 'type 1.0' : $5.0 < R$

For Seyfert 'type 1.2' : $2.0 < R < 5.0$

For Seyfert 'type 1.5' : $0.33 < R < 2.0$

For Seyfert 'type 1.8' : $R < 0.33$, broad component in Hα and H$_\beta$ is visible

For Seyfert 'type 1.9' : broad component is visible in Hα but not in H$_\beta$

For Seyfert 'type 2.0' : no broad component is visible

where 'R' is the ratio of the total H$_\beta$ to the [OIII] λ5007Å flux.

1.4.1.3   Narrow-line Seyfert type 1 galaxies

The typical FWHM of the Balmer lines in Seyfert type 1s lies in the range 2000 - 6000 km s^{-1}. However, there is a group of Seyfert galaxies with all the properties similar to Seyfert 1s, but with unusually narrow Balmer lines (Osterbrock and Pogge 1985; Goodrich 1989) and these are named as 'narrow-line Seyfert type 1s' (NLS1). NLS1s show spectra similar to classical Seyfert 1 galaxies (strong FeII, [OIII] $\lambda\lambda5007, 4959$Å relatively weaker compared to hydrogen Balmer series lines) but widths of permitted emission lines (FWHM of H$_\beta$ < 2000 km s^{-1}) much narrower than for typical Seyfert 1 galaxies (Goodrich 1989). Thus, strong FeII, weak [OIII], and narrow H$_\beta$ lines are the defining characteristics of the NLS1 class.

The current paradigm is that NLS1s possess black holes of relatively lower masses (M$_{\mathrm{BH}}$ $\leq 10^7$ M$_\odot$) but with higher accretion rates compared to their broad-line counterparts (Pounds, Done, and Osborne 1995; Mathur, Kuraszkiewicz, and Czerny 2001; Wandel 2002; Peterson *et al.* 2004) and the narrow-line widths are due to the smaller black hole mass. However, there are also studies which suggest that NLS1 are intrinsically similar to BLS1 and the relative narrow width of the broad permitted lines is due to the smaller viewing angle to BLR which has a disk-like geometry (*e.g.*, (Decarli *et al.* 2008)).

1.4.2   The unification scheme of Seyfert galaxies

Spectropolarimetric observations showed polarized broad permitted emission lines in several Seyfert type 2s which are the characteristic of Seyfert type 1s in direct light. The observed broad emission lines in polarized light suggested that these are due to the scattering of BLR emission that is unseen in type 2s in direct light, and strengthened the notion of the unification of Seyfert type 1s and type 2s (Antonucci and Miller 1985; Miller, Goodrich, and Mathews 1991; Heisler, Lumsden, and Bailey 1997).

The unification scheme of Seyfert galaxies hypothesizes that Seyfert type 1s and type 2s constitute the same parent population and appear different solely due to the differing orientations of the dusty molecular obscuring material having a toroidal geometry around the nucleus (Lawrence and Elvis 1982; Antonucci and Miller 1985). In type 1 Seyfert galaxies, the axis of the torus is close to the observer's line-of-sight (*i.e.*, pole-on view) and one observes the AGN and broad line region directly, while in type 2 Seyfert galaxies, the orientation of the dusty torus is such that it intercepts the observer's line of sight (*i.e.*, edge-on view) and shields the AGN as well as broad line region and only the more extended narrow line clouds are observed directly (Antonucci and Miller 1985; Antonucci 1993; Urry *et al.* 1995) (*cf.*, Figure 1.1). In type 2 Seyferts, BLR is hidden by the torus, and therefore broad emission lines are not seen in the nuclear optical spectra, however, in type 1s, BLR is viewed directly, which gives rise to broad emission lines in the optical spectra. The narrow line region (NLR) is extended and seen irrespective to the orientation of torus, which results narrow emission lines in both type 1s and type 2s spectra. In type 2s, free electrons or dust grains located above the opening of the edge-on torus, scatter non-stellar continuum and broad-line photons into our line-of-sight. As scattered radiation is polarized, the presence of broad emission line in spectropolarimetric observations establishes that atleast some Seyfert 2 galaxies harbor Seyfert 1 nuclei in which innermost regions are obscured from our direct view, presumably by dense circumnuclear material. However, it is a matter of debate whether all type 2 Seyfert galaxies posses hidden type 1 nuclei.

1.5 Motivation

One of the most important issues in testing the predictions of the Seyfert unification scheme is the sample selection. There are several studies present in the literature giving results consistent as well as inconsistent with the predictions of Seyfert unification scheme. In this section, I attempt to justify the necessity of examining

the validity of Seyfert unification and briefly detail some of the previous studies, which made an attempt to examine the validity of Seyfert unification scheme.

properties.

1.5.1 Results consistent with the Seyfert unification scheme

1.5.1.1 Polarized broad emission lines in Seyfert type 2s spectra

Spectropolarimetric observations of Seyfert type 2 galaxies reveal the presence of broad permitted emission lines in many type 2 Seyfert galaxies (*e.g.*, NGC 1068, Mrk 348, NGC 4388, NGC 424, NGC 591, NGC 2273, NGC 3081, and NGC 4507 etc.) in polarized light which is evidence that these Seyferts possess hidden broad line regions which are obscured by a dense circumnuclear material (Antonucci and Miller 1985; Miller and Goodrich 1990; Tran, Miller, and Kay 1992; Tran 1995; Young *et al.* 1996; Heisler, Lumsden, and Bailey 1997).

1.5.1.2 Detection of the broad Paschen-β line in the spectra of type 2 Seyferts

The broad component of Paschen-β emission line is seen in several type 2 Seyfert galaxies which confirms the presence of a broad line region that is hidden by the torus at optical wavelengths (Goodrich, Veilleux, and Hill 1994; Veilleux, Sanders, and Kim 1997).

1.5.1.3 The biconical structure of the narrow line region

Collimation of nuclear radiation due to an obscuring torus is seen as biconical structure of narrow line region in several Seyfert type 2 galaxies (Pogge 1988, 1989; Schmitt, Storchi-Bergmann, and Baldwin 1994). To compare the properties of the NLRs of Seyfert 1s and Seyfert 2s, Schmitt *et al.* (2003) studied extended

[OIII] $\lambda5007\text{Å}$ emission using HST observations and noted that there is a higher percentage of Seyfert 1s with halo-like NLRs, while those of Seyfert 2s are more elongated (Schmitt *et al.* 2003). These results are in agreement with the unification scheme which predicts that the conical NLR of Seyfert 1s is observed closer to face-on, while that of Seyfert 2s is closer to edge-on.

1.5.1.4 Systematically higher X-ray absorbing column density in Seyfert type 2s

It has been shown that the absorbing column density in type 2 Seyfert galaxies is systematically significantly higher than that in type 1 Seyferts as expected from the unification scheme, since in type 2 sources, the nuclei are observed through the torus (Turner *et al.* 1997; Smith and Done 1996; Cappi *et al.* 2006). The observed X-ray absorbing column densities range from 10^{22} H atoms cm^{-2} to 10^{24} H atoms cm^{-2} or higher for $\sim 96\%$ of Seyfert type 2s, while for Seyfert type 1s, it range from 10^{20} H atoms cm^{-2} to 10^{22} H atoms cm^{-2} (Risaliti, Maiolino, and Salvati 1999; Bassani *et al.* 1999).

1.5.1.5 Similar pc-scale radio structure in two sub-types

The obscuring torus is optically thin for radio emission and therefore total radio luminosities of Seyfert type 1s and type 2s are expected to be similar and the radio structures are expected to differ only by projection effects. Indeed, Seyfert type 1s and type 2s have been shown to have similar luminosities on various spatial scales (Ulvestad and Wilson 1989). Lal, Shastri, and Gabuzda (2004) reported similar parsec-scale radio structure and nuclear radio luminosity at 5 GHz for the two Seyfert subtypes using a sample in which the two subtypes were matched in several orientation-independent properties. The distribution of the ratio of pc-

scale to kpc-scale flux densities are similar for type 1 and type 2 Seyfert galaxies (Shastri, Lal, and Gabuzda 2003) which is consistent with the unification scheme and suggests non-relativistic nature of nuclear radio outflows.

1.5.2 Results inconsistent with the Seyfert unification scheme

1.5.2.1 Differences in host galaxies

Malkan, Gorjian, and Tam (1998) did a morphological study of a large sample of Seyfert galaxies using HST observations and reported that Seyfert 1 nuclei are hosted in galaxies of earlier Hubble type than Seyfert 2 nuclei and also Seyfert type 2s show higher number of galaxy interactions than Seyfert type 1s. Malkan, Gorjian, and Tam (1998) argued that Seyfert type 2 galaxies are likely to have more nuclear dust and in particular more irregularly distributed dust suggesting that the higher dust-covering fractions in Seyfert 2s might be the reason for their spectroscopic classification and their hidden type 1 nuclei have been obscured by galactic dust rather than by a circumnuclear torus as hypothesized in the unification scheme.

1.5.2.2 Differences in environments

There are studies reporting an intrinsic difference between the environments of Seyfert type 1s and Seyfert type 2s (Laurikainen *et al.* 1994; De Robertis, Yee, and Hayhoe 1998; Dultzin-Hacyan *et al.* 1999). Dultzin-Hacyan *et al.* (1999) reported a significant excess of large companions in Seyfert type 2s within a search radius of ≤ 100 kpc of projected linear distance as well as within a search radius equal to 3 times of the diameter of each Seyfert galaxy. While, for Seyfert type 1s, there is no clear evidence of any such excess of companion galaxies either within 100 kpc or within search radius of 3 times of the diameter of each Seyfert type 1 galaxy. However, Rafanelli, Violato, and Baruffolo (1995) found no significant difference

between the number of neighboring companions in Seyfert type 1s and Seyfert type 2s.

1.5.2.3   Occurrence of starbursts

Buchanan *et al.* (2006) presented IR spectral properties of a sample of Seyfert galaxies and reported that the Seyfert type 2s tend to show a stronger starburst contribution than the Seyfert type 1s in their sample, contrary to similar content of starburst expected from the Seyfert unification scheme. However, this may be due to the selection effect that only those Seyfert 2 galaxies with strong starburst contributions had high enough integrated 12 μm flux densities to fall above the flux limit of their selected sample.

1.5.2.4   Absence of hidden type 1 nuclei in many type 2s

Tran (2001) presented a spectropolarimetric survey of Seyfert type 2 galaxies and reported a large fraction ($\sim 50\%$) of type 2 Seyferts which did not show any broad component of emission lines in polarized light and presumably lack the hidden broad line region (these sources are named as non-hidden broad line region type 2s, *i.e.*, non-HBLR type 2s). Tran et al. (2001) also showed that in comparison to the non-HBLR Type 2s, the HBLR type 2s display distinctly higher radio power relative to their far-infrared output and hotter dust temperatures as indicated by the $f_{25\mu\mathrm{m}}/f_{60\mu\mathrm{m}}$ color. However, the level of obscuration is indistinguishable between the two subtypes of Seyfert galaxies. There can be two intrinsically different populations of Seyfert type 2 galaxies: one harboring an energetic, hidden type 1 nuclei with a broad-line region (*i.e.*, HBLR type 2) and the other one a pure Seyfert type 2 galaxy, with a weak or absent Seyfert type 1 nuclei and a strong, perhaps dominating starburst component (*i.e.*, non-HBLR type 2) (Tran 2001). There is

also evidence that the fraction of detected HBLRs increases with the radio power of AGN (Tran 2003). Thus, all Seyfert type 2 galaxies may not be intrinsically similar in nature, and evolutionary processes may be at work.

1.5.2.5   Lack of X-ray absorption in several Seyfert 2s

There are cases of type 2 Seyferts showing no or low X-ray absorption (Caccianiga *et al.* 2004; Corral *et al.* 2005; Barcons, Carrera, and Ceballos 2003; Panessa and Bassani 2002; Pappa *et al.* 2001) and Seyfert type 1s with high X-ray absorption (Cappi *et al.* 2006; Mateos *et al.* 2005). Panessa and Bassani (2002) reported that $\sim 10\%$ - 30% of Seyfert type 2s lack sufficient X-ray absorption ($N_H \leq 10^{22}$ cm^{-2}), and the fraction of unabsorbed type 2s appears to increase progressively at lower luminosities. They suggested that the obscuration and orientation based unified model for Seyfert galaxies may not be applicable in such sources since the pc-scale molecular torus is not likely to be responsible for the low column density observed, instead the absorption observed is likely to originate at larger scales. However, the occurrence of unabsorbed type 2s can be explained by an observational selection effect, *i.e.*, in these sources, the optical light of the host galaxy outshines the AGN continuum and broad lines (Severgnini *et al.* 2003; Silverman *et al.* 2005; Page *et al.* 2006; Garcet *et al.* 2007).

1.5.3   Need to test the predictions of Seyfert unification scheme using a rigorously selected sample

In above sections I reviewed some of the studies giving results consistent as well as inconsistent with the Seyfert unification scheme. Some of the inconsistent results indeed may be due to biases present in their respective samples. Here I discuss the possible selection effects generally inherent in the samples selected at different electromagnetic wavelengths and emphasize the need for testing Seyfert unification

with rigorously selected samples.

There are optically selected Seyfert samples, *e.g.*, CfA sample (Huchra and Burg 1992), Palomar sample (Ho, Filippenko, and Sargent 1995), where AGNs are identified by diagnostic intensity ratios and widths of optical emission lines. The samples selected at optical wavelengths are generally biased against heavily obscured sources and also complications arise from dilution of the AGN signal by the emission from HII regions that might be included in the spectrograph aperture. Weaker AGNs may be outshined by brighter contaminating HII regions, especially in late-type galaxies undergoing vigorous star formation. This effect may account in part for the apparent dearth of AGNs among late-type galaxies in the Palomar survey (Ho, Filippenko, and Sargent 1997). The inclination angle of host galaxy may affect the observed optical properties and therefore it may introduce a bias. However, Ho, Filippenko, and Sargent (1997) argued that selection biases due to inclination effects do not appear to be severe in the Palomar sample.

The Seyfert samples selected on the basis of ultraviolet excess (*e.g.*, Markarian survey) are biased toward sources with unusually low dust extinction or exceptionally blue intrinsic spectra. It has been shown that Seyfert 2 nuclei display weaker, featureless blue continua than Seyfert 1 nuclei in their observed spectra (*e.g.*, Koski (1978)). Therefore, samples selected by ultraviolet or blue flux will have an over-representation of Seyfert 2 galaxies with intrinsically luminous, typically blue nuclei or alternatively, Seyfert 2 galaxies with unusually high levels of ultraviolet emission arising from exterior to the nucleus, such as in the near-nuclear or circumnuclear star-forming regions. Thus, ultraviolet selected samples contain mismatched populations of type 1s and type 2s. This selection bias may account for the studies which report that Seyfert 2s tend to have a higher incidence of nuclear star formation compared to Seyfert 1s (*e.g.*, Colina *et al.* (1997); González Delgado *et al.* (1998)).

It has been argued that the IR selected Seyfert samples minimize wavelength-dependent selection effects (*e.g.*, Spinoglio and Malkan (1989)) assuming that the

IR luminosity carries an approximately constant fraction of the AGN bolometric luminosity. The samples selected using 25 μm and 60 μm luminosities may have the advantage of being less susceptible to biases (Keel *et al.* 1994; Kinney *et al.* 2000), nonetheless, selection by mid-IR and far-IR emission may favor dusty objects, as well as those which have enhanced levels of star formation. Kinney *et al.* (2000) noted that the sample used in Schmitt *et al.* (2001), has a preponderance of highly inclined (edge-on) systems. Also, selection by far-IR colors can identify AGNs effectively, but by no means produces a complete sample (de Grijp *et al.* 1985; de Grijp, Lub, and Miley 1987; Keel, de Grijp, and Miley 1988) and therefore IRAS-based Seyfert samples are especially incomplete in low-luminosity sources because of the relatively high contribution from the host galaxy.

X-ray selected samples have also been used to examine the validity of Seyfert unification (Awaki *et al.* 1991; Smith and Done 1996; Turner *et al.* 1997, 1998; Bassani *et al.* 1999), however, X-ray photons below 10 keV are absorbed in heavily obscured Compton-thick AGN (*i.e.*, $N_H \geq 10^{24}$ cm^{-2}) and therefore the X-ray samples selected from flux limited surveys which are sensitive to E $\leq$ 10 keV, are likely to be biased against less luminous and heavily obscured sources. Using a sample of type 2 Seyferts based on [OIII] λ5007Å luminosity, Maiolino *et al.* (1998) and Risaliti, Maiolino, and Salvati (1999) have shown an increased number of heavily obscured sources, suggesting inherent biases against the obscured and faint sources in X-ray selected samples. Hard X-ray selected samples are supposed to be less biased but can not be guaranteed to be free from biases against heavily obscured Compton-thick and low luminosity AGNs (*e.g.*, Heckman *et al.* (2005); Wang, Mao, and Wei (2009)). Recent hard X-ray Seyfert samples based on *INTEGRAL* and *Swift*/BAT surveys preferentially contain relatively large number of high luminosity and less absorbed Seyferts (Tueller *et al.* 2008; Treister, Urry, and Virani 2009; Beckmann *et al.* 2009), possibly due to less effective area which limits the sensitivity only to bright ($\sim$10^{-11} erg s^{-1} cm^{-2}) sources. Therefore, hard X-ray selected samples may miss the low luminosity and highly obscured AGNs.

Indeed, sample selection is very crucial in testing the predictions of the Seyfert unification. For example, early studies by Meurs and Wilson (1984) reported that in their samples Seyfert 2s have higher radio luminosities than Seyfert 1s, and Heckman *et al.* (1989) found that Seyfert 2s have higher molecular CO gas masses than Seyfert 1s. However, further studies with improved sample selection criteria showed that both types have similar radio luminosities (Rush, Malkan, and Edelson 1996) and similar CO masses (Maiolino *et al.* 1997). The quest of testing the validity and limitations of the Seyfert unification scheme with more improved and well defined samples still continues and recent studies by Cappi *et al.* (2006); Dadina (2008); Beckmann *et al.* (2009) used less biased optically and X-ray selected samples and reported results broadly consistent with the unification, nonetheless, issues related to sample selection still remain. Keeping the above arguments in mind I aim to test the predictions of the Seyfert unification scheme using a rigorously selected sample. The details of sample and its selection criteria are described in Chapter 2.

1.6 Thesis outline

In this thesis I examine the validity and limitations of Seyfert unification scheme by studying mainly X-ray and radio properties of our rigorously selected samples of Seyfert galaxies. Chapter 2 details the sample selection criteria and the samples which I have used to test the predictions of the unification scheme. In Chapter 3, I present X-ray data reduction, and analysis methods for *XMM-Newton* and *Suzaku* observations. For the radio study of our sources I used GMRT interferometric observations and present radio interferometric observational techniques, data reduction methods, specifications of GMRT in Chapter 4. In Chapter 5, I present X-ray spectral fittings and analysis for our sample sources using *XMM-Newton* EPIC pn archival data. Furthermore, in Chapter 5, I discuss the statistical comparisons of X-ray spectral properties (*e.g.*, X-ray luminosities in soft and hard

bands, absorbing column density, properties of Fe Kα line, soft excess and reflection components, X-ray - radio correlations etc.) of the two Seyferts subclasses in the framework of Seyfert unification scheme. In Chapter 6, I present a case study of broad-band X-ray spectral analysis of heavily obscured, *i.e.*, Compton-thick Seyfert galaxy NGC 5135 using Suzaku observations. Radio imaging and spectral studies of our sample of Seyfert galaxies is presented in Chapter 7, wherein, I make a statistical comparison of the radio properties of the two Seyfert subclasses in the framework of the Seyfert unification scheme. Chapter 8 summarizes the thesis work and conclusions of our results in the framework of the unification scheme. In this chapter I also discuss the validity and limitations of the Seyfert unification scheme and outline my future work.

Chapter 2

Sample selection and methodology

2.1 Sample selection

In the section 1.5.3 I discussed how samples from the flux limited surveys (*e.g.*, IR optical, UV, X-ray) can be biased. Rigorous tests of the predictions of the unification scheme can be done, however, by ensuring that the two Seyfert subtypes being compared are intrinsically similar within the framework of the unification scheme. I attempt to test the validity of the Seyfert unification scheme using Seyfert samples which are based on matching the orientation-independent and isotropic parameters of AGN and the host galaxies. In this chapter I discuss the merits and selection criteria of our samples selected for the study of X-ray and radio properties of Seyfert galaxies in the framework of the unification scheme.

2.1.1 Sample selection criteria

In order to rigorously test the predictions of the Seyfert unification scheme, it is essential that the two Seyfert subclasses being compared should be intrinsically similar within the framework of the unification scheme. This can be achieved by matching the two Seyfert subclasses in the properties of AGN and host galaxy which are independent of the orientation of AGN-host galaxy system (Lal, Shastri,

and Gabuzda 2001). Since, the Seyfert unification scheme is based on the orientation of the obscuring torus around AGN and different observed properties of type 1s and type 2s are supposedly due to the differing orientations of the torus. Therefore, it is important to choose the AGN and host galaxy parameters which are independent of the orientation and truly represents the characteristic properties of AGN and host galaxy. I choose five orientation-independent parameters, *i.e.*, cosmological redshift, luminosity of [OIII] $\lambda 5007$Å emission line, Hubble stage of the host galaxy and absolute stellar magnitude of the host galaxy, absolute magnitude of the bulge of host galaxy, which are intimately linked to the evolution of AGN as well as host galaxy.

The sample is selected such that the two Seyfert subclasses have matched distributions of the orientation-independent parameters of AGN and host galaxy (*cf.*, Figures 2.1, 2.2). The sources which were deviating in matching the type 1 and type 2 distributions of the orientation-independent parameters were left out. In other words, the sources should lie within the same range of values for a given parameter to enter into the sample. Also, it was ensured that in a given bin of a parameter distribution, type 1s should not outnumber the type 2s and vice-versa.

The orientation-independent properties are discussed in the following sections and the matched distributions of the orientation-independent parameters for the two Seyfert subtypes are shown in Figures 2.1, 2.2 .

2.1.2   Orientation-independent parameters

In our sample selection, five orientation-independent parameters of AGN and host galaxy, have been considered and these parameters are intimately linked to the evolution of AGN and host galaxy. The description of sample selection parameters is given below.

2.1.2.1 Cosmological redshift

Cosmological redshift is an orientation-independent parameter and allows us to have control over cosmological evolution effect. In my samples, two Seyferts sub-classes have similar distributions of redshift (*cf.*, Figures 2.1, 2.2), which ensures that Seyfert type 1s and type 2s are not from two completely different cosmological epochs. All the sources of my samples are nearby (*i.e.*, low redshift, z $\leq$ 0.05).

2.1.2.2 [OIII] λ5007Å line luminosity

[OIII] λ5007Å line emission originates from the narrow line region and its luminosity ($L_{[OIII]}$) is correlated with the nuclear ionizing continuum (Yee, Stockman, and Green 1981). There are studies suggesting that $L_{[OIII]}$ can be considered as a proxy for the intrinsic AGN power and is orientation-independent (Nelson and Whittle 1995; Whittle 1992), even though spatially [OIII] λ5007Å emission could be distributed anisotropically (Pogge 1989; Evans *et al.* 1991). We obtain $L_{[OIII]}$ for our sample sources from the literature (mainly from Whittle (1992); Schmitt *et al.* (2003)). The two Seyfert subtypes in our samples have matched distributions of [OIII] λ5007Å line luminosity (*cf.*, Figures 2.1, 2.2), ensuring that the two subtypes are of similar intrinsic AGN power.

2.1.2.3 Hubble type of the host galaxy

There have been studies which suggest that Seyfert type 1s are preferentially hosted in galaxies of earlier Hubble type than type 2s (*e.g.*, Malkan, Gorjian, and Tam (1998)). The Hubble type of a galaxy depends on the size of central bulge relative to flattened-disk size (Sandage 1975) and is independent of the galaxy/AGN orientation *w.r.t.* the observer's line-of-sight. In our samples type 1s and type 2s have matched distributions of Hubble stage parameter, which ensures that we are not comparing Seyfert type 1s and type 2 hosted in completely different types of host galaxies.

2.1.2.4   Absolute stellar magnitude of the host galaxy

Absolute stellar magnitude of the host galaxy is as an orientation-independent and a characteristic property of host galaxy. We use total absolute stellar magnitude of the host galaxy which is corrected for non-stellar and emission line flux, redshift (K), the internal absorption and the Galactic absorption. The corrected B-band absolute stellar magnitude for the sample sources are given in Lal (2002) and Whittle (1992). The corrected total B-band absolute stellar magnitude ($M_B^{T,corrected}$) can be represented as

$$M_B^{T,corrected} = M_B^T + \Delta m_A + \Delta m_K + \Delta m_i + \Delta m_G \qquad (2.1)$$

where, M_B^T is the uncorrected B-band absolute stellar magnitude and Δm_A, Δm_K, Δm_i, Δm_G are the correction factors for the non-stellar continuum and emission line flux, redshift (K), the internal absorption, the Galactic absorption, respectively. RC3 catalog (de Vaucouleurs *et al.* 1991) gives the B-band absolute stellar magnitude corrected for the redshift (K) (Δm_K), the internal absorption (Δm_i) and the Galactic absorption (Δm_G). To estimate the correction for the non-stellar continuum and emission line fluxes (Δm_A), Whittle (1992) describes a formalism which uses line fluxes of [OIII] λ5007Å and H$_\beta$.

2.1.2.5   Absolute magnitude of the bulge

The absolute magnitude (luminosity/mass) of the bulge of the host galaxy is correlated to the mass of the central supermassive black hole (Kormendy and Richstone 1995). Therefore, the absolute magnitude of the bulge can be considered as a proxy of the mass of supermassive black hole, arguably a fundamental parameter of the AGN system. The absolute B-band magnitude of the bulge component of a host galaxy ($M_{B,bulge}$) is an orientation-independent property and in our samples the two subtypes are matched in $M_{B,bulge}$ distributions (*cf.*, Figures 2.1, 2.2), indicating that the black hole mass distributions of the two Seyfert subtypes are not

much different. The absolute bulge magnitude values for our sample sources are given in Lal (2002); Whittle (1992). The absolute B-band bulge magnitude have been derived by subtracting host galaxy disk magnitude (*i.e.*, disk correction factor Δm_{disk}) from the total absolute magnitude of host galaxy.

$$M_{B,bulge} = M_{B,Total} - \Delta m_{disk} \tag{2.2}$$

The disk correction factor for bulge magnitude was derived using an empirical relation given in Simien and de Vaucouleurs (1986).

$$\Delta m_{disk} = 0.324\tau - 0.054\tau^2 + 0.0047\tau^3 \tag{2.3}$$

where $\tau = $ T + 5, and T is the Hubble stage of the host galaxy. Thus, for elliptical galaxies (T = -5) $\Delta m_{disk} = 0$, while for Sc type spiral galaxy (T = +5) $\Delta m_{disk} =$ -2.54. The Δm_{disk} for most Seyfert galaxies is large and usually dominates over other correction terms applied to M_{Total}.

In case a source had different values in different studies for a given selection parameter, we opted the value given in the latest study and/or obtained by using improved observing equipment. For example, [OIII] luminosity and Hubble stage values obtained from HST observations (Schmitt *et al.* (2003); Malkan, Gorjian, and Tam (1998), respectively) have been preferred over earlier values (*e.g.*, Whittle (1992)). In order to minimize the effects of obscuration by the host galaxy disk on the optical properties, Seyferts with edge-on host galaxies (*i.e.*, ratio of minor to major isophotal diameter axis less than half) were excluded, noting the evidence that there is no correlation between AGN and host galaxy axis (Pringle *et al.* 1999; Nagar and Wilson 1999).

2.2 Our Seyfert galaxy samples

Taking into account the observational feasibility and availability, I used two different Seyfert samples to study the X-ray and radio properties of Seyfert galaxies,

viz., the "X-ray sample" and the "Radio sample". Each sample consists of 20 Seyfert galaxies (10 type 1s and 10 type 2s) and 11 Seyferts galaxies (5 type 1s and 6 type 2s) are common to both. Indeed, it is a possible to increase the sample size following the same sample selection criteria, however, I would like to emphasize that the more important is the sample selection criteria and not the sample size. The samples consist of 20 Seyfert galaxies are large enough to rigorously test the predictions of the Seyfert unification scheme. Larger but heterogeneous and biased sample is likely to give incorrect conclusions. Moreover, our moderate size sample that has fairly limited span in all the sample selection parameters (*i.e.*, redshift, [OIII] luminosity, absolute magnitude of the bulge, total stellar luminosity, Hubble type of the host galaxy), is not complete. The essence of our sample selection is the intrinsic similarity between the two subtypes in the framework of the unification scheme and adherence to the completeness condition may contradict the essence of our sample selection.

2.2.1 The X-ray sample

The X-ray sample is taken from Lal (2002) and consists of 20 (10 type 1 and 10 type 2) Seyfert galaxies. This sample was formulated by Lal (2002) (mainly derived from Whittle (1992)) to study the nuclear parsec-scale radio properties in the framework of the Seyfert unification scheme and I attempt to test the predictions of the Seyfert unification scheme in X-ray regime using the same sample. Although the sample was formulated to study pc-scale radio emission and is constrained by VLBI observing feasibility criteria, X-ray observations are also available for most of the sample sources.

In this sample, Seyfert galaxies are defined as radio quiet ($\frac{F_{5\ GHz}}{F_{B-band}} < 10$) (Kellermann *et al.* 1989), low optical luminosity AGN ($M_B > $ -23) (Schmidt and Green 1983), hosted in spiral or lenticular galaxies (Weedman 1977). All the Seyferts conforming to this definition and with an observed broad permitted line are cat-

egorized as Seyfert of type 1s. Thus all the intermediate subclasses of Seyferts, *i.e.*, 1.0, 1.2, 1.5, 1.8, 1.9 (which show a broad permitted emission line component in their optical spectra (Osterbrock 1981)) are grouped as type 1s, while those which show only narrow permitted emission lines are considered as type 2 Seyferts. The X-ray sample sources and their orientation-independent parameters are given in Table 2.1.

2.2.2 The Radio sample

To test the predictions of the Seyfert unification in the radio regime, I study radio properties of a Seyfert sample using the GMRT observations carried out at 240 MHz, 610 MHz and NRAO VLA Sky Survey (NVSS) observations at 1.4 GHz and 5 GHz VLA observations from the literature. I selected the radio sample of Seyfert galaxies using the same sample selection criteria (*i.e.*, matching the distributions of the orientations-independent parameters for Seyfert type 1s and type 2s) as for the X-ray sample (*i.e.*, Lal (2002) sample). Considering the GMRT observing feasibility and time the sample size is restricted to 20 (10 type 1s and 10 type 2s) Seyfert galaxies. Table 2.2 lists the radio sample sources and values of orientation-independent parameters. Figure 2.2 shows the matched distributions of orientation independent parameters (redshift, $L_{[OIII]}$, Hubble stage (T) of the host galaxy, $M_{B,Total}$, $M_{B,Bulge}$) for type 1s and type 2s of the radio sample.
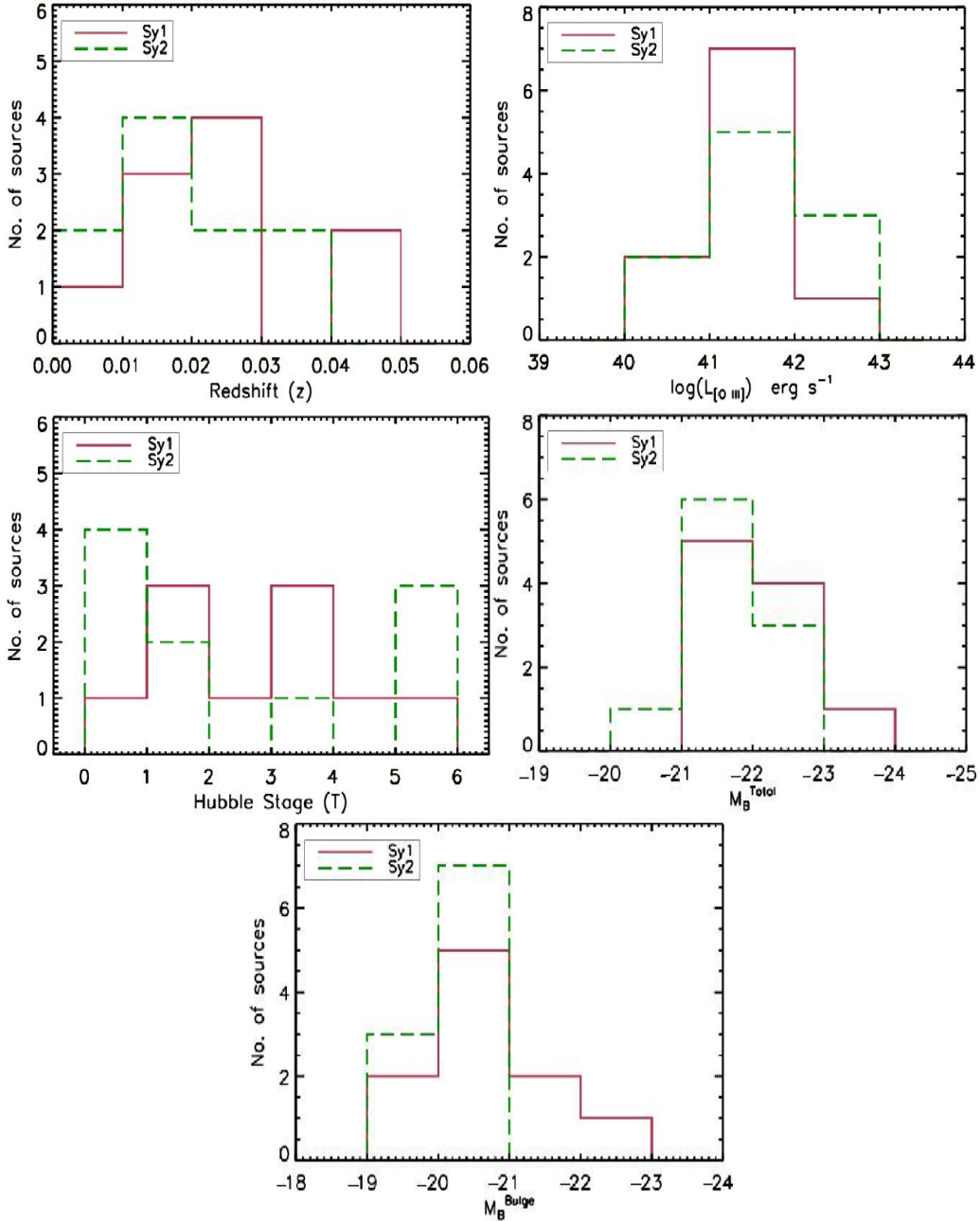
Figure 2.1: Distributions of the redshift, [OIII] $\lambda 5007\text{Å}$ luminosity, Hubble stage (T), total absolute stellar magnitude and absolute magnitude of the bulge, for the two Seyfert subtypes of the X-ray sample.

Table 2.1: The X-ray sample

Name	RA	Dec	T[a]	Redshift	$M_{B_{Total}}^a$	$M_{B_{Bulge}}^a$	$\log L_{[OIII]}$	Ref.
			Seyfert type 1s					
MCG+8-11-11	05 54 53.61	+46 26 21.61	1.0	0.025	-23.1	-22.10	41.95	2
MRK 1218	08 38 10.94	+24 53 43.00	1.0	0.029	-21.1	-20.04	41.50	3
NGC 2639	08 43 38.08	+50 12 20.00	1.0	0.011	-21.4	-20.33	40.45	4
NGC 4151	12 10 32.58	+39 24 20.63	2.0	0.003	-21.2	-19.99	41.35	1
MRK 766	12 18 26.51	+29 48 46.34	1.0	0.013	-21.0	-20.01	41.61	2
MRK 231	12 56 14.23	+56 52 25.24	5.0	0.042	-22.3	-19.75	41.96	3
ARK 564	22 42 39.35	+29 43 31.31	3.0	0.024	-21.7	-20.11	41.38	1
NGC 7469	23 03 15.62	+08 52 26.39	1.0	0.016	-22.0	-20.99	41.51	1
MRK 926	23 04 43.47	-08 41 08.60	1.0	0.047	-22.4	-21.39	42.25	1
MRK 530	23 18 56.62	+00 14 38.23	3.0	0.030	-22.7	-21.20	40.98	1
			Seyfert type 2s					
MRK 348	00 48 47.14	+31 57 25.09	0.0	0.015	-21.1	-20.27	41.31	2
MRK 1	01 16 07.25	+33 05 22.40	0.0	0.016	-20.3	-19.46	41.52	1
NGC 2273	06 50 08.66	+60 50 44.90	1.0	0.006	-21.0	-19.97	40.09	5
MRK 78	07 42 41.73	+65 10 37.46	1.0	0.037	-22.0	-20.78	42.31	1
NGC 5135	13 25 44.06	-29 50 01.20	2.0	0.014	-22.1	-20.91	41.20	6
MRK 477	14 40 38.09	+53 30 15.86	0.0	0.038	-21.0	-20.13	42.69	1
NGC 5929	15 26 06.16	+41 40 14.40	2.0	0.009	-21.4	-20.13	40.21	1
NGC 7212	22 07 01.30	+10 13 52.00	1.0	0.027	-21.2	-20.22	42.15	2
MRK 533	23 27 56.72	+08 46 44.53	4.0	0.029	-22.7	-20.68	41.99	2
NGC 7682	23 29 03.93	+03 32 00.00	2.0	0.017	-21.1	-19.88	41.16	1

Notes: Col. (1), source name; cols. (2) and (3), right ascension (hours, minutes, and seconds) and declination (degrees, arcminutes, and arcseconds), J2000; col. (4), Hubble type; col. (5), cosmological redshift; col. (6), total stellar absolute magnitude corrected for nuclear non-stellar continuum and emission line flux, redshift (K) correction, the internal absorption and the Galactic absorption; col. (7) absolute bulge magnitude in B band; col. (8), [OIII] $\lambda5007$Å luminosity in log; col. (9), references for [OIII] $\lambda5007$Å luminosity. Ref. - 1: Whittle (1992), 2: Schmitt *et al.* (2003), 3: Dahari and De Robertis (1988), 4: Panessa *et al.* (2006), 5: Ferruit, Wilson, and Mulchaey (2000), 6: Polletta *et al.* (1996), a: Lal (2002).
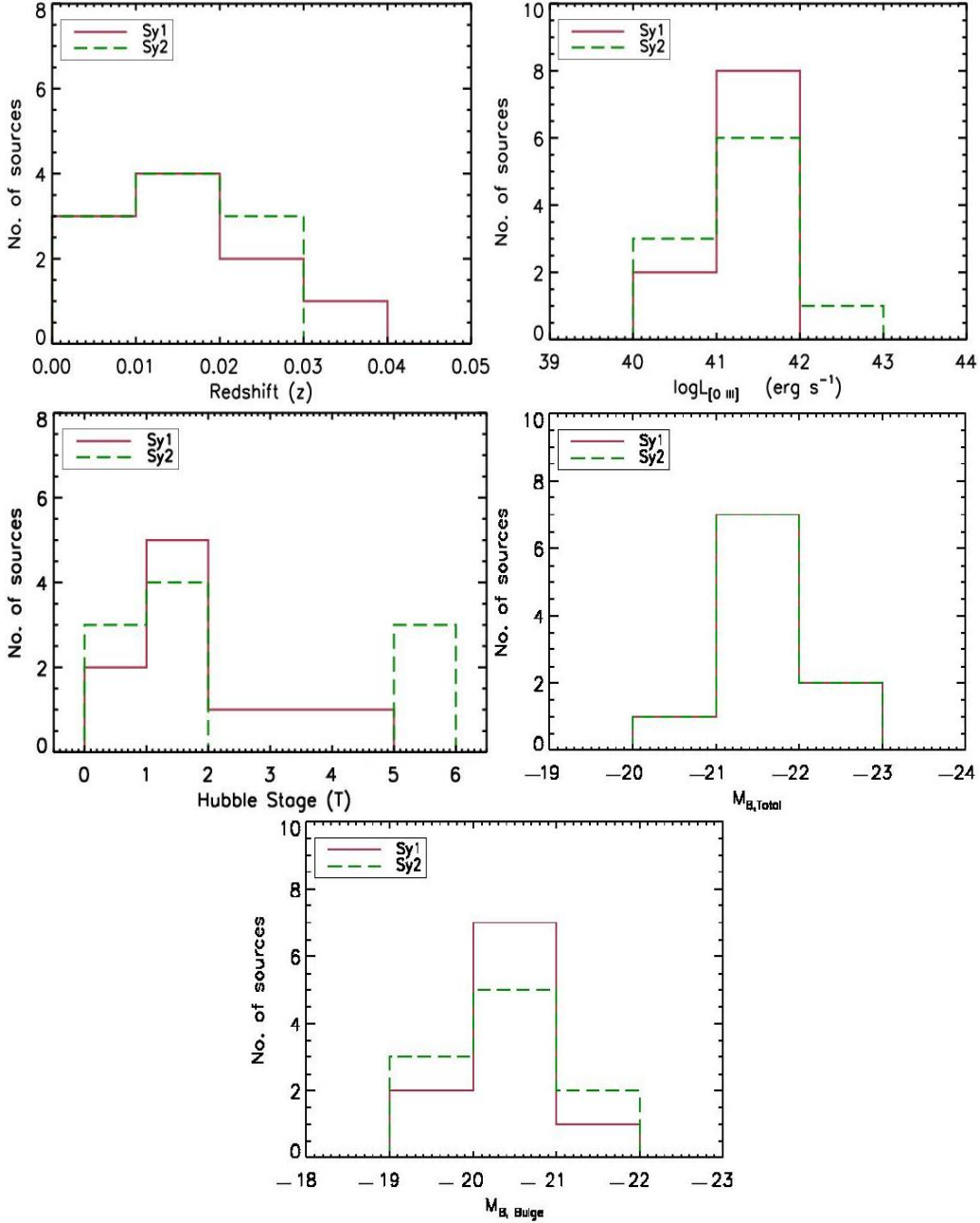
Figure 2.2: Distributions of the redshift, [OIII] $\lambda 5007$Å luminosity, Hubble Stage (T), total absolute stellar magnitude and absolute magnitude of the bulge for the two Seyfert subtypes of the radio sample.

Table 2.2: The radio sample

Source Name	RA	Dec	Hubble Stage (T)	Ref.	Redshift	$M^1_{B_{Total}}$	$M^1_{B_{Bulge}}$	$\log L_{[OIII]}$	Ref.
				Seyfert type 1s					
MRK 6	06 52 12.2	+74 25 37	0	MGT	0.019	-20.30	-19.44	41.79	2
NGC 3227	10 23 30.6	+19 51 54	1	RC3	0.004	-21.47	-20.46	40.31	1
NGC 3516	11 06 47.5	+72 34 07	0	MGT	0.009	-21.61	-20.88	41.07	2
NGC 4151	12 10 32.6	+39 24 21	2	RC3	0.003	-21.20	-19.99	41.35	1
MRK 766	12 18 26.5	+29 48 46	3	MGT	0.013	-21.00	-20.01	41.61	2
MRK 279	13 53 03.4	+69 18 30	1	MGT	0.030	-21.59	-20.98	41.46	1
NGC 5548	14 17 59.5	+25 08 12	1	MGT	0.017	-21.82	-20.89	41.42	2
ARK 564	22 42 39.3	+29 43 31	1	RC3	0.025	-21.70	-20.11	41.38	1
NGC 7469	23 03 15.6	+08 52 26	4	MGT	0.016	-22.00	-20.99	41.51	1
MRK 530	23 18 56.6	+00 14 38	1	MGT	0.029	-22.70	-21.20	40.98	1
				Seyfert type 2s					
MRK 348	00 48 47.1	+31 57 25	0	MGT	0.015	-21.10	-20.27	41.31	2
MRK 1	01 16 07.2	+33 05 22	5	MGT	0.016	-20.30	-19.46	41.52	1
MRK 1066	02 59 58.6	+36 49 14	5	MGT	0.012	-21.06	-20.45	40.88	1
NGC 2110	05 52 11.4	-07 27 22	1	MGT	0.008	-21.57	-20.72	40.35	1
NGC 2273	06 50 08.6	+60 50 45	1	RC3	0.006	-21.00	-19.97	40.09	5
NGC 5252	13 38 15.9	+04 32 33	0	MGT	0.023	-21.96	-21.35	41.41	6
NGC 5728	14 42 23.9	-17 15 11	1	RC3	0.009	-22.35	-21.12	41.11	1
NGC 7212	22 07 01.3	+10 13 52	1	RC3	0.027	-21.2	-20.22	42.15	2
NGC 7682	23 29 03.9	+03 32 00	0	MGT	0.017	-21.1	-19.88	41.16	1
MRK 533	23 27 56.7	+08 46 45	5	MGT	0.029	-22.7	-20.68	41.99	2

Notes: Col. (1), source name; cols. (2) and (3), right ascension (hours, minutes, and seconds) and declination (degrees, arcminutes, and arcseconds), J2000; col. (4), Hubble Stage; col. (5), References for T; col. (6), cosmological redshift; col. (7), total stellar absolute magnitude corrected for nuclear non-stellar continuum and emission line flux, redshift correction (K), the internal absorption and the Galactic absorption; col. (8) absolute bulge magnitude in B band; col. (9), [OIII] λ5007Å luminosity in log; col. (10), references for [OIII] λ5007Å luminosity. Ref. - MGT: Malkan, Gorjian, and Tam (1998), RC3: de Vaucouleurs *et al.* (1991), 1: Whittle (1992), 2: Schmitt *et al.* (2003), 3: Dahari and De Robertis (1988), 4: Panessa *et al.* (2006), 5: Ferruit, Wilson, and Mulchaey (2000), 6: Polletta *et al.* (1996).

Chapter 3

X-ray observational techniques and data reductions

3.1 Introduction: Observing at X-ray wavelengths

X-ray photons coming from cosmic sources are absorbed by the Earth's atmosphere and therefore, in order to study the X-ray emission properties of cosmic sources, X-ray detectors are to be placed above the Earth's atmosphere using balloons, sounding rockets and satellites. Unlike balloon and rocket, satellite instruments can make continuous, long time observations. In 1970s, dedicated X-ray astronomy satellites, *e.g.*, *Uhuru*, *Ariel 5*, *SAS-3*, *OSO-8*, and *HEAO-1* were launched to study the X-ray emission from a variety of astronomical sources, *e.g.*, active galaxies, binary stars with compact companion (such as black holes, neutron stars, white dwarfs), supernovae and their remnants. Seyfert galaxies nuclei emit a substantial fraction of their bolometric luminosity in X-ray wavelengths. I use *XMM-Newton* and *Suzaku* (only for NGC 5135) X-ray observations to study the X-ray spectral properties of Seyfert galaxies of my sample. The following sections describe the *XMM-Newton*, *Suzaku* instruments and their data reduction as well as analysis procedures.

3.2 *XMM-Newton* X-ray observations

XMM-Newton is one of the cornerstone missions of European Space Agency and was launched on December 10th, 1999. There are three types of science instruments are boarded on *XMM-Newton*, *viz*., European Photon Imaging Camera (EPIC), Reflection Grating Spectrometer (RGS) and Optical Monitor (OM). There are three units of EPIC, two are equipped with MOS (Metal Oxide Semi-conductor) CCD arrays and the third one with pn CCD arrays. The *XMM-Newton* EPIC cameras offer the possibility to perform extremely sensitive imaging observations over a field of view of $30'$ and in the energy range of 0.15 to 15 keV, with moderate spectral ($E/\Delta E \sim 20$ - 50) and angular resolution (FWHM $\sim 6''$). The RGS is best suited for high resolution ($E/\Delta E \sim 100$ to 500) X-ray spectroscopy in the energy range ~ 0.33 - 2.5 keV (~ 5 - 38 Å). OM has three optical and three UV filters over the wavelength range of 180 to 600 nm and can provide images of the central part of the field of view with a resolution of $\sim 1''$ and low-resolution grism spectra as well as high time-resolution photometry of the optical counterparts of X-ray sources. The detailed description of the instruments aboard in *XMM-Newton* is given in *XMM-Newton* user support document[1].

I use the *XMM-Newton* EPIC camera observations as these are best suited to study the X-ray emitting and absorbing components by modeling the broad-band ~ 0.5 - 15 keV spectra. *XMM-Newton* EPIC observations were available for 17/20 of the sample sources. I prefer to use EPIC pn observations over EPIC MOS observations since latter one is susceptible to pile-up for X-ray bright sources and a few sources did not had MOS observations. Both EPIC pn and EPIC MOS have similar imaging/spectral capabilities except that the MOS CCD array has slightly better spatial and spectral resolution (see, Table 3.1). Thus, EPIC pn is equally as good as MOS for our purpose of obtaining the X-ray spectral parameters (*e.g.*, photon index, absorbing column density) in 0.5 - 10 keV band. Table 3.1

---

[1]http://xmm.esac.esa.int/external/xmm_user_support/documentation/technical/

lists the energy band-pass, sensitivity, field of view, pixel sizes, timing and spectral resolutions of all the *XMM-Newton* detectors.

Table 3.1: *XMM-Newton* characteristics - an overview

Instrument	EPIC MOS	EPIC pn	RGS	OM
Energy Band-pass	0.15 - 12 keV	0.15 - 15 keV	0.35 - 2.5 keV [1]	180 - 600 nm
Orbital target vis.[2]	5 - 135 ks	5 - 135 ks	5 - 135 ks	5 - 145 ks
Sensitivity [3]	$\sim 10^{-14}$ [4]	$\sim 10^{-14}$ [4]	$\sim 8\times10^{-5}$ [5]	20.7 mag [6]
Field of view (FOV)	$30'$	$30'$ [7]	$\sim 5'$	$17'$
PSF (FWHM)	$5''$	$6''$	N/A	$1.4'' - 2.0''$
Pixel size	40 μm ($1.1''$)	150 μm ($4.1''$)	81 μm (9×10^{-3} Å) [7]	$\sim 0.48''$ [8]
Timing resolution [9]	1.75 ms	0.03 ms	0.6 s	0.5 s
Spectral resolution [10]	~ 70 eV	~ 80 eV	0.04/0.025 Å [11]	350[12]

Notes: (1) In the -1 grating order (wavelength range: 5 - 35 Å).

(2) The maximum continuous observing time is limited by the time available for observation per orbit and minimum time is limited by the observing efficiency. *XMM-Newton* science observations can only be performed outside the Earth's radiation belts.

(3) Considering observing time of 10 ks.

(4) In the range of 0.15 - 15.0 keV and in units of erg s^{-1} cm^{-2}.

(5) In units of photons s^{-1} cm^{-2}.

(6) 5σ detection of an A0 star in 1000 s.

(7) In spectroscopy mode (standard 3×3 pixel on-chip binning applied).

(8) $1''$ with 2×2 binning in default configuration mode.

(9) In fast data acquisition mode.

(10) At 1 keV energy. At the energy of Fe Kα (6.4 keV), the energy resolution of both EPIC cameras is ~ 150 eV.

(11) Spectral resolution at 1 keV for -1 and -2 grating orders.

(12) Resolving power ($\lambda/\Delta\lambda$) with UV and optical grism.

3.2.1 Comparison of *XMM-Newton* with other current generation X-ray observatories

XMM-Newton offers high sensitivity, high-resolution spectroscopy (RGS) with simultaneous medium-resolution spectroscopy and imaging (EPIC) and optical/UV observations (OM). EPIC has high sensitivity in $\sim$ 0.15 - 15.0 keV energy band and can provide high time resolution as well. Table 3.2 shows the comparison of *XMM-Newton* capabilities with other current generation X-ray observatories. Figure 3.1 shows the comparison of effective areas of *XMM-Newton*, with *Chandra*, *Suzaku* and future mission *Astro-H*. It is evident that *XMM-Newton* has the largest effective area in 0.2 - 10.0 keV energy range and thus it is more sensitive than others in this energy band. Owing to high sensitivity, *XMM-Newton* is very suitable for studying faint and obscured sources (*i.e.*, in Seyfert galaxies AGN emission is supposedly obscured) and that is why I preferred to use *XMM-Newton* observations.
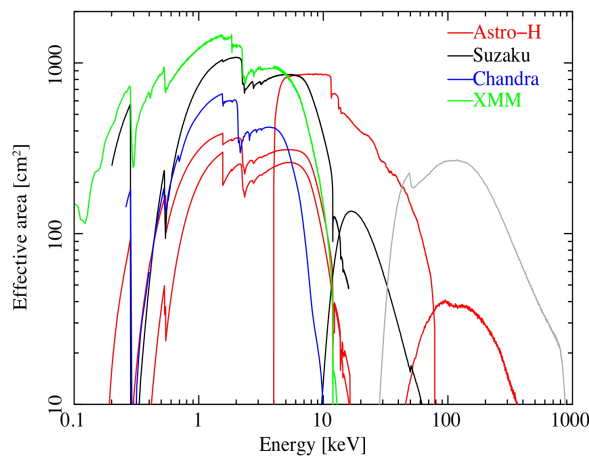
Figure 3.1: Comparison of effective areas of *XMM-Newton*, *Chandra*, *Suzaku* and future mission *Astro-H*.

Table 3.2: Comparison of *XMM-Newton* with other X-ray observatories

X-ray telescope	Mirror PSF FWHM [$''$]	Energy range [keV]	A_e at 1 keV [cm^2]^a	Orbital target visibility [hr]	Energy resolution at 1 keV [eV]
XMM-Newton	6	0.15 - 15	4650	36.7[b]	4 (RGS)
Chandra	0.5[c]	0.1 - 10	555 (ACIS-S)	44.4[b]	1 (HETG)
ROSAT	3.5	0.1 - 2.4	400	1.3[d]	500
ASCA	73	0.5 - 10	350	0.9[d]	100
Suzaku	120 (XIS)	0.2 - 600	1760 (XIS)	0.72[d]	50

Notes: a: Mirror effective area.

b: Orbital visibility outside the particle-radiation dominated zone.

c: The *Chandra* ACIS spatial resolution that is limited by the physical size of the CCD pixels and not by the mirrors.

d: Low orbit with Earth occultation.

3.2.2 *XMM-Newton* data reduction procedure

XMM-Newton data are available in two formats, *i.e.*, Observation Data Files (ODF) and Pipeline Processing System (PPS) products. The ODF contain un-calibrated quantities on a chip-by-chip for the X-ray cameras. Pipeline Processing System (PPS) products are a collection of validated, top-level scientific products including event and source lists, multiwavelength images and cross-correlation products generated at the Survey Science Center (SSC).

Science Analysis Software (SAS)[2] is specifically designed to reduce and analyze *XMM-Newton* data. I used SAS version 7.1 to reduce the *XMM-Newton* data of Seyfert galaxies of our sample. SAS is necessary to extract standard (spectra, light curves etc.) and/or customized science products even if one starts with the pipeline processed data products (PPS). Moreover, SAS allows to reproduce the pipeline reduction procedure, which are being applied to get the PPS products. It is advis-

[2]http://xmm.esac.esa.int/sas/current/documentation/sas_concise.shtml

able to start with ODF data rather than PPS data, whenever substantial changes in the software and/or instrument calibrations occurred from the time when the ODF were processed by the SSC pipeline to get the PPS data. The detailed description of *XMM-Newton* data and its reduction can be found in *XMM-Newton* website[3]. The basic steps of *XMM-Newton* data reduction using SAS are summarized as below.

(i) *Generating a Calibration Index File (CIF)* : *XMM-Newton* observation data files contain information about the instrument used, observation date, exposure time, exposure mode, exposure filter etc. In order to calibrate an ODF, one needs to first identify the calibration files (CCF) to be used. This is done by creating a Calibration Index File (CIF) using SAS task 'cifbuild'. The task 'cifbuild' retrieves the observation date from the observation data file to be analyzed, as reported by the ODF Access Layer (OAL), and selects the corresponding calibration files for that given time period.

(ii) *Obtaining the calibrated data (event list)* : SAS tasks 'epproc' and 'emproc' produce calibrated and concatenated (*i.e.*, one single file including events from all the detector chips) event lists for the EPIC pn and MOS cameras, respectively.

(iii) *Identifying the intervals of flaring particle background* : This can be done by extracting a single event (*i.e.*, 'pattern zero' only), high energy (E > 10 and < 12 keV) light curve from calibrated event list using task 'evselect'. The single event, high energy background light curve is used to identify the intervals of flaring particle background.

(iv) *Creating a Good Time Interval (GTI) event list* : GTI event list is generated by filtering out the intervals of flaring particle background from the calibrated event list using task 'tabgtigen' and 'evselect'.

(v) *Extracting the source and background spectra* : The task 'evselect' is used to extract the source and background spectra from the calibrated GTI event list. The

---

[3]http://xmm.esac.esa.int/

size and co-ordinates of the source and background regions can be obtained from the image (GTI event list) by displaying it using a FITS image viewer package, *e.g.*, 'ds9'.

(vi) *Generating ancillary files and the instrument response functions* : To perform quantitative spectral analysis of X-ray data, the ancillary and instrument response matrices files are created using 'rmfgen' and 'arfgen' tasks for EPIC.

EPIC exposure maps can be generated using task 'eexpmap' and the amount of pile-up affecting target source can be estimated using 'epatplot' task. The extracted source and background spectra along with ancillary and response matrix files can be loaded in the spectral fitting package 'XSPEC' for spectral fitting. I use XSPEC version 12.0 to fit the spectra of my sources.

3.3 *Suzaku* X-ray observations

Suzaku (formerly known as Astro-E2) is Japan's fifth X-ray Astronomy mission and was launched on July 10, 2005. *Suzaku* covers the energy range 0.2 - 600 keV with the three instruments: an X-ray micro-calorimeter (X-ray Spectrometer (XRS)), four units of the X-ray Imaging Spectrometers (XISs) and a hard X-ray detector (HXD). XRS is a non-dispersive imaging spectrometer (FWHM $\sim$ 6.5 eV), however, it prematurely lost its liquid helium of cryogenic refrigerator and is no longer operational. There are 4 units of XIS and each XIS (an X-ray CCD camera) has a single CCD chip with 1024 $\times$ 1024 pixels, and covers a $18'' \times 18''$ region on the sky. One unit of XIS is equipped with a back-side illuminated CCD chip, while the rest contain a front-side illuminated CCD. HXD is a non-imaging instrument, which covers the wide energy band of 10 - 600 keV in combination of the GSO well-type phoswich counters (> 30 keV) and the silicon PIN diodes (< 60 keV). The HXD is characterized by the low background of $\sim$ 5 - 10 cts s^{-1} cm^{-2} keV^{-1} and its sensitivity is higher than any past missions in the energy range from a few tens of keV to several hundreds of keV. The detailed description on the

instruments aboard *Suzaku* can be found at the Suzaku website[4]. Table 3.3 lists the specifications of all the three instruments of *Suzaku*. I use *Suzaku* XISs and HXD - PIN data to study the broad-band X-ray spectral properties of NGC 5135, which is one of the Compton-thick sources in my sample.

Table 3.3: Overview of *Suzaku* instruments

	XRS	XIS	HXD
Energy range	0.3 - 12 keV	0.2 - 12 keV	10 - 600 keV
Number of units	1	4 (identical units)	1 ($4 \times 4 = 16$ sub-units)
Number of pixels	30 pixels	1024×1024 for each CCD	-
Pixel size	625 μm $\times$ 625 μm	24 μm $\times$ 24 μm	-
Effective area per detector	100 cm^2 @ 1 keV	400 cm^2 @ 1.5 keV	160 cm^2 @ 15 keV
	150 cm^2 @ 6 keV	250 cm^2 @ 6 keV	300 cm^2 @ 120 keV
Energy resolution (FWHM)	6.5 eV	120 eV @ 6 keV	3 keV (10 - 30 keV)
		50 eV @ 1 keV	9% (at 662 keV)
Field of view	2.9$'$ $\times$ 2.9$'$	19$'$ $\times$ 19$'$	0.56° $\times$ 0.56° (E < 100 keV)
			4.6° $\times$ 4.6° (E > 200 keV)
Spatial resolution	1.8$'$ (XRT PSF)	1.8$'$ (XRT PSF)	-

3.3.1   *Suzaku* data reduction procedure

Suzaku data reduction is primarily performed using the HEAsoft[5] (also known as 'FTOOLS') package, which is a multimission collection of programs and scripts. All mission-specific softwares required to calibrate and analyze *Suzaku* data are written by the *Suzaku* instruments teams and are released as a part of HEA-soft collectively called as "*Suzaku* FTOOLS". *Suzaku* calibration information are provided via the HEASARC[6] "Calibration Database" (CALDB)[7]. The 'CALDB' provides index files and other information so that *Suzaku* FTOOLS can determine the correct calibration file to use. Standard data formatting and calibration are

---

[4]http://heasarc.nasa.gov/docs/suzaku/about/overview.html

[5]http://heasarc.gsfc.nasa.gov/docs/software/lheasoft/

[6]http://heasarc.gsfc.nasa.gov/

[7]http://suzaku.gsfc.nasa.gov/docs/heasarc/caldb/caldb_intro.html

carried out as the part of pipeline processing, and it is recommended to start scientific data analysis from the pipeline processed products. After standard pipeline processing, *Suzaku* event files do not require any particular analysis software, since they comply with FITS event file standards. Nonetheless, the *Suzaku* observer facility recommends 'xselect' as a convenient and efficient analysis tool. The 'xselect' is a multi-mission program which has been widely used to analyze data from *ASCA*, *ROSAT*, *BeppoSAX*, *Einstein*, *Chandra* and other high energy missions. The 'xselect' is used to extract spectra, images, and lightcurves from *Suzaku* data.

3.3.1.1   XIS data reduction procedure

Suzaku standard pipeline processing produces filtered, calibrated event files and further spectral analysis of XIS data involves following main steps.

(i) *Extracting source and background spectra* : The primary HEASoft task for extracting spectra, light curves, exposure maps from XIS data is 'xselect'. This task can apply filters which select user-defined times, sky regions and particular event flags.

(ii) *Building the response files (RMF and ARF)* : HEASoft task 'xisrmfgen' generates XIS response matrix and takes into account the time variation of the energy response. The task 'Xissimarfgen' is a ray-tracing based task which generates the ancillary response files (ARFs) for the *Suzaku* XIS.

(iii) *Combining the spectra taken with XIS0, XIS2 and XIS3* : Three of the XIS units (each with a frontside illuminated (FI) chip) are sufficiently similar and it is recommended to sum up the spectra from these units to obtain higher signal to noise ratio, under most circumstances. However, one should not combine the event files since it will lead to the loss of information critical to downstream software. Also, XIS1 (with a backside illuminated (BI) chip) has a distinctly different response and therefore XIS1 data should not be combined with those from the other three units. XIS2, one of the XIS units with an FI chip, suffered a catastrophic

damage on November 9, 2006 since then, no astronomically useful data have been obtained with XIS2, although some diagnostic mode data are taken. One should therefore expect no cleaned event files for XIS2 in observations taken after November 9, 2006.

The extracted XIS source and background spectra along with response files can be input in XSPEC for spectral fitting. The particle background is a strong function of the location of the *Suzaku* spacecraft within the geomagnetic field, and therefore, is variable in time. The X-ray background is a function of the pointing direction and therefore, background spectrum should be extracted from the neighboring source-free region(s) of the same CCD chip from the same observation.

3.3.1.2 HXD data reduction procedure

Since the HXD is a non-imaging instrument, the analysis of HXD data follows a different path from that used for XIS data analysis. The HXD consists of two independent detector systems, *i.e.*, GSO/BGO phoswich counters and the PIN silicon diodes. The PIN diodes are sensitive below ~ 60 keV, while the GSO/BGO phoswich counters detect photons above ~ 30 keV. The energy resolution of PIN diodes is ~ 3.0 keV (in 10 -30 keV energy band), while the phoswich counters have a resolution of $7.6\sqrt{E}$ % (FWHM), where E is the photon energy in MeV. The main steps for the spectral analysis of HXD data are described below.

(i) *Obtaining the appropriate background files* : Since PIN is a collimated instrument, it is not possible to obtain background data from the HXD-PIN observations. Therefore, HXD instrument team has developed a model of the time-variable particle background which is provided to users.

(ii) *Creating a good time interval (GTI) event list file* : GTI event file can be generated by correcting for dead-time. It is necessary to correct for the dead time of the observed spectrum to apply the background file correctly. The dead time correction task 'hxddtcor' (included in the *Suzaku* FTOOLS) updates the exposure

keyword of the event file.

(iii) *Extracting spectra* : Source spectra are extracted from calibrated and filtered (GTI) event file.

(iv) *Extracting spectra from the background files and correcting (for PIN) for the factor of 10 oversampling* : The event rate in the PIN background event file is 10 times higher than the real background to suppress the Poisson errors. Therefore, one should increase the exposure time of derived background spectra and light curves by a factor of 10 using 'fv' or 'fmodhead'.

(v) *Selecting the response file* : Due to the changes in instrumental settings (bias voltages used on-board and low energy threshold used in processing on the ground), one must choose PIN response matrices that are appropriate for the epoch of observation. These response files are available from the *Suzaku* calibration database 'CALDB'.

3.4 X-ray spectral fitting package: XSPEC

XSPEC[8] is a command-driven, interactive, X-ray spectral-fitting program designed to be completely detector-independent so that it can be used to fit the X-ray spectra obtained from any spectrometer. XSPEC has been used to analyze data from *ROSAT*, *ASCA*, *Chandra*, *XMM-Newton*, *Suzaku* and other X-ray observatories. I give here a brief description of the basics of XSPEC spectral fitting.

A spectrometer is used to obtain the spectrum of a source, however, the X-ray spectrometer does not give the actual spectrum, but rather, photon counts (C) within specific instrument channels (I). Thus observed spectrum is related to the actual spectrum of source ($f(E)$) by:

$$C(I) = \int_0^\infty f(E)R(I,E) \ dE \qquad (3.1)$$

---

[8]http://heasarc.nasa.gov/docs/xanadu/xspec/

where, *R(I,E)* is the instrumental response and is proportional to the probability of the detection of an incoming photon of energy E to be detected in channel I. From the above equation, one can determine the actual spectrum of a source *f(E)*, by inverting the equation, thus deriving *f(E)* for a given set of *C(I)*. However, inversing solutions tend to be non-unique and unstable to small changes in *C(I)* (*e.g.*, see Blissett and Cruise (1979); Loredo and Epstein (1989)). The usual alternative to obtain *f(E)* is to choose a model spectrum for *f(E)*, that can be described in terms of a few parameters (*i.e.*, *f(E, p1, p2,...)*) and match or fit it to the data obtained by the spectrometer. For each *f(E)*, a predicted count spectrum ($C_p(I)$) is calculated and compared to the observed data (*C(I)*). Then a 'fit statistics' is computed from the comparison and is used to judge whether the model spectrum fits the data obtained by the spectrometer. The model parameters are varied to find the parameter values that give the best fit statistics. These values are referred to as the best-fit parameters. The model spectrum, $f_b(E)$, consists of the best-fit parameters is considered to be the best-fit model. Mostly, χ^2 fitting statistics is used for determining the best fit model. The χ^2 minimization equation can be given as.

$$\chi^2 = \Sigma \left(1 - \frac{C(I)_p}{C(I)} \right)^2 \tag{3.2}$$

The 'goodness-of-fit' is calculated to determine how well the model fits the observed data and confidence intervals for the model parameters are calculated to know the range of values within which one can be confident the true value of the parameter lies.

Chapter 4

Radio interferometric techniques and data reductions

4.1 Introduction: Radio interferometric observations

The radio interferometric observations enable high resolution imaging which is not possible with single dish radio telescopes. I carried out Giant Meterwave Radio Telescope (GMRT) radio interferometric observations of the Seyfert galaxies of my sample and following sections discuss the basic principles of radio interferometric synthesis imaging and data reduction.

4.1.1 Aperture synthesis

Angular resolution of a telescope is given by Rayleigh criteria, $\theta = \lambda/D$, where θ is angular resolution, λ is the observing wavelength and D is the diameter of the reflecting surface of the telescope. Since the radio wavelengths are $\sim 10^4$ - 10^7 times larger than optical wavelengths therefore, to achieve the comparable angular resolution at radio wavelengths, diameter of the radio telescope needs to be $\sim 10^4$ - 10^7 times larger than optical telescope (*e.g.*, 1 arcsec resolution at 1 GHz requires a radio telescope with diameter of 60 km and construction as well as operation of such a large telescope is rather impractical). However, using interferometry, much

larger aperture can be 'synthesized' from two or more smaller telescopes. In radio interferometric observations, two or more radio telescopes observe a radio sources simultaneously and the signal from an antenna is combined interferometrically with the signals from each of the other antennas in an array to provide the measure of the source brightness distribution.

4.1.2 Principle of radio interferometry

If I_ν(l,m) represents the distribution of source intensity, where l, m are the direction cosines with respect to the phase tracking center and ν is the observing frequency, van-Zittert Zernicke theorem states that the *spatial coherence function* is the Fourier transform of the source intensity distribution

$$V_\nu(u,v) = \int_{-\infty}^{+\infty} \int_{-\infty}^{+\infty} I_\nu(l,m)e^{-i2\pi(ul+vm)} \ dl \ dm \tag{4.1}$$

The inverse Fourier transform of the spatial coherence function results I_ν(l,m) (*i.e.*, intensity distribution of the source). A two element radio interferometer measures one (u,v) component of the Fourier plane of the radio source intensity distribution. A radio interferometric array consists of many such two element interferometers is used to sample the entire Fourier plane.

4.2 Radio data reduction

4.2.1 Calibration

The spatial coherence function is usually referred as visibility function denoted by V_{ij} where i and j represents the ith and j^{th} antenna of an array and V_{ij} is the value of spatial coherence function at a location given by the separation between i^{th} and j^{th} antennas (baseline). In a radio interferometric array, signal from one antenna is cross-correlated with the signal from another antennas and one antenna pair results one value of visibility function. The ensemble of visibilities obtained

from antenna pairs (*e.g.*, *N*-element array forms $N(N\text{-}1)/2$ antenna pairs) sample the visibility function (*i.e.*, spatial coherence function). Since the visibilities are sampled at discrete times for each antenna pair, one can write equation 4.1 as

$$V_{ij}(t) = \int_{-\infty}^{+\infty} \int_{-\infty}^{+\infty} I_\nu(l,m)e^{-i2\pi(u_{ij}(t)l+v_{ij}(t)m)} \ dl \ dm \qquad (4.2)$$

Therefore, at a given frequency, visibility is a function of antenna pair (i and j, *i.e.*, baseline) and time. In general, the observed visibilities differ from the true visibilities due to multiple reasons such as phase irregularities in the wavefront of incoming radio waves caused by density irregularities in the ionosphere and phase distortion during the signal processing. In principle, relationship between true visibility (V^{true}) and observed visibility (V^{obs}) can be arbitrary, although within good approximation (*e.g.*, electronic devices are linear (output is a linear function of input or nearly so), response of one antenna pair is independent of other antenna pair) observed visibilities can be considered as linear function of true visibilities. The process of obtaining corrective coefficient required to get true visibilities is called *calibration*. The basic calibration formula can be expressed as

$$V_{ij}^{obs}(t) = G_{ij}(t) \ V_{ij}^{true}(t) \ + \ \epsilon_{ij}(t) \ + \ \eta_{ij}(t) \qquad (4.3)$$

where, G_{ij} is baseline-based complex gain, ϵ_{ij} is baseline-based complex offset, η_{ij} is a stochastic complex noise and t is the time of the observation. Mostly data corruption occurs before signals from two antennas are cross-correlated so the baseline-based complex gain G_{ij} can be approximated as the product of the antenna-based complex gains $g_i(t)$ and $g_j(t)$ and one can write

$$G_{ij}(t) = g_i(t)g_j^*(t) = a_i(t)a_j(t)e^{i(\phi_i(t)-\phi_j(t))} \qquad (4.4)$$

where, a_i is antenna-based amplitude correction and ϕ_i is antenna-based phase correction. Antenna-based calibration values are preferred over baseline-based ones since most variations in the instrument are related to particular antennas, either

arising from the medium above the antenna or in the electronic components. The errors due to a well designed correlator are always significantly smaller. The detailed description of calibration methods can be found in Fomalont and Perley (1999).

4.2.1.1 Flux calibration

Calibration gains can be obtained by observing standard calibrator sources which have high flux density, small angular size (point source), do not vary significantly (over the time scale of observations), position in the sky is known accurately, their spectra are known and simple, they are isolated from nearby confusing sources and are strong enough to allow calibration in short time scale. In other words true visibilities ($V_{ij}^{true}(t)$) are known for the calibrator sources and observed visibilities ($V_{ij}^{obs}(t)$) are obtained by observing them and therefore various calibration gain terms in equation 4.3 can be determined. If calibrator is a point source of flux density S and it's position is accurately known, then the amplitude of true complex visibility is S and the phase is zero degree. Therefore, complex gains can be given as

$$G_{ij}(t) = V_{ij}^{obs}(t)/S \tag{4.5}$$

In equation 4.3, baseline-based offset term ϵ_{ij} is generally negligible unless correlator malfunctions or there is a significant cross-talk between various antenna channels. Also, stochastic noise term η_{ij} is assumed to be negligible after proper averaging of the data in a scan.

4.2.1.2 Phase calibration

The complex gain can be broken into two parts, the amplitude and the phase, and one must calibrate both of these components. The phase calibrator should be observed more frequently (every 5 - 40 minutes depending upon the configuration, weather, and band) and should be as close to the target as possible.

Troposphere and ionosphere introduce time variable phase effects. The troposphere causes polarization-independent amplitude and phase effects due to emission/opacity and refraction. The troposphere effects are more important at $\nu \geq 20$ GHz, where water vapor and oxygen absorb/emit. The ionosphere introduces a dispersive phase shift which is proportional to λ^2 and therefore ionospheric effects are more important at lower radio wavelengths. Also, ionosphere is more active and variable at sunrise/sunset and during maxima of solar cycle.

4.2.1.3 Bandpass calibration

If observations are in the spectral mode one should include a bandpass calibrator, even if doing continuum observations. Bandpass calibration is necessary to correct for complex gain variations as a function of frequency. To estimate the changes in antenna gain with frequency one can consider the baseline-based complex gain as a function of frequency $(G_{ij}(\nu))$. Compensating for the changes in gains with frequency is called *bandpass calibration*. The relative frequency response over the frequency bandwidth can be estimated by observing a strong calibrator source which has flat spectrum over the frequency bandwidth. If the true visibilities of the calibrator are identical in all the channels (over frequency bandwidth), the bandpass complex correlator-based gain function for i - j baseline and the kth frequency channel is the observed visibility $(V_{ij}^{obs}(\nu_k))$ divided by the true visibility $(V_{ij}^{true}(\nu_k))$. The frequency-dependent, baseline-dependent bandpass gain can be expressed as the product of antenna-based gains and can be converted into antenna-based bandpass amplitude and phase calibrations.

4.2.2 Data editing

Radio signal from a cosmic source can be corrupted by several reasons such as interference from terrestrial radio sources, antennas tracking inaccuracies, malfunction of receivers, inclement weather etc. Therefore, discrepant and corrupted

data need to be discarded. The process of identifying and discarding the discrepant and corrupted data is called data 'editing' and also commonly known as 'flagging'. Editing and calibration of the data are being done iteratively.

4.2.3   Self-calibration

Initial calibration by observing a standard calibrator solves for the complex gains but it has limitations, since the calibrator is observed before and/or after the target source and thus gains are derived at different time and for the direction different than the target source (*i.e.*, troposphere and ionosphere are variable and non-uniform, electronics may also vary). Self-calibration uses target source visibilities and allows the antenna gains to be free parameters (*i.e.*, target source itself acts as a calibrator hence called *'Self-calibration'*). In an N-element radio interferometric array, if all baselines are correlated, there are N complex gains errors corrupting $\frac{1}{2}N(N$ - $1)$ visibility measurements at a given time. Therefore, there are $\frac{1}{2}N(N$ - $1)$ - N complex numbers that can be used to constrain the true source brightness distribution. Self-calibration makes use of the closure phase of a triangle of baselines (3 antennas); the error terms for each individual antenna cancel out in summing the visibility phases around the triangle. A similar amplitude closure around a rectangle of baselines (4 antennas) is used to correct error in a priori flux calibration. In an N-element radio interferometric array there are $\frac{1}{2}N(N$ - $1)$ - (N - 1) constraints on the phase and $\frac{1}{2}N(N$ - $1)$ - N constraints on the amplitude. For large N following iterative scheme is used for self-calibration:

1. An initial source brightness distribution model, generally from the initial image (from clean components) or else a point source, is assumed.

2. Antenna gains are solved using above assumed model and closure constraints.

3. The gain corrections are applied to the visibility data and the corrected data is used as new source model in next iteration.

The iterative deconvolution algorithm 'CLEAN' is used to get components which

provide the source model for the next iteration of self-calibration. Self-calibration takes care of antenna-based corrections and is analogous to the adaptive optics used in optical telescopes, where surface of the telescope is distorted to remove the distortions in the phase introduced by the atmosphere.

4.2.4   Radio synthesis imaging

The van-Zittert Zernicke theorem states that the *spatial coherence function* is the Fourier transform of the source brightness distribution. In other words, source image, *i.e.*, source brightness distribution is inverse Fourier transform of the spatial coherence function (visibility function).

$$I_\nu(l,m) = \int_{-\infty}^{+\infty} \int_{-\infty}^{+\infty} V_\nu(u,v)e^{i2\pi(ul+vm)} \ du \ dv \tag{4.6}$$

In practice, the spatial coherence (visibility) function $V_\nu(u,v)$ is not known everywhere but is sampled at particular places in the u-v plane. The sampling function $S_\nu(u,v)$ is such that it has a value '1' where data is present and is '0' elsewhere. Therefore observer obtains the quantity

$$I_\nu^D(l,m) = \int_{-\infty}^{+\infty} \int_{-\infty}^{+\infty} V_\nu(u,v)S(u,v)e^{i2\pi(ul+vm)} \ du \ dv \tag{4.7}$$

where, I_ν^D(l,m) is termed as dirty image or dirty map and is related to the true source brightness distribution by

$$I_\nu^D = I_\nu \ ^* \ DB \tag{4.8}$$

where, asterisk (*) denotes convolution and DB is the inverse Fourier transform of the sampling function $S_\nu(u,v)$ and is termed as dirty beam. It is basically point spread function (PSF) of the synthesized array, corresponding to the sampling function.

4.2.4.1 Deconvolution

The source brightness distribution obtained from the inverse Fourier transform of the sampled spatial coherence function is the convolution of true brightness distribution and dirty beam. Therefore, to obtain the true brightness distribution, dirty beam needs to be deconvolved with the observed brightness distribution (*cf.*, equation 4.7, 4.8). There are two primary deconvolution algorithms used in aperture synthesis imaging, named 'CLEAN' (*e.g.*, Högbom (1974)) and Maximum Entropy Method (MEM) (*e.g.*, Cornwell and Evans (1985); Narayan and Nityananda (1986)). 'CLEAN' algorithm deconvolves the sampling function (dirty beam) from the observed brightness distribution (dirty map) iteratively, while 'MEM' minimizes a smoothness function (entropy) of the dirty image. To obtain the true brightness distribution of the source we opted 'CLEAN' deconvolution algorithm.

4.3 GMRT interferometric observations

To study the low-frequency radio emission of our sample Seyfert galaxies we carried out GMRT observations at 610/240 MHz dual frequency. Here I summarize basic details about the GMRT interferometric array. The GMRT is located about 80 km north of Pune, in India (Latitude = 19.1° N, Longitude = 74.05° E). The GMRT consists of 30 radio dish antennas with diameter of each antennas 45 meter and all the antennas are spread over $\sim$ 25 km^2 area. 14 out of 30 antennas are in a compact, quasi randomly distributed array which spread over 1 km^2 area. The remaining antennas are on 3 arms (North-West, North-East and South, making a 'Y' shape) of length 14 km with 5 or 6 antennas in each arm. The longest baseline of GMRT array is $\sim$ 26 km and the shortest is 100 m without foreshortening.

GMRT presently operates at five frequencies, *i.e.*, 151 MHz, 325 MHz, 610/235 MHz and the 1000-1450 MHz. Both the orthogonal polarizations are brought to the control room from each antenna. The polarizations are circular for all the feeds

except the 1420 MHz feed, for which the polarizations are linear. The 610 and 235 MHz feeds are coaxial, allowing simultaneous dual frequency observations to be carried out at these two frequency bands, which restricts only one polarization per band. Table 4.1 details the GMRT system parameters. More details on GMRT interferometric array can be found at GMRT website[1].

Table 4.1: GMRT system parameters

Parameter	frequency (MHz)				
	151	235	325	610	1420
Primary Beam (arcmin)	186±6	114±5	81±4	43±3	(24±2)×(1400/f)
Synthesized Beam (arcsec)					
Whole Array	20	13	9	5	2
Central Square	420	270	200	100	40
Largest Detectable Source (arcmin)	68	44	32	17	7
Receiver Temperature (T_R) (K)	295[†]	106[†]	53	60	45
Typical T_{sky} (off galactic plane) (K)	308	99	40	10	4
Typical T_{ground} (K)	12	32	13	32	24
Total System Temperature (K)	615	237	106	102	73
(T_R + T_{sky} + T_{ground})					
Antenna Gain (K/Jy/Antenna)	0.33	0.33	0.32	0.32	0.22
Usable Frequency Range (MHz)					
Observatory default	150 to 156	236 to 244	305 to 345	580 to 640	1000 to 1450
Range allowed by electronics	130 to 230	230 to 250	305 to 360	570 to 650	1000 to 1450
Fudge Factor(actual to estimated)					
For Short Observations	10	5	2	2	2
For Long Observations [‡]	5	2	2	1	1
Best rms sensitivities achieved					
so far known (mJy)	1.5	0.6	0.1	0.02	0.03
Typical Dynamic Ranges	1500	1500	1500	2000	2000

Notes: †: With default solar attenuator (14 dB); ‡: For spectral observations fudge factor is close to 1.

Chapter 5

X-ray spectral properties of Seyfert galaxies: testing unification scheme

5.1 Introduction

Seyfert galaxies are well known X-ray emitters with luminosity in X-ray band ranging from 10^{39} - 10^{45} erg s^{-1}. It is believed that the soft X-rays (E < 1.0 keV) are emitted from the inner part of the accretion disk which is heated to the temperature of $\sim 10^6$ - 10^7 K, while the hard X-ray photons are mainly attributed to the Comptonization of optical, UV and soft X-ray photons by relativistic electrons present in a hot corona above the accretion disk (Haardt and Maraschi 1991). However, there are suggestions that X-rays may also come from the base of the jets (Falcke, Körding, and Markoff 2004) and from the circumnuclear material heated by the sub-relativistic jets (Ghisellini, Haardt, and Matt 2004). The obscuring torus around AGN is optically thick for optical, UV and soft X-ray photons, however, hard X-ray photons from AGN can transmit through the torus. Furthermore, X-ray Spectral modeling can enable us to estimate the line-of-sight absorbing column density using photoelectric absorption component. Thus, X-ray study offers an opportunity to investigate the complex mixture of emitting and absorbing components in the circumnuclear regions of AGN and to examine the

validity of Seyfert unification scheme.

There have been several attempts to examine the validity of Seyfert unification scheme at X-ray wavelengths using the X-ray selected samples too (Awaki *et al.* 1991; Smith and Done 1996; Turner *et al.* 1997, 1998; Bassani *et al.* 1999). However, if unification scheme holds true, the Seyfert samples selected from the flux limited surveys are likely to be biased against obscured and faint type 2 sources. Maiolino *et al.* (1998) and Risaliti, Maiolino, and Salvati (1999) have shown the increased number of heavily obscured type 2 sources using a sample based on [OIII] $\lambda5007$Å luminosity and reported the generally inherent bias against less luminous and heavily obscured sources in X-ray selected samples. The hard X-ray selected samples are suppose to be less biased but cannot be granted to be free from biases against heavily obscured Compton-thick and low luminosity AGNs (*e.g.*, Heckman *et al.* (2005); Wang, Mao, and Wei (2009)). Recent Seyfert samples based on IN-TEGRAL and Swift/BAT surveys preferentially contain relatively large number of high luminosity and less absorbed Seyferts (Tueller *et al.* 2008; Treister, Urry, and Virani 2009; Beckmann *et al.* 2009), possibly due to less effective area which limits the sensitivity only to ($\sim10^{-11}$ erg s^{-1} cm^{-2}) bright sources. The quest of testing the validity and limitations of the Seyfert unification with the more improved and well defined samples still continues. Recent studies by Cappi *et al.* (2006); Dadina (2008); Beckmann *et al.* (2009) used less biased optical and X-ray selected samples and reported the results broadly consistent with unification, nonetheless, issues related to sample selection still remains.

Considering the above arguments I aimed to study 0.5 - 10.0 keV *XMM-Newton* X-ray spectral properties of our rigorously selected sample of Seyfert galaxies to test the predictions of Seyfert unification scheme. The detailed description of our sample and selection criteria is presented in chapter 2. In this chapter, I present 0.5 - 10.0 keV *XMM-Newton* X-ray spectral modeling of 17/20 Seyfert galaxies of our sample. The statistical comparison of X-ray spectral properties of the two Seyfert subtypes is performed to test the predictions of the Seyfert unification scheme. For

NGC 5135, one of our sample sources, we are using *Suzaku* X-ray data that are presented in next chapter.

5.2 X-ray observations and data reductions

Compared to X-ray observations from previous generation satellites, *XMM-Newton* has higher sensitivity, which allows to study X-ray spectral components with absorbing column density up to $N_H \approx 10^{24}$ cm^{-2}, and high spatial resolution of *XMM-Newton* (FWHM $\sim 6''$) minimizes any strong contamination from off-nuclear sources.

5.2.1 X-ray observations

I present X-ray spectral analysis of 17 (10 type 1 and 7 type 2) out of 20 Seyfert galaxies using *XMM-Newton* EPIC pn archival data. For 6 Seyfert galaxies, *i.e.*, MRK 1218, NGC 2639, MRK 530, MRK 78, MRK 533 and NGC 7682, *XMM-Newton* X-ray spectra are being presented for the first time and for NGC 4151 and NGC 7469 *XMM-Newton* archival data chosen by us are not published. *XMM-Newton* spectra of rest of the 9 sources have been individually published, however, we re-do the X-ray spectral analysis of these sources using data reduced with the most updated calibration files. For 3 (type 2) Seyfert galaxies of our sample, *i.e.*, NGC 5135, MRK 477 and NGC 5929, there are no *XMM-Newton* data and therefore, for the statistical comparison of X-ray properties of the two Seyfert subtypes of our sample, we are using *Suzaku* and *ASCA* spectral parameters for these sources. *Suzaku* X-ray spectral properties of NGC 5135 are discussed in next chapter and *ASCA* spectral properties of MRK 477 and NGC 5929 have been reported in Levenson, Weaver, and Heckman (2001) and Cardamone, Moran, and Kay (2007), respectively. For our X-ray spectral study, we use only *XMM-Newton* EPIC pn data and do not include EPIC MOS data since it is more susceptible

to pile-up for bright X-ray sources and few sources, *e.g.*, MRK 530 do not have MOS data. Moreover, EPIC pn data is sufficiently good enough for our purpose of obtaining the average X-ray spectral parameters (*e.g.*, equivalent hydrogen column density, photon index, EW of Fe Kα etc.) of our sample sources. In case, if a source had more than one observations in archive, we chose the latest one with sufficient long exposure time. Table 5.1 lists the details of *XMM-Newton* EPIC pn observations such as the observing mode of pn camera, optical light blocking filters, observation dates, observation and net exposure times, count rates, observation IDs and radius (in arcsec) of the circular region around the source position used to extract the X-ray spectra.

Table 5.1: *XMM-Newton* EPIC pn observation log

Source name	Obs. mode/filter	Obs. date	Obs. time (ks)	Net expo. time (ks)	ct/s	Obs. ID	R_S (arcsec)
MCG+8-11-11	SW/Medium	2004-04-10	38.45	25.24	14.93	0201930201	35.0
MRK 1218	SW/Thin	2005-04-09	13.87	6.55	0.53	0302260201	20.0
NGC 2639	FW/Thin	2005-04-03	26.12	4.23	0.24	0301651101	16.0
NGC 4151	SW/Medium	2006-11-29	52.81	24.60	9.57	0402660201	40.0
MRK 766	SW/Medium	2005-05-24	95.51	60.12	4.92	0304030101	40.0
MRK 231	FW/ Medium	2001-06-07	22.34	17.30	0.10	0081340201	30.0
ARK 564	SW/Medium	2005-01-06	101.77	69.07	39.67	0206400101	35.0
NGC 7469	SW/Medium	2004-12-03	79.11	54.95	21.59	0207090201	37.5
MRK 926	SW/Thin	2000-12-01	11.76	7.19	18.33	0109130701	37.5
MRK 530	SW/Thick	2006-06-14	16.82	11.42	12.93	0305600601	20.0
MRK 348	FW/Medium	2002-07-18	49.50	26.54	1.96	0067540201	22.5
MRK 1	FW/Thin	2004-01-09	11.91	8.66	0.07	0200430301	17.5
NGC 2273	FW/Medium	2003-09-05	13.02	5.21	0.08	0140951001	20.0
MRK 78	FW/Thin	2006-03-11	16.12	4.83	0.09	0307001501	22.5
NGC 7212	FW/Thin	2004-05-20	14.22	10.50	0.10	0200430201	20.0
MRK 533	LW/Thick	2004-06-02	10.42	7.51	0.12	0200660101	17.5
NGC 7682	FW/Thin	2005-05-27	20.21	14.27	0.04	0301150501	16.0

Notes: SW: Small Window, FW: Full Window, LW: Large Window, R_S: radius of the circular region around the source used for spectral extraction.

5.2.2   X-ray data reductions

The raw observation data files (ODFs) were reduced and analyzed using the standard Science Analysis System (SAS) software package (version 7.1) with the latest calibration files. High energy background particle flares were removed by applying fixed threshold on single events, using E > 10.0 keV and $\delta t = 50$ s light curves. The background is extracted from a circular regions in the same chip. In order to apply χ^2 statistics, the spectra are binned with minimum 20 counts per bin. The detailed description of *XMM-Newton* data reduction procedure has been presented in Chapter 3.

5.3   X-ray spectral analysis: spectral components

We attempt to obtain the physically motivated best fit models of 0.5 - 10.0 keV *XMM-Newton* pn X-ray spectra of the Seyfert galaxies of our sample. Since the primary aim of spectral analysis is to identify the underlying continuum components, we first tried to fit each spectrum with a simple model consists of a power-law plus absorption fixed at the Galactic value plus intrinsic absorption as a free parameter. However, in most of the cases this simple parametrization is insufficient to model the whole spectrum and residuals often show a soft excess and an emission line feature at 6.4 keV on top of the (absorbed or unabsorbed) power-law. In most of the cases, we found that the best fit model consists of: an absorbed power-law with exponential cutoff which contains cold absorption from the Galactic column density together with absorption from neutral gas at the redshift of the source; a narrow Gaussian line to reproduce the Fe Kα fluorescent line at 6.4 keV in the rest frame with energy, width and intensity as free parameters; soft excess component characterized by either a steep power-law and/or a thermal plasma model with temperature kT; in some cases reflection component characterized by reflection from an isotropically illuminated cold slab, (model 'pexrav' (Magdziarz

and Zdziarski 1995) in XSPEC (Arnaud 1996)) is required for the best fit. The partial covering of primary power-law component is also needed for the best fit in some sources. The partial covering model is equivalent to the combination of an absorbed power-law ($\exp(-N_H \ \sigma_{abs})^\star AE^{-\Gamma}$) plus a scattered power-law ($AE^{-\Gamma}$), assuming that the power-law slopes of these two components are same. In physical scenario AGN X-ray emission characterized by power-law is seen through the absorber (*i.e.*, absorbed power-law component), however, X-ray emission scattered by reprocessing material around the AGN (*i.e.*, scattered component) also contributes to the emission along the observers line-of-sight. We note that for many of our sample sources, 0.5 - 10.0 keV X-ray spectra can approximately be modeled as "$\exp(-N_{H_0} \ \sigma_{abs}) \times$ [soft component + $\exp(-N_{H_1} \ \sigma_{abs})$ ($AE^{-\Gamma}$ + emission lines)]" as suggested by Nandra and Pounds (1994); Awaki *et al.* (2000). Table 5.2 describes the best fit spectral parameters of all the sample sources. Errors on the spectral fit parameters and derived quantities are of 90% confidence level that corresponds to 1.6σ level. In the following sections, I describe the characteristics of the basic X-ray spectral components of Seyfert galaxies in 0.5 - 10.0 keV range.

5.3.1 Absorbed power-law

The presence of a cold, neutral medium along the line-of-sight introduces a sharp photoelectric absorption cutoff in the power-law spectrum emitted by the nuclear source. Thus, it is possible to estimate the equivalent hydrogen column density of the absorbing material as long as the direct X-ray component from AGN is seen in 0.5 - 10.0 keV energy band. When the equivalent hydrogen column density covering all the spectral components is unrealistically less than the Galactic value we fix it to the Galactic value. Figure 5.19 shows the distributions of equivalent hydrogen column density of the two subtypes of Seyferts of our sample. The estimated X-ray absorbing column densities in Seyfert galaxies of our sample varies from the Galactic value to as high as the limiting value ($N_H \geq 1.5 \times 10^{24}$ cm^{-2}) of Compton

thick obscuration. As expected from the unification scheme, Seyfert type 1s of our sample are systematically less absorbed than type 2s.

Among the type 2s many, *e.g.*, MRK 1, NGC 2273, MRK 78, NGC 7212, MRK 533 and NGC 7682 are heavily obscured and show only reflection component in 2.0 - 10.0 keV band. The hard X-ray component in these sources is best fitted by a pure reflection component. At equivalent $N_H \geq 1.5 \times 10^{24}$ cm^{-2}, the obscuring material becomes optically thick to Compton scattering (called as 'Compton-thick') and in such cases the transmitted component of primary X-ray radiation is completely suppressed at energies ≤ 10 keV, resulting the spectra in 2.0 - 10.0 keV energy range, flat and dominated by reprocessed components from a cold and/or warm scatterer (Matt *et al.* 2000). We identify these 7/10 type 2 Seyferts as Compton thick sources with equivalent hydrogen column density along the line-of-sight 1.5 $\times$ 10^{24} H atoms cm^{-2} or higher and exhibiting reflection dominated spectra in 2.0 - 10.0 keV band. The hard (2.0 - 10.0 keV) component of all the Seyfert type 1s is primarily fitted with an absorbed power-law and our best fits render photon indices (Γ) $\sim$ 1.5 - 2.5 with mean value of $\sim$ 2.0, while type 2s have either similar hard X-ray photon indices with high absorption or only pure reflection component modeled with 'pexrav' (Magdziarz and Zdziarski 1995) with photon indices of reflected power-law in 0.5 - 2.5 range with mean value of $\sim$ 1.5. In cases, where both direct as well as reflection components are considered, we fix reflection component photon index same as that of the direct power-law component. In some cases equally good fit can be obtained either using unabsorbed or less absorbed flat ($\Gamma \sim$ 0.5 - 1.0) power-law or with relatively more absorbed steep ($\Gamma \sim$ 1.8 - 2.1) power-law. In such cases we preferred more absorbed steep power-law fit as steeper photon index (Γ) is consistent with the typical Seyfert type 1 photon index ($\Gamma \sim$ 1.9 (*e.g.*, Cappi *et al.* (2006)). We do not perform statistical comparison of the photon indices of the two Seyfert subtypes since in many of the type 2 sources, (2.0 - 10.0 keV) hard X-ray spectrum is being best fitted by pure reflection component and without the presence of any transmitted power-law emission from AGN. Therefore,

in such reflection dominated sources we do not have the photon index of the direct power-law component of AGN.

5.3.2   Soft X-ray excess

17 of 20 Seyfert galaxies of our sample exhibit soft excess emission above the extrapolation of the absorbed AGN power-law while 3 (type 1) sources, *i.e.*, MCG+8-11-11, MRK 1218 and MRK 926 do not show any soft excess. We fit the soft excess by thermal plasma model 'mekal' (Mewe-Kaastra-Liedahl (1995)) and/or by a steep power-law. The typical temperature of thermal plasma corresponds to kT $\simeq$ 0.1 - 1.0 keV and the soft X-ray photon index is typically 2.5 - 3.5. But, in MRK 78 and NGC 7682 the best fit soft X-ray photon indices are as steep as $\sim$ 7.0 and 5.4, respectively. The 'mekal' model represents thermal emission from spatially unresolved gas and describes the emission from hot diffuse gas and also includes line emissions from several elements. In some cases (*e.g.*, NGC 4151, MRK 766 and NGC 7212), we see emission line features in 0.5 - 2.0 keV part of the spectrum, which indicates the presence of sub-keV thermal plasma.

The origin of soft excess can be attributed to circumnuclear gas heated to million degrees by shocks induced by AGN outflows (King 2005), an intense circumnuclear star formation (Cid Fernandes, Storchi-Bergmann, and Schmitt 1998; González Delgado, Heckman, and Leitherer 2001) or the photoionization and photo-excitation of circumnuclear gas by the primary AGN emission. High-resolution X-ray spectra of few sources, *e.g.*, NGC 1068 (Young, Wilson, and Shopbell 2001; Kinkhabwala *et al.* 2002), the Circinus galaxy (Sambruna *et al.* 2001), MRK 3 (Sako *et al.* 2000; Bianchi *et al.* 2005; Pounds and Page 2005) and NGC 4151 (Schurch *et al.* 2004) have furnished the evidence that soft excess is largely due to circumnuclear gas photoionized by primary AGN emission. High resolution grating observations have shown that the X-ray soft excess emission is consist of several emission lines which get blended and appear like a continuum in low resolution

spectra (Guainazzi and Bianchi 2007).

5.3.3 Reflection component

Previous X-ray spectral studies report that many Seyferts, in particular, type 2 show the presence of reflection component (Awaki *et al.* 2000). *ASCA* results have shown that the Compton reflection of nuclear radiation from optically thick material can be an important component in X-ray spectra of Seyfert 2 galaxies and beside absorption, a flat spectrum can result from Compton reflection component (Matt *et al.* 1996). In highly obscured so called Compton-thick sources, the primary radiation is almost completely absorbed (at $E \leq 10$ keV), but these sources are still observable through radiation that is scattered into our line-of-sight either by a cold, Compton-thick medium (cold reflection) or less frequently by a warm medium (warm reflection). There are 7/10 type 2 sources in our sample in which hard (2.0 - 10.0 keV) part of the spectrum is best fitted with reflection component alone ('pexrav' model Magdziarz and Zdziarski (1995) in XSPEC). Compton-thick, reflection-dominated sources are generally characterized by the presence of a prominent Fe Kα line at 6.4 keV (Matt, Perola, and Piro 1991; Ghisellini, Haardt, and Matt 1994; Cappi *et al.* 2006). Large EW of Fe Kα line in these sources supports the Compton thick obscuration and reflection dominated spectrum.

Some type 1 sources, *e.g.*, MCG+8-11-11, NGC 4151, MRK 766 and MRK 926 also show the presence of reflection component at the hard end of the spectrum. This can be expected in the framework of unification scheme since similar obscuring material having toroidal geometry is present but the plane of the torus lies away from the line-of-sight and thus the reflection component is much fainter compared to the direct transmitted component. Moreover, at the hard end of the spectrum ($E \geq 8.0$ keV) the contribution from reflection component is likely to be significant.

5.3.4 Fe Kα and other emission lines

We detect fluorescent Fe Kα emission line at $\sim$ 6.4 keV in all (except in NGC 2639) of our sample sources suggesting the ubiquitous presence of Fe Kα line in the X-ray spectra of Seyfert galaxies. *ASCA* spectrum of NGC 2639 shows Fe Kα line emission of high equivalent width $\sim$ 1.5 keV (Terashima *et al.* 2002), however, in *XMM-Newton* spectrum we do not have enough counts above 2 keV to fit the Fe Kα line. We modeled Fe Kα line in all the sources with a narrow Gaussian line. In most of the sources the centroid energy of Fe Kα emission line is consistent with the emission from neutral or mildly ionized iron. In some sources, *e.g.*, MRK 766, MRK 231, ARK 564, MRK 533 and NGC 7682, an emission line around $\sim$ 6.7 - 7.1 keV is also present, which is possibly either H or He like ionized Fe Kα line component or a neutral component of Fe K$_\beta$ emission line. The equivalent width of a spectral line is defined as the width of the spectral continuum that has the same area as the line. It is used as a measure of the strength of a line. Our analysis shows that when the absorbing column density increases to a few times of 10^{23} H atoms cm^{-2}, the equivalent width (EW) of Fe Kα increases, since it is measured against a depressed continuum. The EW of Fe Kα can be higher than 1.0 keV for column densities of N$_{\rm H} \geq 10^{24}$ cm^{-2}, and such values are indeed observed in highly absorbed and Compton-thick sources (Maiolino *et al.* 1998). Figure 5.21 shows the distributions of the EWs of Fe Kα emission line for the two Seyfert subtypes of our sample. Seyfert type 1s have EW $\sim$ 20 - 250 eV, while for type 2s (except MRK 348) it ranges from $\sim$ 0.5 keV to $\sim$ 2.0 keV. The high EW of Fe Kα line in type 2s suggests high absorbing column density in compared to type 1s.

The addition of a Gaussian emission line at $\sim$ 0.88 keV in NGC 4151 and NGC 7212 improves the fit and is likely to be associated with OVIII radiative recombination continua (*e.g.*, Griffiths *et al.* (1998)). High resolution spectroscopic observations show that the soft X-ray emission in NGC 4151 is dominated by X-ray emission lines and radiative recombination continua (RRC) from hydrogen-like

and helium-like ionization states of neon, oxygen, nitrogen and carbon (Schurch *et al.* 2004). In MRK 766 the addition of a Gaussian emission feature at ~ 0.5 keV improves the fit and may arise due to the blending of a few narrow emission lines.

Table 5.2: The best fit X-ray spectral parameters

Source	Model	Soft X-ray Continuum N_H (10^{20} cm^{-2})	Γ_{SX}	kT (keV)	Hard X-ray Continuum $N_{H,hard}$ (10^{22} cm^{-2})	Γ_{HX}	Emission Lines $E_{c,rest}$ (keV)	I^a_{line}	EW (eV)	χ^2/dof
MCG+8-11-11	pha(PL+R+L)	$18.30^{+0.40}_{-0.43}$				$1.84^{+0.02}_{-0.02}$	$6.44^{+0.01}_{-0.01}$	4.95	$97.9^{+10.4}_{-18.5}$	0.99
MRK 1218	pha(abs*PL+L)	$15.20^{+4.30}_{-13.00}$				$1.48^{+0.11}_{-0.17}$	$6.32^{+0.22}_{-0.49}$	0.19	$63.9^{+46.5}_{-52.4}$	0.99
NGC 2639	pha(T+PL)	$16.20^{+17.60}_{-15.60}$		$0.63^{+0.12}_{-0.09}$		$2.21^{+1.83}_{-1.02}$				0.82
NGC 4151	pha(T+PL+pha*abs*pcf*PL+R+L+L)	$6.33^{+3.30}_{-2.60}$	$3.14^{+0.25}_{-0.06}$	$0.13^{+0.01}_{-0.01}$	$0.12^{+0.08}_{-0.03}$	$1.75^{+0.06}_{-0.03}$	$6.39^{+0.01}_{-0.01}$ $0.88^{+0.01}_{-0.01}$	14.43 1.12	$108.4^{+6.5}_{-6.7}$ $60.1^{+29.0}_{-4.4}$	1.12
MRK 766	pha(T+abs*pcf*pha*PL+R+L+L+L)	1.35^f		$0.20^{+0.01}_{-0.01}$		$2.17^{+0.10}_{-0.08}$	$6.44^{+0.03}_{-0.03}$ $6.67^{+0.06}_{-0.07}$ $0.48^{+0.01}_{-0.01}$	0.50 0.22 5.38	$47.9^{+13.9}_{-13.5}$ $19.3^{+12.6}_{-12.2}$ $137.3^{+45.6}_{-37.5}$	1.09
MRK 231	pha(T+T+pcf*pha*PL+L+L)	1.25^f		$0.33^{+0.04}_{-0.03}$ $0.99^{+0.14}_{-0.15}$	$0.46^{+0.14}_{-0.16}$	$1.57^{+0.14}_{-0.30}$	$6.28^{+0.13}_{-0.13}$ $6.66^{+0.07}_{-0.20}$	0.16 0.15	$215.0^{+123.1}_{-128.1}$ $243.5^{+167.8}_{-163.5}$	1.04
ARK 564	pha(T+PL+pcf*PL+L+L)	6.38^f	$3.42^{+0.13}_{-0.12}$	$0.97^{+0.04}_{-0.04}$		$2.32^{+0.08}_{-0.10}$	$6.33^{+0.05}_{-0.05}$ $6.71^{+0.04}_{-0.03}$	0.29 0.41	$20.9^{+10.4}_{-9.9}$ $32.3^{+11.4}_{-11.5}$	1.09
NGC 7469	pha(T+abs*pcf*PL+L)	4.96^f		$0.18^{+0.01}_{-0.01}$		$2.04^{+0.02}_{-0.02}$	$6.41^{+0.01}_{-0.02}$	2.03	$64.2^{+7.5}_{-9.5}$	1.09
MRK 926	pha(pcf*PL+R+L)	3.59^f				$1.98^{+0.03}_{-0.02}$	$6.33^{+0.06}_{-0.06}$	1.24	$29.1^{+17.3}_{-23.8}$	0.96
MRK 530	pha(T+pcf*PL+L)	4.06^f		$0.20^{+0.02}_{-0.02}$		$2.28^{+0.03}_{-0.01}$	$6.40^{+0.05}_{-0.05}$	1.49	$47.2^{+21.2}_{-20.5}$	1.09
MRK 348	pha(PL+pha*pcf*PL+L)	5.91^f	$2.75^{+0.17}_{-0.16}$		$6.86^{+0.84}_{-1.01}$	$1.70^{+0.07}_{-0.06}$	$6.40^{+0.04}_{-0.04}$	1.59	$34.2^{+10.8}_{-10.4}$	1.05
MRK 1	pha(T+PL+R+L)	5.31^f	$2.55^{+0.30}_{-0.29}$	$0.82^{+0.09}_{-0.10}$	>150	2.00^f R	$6.77^{+0.08}_{-0.09}$	0.01	$1249.2^{+1299.4}_{-857.5}$	0.99
NGC 2273	pha(PL+R+L)	$7.75^{+36.20}_{-7.70}$	$2.79^{+1.87}_{-0.82}$		>150	$0.67^{+0.37}_{-0.92}$ R	$6.40^{+0.03}_{-0.02}$	2.74	$2189.2^{+446.2}_{-441.7}$	0.97
MRK 78	pha(PL+R+L)	$65.38^{+30.02}_{-24.48}$	$7.05^{+1.89}_{-1.84}$		>150	$1.01^{+0.44}_{-0.54}$ R	$6.37^{+0.05}_{-0.09}$	0.56	$673.0^{+402.9}_{-389.2}$	0.85
NGC 5135^S	pha((T+T+PL+pha*PL+R+L)	4.58^f	$2.65^{+0.29}_{-0.37}$	$0.48^{+0.56}_{-0.14}$ $0.89^{+0.28}_{-0.62}$	277^{+184}_{-107}	$1.73^{+0.14}_{-0.33}$	$6.38^{+0.01}_{-0.01}$	0.84	$1760.0^{+298.4}_{-297.1}$	1.69
MRK 477^L	pha(pha*PL+L)	1.3^f			$24.00^{+17.00}_{-12.00}$	1.90^f	$6.40^{+0.21}_{-0.23}$	...	$560.0^{+560.0}_{-500.0}$	0.35
NGC 5929^C	pha(PL+pha*PL+L)	51.60	1.70		27.70	1.70	6.40	...	350.0	....
NGC 7212	pha(PL+R+L+L)	5.41^f	$2.32^{+0.23}_{-0.20}$		>150	$0.99^{+0.54}_{-0.37}$ R	$6.42^{+0.04}_{-0.04}$ $0.89^{+0.04}_{-0.04}$	0.74 0.04	$712.3^{+256.0}_{-133.4}$ $59.6^{+43.1}_{-38.5}$	1.15
MRK 533	pha(T+PL+R+L+L)	5.16^f	$3.75^{+1.45}_{-0.61}$	$0.76^{+0.13}_{-0.10}$	>150	$2.12^{+0.49}_{-0.51}$ R	$6.40^{+0.04}_{-0.05}$ $7.04^{+0.07}_{-0.04}$	0.55 0.53	$557.2^{+241.2}_{-292.7}$ $665.6^{+387.9}_{-333.7}$	0.97
NGC 7682	pha(T+R+L+L)	$34.88^{+57.82}_{-25.11}$	$5.36^{+2.78}_{-2.38}$		>150	$1.77^{+0.58}_{-0.61}$ R	$6.43^{+0.18}_{-0.06}$ $7.11^{+0.39}_{-0.09}$	0.20 0.13	$477.5^{+312.3}_{-310.9}$ $457.6^{+460.3}_{-402.9}$	0.81

Notes: a: 10^{-13} ergs cm^{-2} s^{-1}; f: fixed; s: soft component; pha: photoelectric absorption; PL: power-law; L: Emission line fitted with a Gaussian; T: Thermal emission from hot gas ('MEKAL' model in XSPEC); abs: Ionized absorber ('absori' model in XSPEC); R: Reflection from cold neutral material ('PEXRAV' model in XSPEC); pcf: partial covering;
S: see chapter 6; L: Levenson, Weaver, and Heckman (2001); C: Cardamone, Moran, and Kay (2007)

Table 5.3: Summary of partial covering model parameters

Source Name	N_H $(10^{22}$ cm$^{-2})$	Covering fraction (f)
NGC 4151	$9.06^{+1.27}_{-0.98}$	$0.69^{+0.04}_{-0.05}$
MRK 766	$6.42^{+0.93}_{-0.56}$	$0.51^{+0.02}_{-0.03}$
MRK 231	$8.35^{+4.02}_{-4.64}$	$0.74^{+0.09}_{-0.25}$
ARK 564	$3.09^{+0.52}_{-0.45}$	$0.61^{+0.26}_{-0.15}$
NGC 7469	$35.55^{+9.93}_{-6.77}$	$0.28^{+0.03}_{-0.03}$
MRK 926	$4.35^{+2.86}_{-1.99}$	$0.15^{+0.06}_{-0.06}$
MRK 530	$14.81^{+5.62}_{-4.18}$	$0.27^{+0.27}_{-0.27}$
MRK 348	$10.47^{+0.68}_{-1.00}$	$0.84^{+0.06}_{-0.06}$

Table 5.4: Summary of ionized absorber parameters

Source Name	N_H $(10^{22}$ cm$^{-2})$	Ionization parameter (ξ)
MRK 1218	$0.63^{+0.41}_{-0.32}$	$39.60^{+57.40}_{-38.37}$
NGC 4151	$5.08^{+1.45}_{-1.20}$	$0.31^{+0.40}_{-0.28}$
MRK 766	$0.21^{+0.03}_{-0.02}$	$6.61^{+4.67}_{-1.67}$
NGC 7469	$1.06^{+0.42}_{-0.36}$	$1193.19^{+692.30}_{-232.63}$

Notes: Ionization parameter indicates the ionization state of absorbing material and is defined as $\xi = \frac{L}{nr^2}$, where L is the source luminosity (in $\sim$ 13.6 eV - 13.6 keV energy range), n is the absorbing gas density and r is the distance of absorber from the ionizing source (Osterbrock and Ferland 2006).
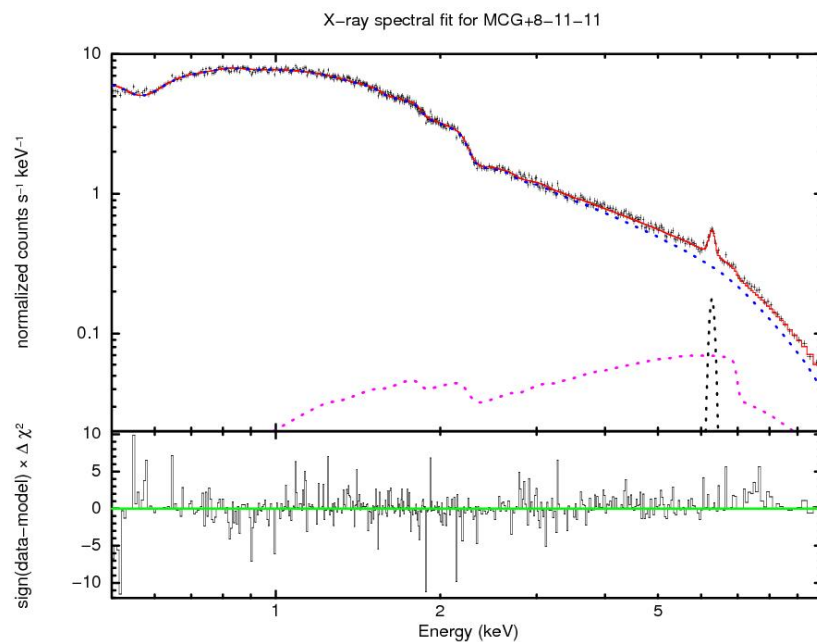
Figure 5.1: *XMM-Newton* pn 0.5 - 10.0 keV X-ray spectral fit for MCG+8-11-11. The top panel shows the cumulative fit (solid curve in 'Red') along with all the additive spectral components (shown in dotted curves) against the spectral data points (shown by '+') and the bottom panel shows the residuals. Figures 5.2 to 5.17 display the same for other sample sources.
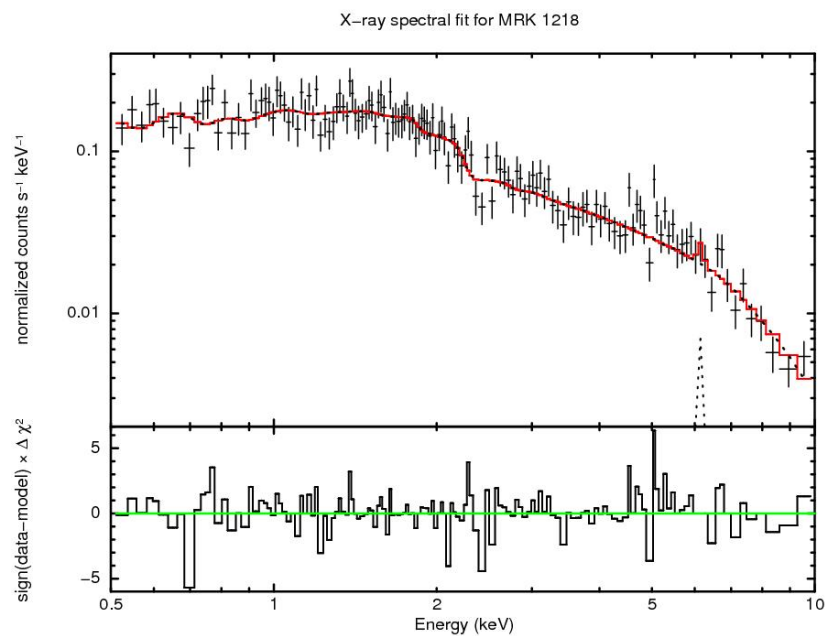
Figure 5.2: *XMM-Newton* pn 0.5 - 10.0 keV X-ray spectral fit for MRK 1218.
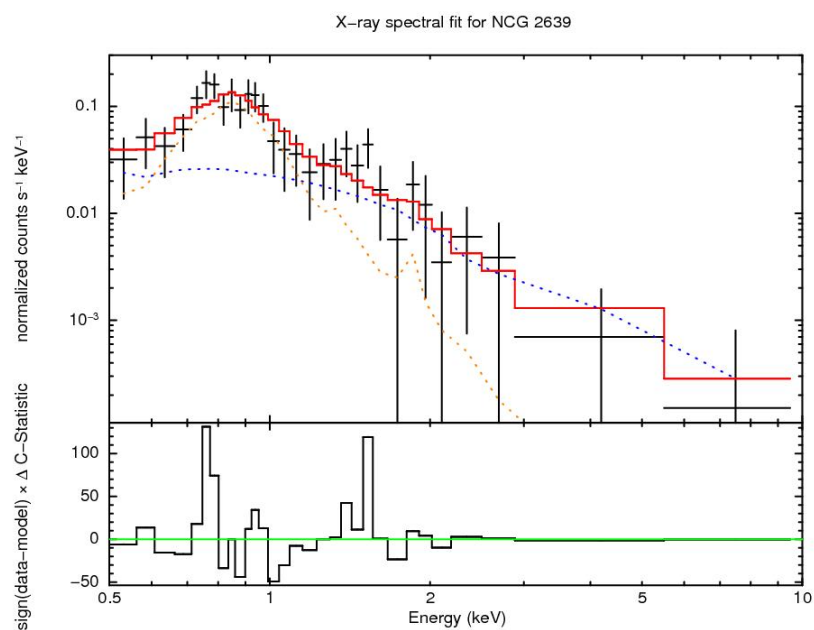
Figure 5.3: *XMM-Newton* pn 0.5 - 10.0 keV X-ray spectral fit for NGC 2639.
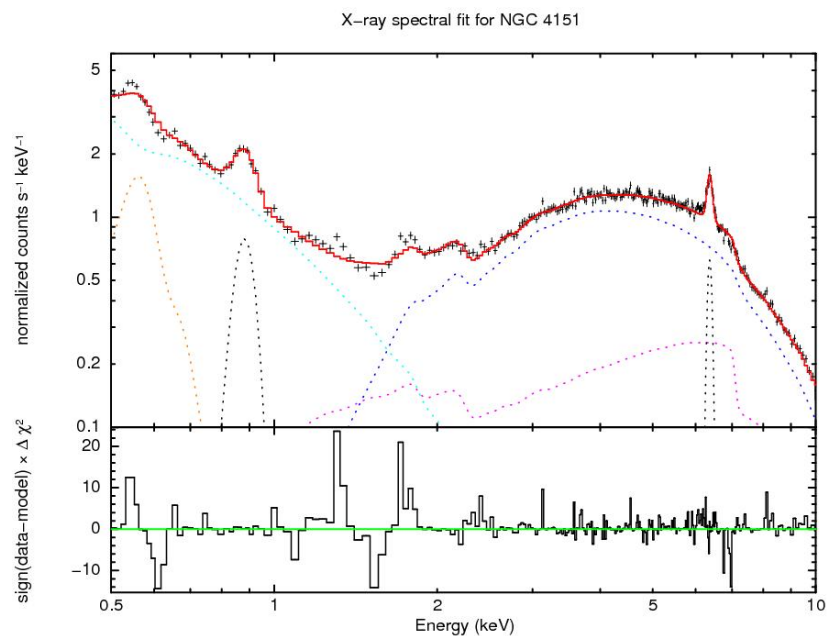
Figure 5.4: *XMM-Newton* pn 0.5 - 10.0 keV X-ray spectral fit for NGC 4151.
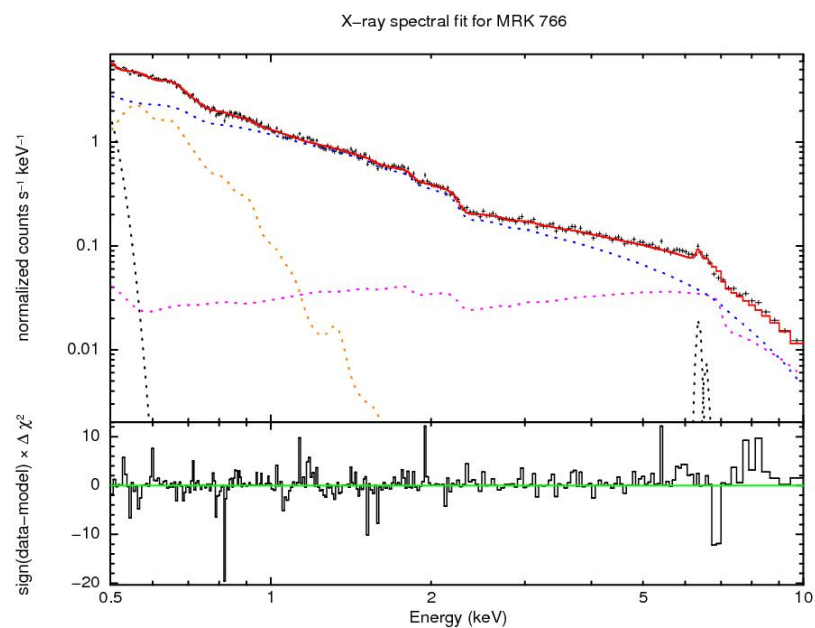
Figure 5.5: *XMM-Newton* pn 0.5 - 10.0 keV X-ray spectral fit for MRK 766.
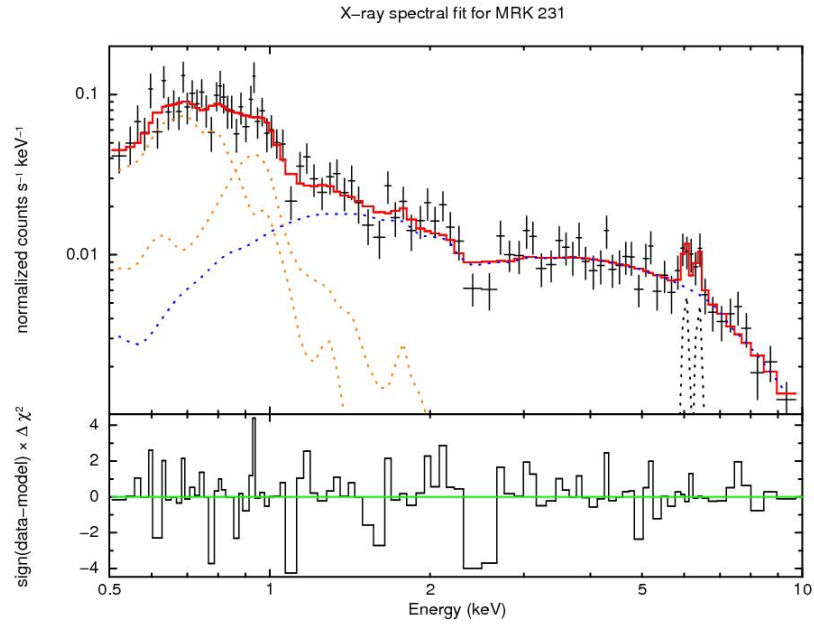
Figure 5.6: *XMM-Newton* pn 0.5 - 10.0 keV X-ray spectral fit for MRK 231.
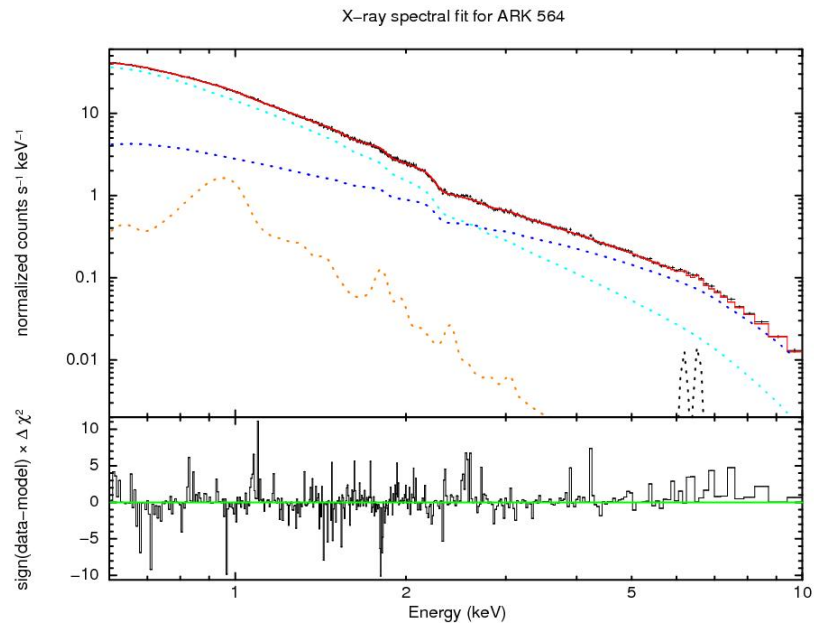
Figure 5.7: *XMM-Newton* pn 0.5 - 10.0 keV X-ray spectral fit for ARK 564.
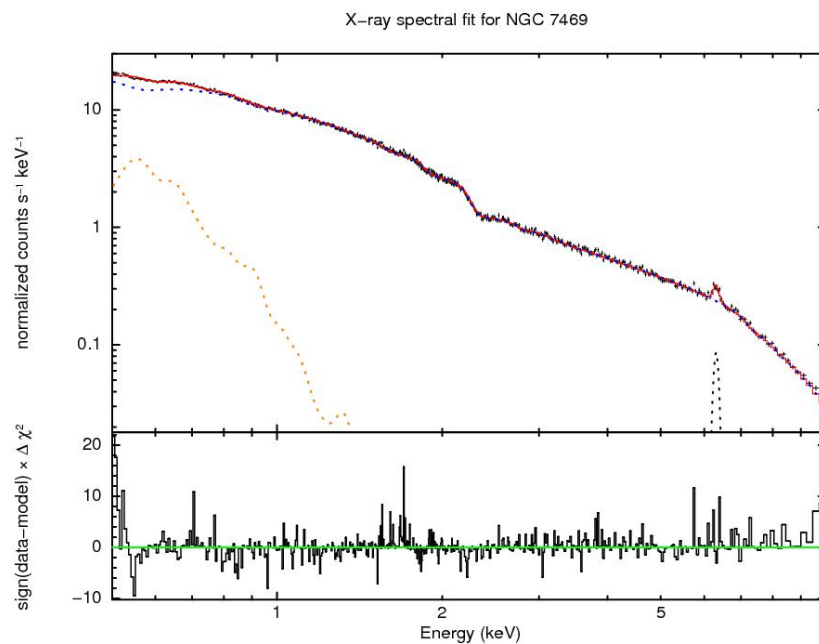
Figure 5.8: *XMM-Newton* pn 0.5 - 10.0 keV X-ray spectral fit for NGC 7469.
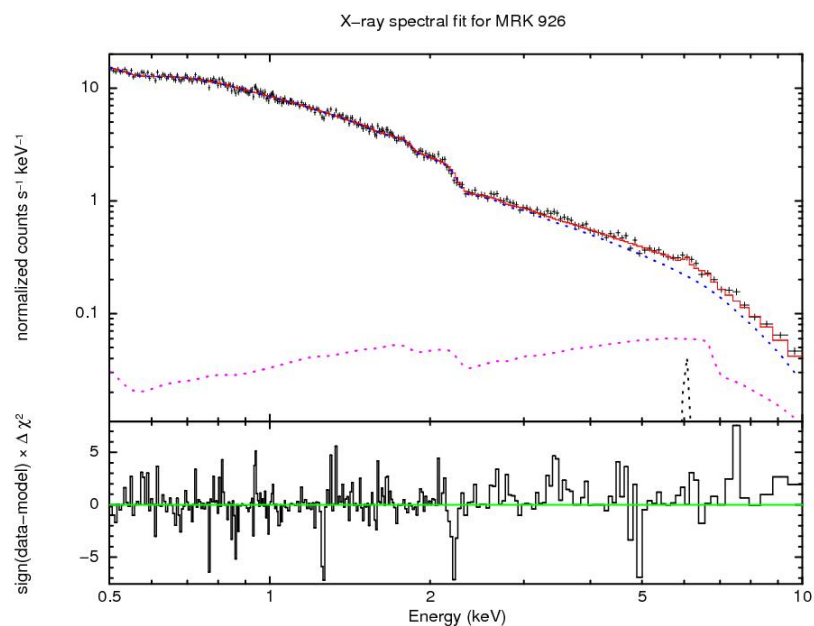
Figure 5.9: *XMM-Newton* pn 0.5 - 10.0 keV X-ray spectral fit for MRK 926.
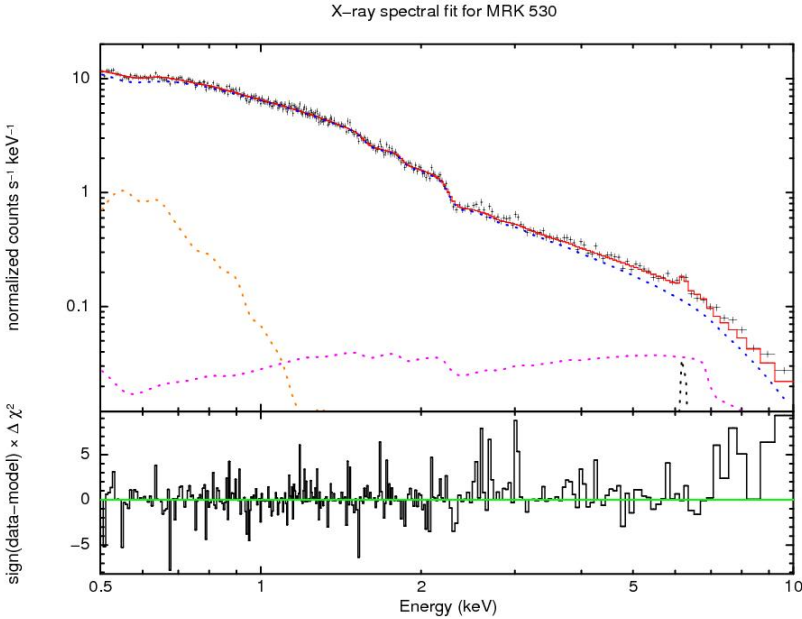
Figure 5.10: *XMM-Newton* pn 0.5 - 10.0 keV X-ray spectral fit for MRK 530.
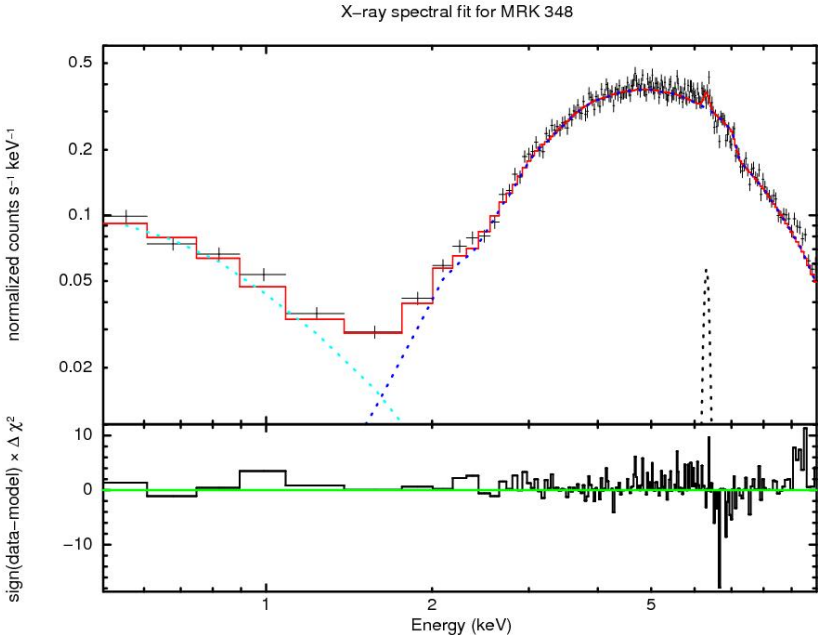
Figure 5.11: *XMM-Newton* pn 0.5 - 10.0 keV X-ray spectral fit for MRK 348.
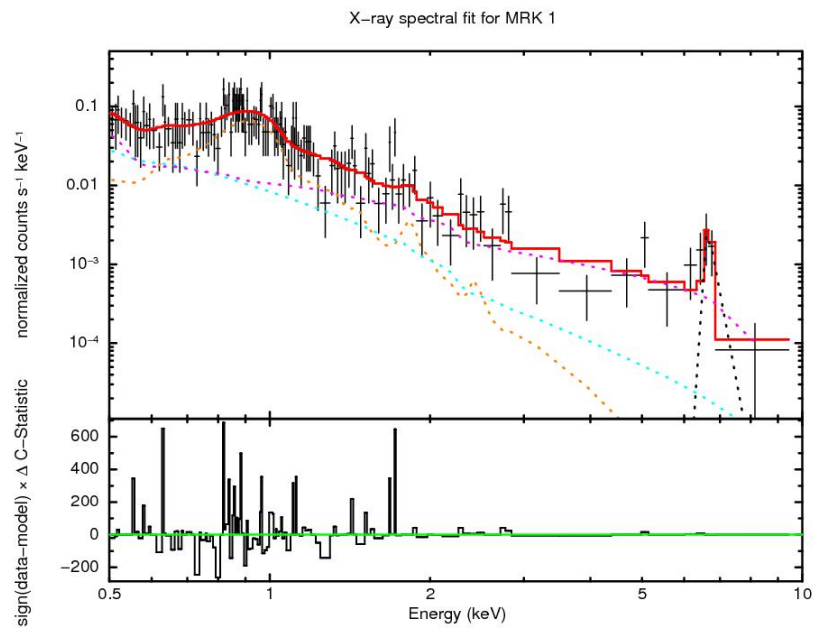
Figure 5.12: *XMM-Newton* pn 0.5 - 10.0 keV X-ray spectral fit for MRK 1.
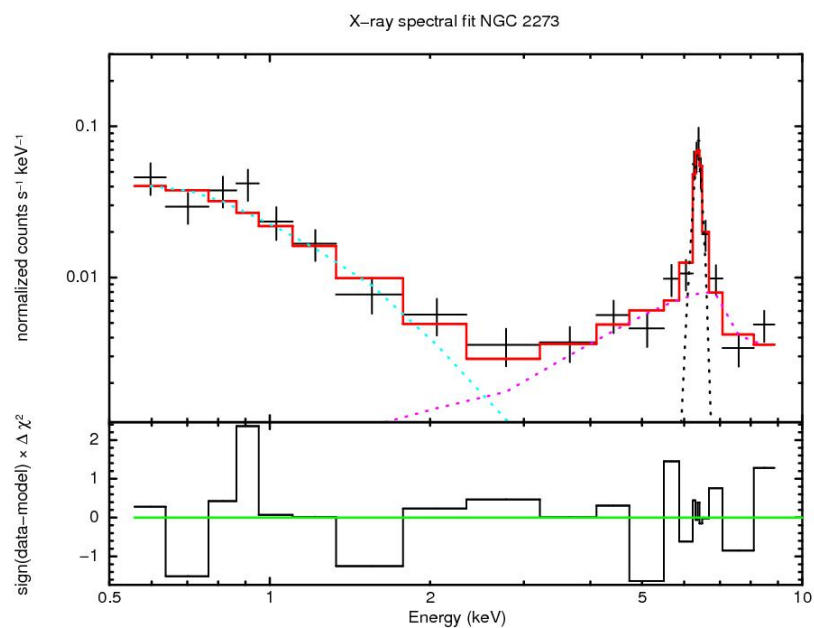
Figure 5.13: *XMM-Newton* pn 0.5 - 10.0 keV X-ray spectral fit for NGC 2273.
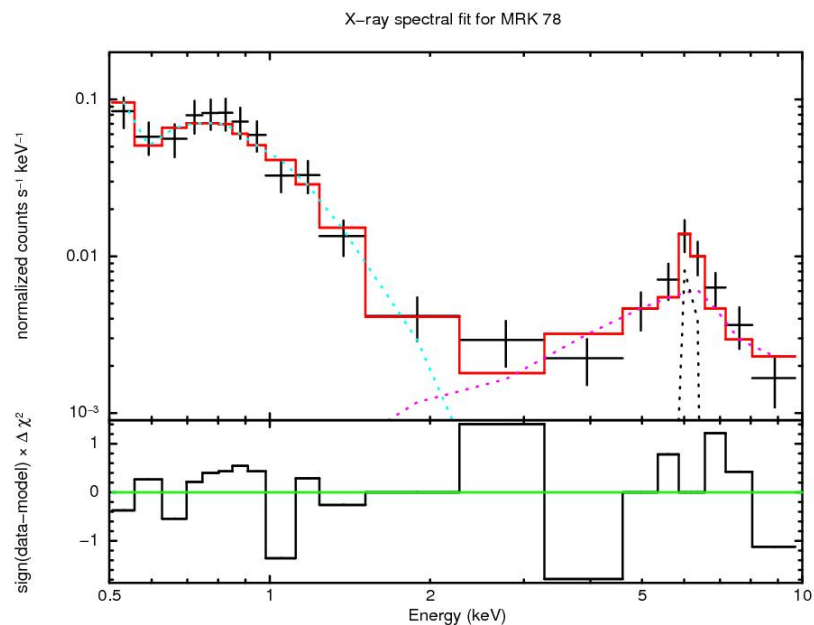
Figure 5.14: *XMM-Newton* pn 0.5 - 10.0 keV X-ray spectral fit for MRK 78.
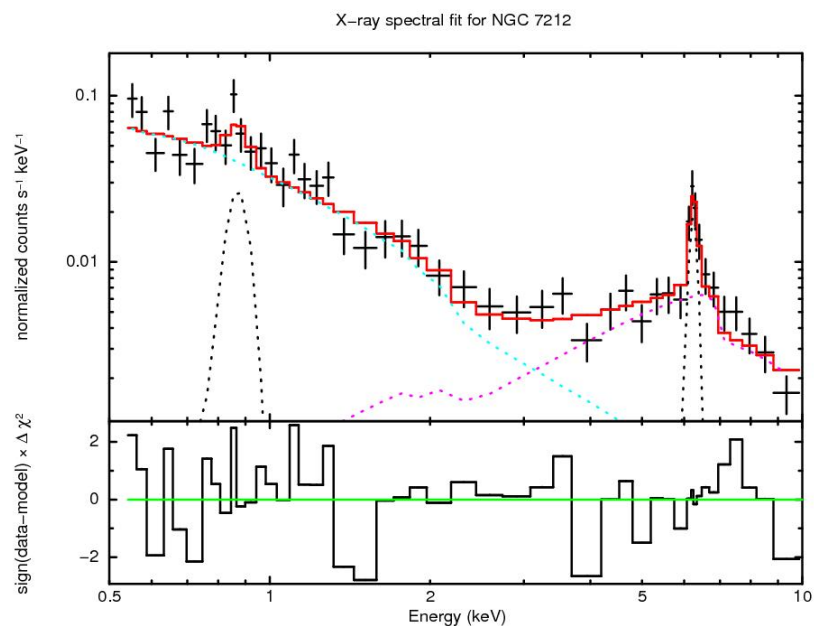
Figure 5.15: *XMM-Newton* pn 0.5 - 10.0 keV X-ray spectral fit for NGC 7212.
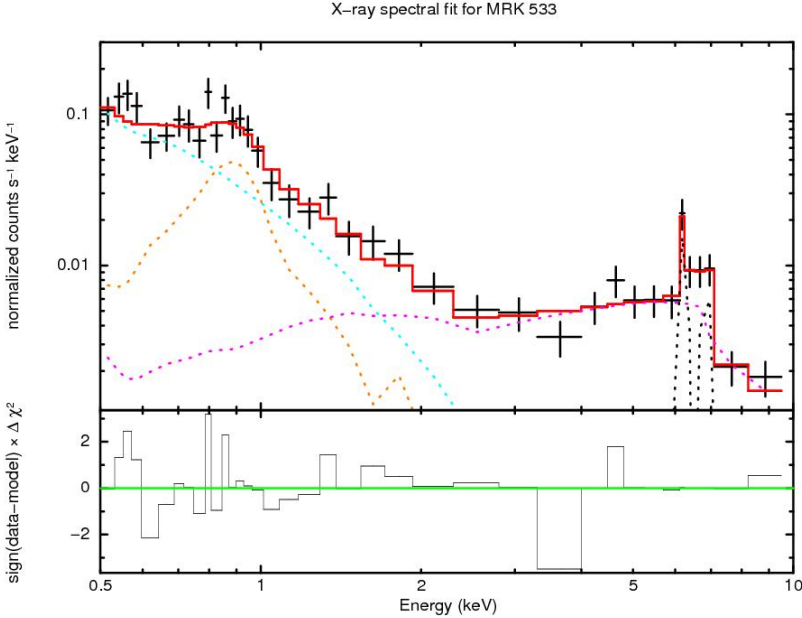
Figure 5.16: *XMM-Newton* pn 0.5 - 10.0 keV X-ray spectral fit for MRK 533.
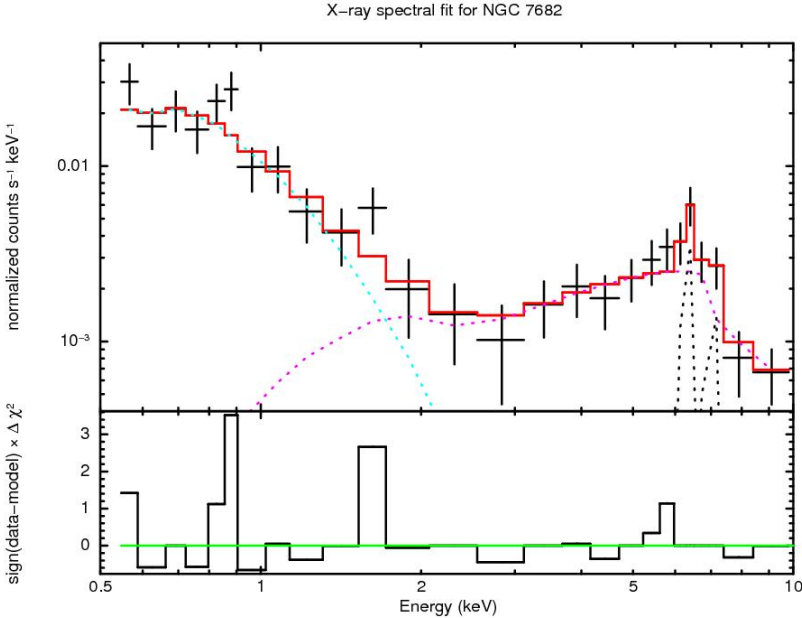
Figure 5.17: *XMM-Newton* pn 0.5 - 10.0 keV X-ray spectral fit for NGC 7682.

5.4 Discussion

In the following sections, I discuss the comparison of X-ray luminosities and spectral properties *i.e.*, X-ray absorbing column densities (N_H), the properties of Fe Kα emission line, flux ratios of hard X-ray (2.0 - 10.0 keV) to [OIII] $\lambda5007\text{Å}$ line emission and the hard X-ray - core radio luminosity correlation for the two Seyfert subtypes in the framework of the Seyfert unification scheme.

5.4.1 X-ray luminosities of the two Seyfert subtypes

The soft (0.5 - 2.0 keV) and hard (2.0 - 10.0 keV) X-ray luminosity distributions for the two Seyfert subtypes are shown in Figure 5.18. Soft X-ray luminosities of Seyfert 1s of our sample range from $\sim 10^{40}$ erg s^{-1} to $\sim 10^{44}$ erg s^{-1} with the median value $\sim 6.58 \times 10^{42}$ erg s^{-1}, while for Seyfert 2s it ranges from $\sim 10^{38}$ erg s^{-1} to $\sim 10^{42}$ erg s^{-1} with the median value $\sim 6.9 \times 10^{40}$ erg s^{-1}. The two sample Kolmogorov - Smirnov test shows that the soft (0.5 - 2.0 keV) X-ray luminosity distributions of type 1 and type 2 Seyferts are completely different (*cf.*, Table 5.6). Seyfert type 2s have systematically lower soft X-ray luminosities than type 1s. The nearly 2 dex difference in the medians of the soft X-ray luminosities of the two Seyfert subtypes can be explained as the presence of more line-of-sight X-ray absorption in type 2s than that in type 1s, which is expected since obscuring torus intercepts observer's line-of-sight according to the orientation based Seyfert unification. In hard X-ray (2.0 - 10.0 keV) band, Seyfert 1s of our sample have luminosities ranging from $\sim 10^{40}$ erg s^{-1} to $\sim 10^{45}$ erg s^{-1} with the median value $\sim 1.1 \times 10^{43}$ erg s^{-1}, while for Seyfert 2s, it range from $\sim 10^{40}$ erg s^{-1} to $\sim 10^{44}$ erg s^{-1} with the median value $\sim 6.8 \times 10^{41}$ erg s^{-1} (*cf.*, Table 5.6). The difference between the hard X-ray luminosity distributions of the two Seyfert subtypes is lower compared to the soft band and can be explained as hard X-ray (2.0 - 10.0 keV) photons suffer less absorption. According to the unification model, at sufficiently high energy one can expect similar X-ray luminosities for the two Seyfert subtypes

as the torus optical thickness decreases with the increase in photon energy and similar central engines are at work in both subtypes. There is noticeable difference between the hard X-ray (2.0 - 10 keV) luminosity distributions of the two Seyfert subtypes, which can be understood as due to the presence high absorption in type 2s. Several of type 2 sources in our sample are heavily obscured (Compton-thick) in which X-ray continuum below 10.0 keV is completely suppressed and dominated by reprocessed components.
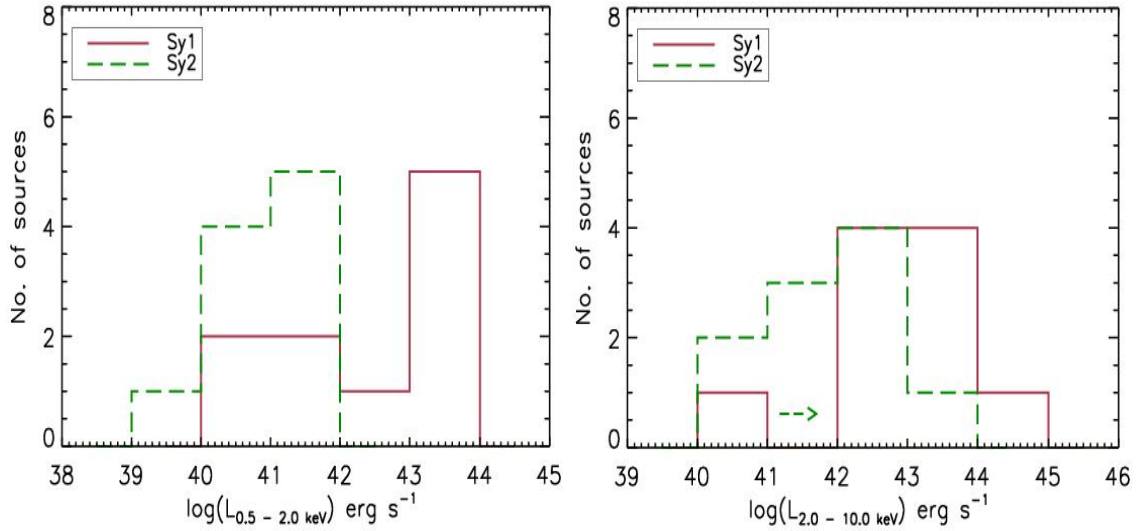
Figure 5.18: Distributions of the soft (0.5 - 2.0 keV) and hard (2.0 - 10.0 keV) X-ray luminosities of the two subtypes of our sample Seyfert galaxies.

Table 5.5: Observed X-ray fluxes, luminosities in soft (0.5 - 2.0 keV) and hard (2.0 - 10.0 keV) bands and the flux ratios of hard X-ray to [OIII]

Name	$F_{0.5-2.0 \text{ keV}}$	$\log L_{0.5-2.0 \text{ keV}}$	$F_{2.0-10 \text{ keV}}$	$\log L_{2.0-10 \text{ keV}}$	$F_{[OIII]}$	logRx
MCG+8-11-11	161.18	43.35	441.97	43.79	6.43	1.84
MRK 1218	4.86	41.96	25.35	42.68	1.70	1.17
NGC 2639	1.26	40.52	0.75	40.29	1.07	-0.15
NGC 4151	29.49	40.75	828.83	42.20	116.00	0.85
MRK 766	33.99	42.10	72.66	42.43	3.95	1.26
MRK 231	0.99	41.60	6.06	42.38	2.30	0.42
ARK 564	364.22	43.67	162.25	43.31	1.90	1.93
NGC 7469	213.27	43.08	293.41	43.21	5.80	1.70
MRK 926	171.95	43.94	299.05	44.18	3.50	1.93
MRK 530	166.48	43.52	182.74	43.56	0.48	2.58
MRK 348	1.17	40.76	269.39	43.12	4.12	1.82
MRK 1	0.98	40.74	0.81	40.66	6.00	-0.87
NGC 2273	0.53	39.62	10.02	40.89	1.60	0.80
MRK 78	0.79	41.39	5.52	42.23	6.60	-0.08
NGC 5135[S]	3.72	41.20	4.18	41.25	3.70	0.05
MRK 477[L]	1.20	41.59	12.00	42.59	15.00	-0.10
NGC 5929[C]	0.81	40.15	>14.00	>41.39	0.93	>1.18
NGC 7212	0.83	41.13	6.96	42.05	8.75	-0.10
MRK 533	1.42	41.42	6.08	42.06	5.21	0.07
NGC 7682	0.27	40.22	2.62	41.22	2.30	0.06

Notes: [OIII] $\lambda5007$Å fluxes are obtained from literature and references are the same as in Table 2.1. [OIII] and X-ray fluxes are in units of 10^{-13} erg cm^{-2} s^{-1}. $R_x = \frac{\text{Flux}(2.0-10.0 \text{ keV})}{\text{Flux}([OIII])}$. S: see chapter 6; L: Levenson, Weaver, and Heckman (2001); C: Cardamone, Moran, and Kay (2007). Ref., 7: Mulchaey *et al.* (1994), 8: Dahari and De Robertis (1988), 9: Bassani *et al.* (1999).

Table 5.6: Medians and Kolmogorov - Smirnov two sample tests for the statistical comparison of various distributions of the two Seyfert subtypes

Distribution	Median		D	p-value
	Type 1s	Type 2s		
$\log L_{0.5-2.0 \text{ keV}}$	42.82	40.91	0.8	2.06×10^{-3}
$\log L_{2.0-10.0 \text{ keV}}$	43.02	41.83	0.6	5.25×10^{-2}
$\log N_H$	21.02	> 24.18	1.0	9.08×10^{-5}
$\log EW$ (eV)	1.81	2.79	0.9	9.30×10^{-4}
$\log R_x$	1.48	0.06	0.6	5.47×10^{-2}

Notes: Kolmogorov - Smirnov two sample test examines the null hypothesis that two samples comes from same distribution. $D = \text{Sup x } |S1(x) - S2(x)|$ is the maximum difference between the cumulative distributions of two samples $S1(x)$ and $S2(x)$, respectively. $R_x = \frac{\text{Flux}(2.0 - 10.0 \text{ keV})}{\text{Flux[OIII]}}$.

5.4.2 Absorbing column densities of the two Seyfert subtypes

The cold matter present in between observer and AGN (mainly consists of the Galactic and the material at the redshift of AGN) absorbs preferentially soft X-ray emitted from AGN. The photoelectric absorption model in the X-ray spectral modeling renders the amount of absorption along the line-of-sight in terms of equivalent hydrogen column density (N_H) as long as the direct transmitted component is seen. In general, we fit the X-ray continuum with a photoelectric absorbed power-law, keeping column density and power-law photon index as free parameters and also all the spectral components are atleast absorbed by the Galactic equivalent hydrogen column density. Figure 5.19 shows the distributions of cumulative N_H of the two Seyfert subtypes. The estimated absorbing equivalent hydrogen column densities for our sample sources varies from as low as to the Galactic value ($N_H \simeq$

10^{20} cm^{-2}) to as high as to the Compton-thick limiting value ($N_H \geq 10^{24}$ cm^{-2}). For type 1 sources the equivalent N_H ranges from $\sim 10^{20}$ cm^{-2} (Galactic value) to $\sim 10^{22}$ cm^{-2}, while for type 2 it ranges from $\sim 10^{22}$ cm^{-2} to $\geq 10^{24}$ cm^{-2} (*cf.*, Figure 5.19). We have $\sim 7/10$ reflection dominated type 2 sources in which hard component (2.0 - 10.0 keV) is accounted by a pure reflection component ('pexrav' model) and therefore we have only upper limit for the N_H values ($\geq 1.5 \times 10^{24}$) in such cases. The Kolmogorov - Smirnov statistical test shows that the distributions of absorbing column densities (N_H) of the two Seyfert subtypes are different, *i.e.*, null hypothesis that the two distributions are same is rejected (*cf.*, Table 5.6). Thus, comparison of the absorbing column densities of the two Seyfert subtypes in our sample are consistent with the orientation based Seyfert unification scheme. In our sample we do not find any unabsorbed type 2 Seyfert galaxy, although some previous studies have reported the presence of 10% - 30% of unabsorbed type 2 Seyferts (*e.g.*, Panessa and Bassani (2002)).

In several of our sample sources we require partial covering of the primary AGN radiation. The best fit values of covering fraction and absorbing equivalent hydrogen column density are mentioned in Table 5.3. In four Seyfert type 1s, *e.g.*, MRK 1218, NGC 4151, MRK 766 and NGC 7469, warm absorption accounted by 'absori' model (ionized absorber) is needed for the best fit. While using 'absori' model we fixed the photon index of the power-law of 'absori' component equal to the photon index of the primary power-law component and the plasma temperature was fixed to 3×10^4 K. The best fit parameter values for N_H and ionization parameters are given in Table 5.4. The estimated ionization parameter reveals low ionizing material in MRK 1218, NGC 4151 and MRK 766, however, in NGC 7469 ionization level is high. Using *XMM-Newton* RGS data Blustin *et al.* (2007) reported that NGC 7469 shows the evidence of ionized outflowing material with a wide range of ionization (log $\xi_i \sim 0.5$ - 3.5) and two distinct velocity ranges ~ 580 - 720 and ~ 2300 km s^{-1}. The presence of warm absorber in NGC 4151 and MRK 766 has also been reported in previous studies (*e.g.*, Schurch *et al.* (2004); Mason *et al.* (2003)).

High spectral resolution X-ray observations show that the warm absorbers give rise narrow absorption lines of ionized elements such as H-like and He-like ions of C, N, O, Ne, Na, Mg, Si, and FeXIV - FeXXI, with a wide range of ionization and blue-shifted by a few hundred km s^{-1} (Kaspi *et al.* 2000; Kaastra *et al.* 2000; Blustin *et al.* 2007).

While comparing the amount of obscuration for the two Seyfert subclasses we consider only cold absorption accounted by the photoelectric absorption component. The location of obscuration in Seyfert galaxies can extend from hundreds of parsec to as close as broad line region. Rapid X-ray variability observed in few AGNs, such as NGC 1365 (Risaliti *et al.* 2005, 2009) supports the notion of clumpy, non-uniform torus and obscuration being as close as the broad line region.
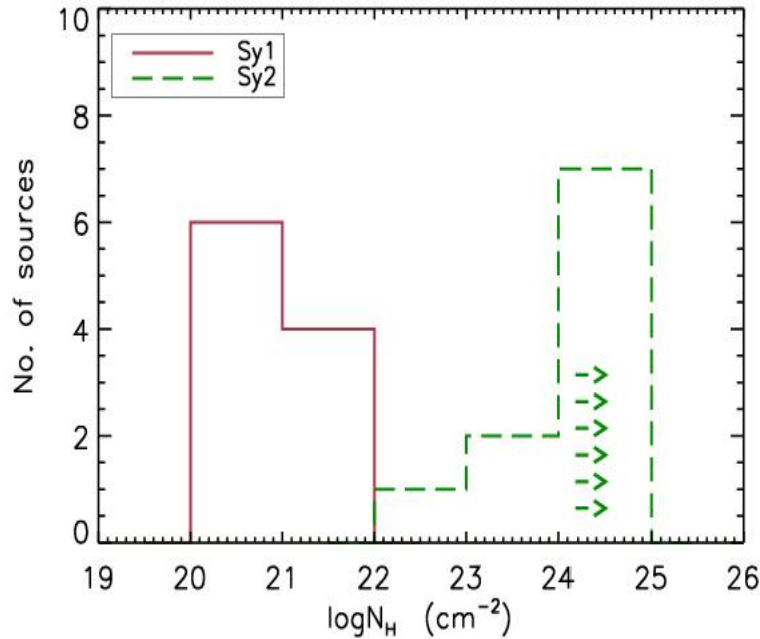
Figure 5.19: Distributions of the absorbing equivalent hydrogen column densities of the two Seyfert subtypes of our sample. Arrows pointing towards right represent the lower limits of absorbing column densities for the Compton-thick sources.

5.4.3 The equivalent widths of Fe Kα emission line of the two Seyfert subtypes

We detected fluorescent Fe Kα emission line in all of our sample sources (except NGC 2639) suggesting the ubiquitous presence of Fe Kα line in the X-ray spectra of Seyfert galaxies. We could not confirm the presence of Fe Kα emission line in NGC 2639 due to lack of enough counts above 2.0 keV. However, using *ASCA* observations of NGC 2639, Terashima *et al.* (2002) reported the presence of Fe Kα line with EW $\sim$ 1.5 - 3.0 keV. The neutral and mildly ionized (less than FeXVIII) fluorescing material gives rise Fe Kα emission line at 6.4 keV, while highly ionized material such as FeXXV and FeXXVI emits line at 6.7 keV and 7.0 keV, respectively. In all our sample sources the centroid energy of Fe Kα emission line is consistent with the emission from neutral or mildly ionized iron. When the absorbing column density increases to a few times of 10^{23} H atoms cm^{-2}, the equivalent width of Fe Kα increases, since it is measured against a much depressed continuum. The equivalent width can be higher than 1 keV for column densities of N$_{\rm H} \geq 10^{24}$ cm^{-2}, and such values are indeed observed in highly absorbed and Compton-thick sources (Maiolino *et al.* 1998). We estimate the EW of Fe Kα line with respect to the modeled continuum and find that Seyfert type 2s have systematically larger EWs (ranges from 350 eV to 2.2 keV, except MRK 348) with the median value $\sim$ 600 eV than that of type 1s (in $\sim$ 20 - 200 eV range) with the median value $\sim$ 64.0 eV. Kolmogorov - Smirnov two sample test shows that the distributions of the EW of Fe Kα line for the two Seyfert subtypes are different, *i.e.*, null hypothesis that the two distributions are same is rejected (*cf*., Table 5.6). Heavily obscured Compton-thick sources are characterized by large EW of Fe Kα line (Krolik, Madau, and Zycki 1994; Levenson *et al.* 2006) and therefore we use large EW ($\sim$ 1.0 keV) of Fe Kα line as an indicator of heavy obscuration as it is measured against much depressed continuum (N$_{\rm H} \sim 10^{23}$ - 10^{24} cm^{-2}; Leahy and Creighton (1993)) or against pure reflection component (N$_{\rm H} \sim 10^{24}$ - 10^{25}

cm^{-2}; Bassani *et al.* (1999)). However, identifying all sources with large EW as Compton-thick may not be correct, since large EW can also arise if the ionizing radiation is anisotropic (Ghisellini *et al.* 1991), or if there is a lag between a drop in AGN continuum and Fe Kα line emissions, as observed in NGC 2992 by Weaver *et al.* (1996).
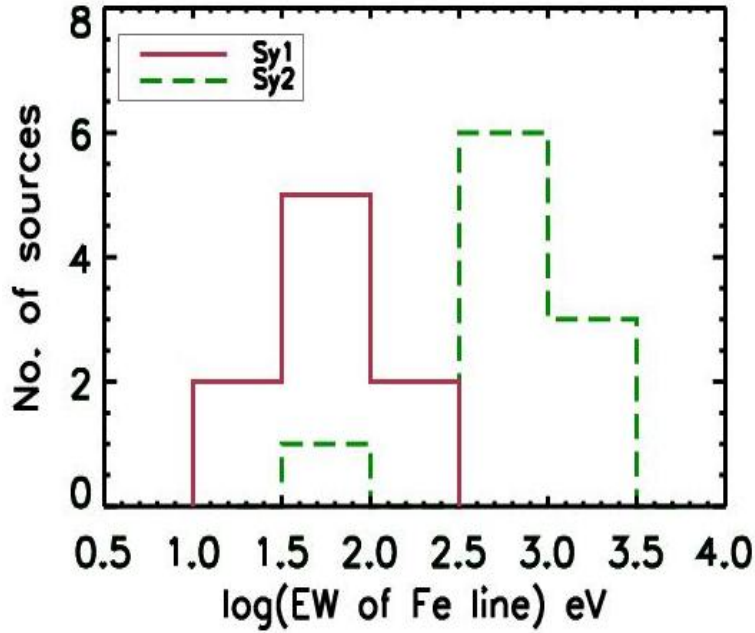
Figure 5.20: Distributions of the equivalent widths of Fe Kα emission line of the two subtypes of our sample Seyfert galaxies.

5.4.4 The flux ratios of hard X-ray to [OIII] λ5007Å line of the two Seyfert subtypes

In order to confirm the high obscuration in Seyfert type 2s compared to type 1s we use flux ratio of hard (2.0 - 10.0 keV) X-ray to [OIII] λ5007Å and equivalent width of Fe Kα line as diagnostic tools (*e.g.*, Cappi *et al.* (2006)). Bassani *et al.* (1999) reported that the flux ratio of hard X-ray to [OIII] λ5007Å can effectively be used in identifying Compton-thin and Compton-thick sources with latter having flux ratio $\leq$ 1. The flux ratio of hard X-ray to [OIII] λ 5007Å can be used as an

indicator of the amount of obscuration since [OIII] originates from the NLR region largely unaffected by the torus obscuration and can be considered as the proxy of the intrinsic AGN power since it is produced by photoionization of NLR clouds by the AGN continuum (Yee, Stockman, and Green 1981; Nelson and Whittle 1995). A statistical comparison of the distributions of the flux ratios of hard X-ray (2.0 - 10.0 keV) to [OIII] for the two Seyfert subtypes again confirms the systematically higher obscuration is type 2s than type 1s (*cf.*, Table 5.6, Figure 5.21). Also, using this flux ratio as an indicator we note that MRK 1, MRK 78, NGC 5135, MRK 477, NGC 7212, MRK 533 and NGC 7682 have Compton-thick obscuration. X-ray spectral properties, *e.g.*, reflection dominated hard X-ray component, low value of the flux ratio of hard X-ray to [OIII] and high EW of Fe Kα line implies that $\sim$ 7 - 8 out of 10 type 2 sources of our sample are Compton-thick ($N_H \geq 1.5 \times 10^{24}$ cm^{-2}). Some of our sample sources, *e.g.*, MRK 477 (Bassani *et al.* 1999), NGC 7212 (Levenson *et al.* 2006), NGC 2273 (Guainazzi *et al.* 2005) and MRK 533 (Bianchi *et al.* 2005) have already been reported as Compton-thick. In our sample we have only one Seyfert subtype 1.8 (MRK 1218) and one subtype 1.9 (NGC 2639) which are included into type 1s and thus even if we include subtypes 1.8, 1.9 into type 2s, the relative fraction of Compton-thick sources remains high $\sim$ 60% (7-8 source out of 12 type 2s). The large fraction (*i.e.*, $\sim$ 70%) of Compton-thick sources among type 2 population in our sample is in agreement with previous studies by Risaliti, Maiolino, and Salvati (1999) and emphasizes that the sample selection based on the isotropic properties is essential to estimate the correct relative fraction of absorbed/unabsorbed AGN.
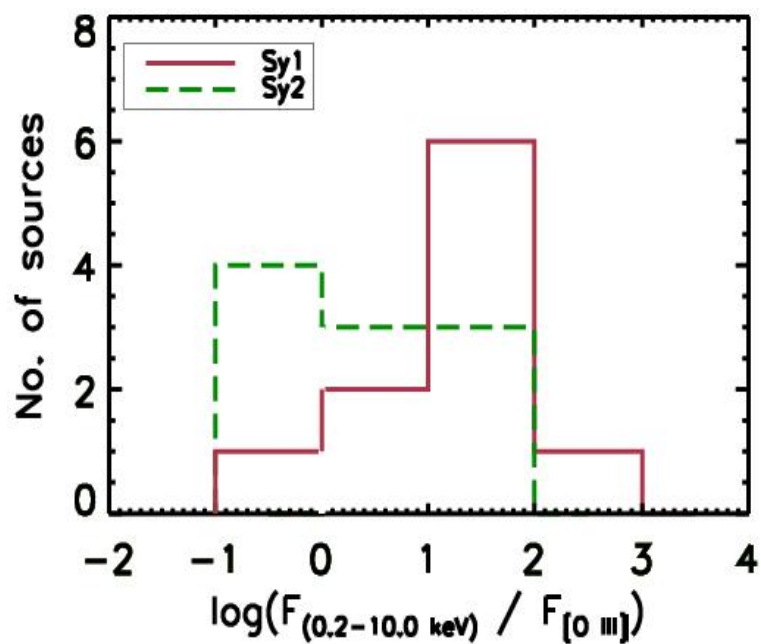
Figure 5.21: Distributions of flux ratios of hard (2.0 - 10.0 keV) X-ray to [OIII] $\lambda 5007$Å line for the two subtypes of our sample Seyfert galaxies.

5.4.5   Correlation between X-ray and radio luminosities

The nuclear X-ray and radio emission are one of the most direct evidence of AGN activity and therefore, are fundamental to study the accretion and outflow processes in AGN. The combination of X-ray and radio emission from AGN can provide useful insights to the relationship between the physical mechanisms of the X-ray and radio emission. The sample which we used to study the X-ray spectral properties of Seyferts, has the advantage of being observed by Very Long Baseline Interferometer (VLBI) and Very Large Array (VLA) at 5.0 GHz and NRAO VLA Sky Survey (NVSS)[1] at 1.4 GHz. The angular resolution of VLBI ($\sim$ milli-arcsec), VLA ($\sim$ arcsec) and NVSS ($\sim$ 43 arcsec) correspond to the parsec-scale, a kiloparsec-scale and tens of kiloparsec-scale size, respectively, for the typical redshifts (z < 0.05) of our sample sources. Thus we have radio flux densities/luminosities of our sample sources at different spatial scales ranging from the nuclear pc-scale to the size of nearly entire host galaxy. The 5 GHz VLBI and VLA radio flux densities of our sample sources are given in Lal, Shastri, and Gabuzda (2004) and 1.4 GHz flux densities are from NVSS. Here we investigate the correlation of the 2.0 - 10.0 keV X-ray luminosity to the pc-scale and kpc-scale radio luminosities for the two Seyfert subtypes of our sample. The X-ray luminosities are derived from *XMM-Newton* spectral analysis (*cf.*, Table 5.5). We plot the 2.0 - 10.0 keV X-ray luminosities ($L_{2.0-10.0 \text{ keV}}$) versus the 5 GHz VLBI and VLA radio luminosities ($L_{5 \text{ GHz}}^{\text{VLBI}}$, $L_{5 \text{ GHz}}^{\text{VLA}}$) and 1.4 GHz NVSS radio luminosities ($L_{1.4 \text{ GHz}}^{\text{NVSS}}$). The plots show that there is a trend of increase in 2.0 - 10.0 keV X-ray luminosity with the increase in radio luminosities at pc-scale (VLBI), kpc-scale (VLA) and tens of kpc-scale (NVSS) (*cf.*, Figure 5.23). We use Spearman rank correlation test to measure the strengths of correlations between the X-ray luminosities ($L_{2.0-10.0 \text{ keV}}$) and radio luminosities ($L_{5 \text{ GHz}}^{\text{VLBI}}$, $L_{5 \text{ GHz}}^{\text{VLA}}$, $L_{1.4 \text{ GHz}}^{\text{NVSS}}$) for the two Seyfert subtypes. Table 5.8 lists the correlation coefficients (ρ), p-values and the linear regression line

---

[1]http://www.cv.nrao.edu/nvss/

equations for the two Seyfert subtypes. MRK 231, a type 1 Seyfert galaxy, has unusually high radio luminosity and is known to show radio variability (Lal 2002). In our correlation plots MRK 231 is lying away from the trend as an outlier and therefore it has not been considered while measuring the strengths of the correlations between the X-ray and radio luminosities. The correlation tests show that for both the Seyfert subtypes the X-ray luminosities ($L_{2.0-10.0 \text{ keV}}$) are significantly correlated with the radio luminosities of different spatial scales. The significant correlation of X-ray luminosity to (tens of) kpc-scale radio luminosity infers that the large kpc-scale radio emission is primarily AGN related. In the correlation plots Seyfert types 2s are shifted downward than type 1s which is expected as type 2s have systematically lower observed 2.0 - 10.0 keV X-ray luminosities than type 1s due to higher absorbing column densities. Seyfert type 1s and type 2s show the similar X-ray - radio luminosity correlation coefficients and the slops of regression lines (*cf.*, Table 5.8) which is consistent with the unification scheme. The lower $L_{2.0-10.0 \text{ keV}}$ - $L_{5 \text{ GHz}}^{\text{VLBI}}$ correlation coefficient and slope for the type 1s than type 2s is due to NGC 2639 that has significantly low observed 2.0 - 10.0 keV X-ray luminosity. The same reason is valid for the high $L_{2.0-10.0 \text{ keV}}$ - $L_{\text{[OIII]}}$ slope for the type 1s than type 2s. NGC 2639, a type 1.9 Seyfert, has high absorption and therefore low observed 2.0 - 10.0 keV X-ray luminosity.

The previous studies on the correlation between X-ray and radio luminosities for radio-quiet and radio-loud AGNs report that the X-ray and the radio emission are correlated down to very low luminosities (Salvato, Greiner, and Kuhlbrodt 2004; Brinkmann *et al.* 2000; Canosa *et al.* 1999). Panessa *et al.* (2007) reported that the X-ray and radio luminosities are significantly correlated in Seyfert galaxies as well as in low luminosity radio galaxies (LLRGs) and both the Seyferts and LLRGs show similar correlation slopes, although shifted by nearly three orders of magnitude. Falcke, Körding, and Markoff (2004) and Merloni, Heinz, and di Matteo (2003) derived a correlation among the X-ray, radio luminosities, and black hole masses, so called 'fundamental plane' of supermassive black hole activity. The

'fundamental plane' has been used to constrain the origin of X-ray and radio emission in low luminosity AGN (LLAGN), however, the different scenarios for the X-ray and radio emission relationship have been proposed. For example, Falcke, Körding, and Markoff (2004) suggested that the radio to X-ray emission in LLAGN is attributed to synchrotron emission from a relativistic jet, analogous to the scenario proposed for X-ray binaries in their low/hard state. In contrast, Merloni, Heinz, and di Matteo (2003) proposed that the X-ray emission possibly originates from a radiatively inefficient accretion flow (Narayan and Yi 1994) and the radio emission is attributed to synchrotron emission from a relativistic or sub-relativistic jet. Our study shows that the nuclear X-ray and radio luminosities are correlated in Seyfert galaxies suggesting that either similar physical mechanisms are responsible for the X-ray and radio emission or a combination of different mechanisms give rise the X-ray - radio correlations. It is believed that in Seyfert galaxies the X-ray emission probably arises from an accretion disk-corona system and the radio emission is attributed to a jet/outflow component. Therefore, a strong correlation between the X-ray and radio emission implies that the accretion disk and outflowing jet are coupled, however, the exact nature of disk - jet coupling is not well understood.

5.4.6 Correlation between X-ray and [OIII] $\lambda5007$Å luminosities

We investigate the correlation between the observed 2.0 - 10.0 keV X-ray luminosity and [OIII] $\lambda5007$Å line luminosity. Our results show that the 2.0 - 10.0 keV X-ray luminosity is correlated with the [OIII] $\lambda5007$Å line luminosity for both the Seyfert subtypes (*cf*., Figure 5.23, Table 5.8). The two Seyfert subtypes show similar $L_{2.0-10 \text{ keV}}$ - $L_{[OIII]}$ correlation coefficients. The physical interpretation for the observed correlation between the $L_{2.0-10 \text{ keV}}$ and $L_{[OIII]}$ can understood as both $L_{2.0-10 \text{ keV}}$ and $L_{[OIII]}$ are supposed to be related to the AGN power. The [OIII]

$\lambda 5007\text{Å}$ line emission arises from the gas located several hundred parsec away from the central engine and is excited by the AGN ionizing continuum. Since the [OIII] emitting material primarily lies outside the obscuring torus, the line emission suffers only moderate amount of dust obscuration (*e.g.*, Dahari and De Robertis (1988); Keel *et al.* (1994)), even in the cases of Compton-thick sources. Thus [OIII] line luminosity is expected to provide an unbiased orientation-independent indicator of the ionizing luminosity of the AGN in both type 1s and type 2s (Nelson and Whittle 1995). As discussed above that the X-ray emission is believed to come from the inner region of accretion disk and likely to represent the AGN power. Therefore, the X-ray luminosity and [OIII] luminosity can be expected to be correlated as both are considered as the proxy of AGN power.
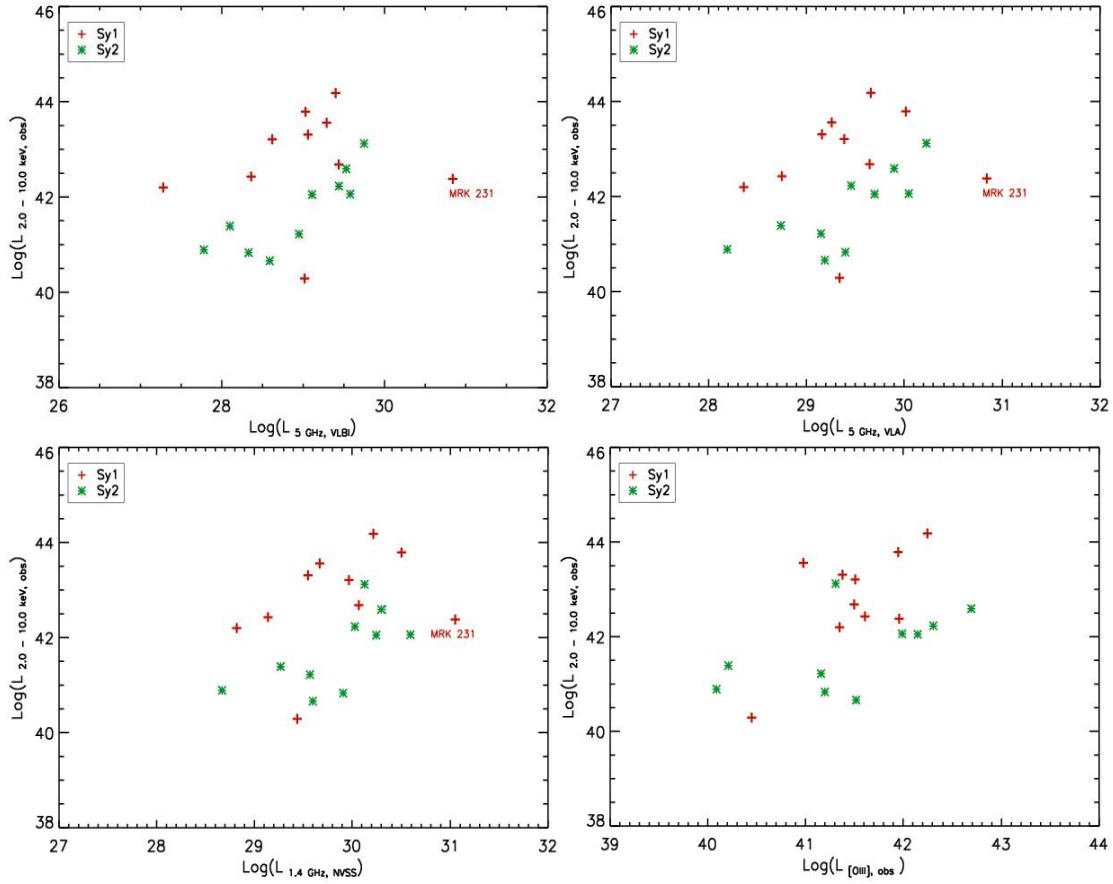
Figure 5.22: The observed 2.0 - 10.0 keV X-ray luminosities versus 5 GHz pc-scale (VLBI) radio luminosities, 5 GHz kpc-scale (VLA) radio luminosities, 1.4 GHz tens of kpc-scale (NVSS) radio luminosities and [OIII] luminosities for the two Seyfert subtypes of our sample.

Table 5.7: 5 GHz VLBI (pc-scale), VLA (kpc-scale) and 1.4 GHz NVSS (tens of kpc-scale) radio and [OIII] line luminosities of our sample sources

Name	$\log L_{5\ \mathrm{GHz}}^{\mathrm{VLBI}}$	$\log L_{5\ \mathrm{GHz}}^{\mathrm{VLA}}$	$\log L_{1.4\ \mathrm{GHz}}^{\mathrm{NVSS}}$	$\log L_{[\mathrm{OIII}]}$
MCG+8-11-11	29.03	30.02	30.50	41.95
MRK 1218	29.44	29.65	30.07	41.50
NGC 2639	29.02	29.34	29.44	40.45
NGC 4151	27.28	28.36	28.82	41.35
MRK 766	28.36	28.75	29.14	41.16
MRK 231	30.84	30.84	31.05	41.96
ARK 564	29.06	29.16	29.55	41.38
NGC 7469	28.62	29.39	29.97	41.51
MRK 926	29.40	29.66	30.22	42.25
MRK 530	29.29	29.26	29.67	40.98
MRK 348	29.75	30.23	30.13	41.31
MRK 1	28.59	29.19	29.60	41.52
NGC 2273	27.78	28.19	28.67	40.09
MRK 78	29.44	29.46	30.03	42.31
NGC 5135	28.33	29.40	29.91	41.20
MRK 477	29.53	29.90	30.30	42.69
NGC 5929	28.10	28.74	29.27	40.21
NGC 7212	29.11	29.70	30.25	42.15
MRK 533	29.58	30.05	30.59	41.99
NGC 7682	28.95	29.15	29.57	41.16

Notes: luminosities are in units of erg s^{-1}. X-ray 2.0 - 10.0 keV luminosities are given in Table 5.5 .

Table 5.8: Results on the correlations of 2.0 - 10.0 keV X-ray luminosity to radio and [OIII] $\lambda5007$Å luminosities

Seyfert sample	Spearman rank correlation test		Linear regression equation
	ρ	p-value	
		$\log L_{2.0-10 \text{ keV}}$ versus $\log L_{5 \text{ GHz}}^{\text{VLBI}}$	
Type 1s	0.58	1.1×10^{-1}	$\log L_{2.0-10 \text{ keV}} = 0.52 \log L_{5 \text{ GHz}}^{\text{VLBI}} + 27.92$
Type 2s	0.82	6.2×10^{-3}	$\log L_{2.0-10 \text{ keV}} = 1.02 \log L_{5 \text{ GHz}}^{\text{VLBI}} + 12.19$
		$\log L_{2.0-10 \text{ keV}}$ versus $\log L_{5 \text{ GHz}}^{\text{VLA}}$	
Type 1s	0.60	9.7×10^{-2}	$\log L_{2.0-10 \text{ keV}} = 0.89 \log L_{5 \text{ GHz}}^{\text{VLA}} + 16.67$
Type 2s	0.75	1.7×10^{-2}	$\log L_{2.0-10 \text{ keV}} = 1.02 \log L_{5 \text{ GHz}}^{\text{VLA}} + 11.83$
		$\log L_{2.0-10 \text{ keV}}$ versus $\log L_{1.4 \text{ GHz}}^{\text{NVSS}}$	
Type 1s	0.78	1.7×10^{-2}	$\log L_{2.0-10 \text{ keV}} = 1.24 \log L_{1.4 \text{ GHz}}^{\text{NVSS}} + 5.87$
Type 2s	0.65	4.6×10^{-2}	$\log L_{2.0-10 \text{ keV}} = 0.96 \log L_{1.4 \text{ GHz}}^{\text{NVSS}} + 13.03$
		$\log L_{2.0-10 \text{ keV}}$ versus $\log L_{[\text{OIII}]\lambda5007\text{Å}}$	
Type 1s	0.55	1.0×10^{-1}	$\log L_{2.0-10 \text{ keV}} = 1.49 \log L_{[\text{OIII}]}$ - 18.93
Type 2s	0.49	1.5×10^{-1}	$\log L_{2.0-10 \text{ keV}} = 0.54 \log L_{[\text{OIII}]} + 19.33$

Notes: The p-value is the probability of rejecting the null hypothesis that the two quantities are correlated.

5.5 X-ray spectral properties of individual sources

In this section I discuss the 0.5 - 10.0 keV X-ray spectral fittings of all our sample sources and compare our best spectral fits with previous X-ray spectral fits given in the literature.

5.5.1 MCG+8-11-11

MCG+8-11-11 has been observed by all the major X-ray satellites, with the exception of *Chandra*. The *ASCA* (Grandi *et al.* 1998) and *BeppoSAX* (Perola *et al.* 2000) data were well fitted by a fairly standard model composed of a power-law, a warm absorber, a Compton reflection component, and an Fe Kα line. Matt *et al.* (2006) fitted the *XMM-Newton* EPIC pn spectrum with a model composed of an absorbed power-law ($\Gamma \simeq 1.805 \pm 0.015$, $N_H \simeq 1.83^{+0.06}_{-0.03} \times 10^{21}$ cm^{-2}), a Compton reflection component (with the inclination angle kept fixed to 30°), a Gaussian Fe Kα line (EW $\sim 75 \pm 15$ eV), warm absorption ($N_{H,warm} \simeq 1.1^{+0.06}_{-0.06} \times 10^{22}$ cm^{-2}) with the temperature of the material fixed at 10^6 K and an absorption edge at 0.74 keV, corresponding to He-like oxygen. We use the same data-set and our best fit spectral parameters are broadly consistent with Matt *et al.* (2006), although we get a good fit without using warm absorption. We also confirm the absence of a soft excess in this source using the *XMM-Newton* EPIC pn data.

5.5.2 MRK 1218

MRK 1218 does not have *Chandra* and *ASCA* observations but has been detected by *RoSAT*. We present the *XMM-Newton* spectrum of MRK 1218 for the first time. We find that an absorbed power-law ($\Gamma \simeq 1.48^{+0.11}_{-0.17}$, $N_H \simeq 1.52^{+0.43}_{-1.3} \times 10^{21}$ cm^{-2}), with warm absorption ($N_{H,warm} \simeq 0.63^{+0.41}_{-0.32} \times 10^{22}$ cm^{-2}) having plasma temperature kept fixed at 3×10^4 K and an Fe Kα line of EW $\simeq 63.9$ eV gives the best fit.

5.5.3   NGC 2639

Terashima *et al.* (2002) fitted the *ASCA* spectrum of NGC 2639 by a partially covered power-law (with $N_{H,1} \sim 0.08$ (≤ 0.32) $\times 10^{22}$ cm^{-2} , $N_{H,2} \sim 32^{+12.5}_{-30} \times 10^{22}$ cm^{-2}, covering fraction $\sim 0.89^{+0.08}_{-0.81}$, $\Gamma \sim 2.8^{+1.0}_{-0.6}$ and $\chi^2/\text{dof} \simeq 45.8/49$). They also attempted a model consisting of an absorbed power-law plus a Raymond-Smith (Raymond & Smith 1977) thermal plasma modified by the Galactic absorption. The best fit parameters reported by Terashima *et al.* (2002) using this model are $N_{H,1} \simeq 0.027 \times 10^{22}$ cm^{-2} (fixed), $kT \simeq 0.80^{+0.27}_{-0.40}$, abundances fixed to 0.5 of solar, $N_{H,2} \leq 0.31 \times 10^{22}$ cm^{-2}, $\Gamma \simeq 1.92^{+0.70}_{-0.37}$ and $\chi^2/\text{dof} \simeq 45.6/49$. The reported equivalent widths of Fe Kα for these two models are $1.49^{+11.11}_{-1.27}$ keV and $3.13^{+2.27}_{-2.00}$ keV, respectively. We present *XMM-Newton* X-ray spectrum of NGC 2639 for the first time and find that the best fit consists of an absorbed power-law ($\Gamma \simeq 2.21^{+1.83}_{-1.02}$, $N_H \simeq 1.62^{+1.76}_{-1.56} \times 10^{21}$ cm^{-2}) plus a soft component modeled with a thermal plasma ('mekal' in XSPEC) of temperature $kT \simeq 0.63^{+0.12}_{-0.09}$. We do not detect Fe K$\alpha$ line in the *XMM-Newton* pn spectrum probably due to lack of sufficient counts above 2.0 keV. Observations with longer exposure time are required to constrain the properties of Fe Kα line.

5.5.4   NGC 4151

NGC 4151 is one of the most extensively studied Seyfert galaxies in nearly all wavelengths. The *ASCA* and *BeppoSAX* X-ray spectra are fitted with a flat absorbed power-law ($\Gamma \simeq 1.65$), a contribution from a cold reflector and a two-component absorber, *i.e.*, an intrinsic neutral component with $N_H \simeq 3.4 \times 10^{22}$ cm^{-2} and a highly ionized absorber with $N_H \simeq 2.4 \times 10^{23}$ cm^{-2} (Schurch and Warwick 2002; Piro *et al.* 2005). Yang, Wilson, and Ferruit (2001) reported the *Chandra* ACIS observation of NGC 4151 with notable extended soft X-ray emission on a scale of several hundred parsecs and a spatially unresolved hard X-ray (≥ 2.0 keV) component. The spectrum of the unresolved nuclear source is described by an

absorbed ($N_H \sim 10^{22}$ cm^{-2}), flat power-law ($\Gamma \simeq 0.3$) plus soft emission fitted with either a power-law ($\Gamma \simeq 2.6$) or a thermal (kT $\simeq 0.6$ keV) component. We fit the *XMM-Newton* pn spectrum with a model consists of an absorbed power-law ($\Gamma \simeq 1.75^{+0.06}_{-0.03}$, $N_H \simeq 1.8 \times 10^{21}$ cm^{-2}), with warm absorption ($N_H \simeq 5.2^{+1.45}_{-1.20} \times 10^{22}$ cm^{-2}), partial covering ($N_H \simeq 9.06^{+1.27}_{-0.98} \times 10^{22}$ cm^{-2}, covering fraction $f \simeq 0.69^{+0.04}_{-0.05}$) and a reflection component and a soft component modeled with an absorbed power-law plus thermal plasma model with a temperature of kT $\simeq 0.13$ keV and emission lines at 0.88 keV and 6.4 keV. The Fe Kα line is fitted with a narrow Gaussian component resulting EW $\simeq 108.4^{+6.5}_{-6.7}$ eV.

5.5.5 MRK 766

RoSAT and *ASCA* observations showed that the X-ray spectrum of MRK 766 can be described by a power-law of index $\sim$ 1.6 - 2.0 (increasing strongly with flux), a reflection component, and a narrow Fe Kα emission line (EW $\sim$ 100 eV) (Leighly *et al.* 1996). Later observations with *BeppoSAX* found a steeper power-law ($\Gamma \simeq 2.2$), and evidence for an absorption edge at 7.4 keV (Matt *et al.* 2000). Using *XMM-Newton* observations Miller *et al.* (2006) reported variations in the flux of Fe Kα line on short (5 - 20 ks) time scales and its strong correlation with the continuum emission. We fit the *XMM-Newton* pn X-ray spectrum of MRK 766 with a less absorbed fairly steep power-law ($\Gamma \simeq 2.17^{+0.10}_{-0.08}$, N_H fixed to Galactic value) with partial covering ($N_H \simeq 6.42^{+0.93}_{-0.56} \times 10^{22}$ cm^{-2}, covering fraction $f \simeq 0.51^{+0.02}_{-0.03}$) and warm absorption ($N_H \simeq 2.1^{+0.28}_{-0.24} \times 10^{21}$ cm^{-2}), a reflection component at the hard end, a soft component fitted with a thermal plasma model of temperature kT $\sim$ 0.2 keV and narrow Gaussian emission lines at 0.48 keV, 6.44 keV and 6.67 keV. The Fe Kα emission may have broad component but we get a better fit with a narrow Gaussian fitted to the emission line with centroid energy at 6.44 keV and a second narrow Gaussian fitted to the emission line at 6.67 keV. The latter line could be Fe Kα from highly ionized (FeXXV) material or a K$_\beta$ line from

neutral material.

5.5.6 MRK 231

X-ray observations by *ROSAT*, *ASCA* (Turner 1999; Maloney and Reynolds 2000) and more recently by *Chandra* (Gallagher *et al.* 2002; Ptak *et al.* 2003) have revealed the presence of extended soft X-ray emission of thermal origin that is likely to be associated with the circumnuclear starburst and a hard and flat ($\Gamma \simeq 0.7$) power-law component as well as an Fe Kα emission line with EW $\sim$ 300 eV. The Fe Kα line was detected by *ASCA* but not by *Chandra*. The *Chandra* observing time ($\sim$ 40 ks) for MRK 231 is much smaller compared to *ASCA* observing time ($\sim$ 111 ks) and this could be the one reason for non-detection of 6.4 keV Fe Kα line, noting the fact that both ASCA and Chandra have similar effective area (sensitivity) at 6.4 keV. Although, line variability cannot be ruled out. From combined *XMM-Newton* and *BeppoSAX* observations of MRK 231, Braito *et al.* (2004) found a highly absorbed ($N_H \sim 2 \times 10^{24}$ cm^{-2}) power-law component. We obtain the best fit with an absorbed power-law ($\Gamma \simeq 1.57^{+0.14}_{-0.30}$, $N_H \simeq 4.6^{+1.4}_{-1.6} \times 10^{21}$ cm^{-2}), a partial covering ($N_H \simeq 8.35^{+4.02}_{-4.64} \times 10^{22}$ cm^{-2}, covering fraction $f \simeq 0.74^{+0.09}_{-0.25}$) and a soft component fitted with two thermal plasma models with temperatures kT $\simeq 0.33$ keV and $\simeq 0.99$ keV and narrow emission lines at $\sim$ 6.28 keV and $\sim$ 6.66 keV. The soft X-ray component may have significant contribution from starburst activity (Braito *et al.* 2004).

5.5.7 ARK 564

Vignali *et al.* (2004) analyzed two sets of *XMM-Newton* observations of ARK 564 taken a year apart (2000 June and 2001 June) and fitted the 0.6 - 10.0 keV continuum by a soft blackbody component (kT $\simeq$ 140 - 150 eV), a steep power-law ($\Gamma \simeq 2.50-2.55$) and an absorption edge at a rest-frame energy of $\sim$ 0.73 keV, corresponding to OVII. No significant spectral changes were observed between the

two observations, although the X-ray flux in the second observation is 40 - 50% lower. We obtain the best fit to the 0.6 - 10.0 keV *XMM-Newton* pn spectrum by a less absorbed steep power-law ($\Gamma \simeq 2.32^{+0.08}_{-0.10}$, N_H fixed to the Galactic value) with partial covering ($N_H \simeq 3.09^{+0.52}_{-0.45} \times 10^{22}$ cm^{-2}, covering fraction $f \simeq 0.61^{+0.26}_{-0.15}$), a soft component fitted with a steep power-law ($\Gamma \simeq 3.42^{+0.13}_{-0.12}$) plus a thermal plasma model with temperature kT $\simeq 0.97$ keV and narrow emission lines at $\sim$ 6.33 keV and $\sim$ 6.71 keV. While fitting we excluded the 0.5 - 0.6 keV part of the spectrum since these data are of poor quality and make it difficult to obtain even a reasonably good fit.

5.5.8 NGC 7469

Blustin *et al.* (2003) fitted the 0.2 - 10.0 keV *XMM-Newton* EPIC pn spectrum of NGC 7469 with a combination of a Galactic absorbed power-law ($\Gamma \simeq 1.75$), two blackbody models and a narrow Fe Kα emission line. They noted significant residuals at low energies for which they suggested an instrumental origin. We fitted the 0.5 - 10.0 *XMM-Newton* pn spectrum of NGC 7469 with an absorbed power-law ($\Gamma \simeq 2.04^{+0.02}_{-0.02}$, N_H fixed to Galactic value), a partial covering ($N_H \simeq 35.55^{+9.93}_{-6.77} \times 10^{22}$ cm^{-2}, covering fraction $f \simeq 0.28^{+0.03}_{-0.03}$), a soft component fitted with a thermal plasma model of temperature kT $\simeq 0.18$ keV and a narrow Gaussian fitted to the Fe Kα line. Using *ASCA* observations, Reynolds (1997) had reported both the narrow and broad components to Fe Kα line, which was supported by De Rosa, Fabian, and Piro (2002) using *BeppoSAX* data, while Nandra *et al.* (1997) suggested that the line was relativistically broadened. However, we fit the Fe Kα line with a narrow Gaussian component and do not require a broad component for a good fit which is consistent with Blustin *et al.* (2003).

5.5.9 MRK 926

Bianchi *et al.* (2004) fitted the combined 2.5 - 220 keV *XMM-Newton* and *BeppoSAX* spectrum of MRK 926 with a baseline model consisting of a power-law ($\Gamma \simeq 1.72^{+0.08}_{-0.06}$) with intrinsic absorption in addition to the Galactic value, a reflection component ($R \simeq 0.41^{+0.30}_{-0.27}$ from an isotropically illuminated cold slab with the inclination angle fixed to 30°; model 'pexrav') and a Gaussian to reproduce the Fe Kα line (EW $\simeq 45^{+85}_{-24}$ eV). They also reported an upper limit to the Fe K$_\beta$ line flux of the order of the Kα line flux, and suggested the possibility of significant contribution from an FeXXVI line. Weaver, Gelbord, and Yaqoob (2001) reported strong line variability, both in centroid and in flux, between three *ASCA* observations. We fit the 0.5 - 10.0 keV *XMM-Newton* spectrum of MRK 926 with an absorbed partially covered power-law ($\Gamma \simeq 1.98^{+0.03}_{-0.02}$, N_H fixed to the Galactic value, $N_{H,\ part} \simeq 4.35^{+2.86}_{-1.99} \times 10^{22}$ cm^{-2}, covering fraction $f \simeq 0.15^{+0.06}_{-0.06}$), a reflection component and a narrow Gaussian to fit the Fe Kα line. Notably we do not see any soft excess in this Seyfert galaxy.

5.5.10 MRK 530

MRK 530 has not been observed by either *Chandra* or *ASCA*. We present *XMM-Newton* pn spectrum of MRK 530 for the first time. We fit the 0.5 - 10.0 keV spectrum by an absorbed partially covered power-law ($\Gamma \simeq 2.28^{+0.03}_{-0.01}$, N_H fixed to Galactic value, $N_{H,\ part} \simeq 14.81^{+5.62}_{-4.18} \times 10^{22}$ cm^{-2}, covering fraction $f \simeq 0.27^{+0.27}_{-0.27}$), a soft component modeled with thermal plasma at a temperature kT $\simeq 0.20$ keV and a narrow Gaussian fitted to the Fe Kα line.

5.5.11 MRK 348

Awaki *et al.* (2006) fitted the *XMM-Newton* pn 0.2 - 10.0 keV spectrum of MRK 348 with an absorbed power-law ($\Gamma \simeq 1.61 \pm 0.02$, $N_H \simeq 13.5 \pm 0.02 \times 10^{22}$ cm^{-2}) plus a soft component fitted with a thermal plasma (kT $\simeq 0.56^{+0.01}_{-0.02}$ keV; 'mekal' model)

and an Fe Kα line (EW $\sim$ 46.4$\pm$20 eV) and obtain χ^2/dof $\sim$ 1.46. They fixed the metal abundance of the thermal plasma to 0.1 times the solar abundance, the characteristic value of a normal galaxy (Terashima *et al.* 2002). We use the same *XMM-Newton* data and find the best fit to the 0.5 - 10.0 keV spectrum using an absorbed power-law ($\Gamma \simeq 1.70^{+0.07}_{-0.06}$, $N_H \simeq 6.86^{+0.84}_{-1.01} \times 10^{22}$ cm^{-2}) with partial covering ($N_{H,\ part} \simeq 10.47^{+0.68}_{-1.00} \times 10^{22}$ cm^{-2}, covering fraction $f \simeq 0.84^{+0.06}_{-0.06}$) plus a soft component fitted with a power-law ($\Gamma \simeq 2.75^{+0.17}_{-0.16}$) and a narrow Gaussian fitted to Fe Kα line (EW $\sim$ 34.2$^{+10.8}_{-10.4}$) and obtained χ^2/dof $\sim$ 1.05.

5.5.12   MRK 1

Guainazzi, Matt, and Perola (2005) fitted the 0.5 - 10.0 keV *XMM-Newton* pn spectrum of MRK 1 with a highly absorbed power-law ($N_H \geq 110 \times 10^{22}$ cm^{-2}, $\Gamma \simeq 2.41^{+0.13}_{-0.11}$) and a scattered component with partial covering factor fixed to 1 and obtained χ^2/dof $\sim$ 36/32. They reported several emission lines including iron K shell lines in 0.5 - 2.0 keV band but no thermal component. In order to constrain the Fe Kα line they performed both global and local fits with centroid energy fixed at 6.4 keV, and found upper limits to the equivalent width of $\sim$ 800 eV and $\sim$ 2.0 keV respectively. Due to the relatively low counts in the data, we use C-statistics to fit the spectrum and find that the best fit consists of a hard component (2.0 - 10.0 keV) completely dominated by reflection ($\Gamma \simeq 2.0$), a soft component fitted with a power-law ($\Gamma \simeq 2.55^{+0.30}_{-0.29}$) plus a thermal plasma model ($kT \simeq 0.82^{+0.08}_{-0.09}$ keV) and a Gaussian fitted to the Fe Kα line (EW $\sim$ 1.25$^{+1.29}_{-0.86}$ keV). The reflection dominated spectrum, high EW of the Fe line and the low ratio of hard X-ray to [OIII] flux suggest that MRK 1 is likely to be a Compton-thick source. Large residuals seen below 2.0 keV in MRK 1 may be due the presence emission lines such as Ne IX, Ne X, Mg XI, S XIV, and Fe L lines (Guainazzi, Matt, and Perola 2005), which we have not accounted for in our spectral fitting, since we are primarily interested in modeling the broad band continuum and Fe

Kα line.

5.5.13   NGC 2273

Guainazzi *et al.* (2005) attempted to fit the *XMM-Newton* spectrum of NGC 2273 with a family of models in which hard X-ray component is accounted by an absorbed power-law but yield an unacceptable flat intrinsic spectral index ($\Gamma \simeq$ -0.2 - -0.5) and also a large EW ($\simeq$ 2.0 - 3.6 keV) of the Fe Kα line with respect to the measured column density ($N_H \simeq$ 1.4 - 12.0 $\times$ 10^{22} cm^{-2}), and suggested that the spectrum is dominated by Compton reflection. In the best fit reported by Guainazzi *et al.* (2005), the soft X-ray spectrum is accounted by thermal emission model with temperature kT $\simeq$ 0.8$\pm$0.2 keV, hard X-ray fitted by reflection model ($\Gamma_{hard} \simeq$ 1.5$\pm$0.4, $N_H \geq$ 18.0 $\times$ 10^{23} cm^{-2}), and an Fe Kα line with EW $\simeq$ 2.2$^{+0.4}_{-0.3}$ keV. We find the best fit in which hard component is completely accounted by reflection component ($\Gamma \simeq$ 0.67$^{+0.37}_{-0.92}$, 'pexrav' model), soft component is fitted with a power-law ($\Gamma \simeq$ 2.79$^{+1.87}_{-0.82}$) and a Gaussian line fitted to Fe Kα (EW $\sim$ 2.18$^{+0.45}_{-0.44}$ keV). Compton-thick nature of this source is evident from the reflection dominated spectrum, high EW of Fe Kα line and low flux ratio of hard X-ray to [O III].

5.5.14   MRK 78

MRK 78 has not been observed either by *Chandra* or *ASCA*. Levenson, Weaver, and Heckman (2001) fitted its *RoSAT* PSPC soft X-ray spectrum with a thermal plasma (kT $\simeq$ 0.76 keV) model absorbed by the Galactic column density and reported extended soft X-ray emission indicative of a circumnuclear starburst. We present the *XMM-Newton* spectrum of MRK 78 for the first time. Our best fit has the hard component completely accounted by a reflection component ($\Gamma \simeq$ 1.01$^{+0.44}_{-0.54}$, 'pexrav' model), the soft component fitted with a very steep power-law ($\Gamma \simeq$ 7.05$^{+1.89}_{-1.84}$), and a Gaussian fitted to Fe Kα (EW $\sim$ 0.67 keV). All the spectral components are absorbed by an equivalent hydrogen column density of

$N_H \simeq 6.54^{+3.0}_{-2.5} \times 10^{21}$ cm^{-2}. The predominance of the reflection component, high EW of the Fe Kα line and the ratio of hard X-ray flux to [OIII] line flux ratio suggest that obscuration is nearly Compton-thick.

5.5.15 NGC 5135

NGC 5135 has not been observed by *XMM-Newton* and for our study we used the *Suzaku* X-ray spectral properties. The detailed discussion on *Suzaku* X-ray spectral properties of NGC 5135 and the comparison with its *Chandra, ASCA* spectral properties is presented in next chapter (see chapter 6).

5.5.16 MRK 477

MRK 477 has not been observed by *XMM-Newton* or *Chandra* and we therefore use the *ASCA* spectral properties given in Levenson, Weaver, and Heckman (2001) for our study. The best fit reported by Levenson, Weaver, and Heckman (2001) consists of an absorbed power-law ($N_H \simeq 2.4^{+1.7}_{-1.2} \times 10^{23}$ cm^{-2}, $\Gamma \simeq 1.9$ fixed) and an unresolved Fe Kα emission line of EW $\sim 560^{+560}_{-500}$ eV. The addition of a thermal component kT ~ 0.9 keV to this model renders the reasonable spectral parameter values but did not statistically improve the fit. Heckman *et al.* (1997) pointed out that MRK 477 has a powerful circumnuclear starburst with the bolometric luminosity of $\sim 3 \times 10^{10}$ - 10^{11} L$_\odot$. This luminosity is comparable to the AGN activity. However, Levenson, Weaver, and Heckman (2001) concluded that the soft X-ray spectrum is dominated by the AGN.

5.5.17 NGC 5929

NGC 5929 has not been observed by *XMM-Newton* or *Chandra* and therefore we use the *ASCA* spectral properties of NGC 5929 for our study. Cardamone, Moran, and Kay (2007) modeled the 0.5 - 8.0 keV *ASCA* spectrum as a sum of three components: a weakly absorbed ($N_{H, 1} \simeq 5.16 \times 10^{21}$ cm^{-2}) power-law with

photon index $\Gamma \simeq 1.7$, a heavily absorbed power-law ($N_{H, 2} \simeq 2.77 \times 10^{23}$ cm^{-2}) with the same photon index and a Gaussian Fe Kα line of EW of ~ 0.35 keV centered at ~ 6.19 keV.

5.5.18 NGC 7212

Guainazzi, Matt, and Perola (2005) fitted the 0.5 - 10.0 keV *XMM-Newton* spectrum with a heavily absorbed power-law ($N_H \geq 160 \times 10^{22}$ cm^{-2}, $\Gamma \simeq 1.5^{+0.3}_{-0.6}$) plus two thermal plasma components with kT $\simeq 0.16$ and $\simeq 0.72$ keV and an Fe Kα line and obtain χ^2/dof $\sim 97.0/65$. The Fe Kα line was fitted globally as well as locally giving EWs $\sim 900^{+200}_{-300}$ eV and $\sim 1100\pm200$ eV, respectively. We fitted the 0.5 - 10.0 keV *XMM-Newton* spectrum with the hard component completely accounted by reflection ($\Gamma \simeq 0.99^{+0.54}_{-0.37}$), the soft component fitted with a power-law ($\Gamma \simeq 2.32^{+0.23}_{-0.20}$), a narrow Gaussian fitted to the emission line feature at ~ 0.9 keV and another Gaussian fitted to the Fe Kα emission line at 6.4 keV with EW $\sim 0.71^{+0.25}_{-0.13}$ keV.

5.5.19 MRK 533

MRK 533 has not been observed by *Chandra* or *ASCA*. Levenson, Weaver, and Heckman (2001) fitted its *ROSAT* PSPC soft X-ray spectrum with a power-law ($\Gamma \simeq 2.0^{+0.7}_{-1.3}$). We present the *XMM-Newton* pn spectrum of MRK 533 for the first time. We fitted the 0.5 - 10.0 keV spectrum by a model in which the soft component is fitted with a power-law ($\Gamma \simeq 3.75^{+1.45}_{-0.61}$) and thermal plasma emission with the temperature kT $\simeq 0.76^{+0.13}_{-0.10}$, the hard component completely accounted by reflection ($\Gamma \simeq 2.12^{+0.49}_{-0.51}$, 'pexrav' model) and narrow Gaussian fitted to the Fe Kα line at 6.4 keV and to the Fe K$_\beta$ line at 7.04 keV with EWs $\sim 0.56^{+0.24}_{-0.29}$ keV and $\sim 0.67^{+0.39}_{-0.33}$ keV, respectively. Our X-ray spectral properties suggest Compton-thick obscuration in MRK 533.

5.5.20 NGC 7682

We present the *XMM-Newton* spectrum of NGC 7682 for the first time and find that the best fit consists of a soft component fitted with a steep power-law ($\Gamma \simeq 5.36^{+2.78}_{-2.38}$) and a hard component completely accounted by reflection ($\Gamma \simeq 1.77^{+0.58}_{-0.61}$, 'pexrav' model) and narrow Gaussian profiles fitted to Fe Kα line at 6.4 keV and Fe K$_\beta$ line at 7.11 keV with EWs $\sim 0.48^{+0.31}_{-0.31}$ keV and $\sim 0.46^{+0.46}_{-0.40}$ keV, respectively. All the spectral components are absorbed by an equivalent hydrogen column density $N_H \simeq 3.48^{+5.78}_{-2.51} \times 10^{21}$ cm^{-2}. Our *XMM-Newton* X-ray spectral properties suggest Compton-thick obscuration in NGC 7682.

5.6   Conclusions

I investigated the 0.5 - 10.0 keV X-ray spectral properties of a sample of 20 Seyfert galaxies and summarize the conclusions as below.

– X-ray spectra of our sample Seyfert galaxies are, in general, best fitted with a model consists of: a power-law with a photoelectric cutoff due to the cold absorption from the Galactic column density and neutral gas at the redshift of the AGN; a narrow Gaussian line fitted to the Fe Kα fluorescent emission line at 6.4 keV; often seen soft excess component characterized by either a steep power-law and/or a thermal plasma model with temperature kT $\sim$ 0.1 - 1.0 keV.

– In several of the heavily obscured type 2 sources, X-ray spectra are completely dominated by reflection component and the hard part of spectra can be characterized with the reflection model 'pexrav' and a prominent Fe Kα line.

– The Seyfert type 1s have systematically higher soft X-ray luminosities than that of type 2s, as would be expected if unification holds. The distributions of the hard (2.0 - 10.0 keV) X-ray luminosities of the two subtypes differ much less significantly, consistent with the prediction of unification, as optical thickness of obscuring material decreases with the increase in X-ray photon energy.

– The X-ray absorbing column density for Seyfert type 1s in our sample ranges from $\sim 10^{20}$ H atoms cm^{-2} (Galactic value) to $\sim 10^{22}$ H atoms cm^{-2} with the median value $\sim 10^{21}$ H atoms cm^{-2}, while for type 2s it ranges from $\sim 10^{22}$ H atoms cm^{-2} to the Compton-thick limiting value $\geq 10^{24}$ H atoms cm^{-2} with the median value $\geq 10^{24}$ H atoms cm^{-2}. The distribution of X-ray absorbing column densities (N_H) for Seyfert galaxies of our sample is broadly consistent with previous studies (*e.g.*, Cappi *et al.* (2006); Akylas and Georgantopoulos (2009)).

– The Fe Kα fluorescent emission line has been detected in all (except one) of our sample sources suggesting the ubiquitous presence of the Fe Kα line in the X-ray spectra of Seyfert galaxies. The centroid energy $\sim$ 6.4 keV of the line is consistent with the emission from neutral or mildly ionized iron. The equivalent width of Fe Kα line in type 2s ranges from $\sim$ 350 eV to 2.2 keV and is systematically higher than that of type 1s ($\sim$ 20 - 200 eV).

– The statistical comparison of X-ray spectral properties, *i.e.*, X-ray absorbing column densities, the hard X-ray spectral shape (absorbed power-law versus reflection dominated), EWs of Fe Kα line, the flux ratios of hard X-ray to [OIII] λ5007 Å, and luminosity distributions in soft and hard X-ray bands of the two subtypes of Seyfert galaxies are consistent with the orientation and obscuration based Seyfert unification scheme.

– The 2.0 - 10.0 keV X-ray luminosity ($L_{2.0-10\ keV}$) is found to be correlated with the 5 GHz pc-scale (VLBI), kpc-scale (VLA) and tens of kpc-scale (NVSS) radio luminosities in Seyfert galaxies. The $L_{2.0-10\ keV}$ is also significantly correlated with $L_{[OIII]}$. The strengths of correlations and slops of regression lines for the two Seyfert subtypes are similar which is consistent with the unification scheme.

– We also note a high fraction ($\sim$ 70%) of heavily absorbed likely to be Compton-thick sources among the type 2 Seyfert population. This high fraction is in agreement with the previous study reported by Risaliti, Maiolino, and Salvati (1999) based on a [OIII] λ5007Å luminosity selected sample of Seyfert 2s and implies that a rigorously selected unbiased sample is essential to estimate the accurate relative fraction of the heavily absorbed, *i.e.*, Compton-thick AGNs. Also, the heavily obscured AGNs may in part responsible to account for the missing sources contributing to the Cosmic X-ray background (Worsley *et al.* 2005; Gilli, Comastri, and Hasinger 2007).

Chapter 6

A case study of Compton-thick Seyfert galaxy NGC 5135: *Suzaku* broad-band X-ray spectral analysis

6.1   Introduction: Compton-thick obscuration in Seyfert galaxies

When the obscuring torus intercepts the observer's line-of-sight (*i.e.*, in type 2 AGN), absorbing column density for the X-ray photons originating from AGN increases substantially. If absorbing column density is larger than $N_H \simeq \sigma^{-1} \simeq 1.5 \times 10^{24}$ cm^{-2}, the obscuring torus becomes Compton-thick for the X-ray photons below 10 keV, since the cross-sections for Compton scattering and photoelectric absorption are approximately same at energies of the order of 10 keV.

Due to high absorbing column density, sometimes it becomes difficult to identify Compton-thick AGNs directly, using X-ray observations which are sensitive only to energy $\leq$ 10 keV and there is a possibility that an intrinsically X-ray bright but heavily obscured (*i.e.*, Compton-thick) AGN can erroneously be classified as X-ray weak and unabsorbed/less-absorbed AGN. Moreover, the presence of Compton-

thick obscuration around AGN can be inferred through indirect arguments, such as high equivalent width (EW) of Fe Kα emission line and the characteristic reflection dominated 2.0 - 10.0 keV X-ray spectrum (Comastri 2004). The high absorbing column density suppresses the X-ray continuum that in turn, increases the EW of the Fe Kα line. The increase in the EW of Fe Kα line may also arise due to the increase in the line width itself. However, both Seyfert type 1s and type 2s commonly show narrow Fe Kα line that is believed to originate in distant matter, especially the putative obscuring torus (Bianchi *et al.* 2009; Shu, Yaqoob, and Wang 2010). Although, contributions from the inner region (*e.g.*, BLR or the outer part of the accretion disk) could not be ruled out as the Fe Kα velocity widths in some of the sources were found consistent with those of the optical broad emission lines (Yaqoob *et al.* 2001; Bianchi *et al.* 2003). Moreover, the viable explanation for the large EW ($\sim$ 1 keV or higher) of the narrow Fe Kα line, is the attenuation of the underlying continuum due to extreme X-ray obscuration (*i.e.*, Compton-thick) along the line-of-sight (Levenson *et al.* 2006; LaMassa *et al.* 2009).

If the absorbing column density is of the order of 10^{25} H atoms cm^{-2} (*i.e.*, mildly Compton-thick), the nuclear X-ray radiation is visible above 10 keV, while, for even higher column densities (*i.e.*, heavily Compton-thick), the entire high energy spectrum is down-scattered by Compton recoil and hence depressed over the entire X-ray energy range. In Compton-thick AGNs, observed X-ray emission is strongly reprocessed by the material around AGN and therefore Compton-thick sources are suitable candidates to study the reprocessed emission which carries imprints of obscuring material around AGN. It is important to study Compton-thick AGNs as these are predicted to constitute more than half of the total population of Seyfert type 2s (Risaliti, Maiolino, and Salvati 1999) and are important contributors to cosmic X-ray background (Comastri 2004).

The study of *XMM-Newton* X-ray spectral properties of the Seyfert galaxies of our sample reveals that a large fraction of Seyfert type 2s are Compton-thick (see, chapter 5). However, X-ray observations from *Chandra*, *XMM-Newton* etc., which

were sensitive up to 10 keV or so, Compton-thick AGNs have been identified using only diagnostic properties such as high EW ($\geq$ 1.0 keV) of Fe Kα line (Bassani *et al.* 1999), low flux ratio of hard X-ray (2.0 - 10.0 keV) to [OIII] λ5007Å (Maiolino *et al.* 1998) and there are no measurements of the true value of absorbing column density. In this chapter I present a case study of Suzaku broad-band X-ray spectral properties of NGC 5135, which is one of the Compton-thick sources in our sample and has no previous X-ray spectral study above 10 keV.

6.2   NGC 5135: a Compton-thick Seyfert galaxy

NGC 5135 is a relatively nearby (redshift z $\simeq$ 0.014) galaxy and optically classified as a Seyfert type 2 on the basis of emission line ratios (Phillips, Charles, and Baldwin 1983). UV studies have shown that NGC 5135 also contains a powerful compact nuclear starburst (González Delgado *et al.* 1998). *ASCA* and *Chandra* X-ray observations have shown that X-ray spectrum of NGC 5135 is dominated by reprocessed continuum and high EW ($\sim$ 2.4 keV) Fe Kα emission line, inferring Compton-thick obscuration (Turner *et al.* 1997; Levenson *et al.* 2004). Notably, there is no *XMM-Newton* observation of NGC 5135.

In order to unveil the detailed nature of hidden AGN and its X-ray spectrum, one requires broad-band X-ray spectrum covering energy band well above 10 keV. *BeppoSAX* has detected hard X-ray above 10 keV from several Compton-thick Seyfert 2s, *e.g.*, NGC 1068 (Matt *et al.* 1997), NGC 4945 (Guainazzi *et al.* 2000), Mrk 3 (Cappi *et al.* 1999), Circinus galaxy (Matt *et al.* 1999), NGC 3393 and NGC 4939 (Maiolino *et al.* 1998). Further observations from *INTEGRAL*, *Swift*/BAT, and *Suzaku*, have increased the number of Compton-thick sources detected in hard X-ray (Della Ceca *et al.* (2008), and references therein). However, the number of Compton-thick sources whose broad-band spectra were analyzed in detail is still limited, *e.g.*, NGC 1068 (Matt *et al.* 1997), Circinus galaxy (Matt *et al.* 1999; Yang *et al.* 2009), Mrk 3 (Cappi *et al.* 1999; Awaki *et al.* 2008), NGC 4945 (Guainazzi

et al. 2000; Itoh *et al.* 2008), NGC 2273 (Awaki *et al.* 2009).

ASCA, *Chandra* and *XMM-Newton* detections are sensitive up to 10 keV and *BeppoSAX* lacked complete spectral coverage at energies $\leq$ 10 keV and thus earlier observations turn out to be insufficient for studying Compton-thick AGNs and therefore, detailed nature of Compton-thick AGNs remained poorly understood. *Suzaku* (XIS combined with HXD) observations offer broad-band (sub keV to few hundred keV) X-ray spectra adequately suited to study heavily obscured Compton-thick sources. I present broad-band X-ray spectral study of heavily obscured Compton-thick Seyfert galaxy NGC 5135 using *Suzaku* observations.

6.3 *Suzaku* observations and data reductions

NGC 5135 was observed by *Suzaku* on 2007 July 03 (observation ID 702005010) with exposure time of $\sim$ 52.5 ks. We use *Suzaku* XIS and HXD data to study the broad-band X-ray spectrum. *Suzaku* carries four X-ray telescopes (XRTs: Serlemitsos *et al.* (2007)) with X-ray CCD cameras (XIS) at their focal-planes. The XISs are sensitive to 0.2 - 12.0 keV energy band with $18'' \times 18''$ field of view. Among the four XISs, three (XIS 0, 2, and 3) are front-illuminated (FI) and one (XIS 1) is back-illuminated (BI) (Koyama *et al.* 2007). XIS 2 has malfunctioned on 2006 November and therefore there are no observations with XIS 2. *Suzaku* also has a non-imaging hard X-ray detector (HXD) (Takahashi *et al.* 2007). The HXD has two types of detectors, the PIN and the GSO, which are sensitive in 10 - 600 keV energy band. The detailed description on *Suzaku* instruments is given in Chapter 3.

6.3.1 XIS data reductions

The reduction and calibration were done following the standard procedure illustrated in the *Suzaku* reduction guide[1], and using the most recent calibration files. For the low-energy instruments (XISs) the source spectrum was extracted from a circular region with radius of 2.9 arcmin, centered on the source. The background was obtained from a source free region in the same field of view. Calibration files were produced using the FTOOLS 6.6 package[2]. The spectra and calibrations from the two front-illuminated CCDs (XIS0 and XIS3) were merged. The details of *Suzaku* data reduction procedure have been presented in Chapter 3.

6.3.2 HXD data reductions

For the HXD-PIN data, we used the rev2 data, which include all the 4 cluster units, and the best available background (Fukazawa *et al.* 2009), which accounts for the instrumental background (NXB, Takahashi *et al.* (2007); Kokubun *et al.* (2007)) and is affected by systematic uncertainties of about 1.3% (at 1 σ). We then simulated a spectrum for the cosmic X-ray background counts (Boldt 1987; Gruber *et al.* 1999) and added it to the instrumental one, as suggested by the *Suzaku*-HXD reduction guide[3]. Section 7.5.4 of the *Suzaku*-HXD reduction guide suggests the use of CXB spectrum based on Boldt (1987) and indeed, this is commonly used in the current literature (*e.g.*, Braito *et al.* (2009)). Using this background, NGC 5135 is detected in the 15 - 70 keV band at $\sim 7\%$ above the background with a net count rate of $(2.7\pm0.2)\times10^{-2}$ (a total of ~ 1400 source counts), corresponding to a signal-to-noise ratio (S/N) ~ 9.2. In the spectral analysis, we used a cross-calibration constant of 1.16 between the HXD and XIS spectra, as suggested by the *Suzaku*-HXD calibration team[4].

---

[1]http://heasarc.gsfc.nasa.gov/docs/suzaku/analysis/abc/
[2]http://heasarc.gsfc.nasa.gov/docs/software/ftools/ftools_menu.html
[3]http://heasarc.gsfc.nasa.gov/docs/suzaku/analysis/abc/node10.html
[4]http://www.astro.isas.jaxa.jp/suzaku/doc/suzakumemo/ suzakumemo-2008-06.pdf

6.4   *Suzaku* X-ray spectral fit of NGC 5135

Previous observations (*e.g.*, *ASCA*, *Chandra*) of NGC 5135 were sensitive up to 10 keV and owing to heavy obscuration, hard X-ray spectral component remained poorly constrained (*e.g.*, Turner *et al.* (1997); Levenson *et al.* (2004)). We aim to obtain a physically motivated spectral fit of the *Suzaku* broad-band (0.5 - 50 keV) X-ray spectrum of NGC 5135 and improved constraints on the spectral components, particularly on the reflection component. *Suzaku* HXD clearly detects hard X-ray up to $\sim$ 50 keV from AGN in NGC 5135. We combine XIS (0.5 - 10.0 keV) and HXD observations to fit the observed broad-band spectrum and find that 0.5 - 50 keV spectrum can be modeled by: a soft component best fitted with two thermal plasma models ('mekal' in XSPEC) of temperatures kT $\sim$ 0.5 keV and $\sim$ 0.9 keV plus a power-law ($\Gamma \sim 2.7$) and a hard component best fitted with highly absorbed power-law ($N_H \simeq 2.77^{+1.84}_{-1.07} \times 10^{24}$ cm^{-2}, $\Gamma \simeq 1.7$) and a reflection component ('pexrav' in XSPEC) plus an Fe Kα emission line fitted with a Gaussian. All X-ray spectral components were absorbed atleast by the Galactic column density and hard component power-law is further accompanied by photoelectric absorption with N_H as a free parameter. The photoelectric absorption component parametrizes effective absorbing column density in terms of the equivalent hydrogen column density (N_H), assuming the cross sections and abundances given by Morrison and McCammon (1983). We caution that this absorption model does not include the effects of Thompson scattering and therefore can underestimate the absorbing column density in the regime of $N_H \sim 10^{24}$ cm^{-2}. While fitting we fix the photon index of reflection component equal to the photon index of absorbed power-law. The best fit parameters are described in Table 6.1 and fitted spectrum with residuals and their unfolded models are shown in Figures 6.1 to 6.4. The mentioned errors are of 90% confidence level for a given parameter.

The soft component below 2.0 keV is mainly fitted by two thermal plasma models ('mekal' in XSPEC) with sub keV temperatures. The 'mekal' model repre-

sents an emission spectrum from hot diffuse gas based on the model calculations of Mewe, Gronenschild, and van den Oord (1985) with Fe L calculations by Liedahl, Osterheld, and Goldstein (1995). The 'mekal' model also includes line emissions from several elements (*e.g.*, C, N, O, Mg, Si etc.) and uses abundances given by Anders and Grevesse (1989). The hard X-ray spectral component above 10 keV is accounted by a heavily absorbed power-law and a reflection component. The reflection component is represented by 'pexrav' model, which is exponentially cut off power law spectrum reflected from neutral material with the output spectrum as a sum of the cut-off power law and the reflection component. While using 'pexrav' model we fix 'rel$_{\mathrm{refl}}$ = -1', and therefore considering only reflection component. The cosine of inclination and the iron abundances in 'pexrav' were fixed to default values, *i.e.*, 0.45 and solar abundances, respectively.

Using *Chandra* observations Levenson *et al.* (2004) reported that the soft X-ray emission has significant contribution from circumnuclear starburst than AGN, which results a more complicated soft X-ray spectrum. Therefore, we also fit 2.0 - 50.0 keV spectrum excluding the 0.5 - 2.0 keV soft X-ray part to confirm the consistency of hard X-ray spectral parameters. The exclusion of soft part below 2.0 keV gives slightly better fit with reduced χ^2 value ~ 1.2 than ~ 1.7, although hard X-ray spectral parameters remain nearly similar (*cf.*, Table 6.1). Figure 6.3 shows 2.0 - 50.0 keV spectral fit in which continuum below 10.0 keV is primarily accounted by a power-law ($\Gamma \sim 2.7$) and continuum above 10.0 keV is characterized by a heavily absorbed power-law and a reflection component. Using broad-band X-ray spectral fitting we could accurately estimate the absorbing column density in NGC 5135 for the first time. The estimated value of equivalent hydrogen column density (*i.e.*, $N_{\mathrm{H}} \simeq 2.95^{+2.34}_{-1.32} \times 10^{24}$ cm^{-2}) confirms that the circumnuclear absorbing material around AGN in NGC 5135 is moderately Compton-thick.
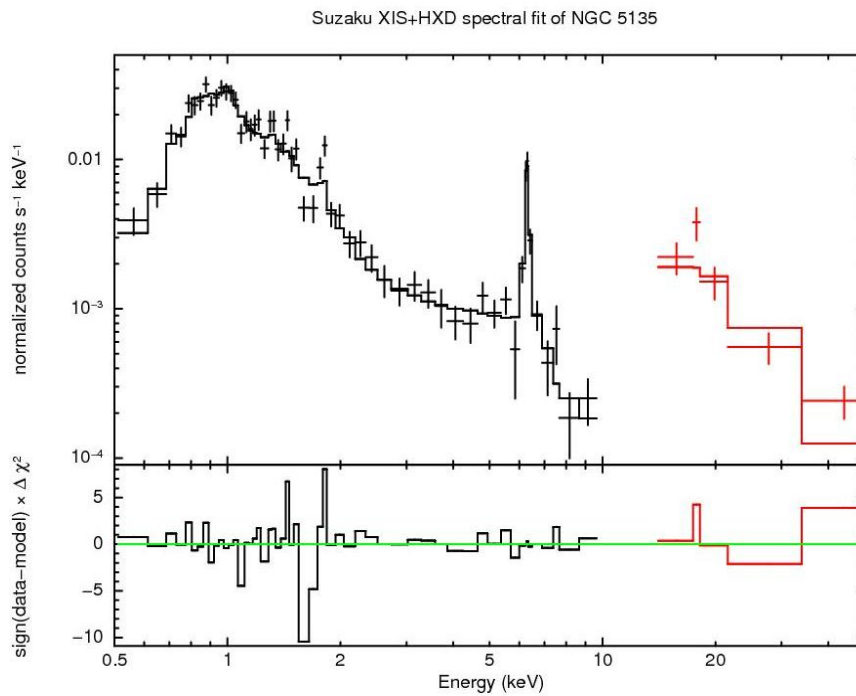
Figure 6.1: *Suzaku* 0.5 - 50 keV X-ray spectral fit of NGC 5135. The top panel shows the cumulative fit (solid curve) against the spectral data points (shown by '+') and the bottom panel shows the residuals. *Suzaku* XIS and HXD-PIN data points are shown in black and red, respectively.
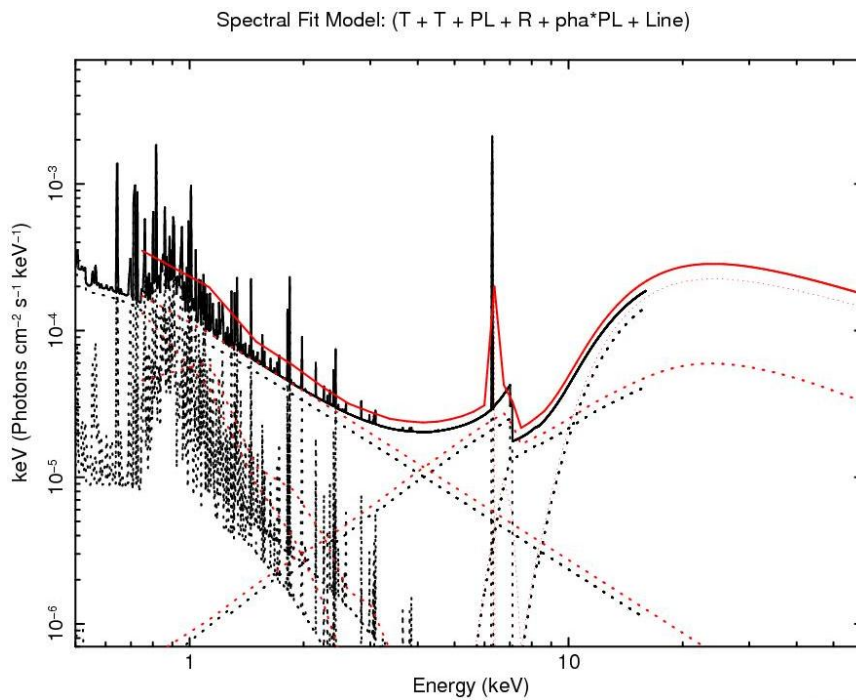
Figure 6.2: Unfolded model for the *Suzaku* 0.5 - 50 keV spectral fit. The cumulative model consists of: two thermal plasma models and a power-law fitting the soft X-ray part, an absorbed power-law plus reflection component accounting for the hard X-ray continuum and a narrow Gaussian fitted to the Fe Kα line. The model components fitted to *Suzaku* XIS and HXD-PIN data are shown in black and red, respectively.
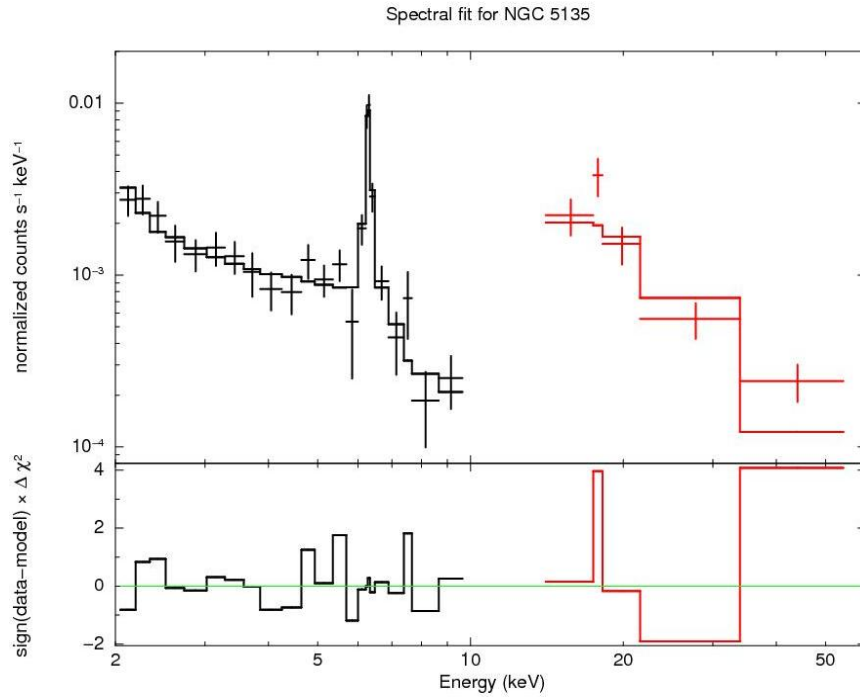
Figure 6.3: *Suzaku* 2.0 - 50 keV X-ray spectral fit of NGC 5135. Display strategy is the same as in Figure 6.1.
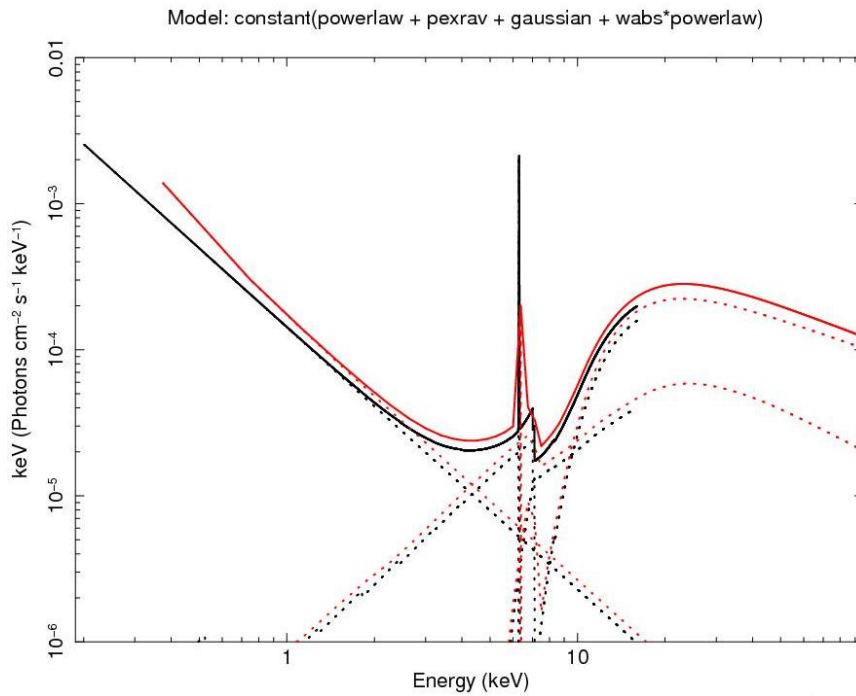
Figure 6.4: Unfolded model for the *Suzaku* 2.0 - 50 keV spectral fit. The cumulative model consists of: a power-law for the soft part of the spectrum and an absorbed power-law plus reflection component accounting for the hard X-ray continuum and a narrow Gaussian fitted to the Fe Kα line. Display strategy is the same as in Figure 6.2.

Table 6.1: The best fit *Suzaku* X-ray spectral parameters

Energy range	2.0 - 50 keV	0.5 - 50 keV
Model	(PL + R + abs*PL + Line)	(T + T + PL + R + abs*PL + Line)
$\chi^2/d.o.f$	23/20	83/49
Soft Component		
$\Gamma_{\rm soft}$	$2.79^{+0.56}_{-0.63}$	$2.65^{+0.29}_{-0.37}$
kT (keV)		$0.48^{+0.56}_{-0.14}$
kT (keV)		$0.89^{+0.28}_{-0.62}$
Hard Component		
$\Gamma_{\rm hard}$	$1.70^{+0.30}_{-0.79}$	$1.73^{+0.14}_{-0.33}$
$N_{\rm H}$ (10^{24} cm^{-2})	$2.95^{+2.34}_{-1.32}$	$2.77^{+1.84}_{-1.07}$
R	$0.38^{+0.16}_{-0.14}$	$0.33^{+0.14}_{-0.12}$
Fe Kα line		
$E_{\rm Fe}$ (keV)	$6.38^{+0.01}_{-0.01}$	$6.38^{+0.01}_{-0.01}$
$EW_{\rm Fe}$ (keV)	$1.86^{+0.32}_{-0.31}$	$1.76^{+0.30}_{-0.30}$

Notes: T: thermal model ('mekal' in XSPEC), PL: power-law, abs: photoelectric absorption, R: strength of reflection component relative to the hard power-law continuum.

Table 6.2: *Suzaku* X-ray fluxes and luminosities of NGC 5135

Energy band (keV)	Flux (erg cm^{-2} s^{-1})	Luminosity (erg s^{-1})
0.5 - 2.0	3.72×10^{-13}	1.59×10^{41}
2.0 - 10.0	4.18×10^{-13}	1.78×10^{41}
10.0 - 50.0	1.49×10^{-11}	6.37×10^{42}
Fe Kα	8.4×10^{-14}	3.58×10^{40}

6.5 Comparison with previous X-ray observations

Using *Chandra* X-ray observations of NGC 5135, Levenson *et al.* (2004) reported that both AGN and circumnuclear starburst contribute significantly to its X-ray emission below 10 keV. *Chandra* high spatial resolution enabled to isolate AGN and

starburst emission and has shown that the AGN is completely obscured by column density $N_H \geq 10^{24}$ cm^{-2} and thus Compton-thick in nature. Levenson *et al.* (2004) fitted 0.5 - 10 keV *Chandra* X-ray spectrum of AGN emission with two thermal components with temperatures kT ~ 0.05 keV and ~ 0.6 keV required for the soft component, a flat power-law for the hard component ($\Gamma \simeq 0$) and a Gaussian for Fe Kα emission line. Flat power-law representing hard continuum accounts for reflection components as *Chandra* observations lack enough counts above 7.5 keV. The High EW $\simeq 2.4$ keV of Fe Kα line and flat power-law representing reflection component vindicate Compton-thick absorption ($N_H \geq 10^{24}$ cm^{-2}) (Levenson *et al.* 2004). The use of Compton reflection to fit the hard X-ray continuum in *Chandra* data did not improve the fit due to fewer counts at higher energy end and therefore reflection component remained unconstrained.

Guainazzi *et al.* (2005) have also analyzed the same *Chandra* data of NGC 5135 and find the results similar to Levenson *et al.* (2004). Guainazzi *et al.* (2005) best fitted the *Chandra* ACIS-S3 spectrum with the 'thermal + reflection' model in which the soft X-ray component was fitted with two thermal components with kT ~ 0.08 and ~ 0.39 keV plus an additional emission line with centroid energy E$c \simeq$ 1.78 keV. Above 2 keV the spectrum is Compton-reflection dominated, consistent with the heavily obscured AGN with column density $N_H \geq 9 \times 10^{23}$ cm^{-2} (for an intrinsic photon index of 1.5 and a reflection fraction ≤ 0.5). The intensity of the Fe Kα fluorescent emission line is $\sim 5.2^{+1.9}_{-2.6} \times 10^{-6}$ photon cm^{-2} s^{-1}, corresponding to an EW $\sim 1.7^{+0.6}_{-0.8}$ keV against the reflection continuum. The fluxes in the 0.5 - 2.0 and 2.0 - 10.0 keV energy bands are $\sim 1.9^{+2.8}_{-1.0} \times 10^{-13}$ erg cm^{-2} s^{-1} and $\sim 1.6^{+1.0}_{-0.6} \times 10^{-13}$ erg cm^{-2} s^{-1}, respectively. Turner *et al.* (1997) tried various models to fit 0.5 - 10.0 keV *ASCA* spectra of a sample of Seyfert type 2 galaxies including NGC 5135 and found that the observed *ASCA* spectrum of NGC 5135 can be well fitted with a soft component accounted by thermal plasma model with temperature kT ~ 0.77 keV and a relatively steep power-law ($\Gamma \sim 2.4$) plus a broad Fe Kα emission line of high EW.

The observed fluxes of NGC 5135 from *Suzaku* in the 0.5 - 2.0 keV, 2.0 -10 keV and 10 - 50 keV energy bands are mentioned in Table 6.2. *Suzaku* fluxes in 0.5 - 2.0 and 2.0 - 10 keV bands are consistent with *Chandra* observations once we consider total AGN plus starburst emission in the *Chandra* analysis, since *Suzaku* observations can not isolate AGN and nuclear starburst spatially. *ASCA* fluxes and luminosities are also similar to the *Suzaku* observations within the uncertainty limits. Using *Suzaku* broad-band spectral analysis we could see heavily absorbed power-law ($N_H \sim 2.95^{+2.34}_{-1.32} \times 10^{24}$ cm^{-2}, $\Gamma \sim 1.7$) component which has not been constrained with previous (*Chandra* and *ASCA*) observations. If we fix the photon index to the canonical value ~ 1.9 of unobscured AGNs (*e.g.*, Nandra *et al.* (1997)), the column density increases slightly and the fit remains nearly the same. We estimate EW of Fe K$\alpha \simeq 1.86$ keV which is consistent with *Chandra* observations within the uncertainty limits. The reflection parameter R, *i.e.*, the ratio of the normalization of cold reflection to the normalization of absorbed power-law is $\simeq$ 0.33.

6.6 Discussion

Using *Suzaku* broad-band X-ray spectral properties of NGC 5135, I attempt to understand the nature of Compton-thick obscuring material around AGN, *i.e.*, optical thickness and viewing angle of the obscuring torus. In the following sections I discuss the inferred nature of circumnuclear obscuring material in NGC 5135 using *Suzaku* broad-band X-ray spectral properties.

6.6.1 Soft X-ray emission

In our *Suzaku* broad-band X-ray spectral fit of NGC 5135, soft X-ray emission below 2.0 keV is primarily accounted by two thermal plasma models of sub-keV temperatures, which is consistent with the *Chandra* X-ray observations showing

124

that the soft X-ray (≤ 2.0 keV) emission is dominated by circumnuclear starburst (Levenson *et al.* 2004). The ratio of soft X-ray to far infrared emission ($L_{0.5-2.0 \text{ keV}}/L_{FIR}$) $\sim 2.9 \times 10^{-4}$ for NGC 5135 is consistent with the ratio for starburst galaxies (*e.g.*, Ranalli, Comastri, and Setti (2003)) and suggests that soft X-ray emission is dominated by starburst than AGN. The ratio of 2.0 - 10.0 keV X-ray luminosity to far infrared luminosity ($L_{2.0-10 \text{ keV}}/L_{FIR}$) tends to be greater than 10^{-2} for Seyfert galaxies which do not contain circumnuclear starburst, while, this ratio is generally much lower in case of starburst and ultraluminous infrared galaxies (Levenson, Weaver, and Heckman 2001; Ptak *et al.* 2003). Using X-ray luminosity obtained from our *Suzaku* X-ray spectral fitting and FIR luminosity $L_{FIR} \simeq 5.5 \times 10^{44}$ erg s^{-1} given in Sanders and Mirabel (1996), we find that the ratio $L_{2.0-10 \text{ keV}}/L_{FIR}$ is $\sim 3.3 \times 10^{-4}$, consistent with the findings that NGC 5135 hosts circumnuclear starburst. Apart from starburst, soft X-ray emission in NGC 5135 may have contributions from hot gas photoionized by AGN emission and some scattered emission as well but difficult to quantize.

6.6.2   Hard X-ray emission

In NGC 5135, *Suzaku* HXD detected hard X-ray emission up to ~ 50 keV and combination of XIS and HXD data is useful in unveiling heavily obscured AGN emission. The hard X-ray spectral component is primarily fitted with heavily absorbed power-law ($N_H \sim 2.95^{+2.34}_{-1.32} \times 10^{24}$ cm^{-2}, $\Gamma \sim 1.7$) and a reflection component (R $\simeq 0.33$). The hard X-ray fluxes in 2.0 - 10 keV and 10 - 50 keV bands are $\sim 4.18 \times 10^{-13}$ erg cm^{-2} s^{-1} and $\sim 1.49 \times 10^{-11}$ erg cm^{-2} s^{-1}, respectively which gives luminosities $\sim 1.78 \times 10^{41}$ erg s^{-1} and $\sim 6.37 \times 10^{42}$ erg s^{-1}, respectively. The intrinsic flux and luminosity in 2.0 - 10.0 keV band are $\sim 9.4 \times 10^{-12}$ erg cm^2 s^{-1} and $\sim 4.0 \times 10^{42}$ erg s^{-1}, which is estimated by keeping absorbing $N_H = 0$ in the best fit. The high absorbing column density ($N_H \sim 2.95^{+2.34}_{-1.32} \times 10^{24}$ cm^{-2}) and high ratio of intrinsic to observed 2.0 - 10.0 keV luminosity ($L_{2.0-10 \text{ keV, obs}}/L_{2.0-10 \text{ keV, int}}$

125

~ 22.5) vindicate a heavily obscured luminous AGN. The flux ratio of observed 2.0 - 10.0 keV hard X-ray to [OIII] $\lambda 5007$Å ($F_{2.0 - 10 \text{ keV, obs}}/F_{[OIII]} \sim 1.1$) is also consistent with the AGN being heavily obscured (Bassani *et al.* 1999). The flux ratio of intrinsic 2.0 - 10.0 keV hard X-ray to [OIII] $\lambda 5007$Å ($F_{2.0 - 10 \text{ keV, int}}/F_{[OIII]}$) is ~ 25.5 which is similar to the mean ratio of $F_{2.0 - 10 \text{ keV, int}}/F_{[OIII]}$ for Seyfert 1 galaxies (*e.g.*, Heckman *et al.* (2005)), supporting the notion that obscured nucleus in NGC 5135, a Seyfert type 2 is intrinsically similar to Seyfert type 1 nuclei (the unification scheme, Antonucci and Miller (1985); Antonucci (1993)).

6.6.3 Obscuration and reflection in NGC 5135

Due to limiting sensitivity and energy range, *ASCA* and *Chandra* observations could provide only lower limits to the absorbing column density ($N_H \geq 1.5 \times 10^{24}$ cm^{-2}) and the reflection component remained unconstrained. The *Suzaku* spectral fitting provides accurate estimation of absorbing column density and the strength of reflection component, which are essential in understanding the nature of obscuring torus surrounding AGN. The hard X-ray spectral component is primarily fitted with a heavily absorbed power-law ($N_H \sim 2.95^{+2.34}_{-1.32} \times 10^{24}$ cm^{-2}, $\Gamma \sim 1.7$) and a reflection component ($R \simeq 0.33$). The signature of Compton-thick matter around AGN can be characterized by "Compton reflection" continuum with a broad bump peaking around 20 - 30 keV, which rapidly decreases at both low and high energies due to photoelectric absorption and Compton down-scattering, respectively. The shape of the reflection spectrum depends on the column density, the ionization status, and the metalicity of the reflecting matter (Matt 2002). Its strength depends on the solid angle subtended by the reflector at the primary illuminating source. We fit the reflection component with 'pexrav' model and assume cosine of inclination equal to 0.45 and the iron abundances equal to the solar abundances. In Compton-thick sources, the EW of Fe Kα emission with respect to the reflected continuum is always greater than 1 keV (George and Fabian

1991; Matt, Perola, and Piro 1991) and depends on the geometry of obscuring torus around AGN (*e.g.*, Awaki *et al.* (1991); Ghisellini, Haardt, and Matt (1994); Levenson *et al.* (2002)). We fit Fe Kα line with a narrow unresolved Gaussian with centroid energy at ~ 6.4 keV which is consistent with fluorescence in a cold neutral medium. The centroid energy of Fe Kα for neutral as well as moderately ionized (up to FeXVII) fluorescence material lies at 6.4 keV and highly ionized material, *i.e.*, He-like and H-like Fe give rise Fe Kα centroid energy at 6.7 and 6.9 keV, respectively. The properties of Fe Kα line (*i.e.*, narrow and neutral or moderately ionized) in NGC 5135 using *Suzaku* XIS data are in agreement with *Chandra* observations reported by Levenson *et al.* (2004). However, using *ASCA* observations, Turner *et al.* (1997) reported the presence of strongly ionized Fe lines. The hard X-ray fluxes of *ASCA* and *Chandra* observations separated by over 5 years are similar, so AGN variability is an unlikely explanation for this discrepancy.

Levenson *et al.* (2002) showed that variations in the geometry of obscuring torus, not iron abundance or intrinsic spectral shape, are required to produce EWs significantly larger than 1 keV. The significantly large EW of Fe Kα in NGC 5135 may suggest a small opening angle ($\sim 20°$) of the obscuring torus giving a covering fraction over AGN $\sim 90\%$ (Levenson *et al.* 2002). Our spectral fitting renders EW of Fe Kα line in NGC 5135 ~ 1.8 keV which supports the presence of high absorbing column density ($N_H \geq 10^{24}$ cm^{-2}) in the fluorescing region (*e.g.*, Ghisellini, Haardt, and Matt (1994); Krolik, Madau, and Zycki (1994); Bassani *et al.* (1999)). Using Monte Carlo simulations Levenson *et al.* (2006) reported an empirical relationship between Fe Kα line luminosity and intrinsic 2.0 - 10.0 keV AGN luminosity and suggest typical ratio ($L_{Fe}/L_{2-10 \text{ keV, int}}$) $\sim 2 \times 10^{-3}$, however, this depends on the geometry of the torus. Our *Suzaku* X-ray spectral fitting gives $L_{Fe} \simeq 3.58 \times 10^{40}$ erg s^{-1} and using Levenson *et al.* (2006) empirical ratio of Fe Kα line luminosity to intrinsic 2.0 - 10.0 keV luminosity, we obtain $L_{2-10 \text{ keV, int}} \sim 1.79 \times 10^{43}$ erg s^{-1}, *i.e.*, nearly 100 times of the observed 2.0 - 10.0 keV luminosity. However,

we caution about the large uncertainty involved in L_{Fe} - $L_{2-10 \text{ keV, int}}$ empirical relation.

Intriguingly, we note that the $L_{2-10 \text{ keV, int}}$ obtained from our spectral fitting is ~ 4 time lower than the one estimated using L_{Fe} - $L_{2-10 \text{ keV, int}}$ empirical relation given in Levenson *et al.* (2006). One viable explanation for this discrepancy may be that we have not taken Compton scattering into account while modeling the spectrum. The Compton cross-section starts dominating over the photoelectric cross-section above ~ 10 keV, therefore Compton scattering effect is significant, especially for large column densities and high energy photons (*e.g.*, Matt *et al.* (1999); Yaqoob (1997)). We notice that the addition of Compton scattering model components (*e.g.*, 'plcabs' in XSPEC) increases the estimated 2.0 - 10 keV and 10 - 50 keV intrinsic luminosities slightly. However, 'plcabs' model is valid for the energy range between 10 and 18.5 keV (Yaqoob 1997) and insufficient to account for the Compton scattering at larger energies. The intrinsic 10 - 50 keV X-ray emission may be significantly higher than what we observe in the 10 - 50 keV band, due to the effect of Compton scattering which depends on the geometry of the scatterer/absorber, as discussed, for example, in the case of NGC 1365 (Risaliti *et al.* 2009).

It is important to note that the 'pexrav' model used for representing the reflection component was developed for an accretion disk geometry and thus inefficient to understand the geometry of the surrounding obscuring, reflecting material, *i.e.*, torus. Monte Carlo simulations considering various geometries such as reflection from semi-infinite, plane parallel slab (George and Fabian 1991) have been used to investigate the geometry of circumnuclear obscuring material in AGN. Awaki *et al.* (1991) and Ghisellini, Haardt, and Matt (1994) modeled AGN X-ray spectra assuming reprocessing material having torus geometry with an open reflecting area characterized by its half-opening angle. Ikeda, Awaki, and Terashima (2009) simulated MRK 3 X-ray spectrum considering reprocessing material a three-dimensional torus around AGN, and characterized by half opening angle, inclina-

tion angle of torus with respect to the observer's line-of-sight, absorbing column density and ratio of inner to outer radii of torus. The simulated spectra were consist of three components, one direct transmitted component and two reflection components, one reflected from the visible inner wall of the torus and the other scattered through the torus. Levenson *et al.* (2002) used Monte Carlo simulation and reported that the obscuring torus in NGC 5135 is likely have small half opening angle $\leq 20°$. Simulating *Suzaku* broad-band X-ray spectrum of NGC 5135 with the reflection models which take the geometry of obscuring material in to account, may help in unveiling the geometry of obscuring material more accurately (*e.g.*, Ikeda, Awaki, and Terashima (2009); Awaki *et al.* (2009)).

6.7 Conclusions

We note that the *Suzaku* broad-band X-ray spectrum of heavily obscured NGC 5135 is much complex than a single absorbed power-law and additional components, *i.e.*, thermal emission from a starburst region and photoionized gas are required below 10 keV and a fairly strong reflection component above 10 keV. *Suzaku* broadband spectral fitting could measure photoelectric cut-off (slightly below to 10 keV) and subsequently amount of circumnuclear absorption ($N_H \sim 2.95^{+2.34}_{-1.32} \times 10^{24}$ cm^{-2}) which could not be estimated with previous observations. *Suzaku* X-ray spectral study of NGC 5135 can represent a case study of some of the complex realities in the Compton-thick obscured AGNs which are also likely to be present in other sources (*e.g.*, Risaliti, Maiolino, and Salvati (1999)).

Chapter 7

Testing Seyfert unification scheme in radio wavelengths

7.1 Introduction

Seyfert galaxies are categorized as radio-quiet AGNs, *i.e.*, $\frac{F_{5\ GHz}}{F_{B-Band}} < 10$ (Kellermann *et al.* 1989), nonetheless, radio continuum emission can be used as effective tracer of the nuclear activity since the radio emission at centimeter wavelengths is optically thin to torus obscuration in comparison to shorter wavelengths, *e.g.*, optical, UV and soft X-ray. High resolution radio observations show that Seyfert nuclei produce weak bipolar radio-emitting jets that are largely confined within the host galaxy (Wilson and Ulvestad 1982; Thean *et al.* 2000; Lal, Shastri, and Gabuzda 2004), however, a substantial fraction of low-frequency radio emission may also arise from the host galaxy disk apart from the AGN jet related features (*e.g.*, Baum *et al.* (1993); Colbert *et al.* (1996)). In a number of Seyfert galaxies the parsec-scale flux density measured from high resolution observations is often much lower than that measured from observations with lower resolution, suggesting that radio emission is not only concentrated to the nuclear region, as in the case of radio-loud AGNs, but rather extends on scales of tens or hundreds of parsecs (see, *e.g.*, Sadler *et al.* (1995); Lal, Shastri, and Gabuzda (2004); Orienti and Prieto (2010)). Most of the Seyfert samples have been studied at relatively high frequency (≥ 1.4 GHz) with high resolution (few arcsec) obser-

vations (*e.g.*, Ulvestad and Wilson (1984, 1989); Kukula *et al.* (1995); Morganti *et al.* (1999); Nagar *et al.* (1999); Thean *et al.* (2000, 2001)), which effectively filter out the low-surface-brightness and extended radio emission. Therefore, in this thesis I study the low-frequency radio properties of our sample of Seyfert galaxies using GMRT observations carried out at 240 MHz, 610 MHz and NRAO VLA Sky Survey (NVSS)[1] observations at 1.4 GHz and the 5 GHz VLA observations present in the literature.

There have been several studies of Seyfert samples to test the predictions of Seyfert unification scheme at radio regime (de Bruyn and Wilson 1976, 1978; Meurs and Wilson 1984; Ulvestad and Wilson 1984, 1989; Roy *et al.* 1994; Kukula *et al.* 1995; Nagar *et al.* 1999; Morganti *et al.* 1999; Thean *et al.* 2000, 2001; Schmitt *et al.* 2001), however, certain subtle selection effects are inherent in most of the samples (see, Kukula *et al.* (1995); Morganti *et al.* (1999); Nagar *et al.* (1999); Ulvestad and Ho (2001); Schmitt *et al.* (2001)). A comprehensive description of the possible selection effects in the different samples is given in Ho and Ulvestad (2001). Also, the conclusions derived from the comparison of the two Seyfert subtypes are often limited by the sample selection than the sample size. Therefore, I attempt to test the predictions of Seyfert unification scheme at radio wavelengths using our rigorously selected, moderate size sample. The details of our sample and it's selection criteria have been presented in Chapter 2.

7.2 Observations and data reductions

We carried out full array GMRT (Swarup *et al.* 1991) snapshot observations at 610/240 MHz dual frequency using bandwidth of 32 MHz and 4 second integration time on 9 - 10 August 2008 under the observing proposal '14VSA01'. All the target sources (except NGC 7469, NGC 5548) have 2 - 4 scans each of 10 minutes with weaker sources having more scans than stronger ones. Absolute flux and

---

[1]http://www.cv.nrao.edu/nvss/

bandpass calibration was done by observing standard flux calibrators 3C 147 and 3C 286, at the start and end of the observing run. The phase calibration was done by observing a nearby phase calibrator source before and after every scan of the target sources. The observing log is given in Table 7.1. The data were reduced in a standard way using NRAO 'AIPS' package. For each run, bad visibility points were edited out, after which the data were calibrated. The edited and calibrated visibilities were Fourier transformed into radio maps using 'IMAGR' task in AIPS with uniform weightage. Primary beam size of full array GMRT at 610/240 MHz is rather large $\sim 43'/81'$ and therefore we performed wide field imaging by dividing whole field of view in $\sim 25/49$ sub-fields. For all our sample sources the signal to noise ratio is sufficiently high enough to apply self-calibration which removes antenna-based phase and amplitude errors. The use of few iterations of self-calibration improved the signal to noise ratio significantly in all our sample sources.

We acquired the images for all the 20 sources of our sample at 610 MHz, while due to the poor quality of data at 240 MHz we could obtain images for only 13/20 (6 type 1s and 7 type 2s) sources of our sample. Table 7.2 and 7.4 list the Seyfert type, linear scale, synthesized beam size with it's position angle (P.A.), rms of the noise in radio map, peak flux density (S_{peak}), integrated flux density (S_{int}) and radio power for our sample sources at 610 MHz and 240 MHz, respectively. NVSS has detection of all the 20 sources of our sample and we use the 1.4 GHz NVSS flux densities for our study. NVSS is a continuum survey at 1.4 GHz carried out using VLA in 'D' and 'DnC' configurations which gives the radio images with rms ~ 0.45 mJy/beam and of resolution $\sim 45''$. The flux densities at 5 GHz measured with low resolution observations (*e.g.*, either using VLA in 'D' configuration or using single dish observations) are available in literature for 18/20 (9 type 1s and 9 type 2s) sources of our sample.

Table 7.1: GMRT observational log for our sample Seyfert galaxies

Source name	No. of scans	Phase Calibrator	observation date
MRK 6	3	0614+607	2008 August 09, 10
NGC 3227	3	1111+199	2008 August 09
NGC 3516	4	1313+675	2008 August 09, 10
NGC 4151	2	1331+305	2008 August 09
MRK 766	3	1331+305	2008 August 09, 10
MRK 279	4	1313+675	2008 August 09, 10
NGC 5548	5	1331+305	2008 August 09, 10
ARK 564	3	2236+284	2008 August 10
NGC 7469	1	2212+018	2008 August 10
MRK 530	4	2212+018	2008 August 10
MRK 348	3	0137+331	2008 August 10
MRK 1	3	0137+331	2008 August 10
MRK 1066	3	0137+331	2008 August 10
NGC 2110	2	0607-085	2008 August 10
NGC 2273	3	0614+607	2008 August 09, 10
NGC 5252	4	1351-148	2008 August 09, 10
NGC 5728	2	1351-148	2008 August 09
NGC 7212	2	2212+018	2008 August 10
NGC 7682	2	2212+018	2008 August 10
MRK 533	2	2212+018	2008 August 10

Notes: All the 20 sample sources were observed with GMRT at 610/240 MHz dual frequency with 32 MHz bandwidth and 4 second integration time. Each scan of a target source spans for 10 minutes while for a phase calibrator it is 4 minutes. The flux calibrators 3C 147 and 3C 286, were observed for 15 minutes at the start and end of the observing run, respectively.

Table 7.2: 610 MHz radio image parameters for our sample Seyfert galaxies

Sources name	Scale (kpc/$''$)	Beam size (arcsec^2)	P.A. (deg)	rms noise (mJy/beam)	S_{Peak} (mJy/beam)	$S_{Int.}$ (mJy)	log $P_{610\ MHz}$ (erg s^{-1})
			Seyfert type 1s				
MRK 6	0.377	10.33×4.98	-23.98	1.85	379.7	442	30.5
NGC 3227	0.079	8.09×6.02	-64.85	1.20	130.1	177	28.7
NGC 3516	0.179	7.53×4.90	-12.96	0.89	13.5	18	28.5
NGC 4151	0.068	7.64×4.56	-25.14	2.60	316.7	646	29.2
MRK 766	0.261	7.52×4.63	-25.68	0.80	53.3	63	29.4
MRK 279	0.601	7.45×5.26	19.68	0.68	39.6	44	29.9
NGC 5548	0.344	6.31×5.19	-10.90	0.85	19.7	51	29.5
ARK 564	0.491	7.69×5.12	-45.09	0.85	61.0	62	29.9
NGC 7469	0.328	9.67×5.37	-24.77	0.40	218.5	302	30.2
MRK 530	0.584	7.18×6.85	35.11	0.60	37.1	38	29.8
			Seyfert type 2s				
MRK 348	0.302	6.28×5.69	-14.78	1.15	480.9	500	30.4
MRK 1	0.320	6.27×5.19	0.87	0.75	109.8	115	29.8
MRK 1066	0.243	6.56×5.21	19.39	0.80	166.8	193	29.8
NGC 2110	0.158	6.79×5.09	5.93	1.20	494.4	565	29.9
NGC 2273	0.125	7.92×4.71	-28.93	1.20	80.6	96	28.9
NGC 5252	0.458	10.67×5.11	-24.05	0.55	18.9	24	29.4
NGC 5728	0.189	11.59×5.98	-22.67	0.75	25.6	68	29.2
NGC 7212	0.528	6.37×4.89	-6.04	0.45	205.5	223	30.6
NGC 7682	0.344	6.42×5.30	7.04	0.40	104.1	109	29.9
MRK 533	0.572	6.78×6.15	46.30	0.40	340.7	380	30.8

Table 7.3: Fitted parameters of the 610 MHz radio images of our sample Seyfert galaxies

Source name	Scale (kpc/″)	S_{peak} (mJy/beam)	$S_{Int.}$ (mJy)	Measured size			Deconvolved size		
				Maj.	Min.	P.A.	Maj.	Min.	P.A.
Seyfert type 1s									
MRK 6	0.377	385.4	398.7	10.67	4.98	155.8	2.68	0.23	153.7
NGC 3227	0.079	127.3	146.0	8.85	6.69	119.4	3.79	1.70	130.0
NGC 3516	0.179	11.6	24.3	10.44	7.38	4.0	7.63	4.99	20.5
NGC 4151	0.068	323.6	342.6	7.38	4.99	160.4	2.31	2.21	138.0
		221.4	341.3	10.26	5.23	140.0	7.15	1.51	129.0
MRK 766	0.261	52.6	57.5	7.92	4.81	150.0	2.74	0.63	127.0
MRK 279	0.601	38.8	42.9	7.86	5.54	19.0	2.45	1.70	13.4
NGC 5548	0.344	17.7	55.2	14.33	7.11	158.5	12.88	4.80	157.6
ARK 564	0.491	62.2	62.4	7.62	4.91	132.3	0.0	0.0	0.0
NGC 7469	0.328	215.0	290.3	10.43	6.70	154.7	4.07	3.87	88.5
MRK 530	0.584	37.2	39.5	7.28	7.18	97.0	2.42	0.35	116.4
Seyfert type 2s									
MRK 348	0.302	482.5	497.5	6.34	5.81	157.0	1.44	0.26	107.6
MRK 1	0.320	111.3	114.9	6.31	5.32	177.3	1.35	0.30	118.6
MRK 1066	0.243	168.9	185.4	6.69	5.63	18.9	2.12	1.18	111.0
NGC 2110	0.158	493.5	552.8	7.68	5.11	9.0	3.44	0.15	14.8
NGC 2273	0.125	80.6	94.0	8.34	5.19	152.4	2.68	2.14	176.0
NGC 5252	0.458	18.7	20.5	10.56	5.66	159.6	2.59	0.0	142.0
NGC 5728	0.189	24.5	34.3	12.60	7.46	154.7	5.76	4.34	137.0
		17.5	39.4	16.10	9.39	159.9	11.48	7.24	162.9
NGC 7212	0.528	206.3	208.3	6.44	4.88	174.4	0.96	0.0	2.4
NGC 7682	0.344	103.8	105.4	6.46	5.35	6.1	0.88	0.46	121.8
MRK 533	0.572	347	362.7	6.98	6.26	44.1	1.59	1.15	28.0

Notes: The radio structures are being fitted with AIPS task 'JMFIT' which fits the structures with Gaussian components. A value of 0.0 in deconvolved source size means that the source is smaller than the synthesized beam in some dimension. Maj.: Major axis of the FWHM of the fitted Gaussian component in arcsecond, Min.: Minor axis of the FWHM of the fitted Gaussian component in arcsecond, P.A.: position angle of the fitted Gaussian component in degree.

Table 7.4: 240 MHz radio image parameters for our sample Seyfert galaxies

Source name	Scale (kpc/$''$)	Beam size (arcsec^2)	P.A. (deg)	rms noise (mJy/beam)	S_{Peak} (mJy/beam)	$S_{Int.}$ (mJy)	log $P_{240\ MHz}$ (erg s^{-1})
			Seyfert type 1s				
MRK 6	0.377	31.66×13.34	0.24	10.0	871.2	990	30.89
NGC 3227	0.079	....	....	....	....	....	....
NGC 3516	0.179	....	....	....	....	....	....
NGC 4151	0.068	17.27×11.68	-14.00	12.0	1324.4	1330	29.50
MRK 766	0.261	18.13×12.75	-18.95	7.5	74.8	75	29.44
MRK 279	0.601	....	....	....	....	....	....
NGC 5548	0.344	21.65×15.17	-30.72	6.5	77.6	78	29.70
ARK 564	0.491	....	....	....	....	....	....
NGC 7469	0.328	38.01×22.06	-1.01	9.5	793.5	796	30.67
MRK 530	0.584	38.13×18.73	-17.42	8.5	107.3	108	30.32
			Seyfert type 2s				
MRK 348	0.302	18.52×12.88	-35.86	5.6	763.4	785	30.59
MRK 1	0.320	18.14×12.64	-22.12	5.5	181.9	182	30.01
MRK 1066	0.243	16.89×13.25	-1.87	5.0	288.6	310	29.99
NGC 2110	0.158	43.63×34.50	-0.18	23.0	1498.5	1500	30.29
NGC 2273	0.125	....	....	....	....	....	....
NGC 5252	0.458	....	....	....	....	....	....
NGC 5728	0.189	....	....	....	....	....	....
NGC 7212	0.528	40.16×29.61	-1.95	7.5	523.1	528	30.92
NGC 7682	0.344	46.13×34.28	0.87	7.5	235.5	236	30.18
MRK 533	0.572	17.87×16.98	-33.83	7.0	639.2	842	31.20

Table 7.5: Fitted parameters of the 240 MHz radio images of our sample Seyfert galaxies

Source name	Scale (kpc/″)	S_{peak} (mJy/beam)	$S_{Int.}$ (mJy)	Measured size Maj.	Min.	P.A.	Deconvolved size Maj.	Min.	P.A.
				Seyfert type 1s					
MRK 6	0.377	869.1	883.5	32.40	13.30	180.0	6.90	0.0	175.7
NGC 3227	0.079	....	....	....	....	....	....	....	....
NGC 3516	0.179	....	....	....	....	....	....	....	....
NGC 4151	0.068	1346.9	1347.0	17.10	11.64	165.9	0.0	0.0	0.0
MRK 766	0.261	84.6	84.9	16.20	9.90	152.5	0.0	0.0	0.0
MRK 279	0.601	....	....	....	....	....	....	....	....
NGC 5548	0.344	77.8	82.7	23.54	14.83	154.0	9.52	0.0	164.9
ARK 564	0.491	....	....	....	....	....	....	....	....
NGC 7469	0.328	766.7	768.0	36.80	14.60	167.0	0.0	0.0	0.0
MRK 530	0.584	91.2	97.4	40.40	16.95	157.0	17.27	0.0	144.9
				Seyfert type 2s					
MRK 348	0.302	789.3	809.6	18.96	12.90	148.2	4.87	0.0	175.6
MRK 1	0.320	185.6	186.0	17.57	12.36	163.6	1.87	0.0	127.0
MRK 1066	0.243	287.7	300.0	17.25	13.53	177.0	3.59	2.62	160.0
NGC 2110	0.158	1438.0	1440.0	40.20	14.10	160.0	0.0	0.0	0.0
NGC 2273	0.125	....	....	....	....	....	....	....	....
NGC 5252	0.458	....	....	....	....	....	....	....	....
NGC 5728	0.189	....	....	....	....	....	....	....	....
NGC 7212	0.528	495.6	496.0	32.10	25.30	153.0	0.0	0.0	0.0
NGC 7682	0.344	197.3	197.6	34.40	33.50	125.0	0.0	0.0	0.0
MRK 533	0.572	581.6	726.9	19.80	19.20	66.0	10.38	6.53	64.4

Notes: The radio structures are being fitted with AIPS task 'JMFIT' which fits the structures with Gaussian components. A value of 0.0 in deconvolved source size means that the source is smaller than the synthesized beam in some dimension. Maj.: Major axis of the FWHM of the fitted Gaussian component in arcsecond, Min.: Minor axis of the FWHM of the fitted Gaussian component in arcsecond, P.A.: position angle of the fitted Gaussian component in degree.

Table 7.6: Integrated flux densities, radio powers at 1.4 GHz, 5.0 GHz and spectral indices of our sample sources

Source name	$S_{1.4\mathrm{GHz}}$ (mJy)	$\log P_{1.4\mathrm{GHz}}$ (mJy)	$S_{5.0\mathrm{GHz}}$ (erg s^{-1})	Ref. (mJy)	$\log P_{5.0\mathrm{GHz}}$	$\alpha_{240\mathrm{MHz}}^{610\mathrm{MHz}}$	$\alpha_{610\mathrm{MHz}}^{1.4\mathrm{GHz}}$	$\alpha_{1.4\mathrm{GHz}}^{5.0\mathrm{GHz}}$	$\alpha_{\mathrm{Int.}}$
				Seyfert type 1s					
MRK 6	269.5	30.3	100.5	K06	29.89	-0.86	-0.60	-0.77	-0.74±0.03
NGC 3227	97.5	28.5	35.0	G06	28.04	....	-0.57	-0.80	-0.77±0.02
NGC 3516	31.3	28.7	7.4	G06	28.10	....	+0.66	-1.13	....
NGC 4151	359.6	28.9	128.0	G06	28.48	-0.77	-0.71	-0.81	-0.77±0.01
MRK 766	38.1	29.1	20.4	G06	28.87	-0.19	-0.61	-0.49	-0.45±0.06
MRK 279	23.2	29.7	7.4	E87	29.19	....	-0.76	-0.90	-0.85±0.04
NGC 5548	28.2	29.3	11.2	G06	28.86	-0.45	-0.72	-0.73	-0.65±0.05
ARK 564	28.6	29.6	....	....	....	....	-0.93	....	....
NGC 7469	180.5	30.0	61.6	G06	29.55	-1.04	-0.62	-0.84	-0.82±0.05
MRK 530	24.4	29.7	11.5	E87	29.35	-1.12	-0.53	-0.59	-0.71±0.08
				Seyfert type 2s					
MRK 348	292.2	28.7	801.7	G06	30.60	-0.48	-0.65	+0.79	-0.56±0.05
MRK 1	75.4	29.6	32.0	G91	29.25	-0.49	-0.51	-0.67	-0.57±0.04
MRK 1066	100.4	29.5	35.0	G91	29.04	-0.51	-0.78	-0.83	-0.73±0.05
NGC 2110	298.8	29.6	165.0	G95	29.33	-1.07	-0.74	-0.47	-0.72±0.10
NGC 2273	62.6	28.7	44.0	G91	28.55	....	-0.51	-0.28	-0.36±0.06
NGC 5252	16.3	29.3	18.1	E87	29.32	....	-0.44	+0.08	....
NGC 5728	70.0	29.1	....	....	....	....	+0.04	....	....
NGC 7212	128.0	30.3	46.0	G95	29.86	-0.92	-0.67	-0.80	-0.79±0.03
NGC 7682	59.8	29.6	24.6	E87	29.20	-0.83	-0.72	-0.70	-0.72±0.02
MRK 533	220.9	30.6	75.1	E87	30.14	-0.85	-0.65	-0.85	-0.79±0.03

Notes: K06: Kharb *et al.* (2006), E87: Edelson (1987) (VLA observations at 4.89 GHz), G06: Gallimore *et al.* (2006) (VLA-D observations at 5.0 GHz), G91: Gregory and Condon (1991) (Green Bank telescope observations at 4.85 MHz in 1987), G95: Griffith *et al.* (1995) (observations with the Parkes 64 m radio telescope at 4.85 GHz during 1990).
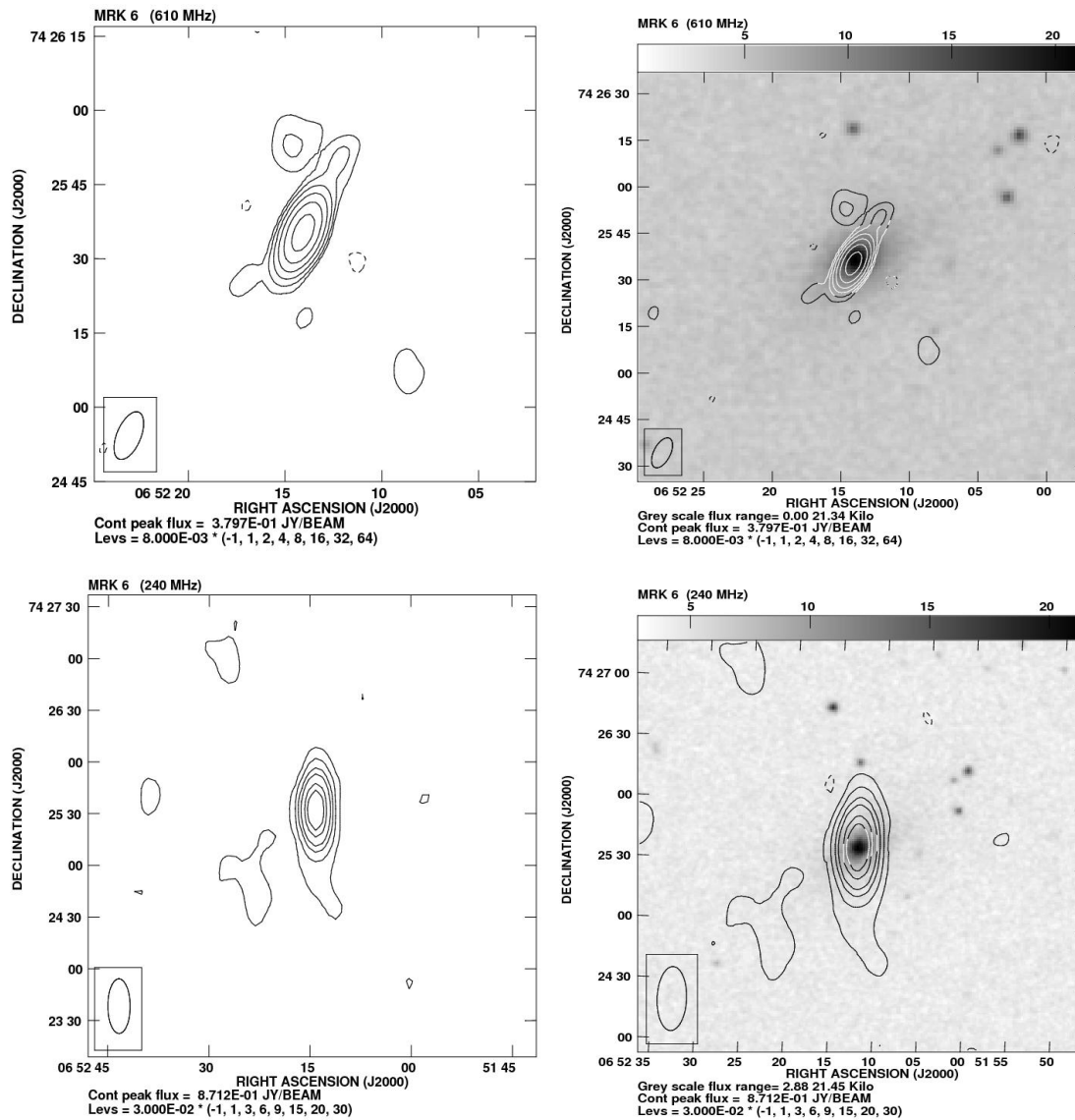
Figure 7.1: 610 MHz, 240 MHz radio contour images of MRK 6 (upper left and lower left) and radio contours overlaid on its DSS optical image (upper right and lower right). The restoring beam is shown in lower left corner of each map. The first lowest radio contour is above 3σ of the rms value in each map. The same plotting convention is followed for other sources.
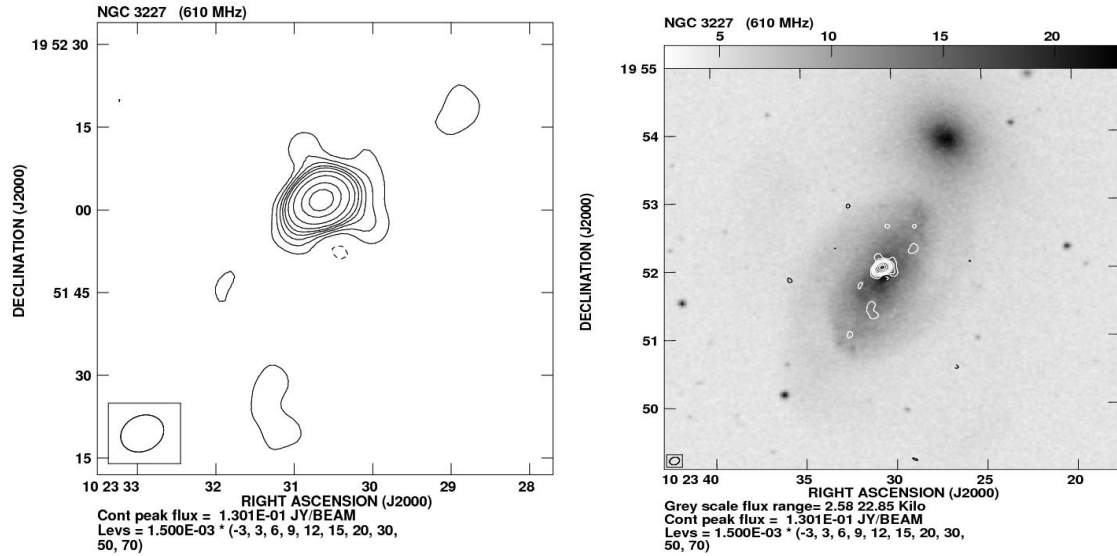
Figure 7.2: 610 MHz radio contour image of NGC 3227 and radio contours overlaid on its DSS optical image.
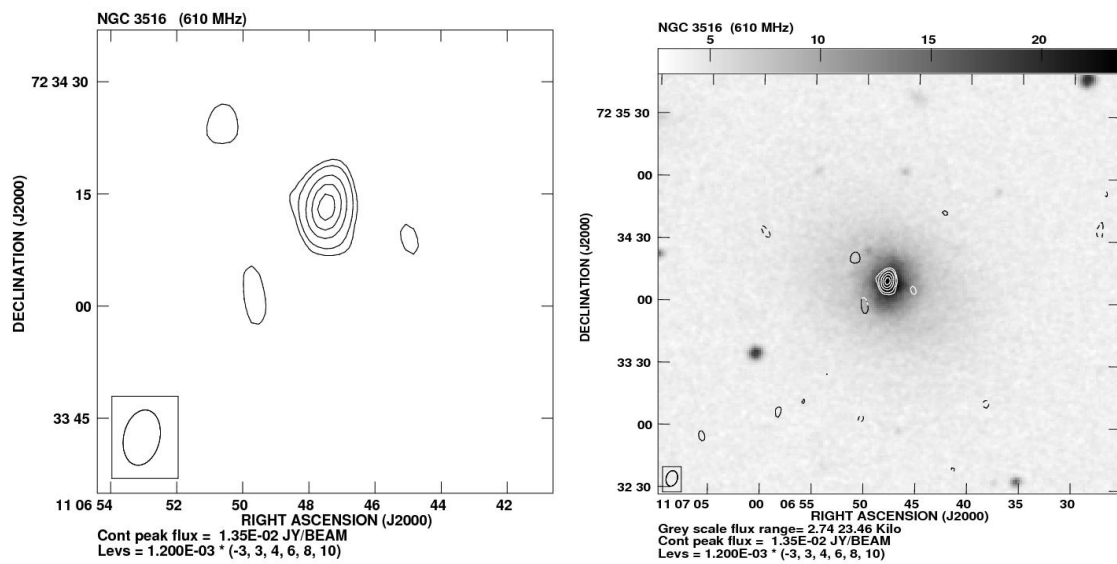
Figure 7.3: 610 MHz radio contour image of NGC 3516 and radio contours overlaid on its DSS optical image.
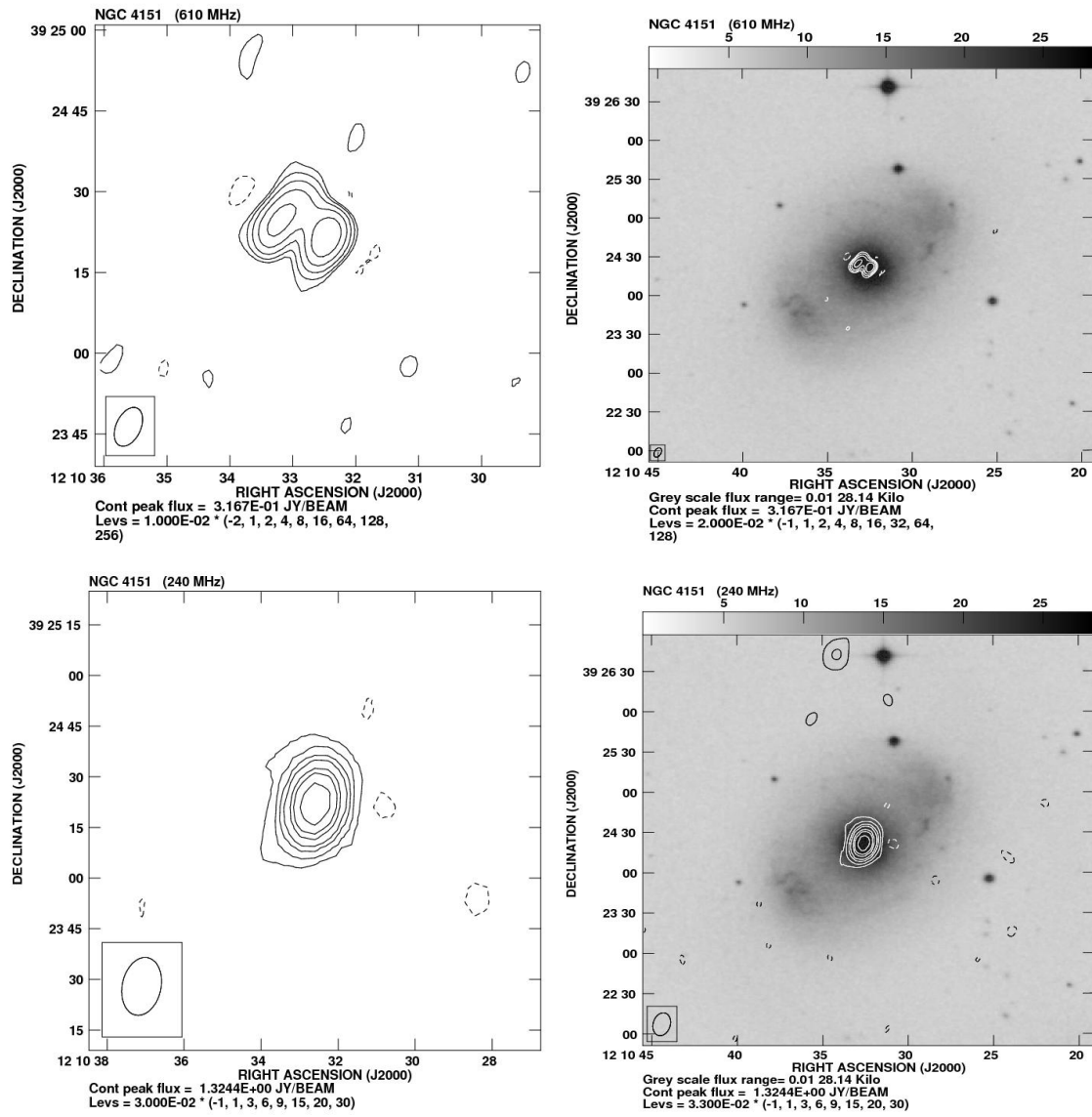
Figure 7.4: 610 MHz, 240 MHz radio contour images of NGC 4151 and radio contours overlaid on its DSS optical image.
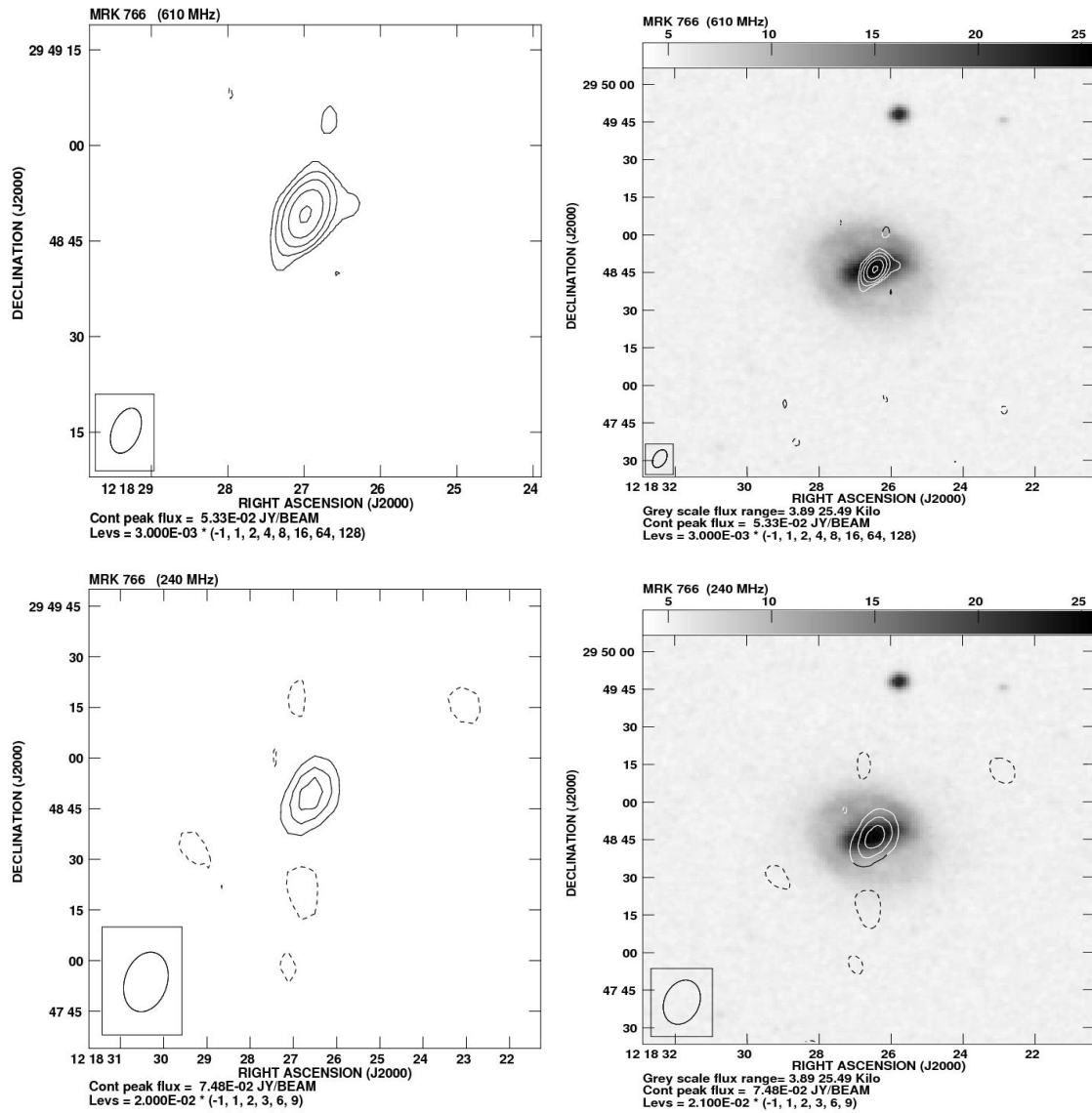
Figure 7.5: 610 MHz, 240 MHz radio contour images of MRK 766 and radio contours overlaid on its DSS optical image.
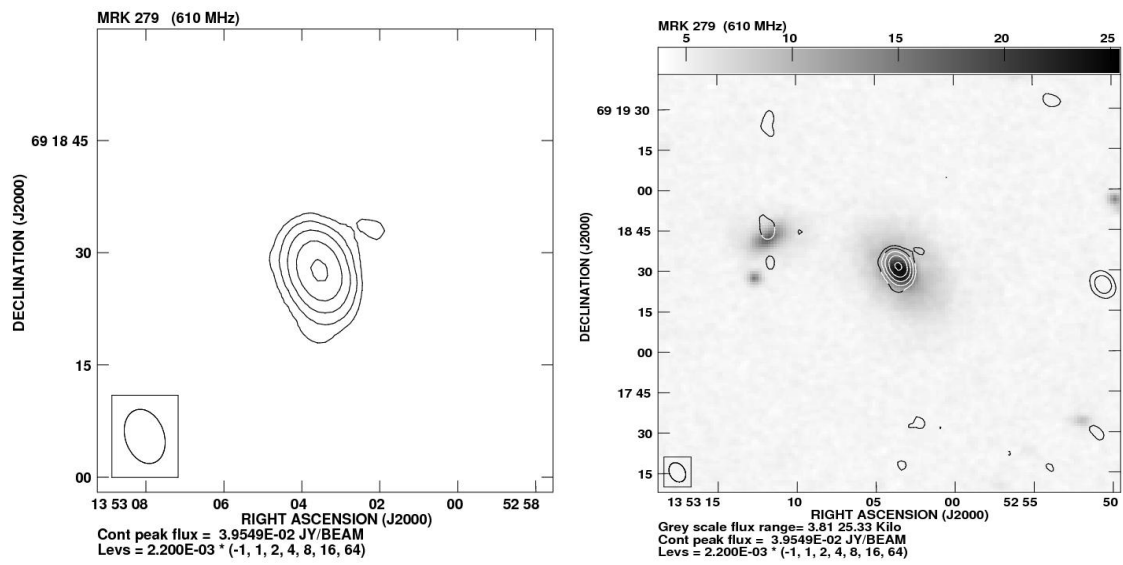
Figure 7.6: 610 MHz radio contour image of MRK 279 and radio contours overlaid on its DSS optical image.
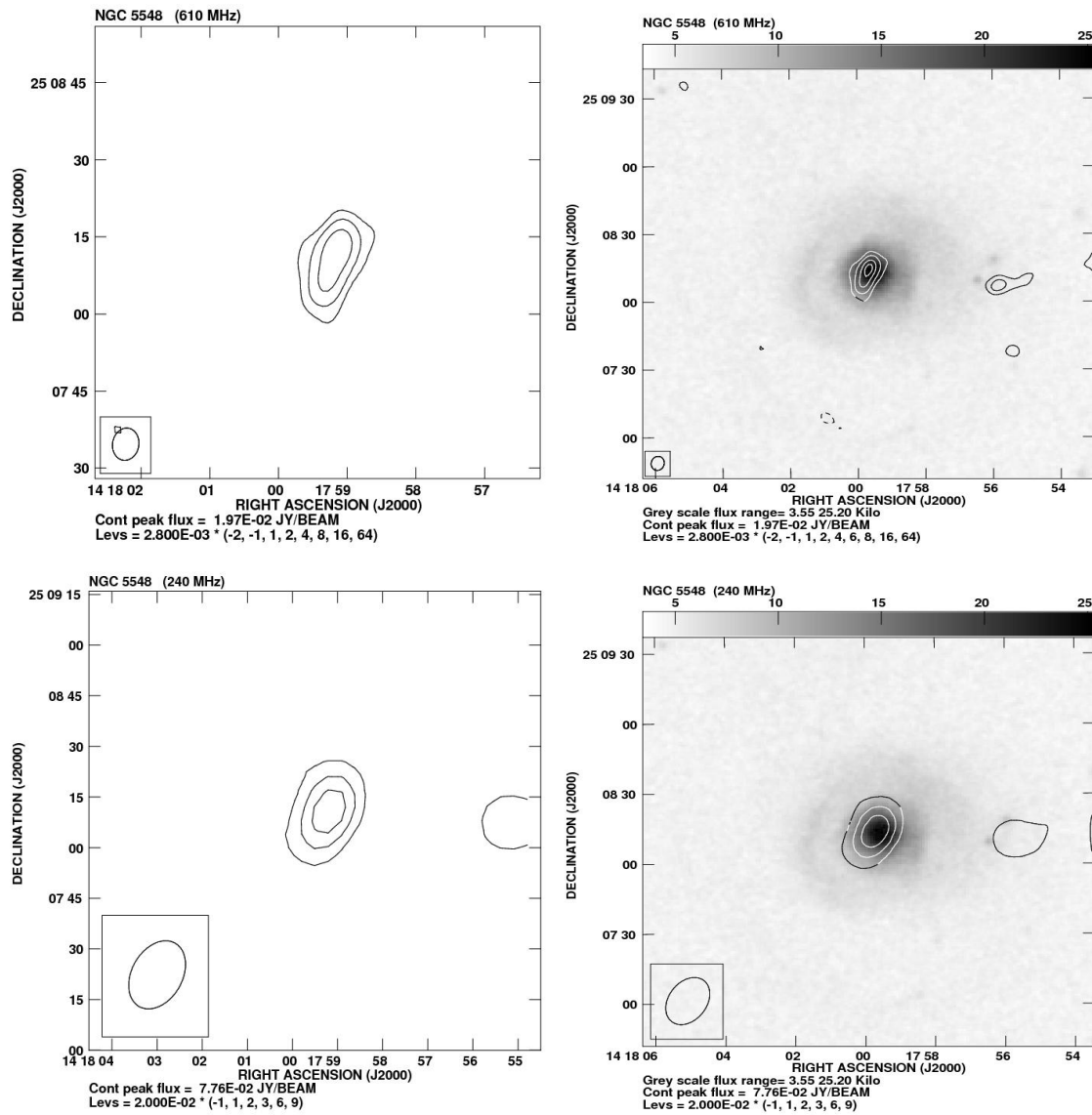
Figure 7.7: 610 MHz, 240 MHz radio contour images of NGC 5548 and radio contours overlaid on its DSS optical image.
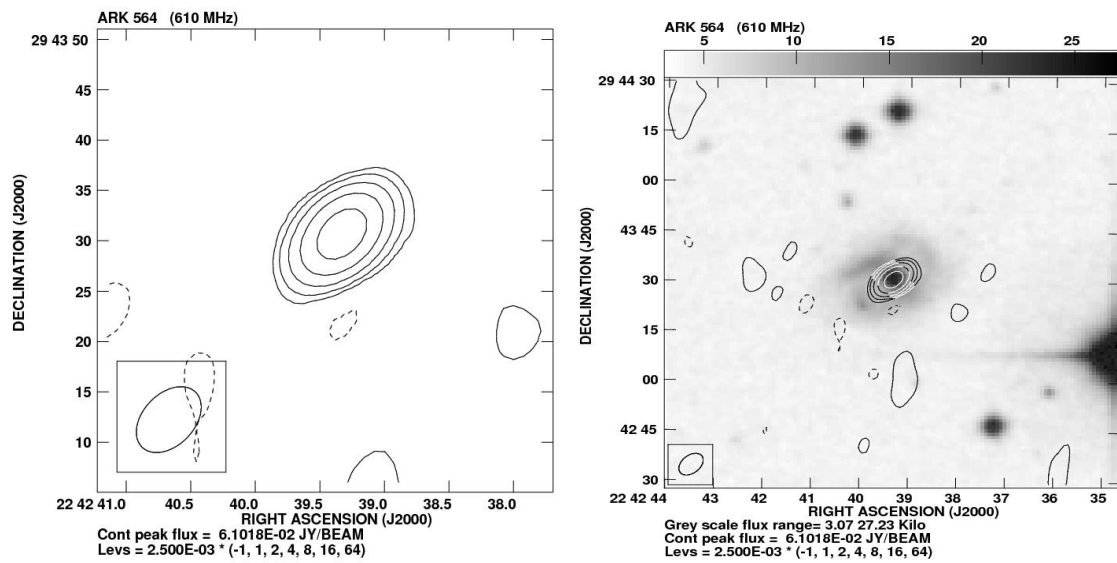
Figure 7.8: 610 MHz radio contour image of ARK 564 and radio contours overlaid on its DSS optical image.
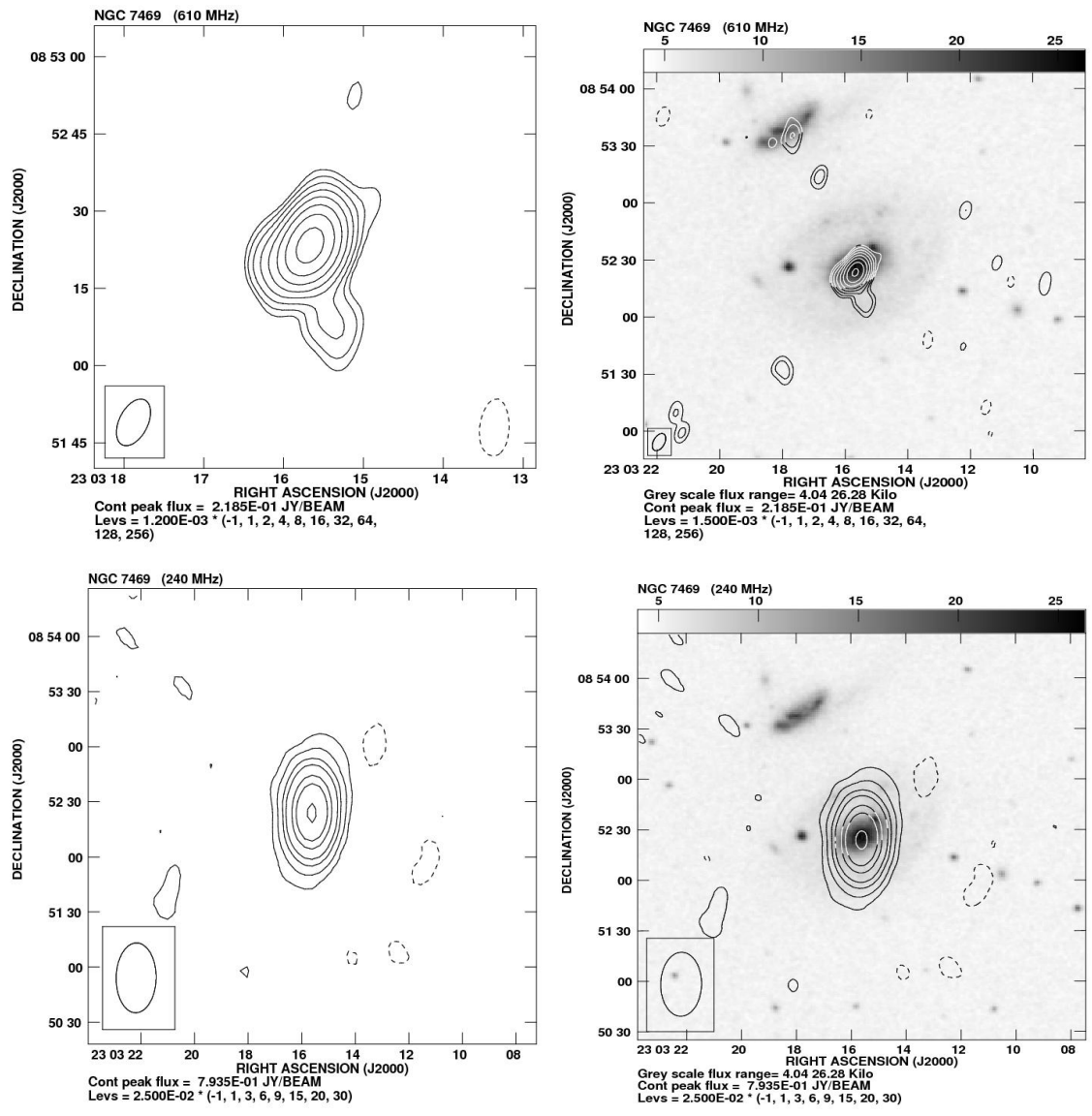
Figure 7.9: 610 MHz, 240 MHz radio contour images of NGC 7469 and radio contours overlaid on its DSS optical image.
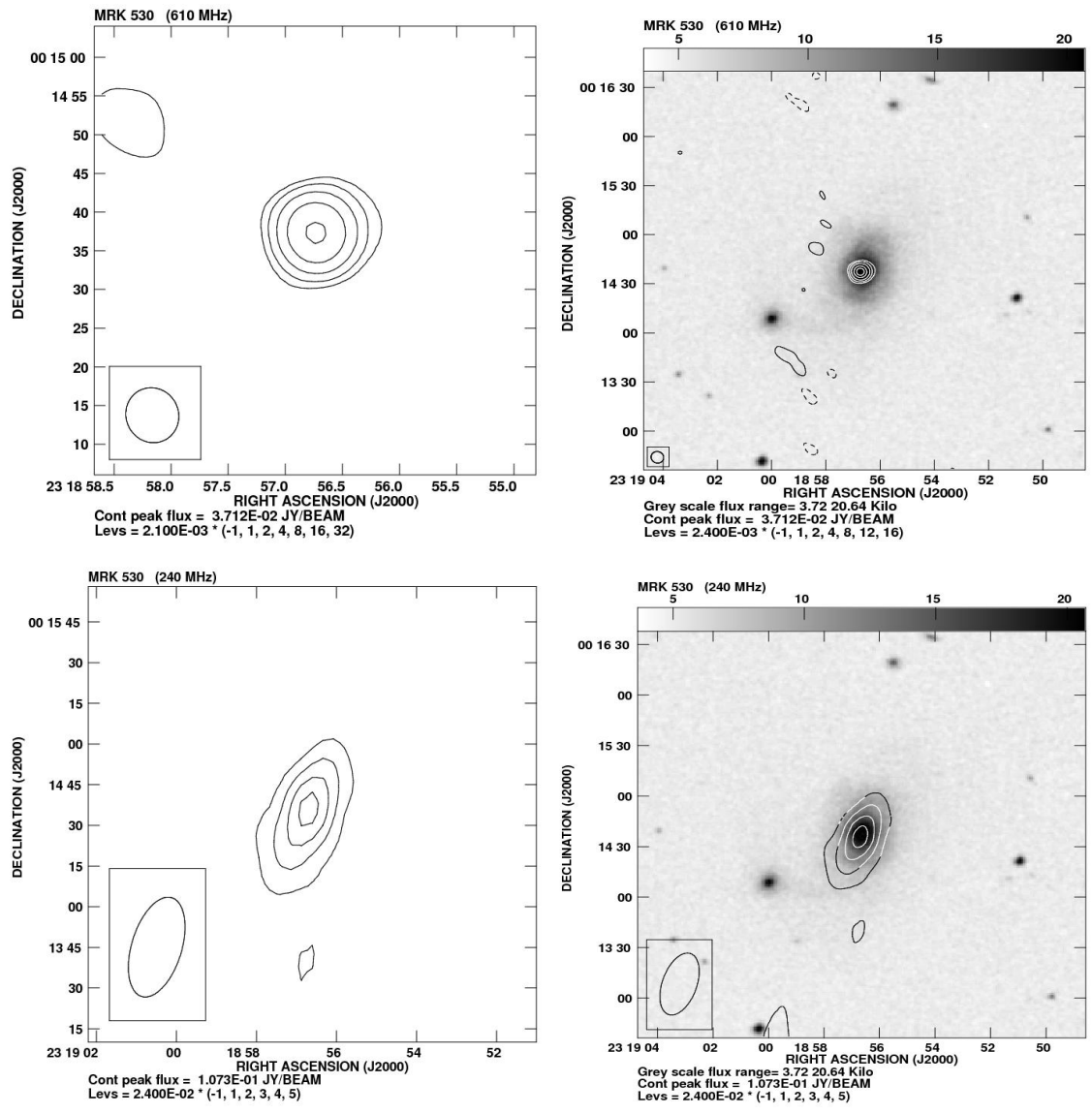
Figure 7.10: 610 MHz, 240 MHz radio contour images of MRK 530 and radio contours overlaid on its DSS optical image.
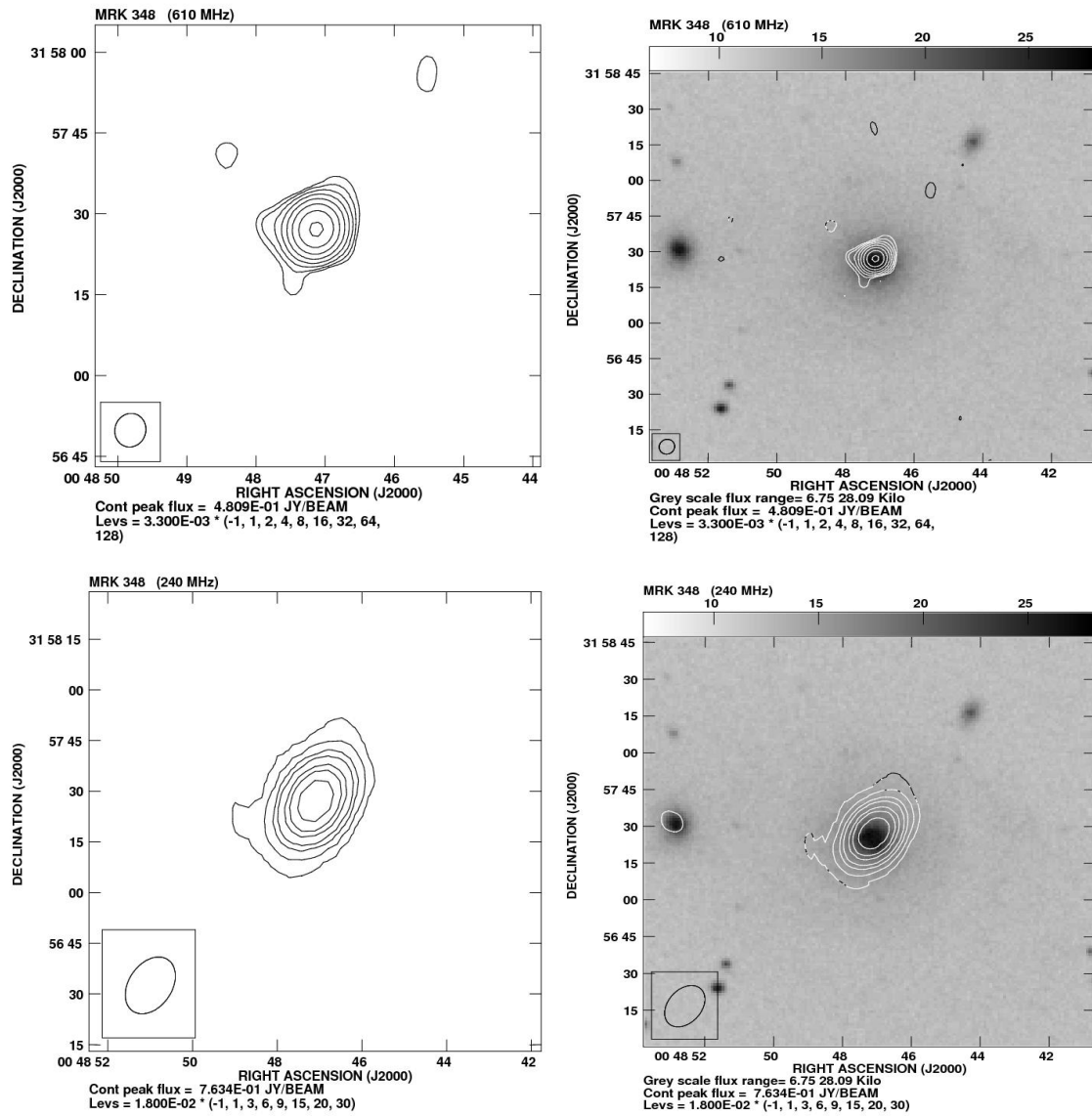
Figure 7.11: 610 MHz, 240 MHz radio contour images of MRK 348 and radio contours overlaid on its DSS optical image.
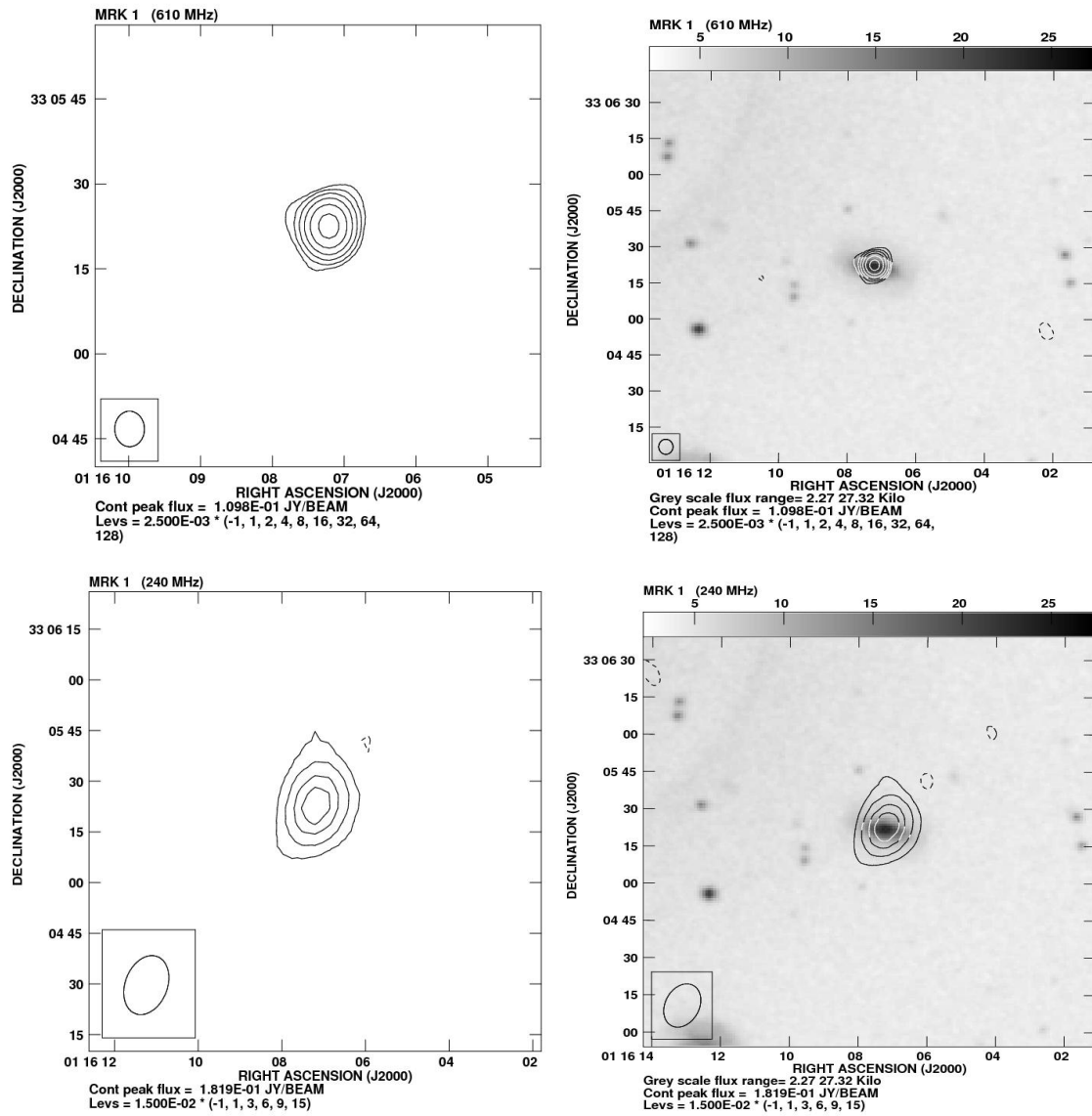
Figure 7.12: 610 MHz, 240 MHz radio contour images of MRK 1 and radio contours overlaid on its DSS optical image.
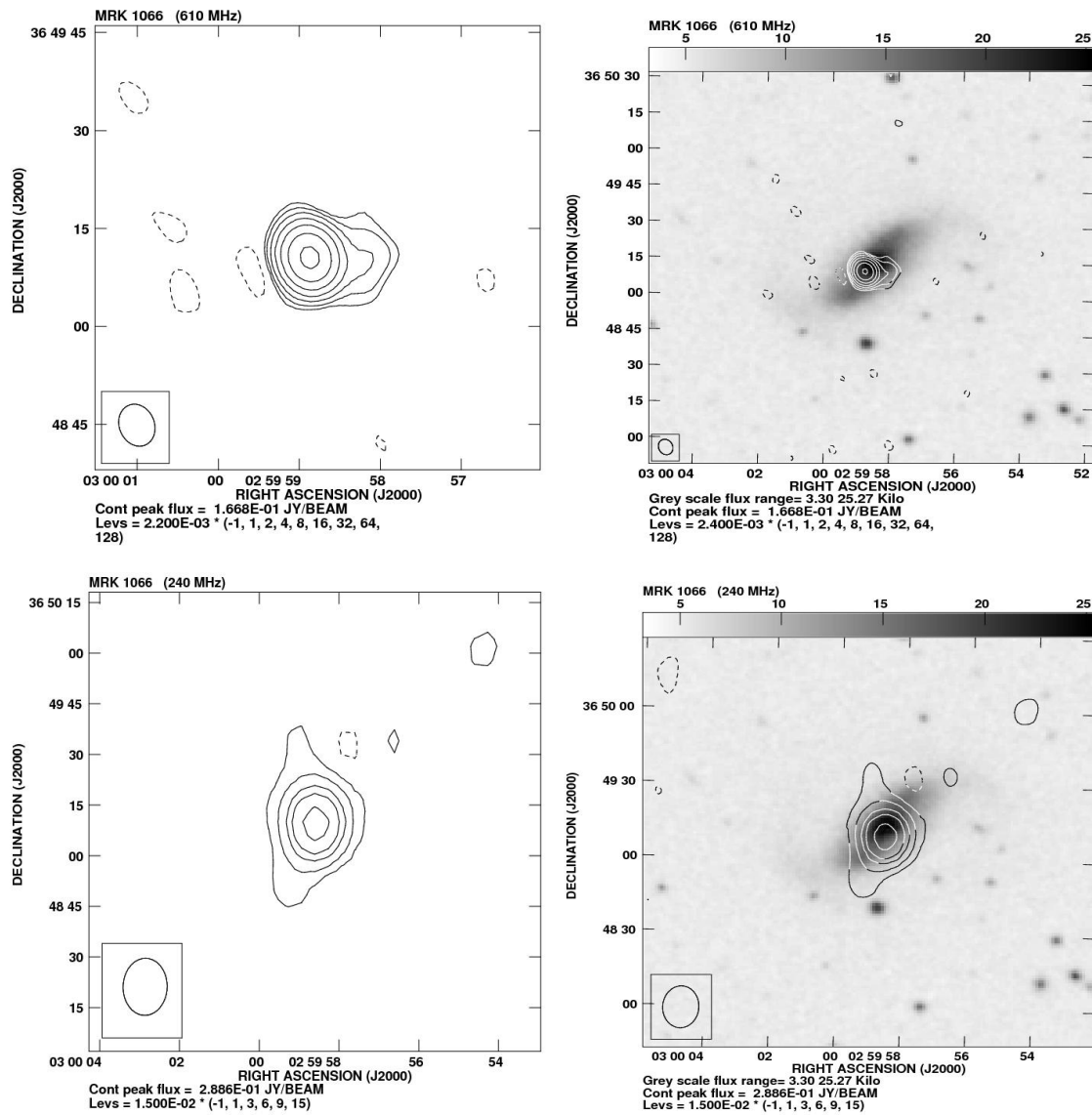
Figure 7.13: 610 MHz, 240 MHz radio contour images of MRK 1066 and radio contours overlaid on its DSS optical image.
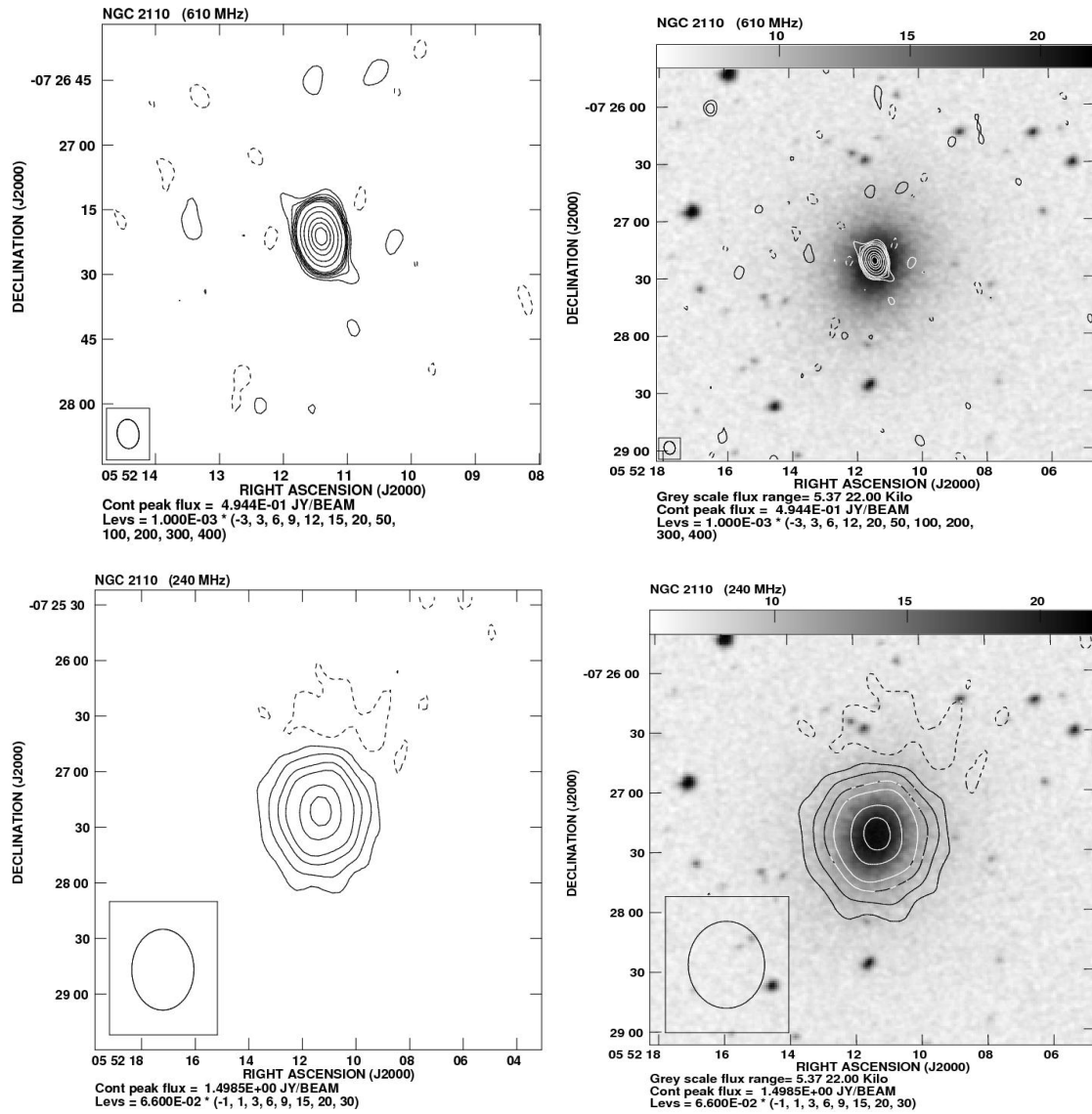
Figure 7.14: 610 MHz, 240 MHz radio contour images of NGC 2110 and radio contours overlaid on its DSS optical image.
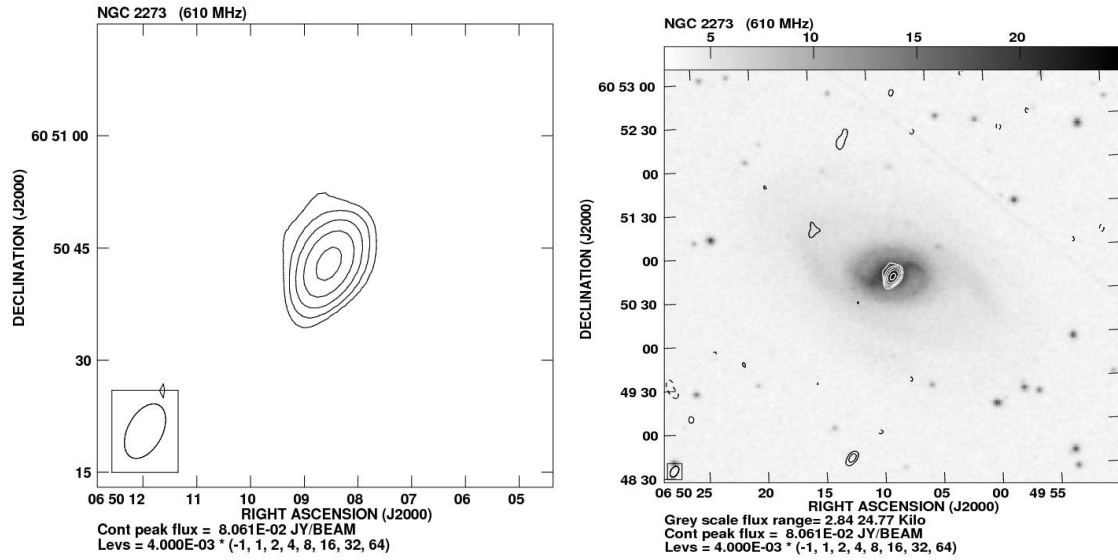
Figure 7.15: 610 MHz radio contour image of NGC 2273 and radio contours overlaid on its DSS optical image.
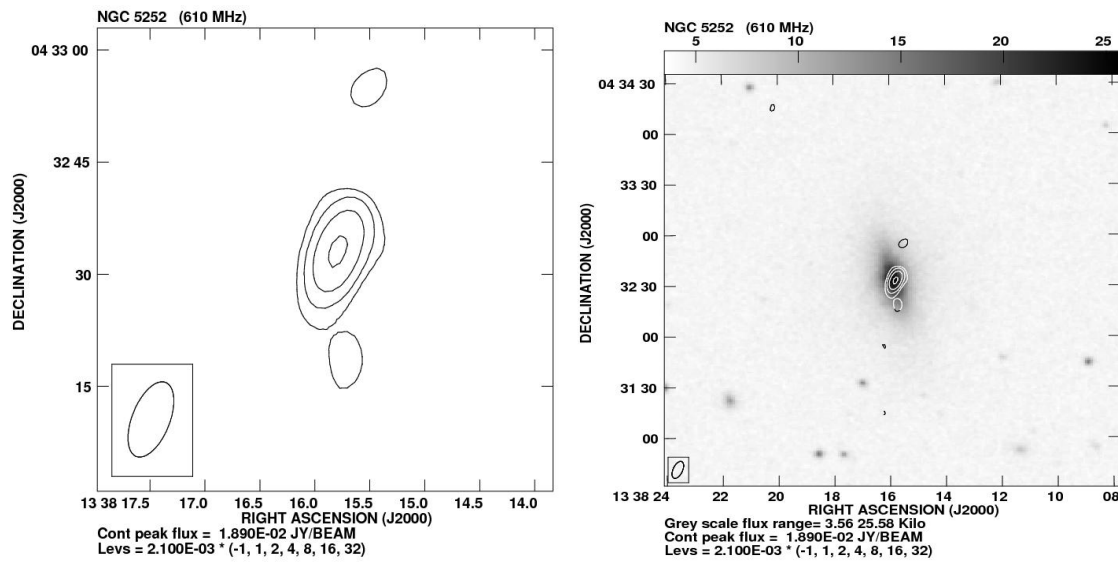
Figure 7.16: 610 MHz radio contour image of NGC 5252 and radio contours overlaid on its DSS optical image.
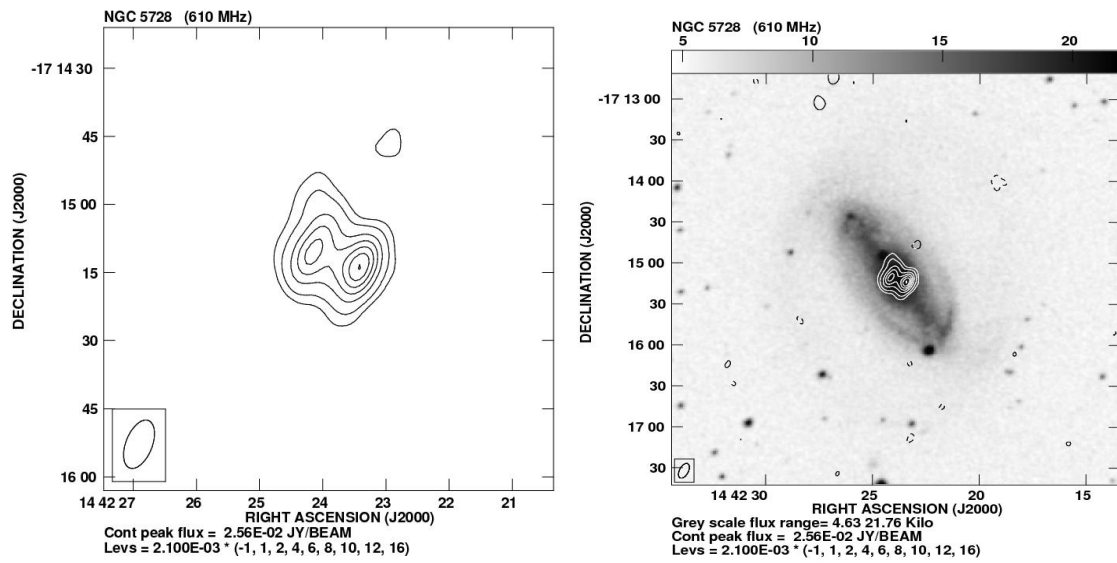
Figure 7.17: 610 MHz radio contour image of NGC 5728 and radio contours overlaid on its DSS optical image.
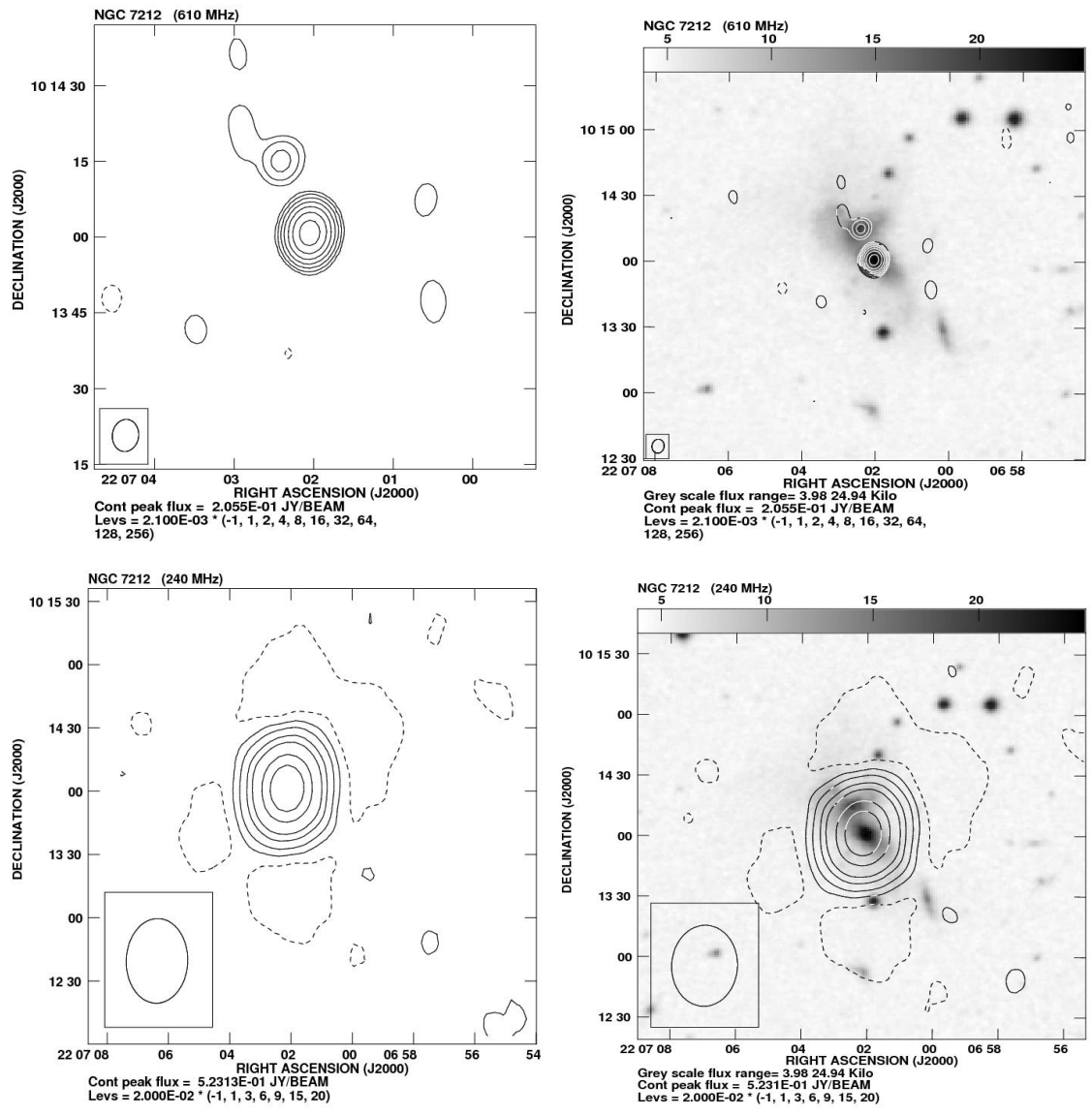
Figure 7.18: 610 MHz, 240 MHz radio contour images of NGC 7212 and radio contours overlaid on its DSS optical image.
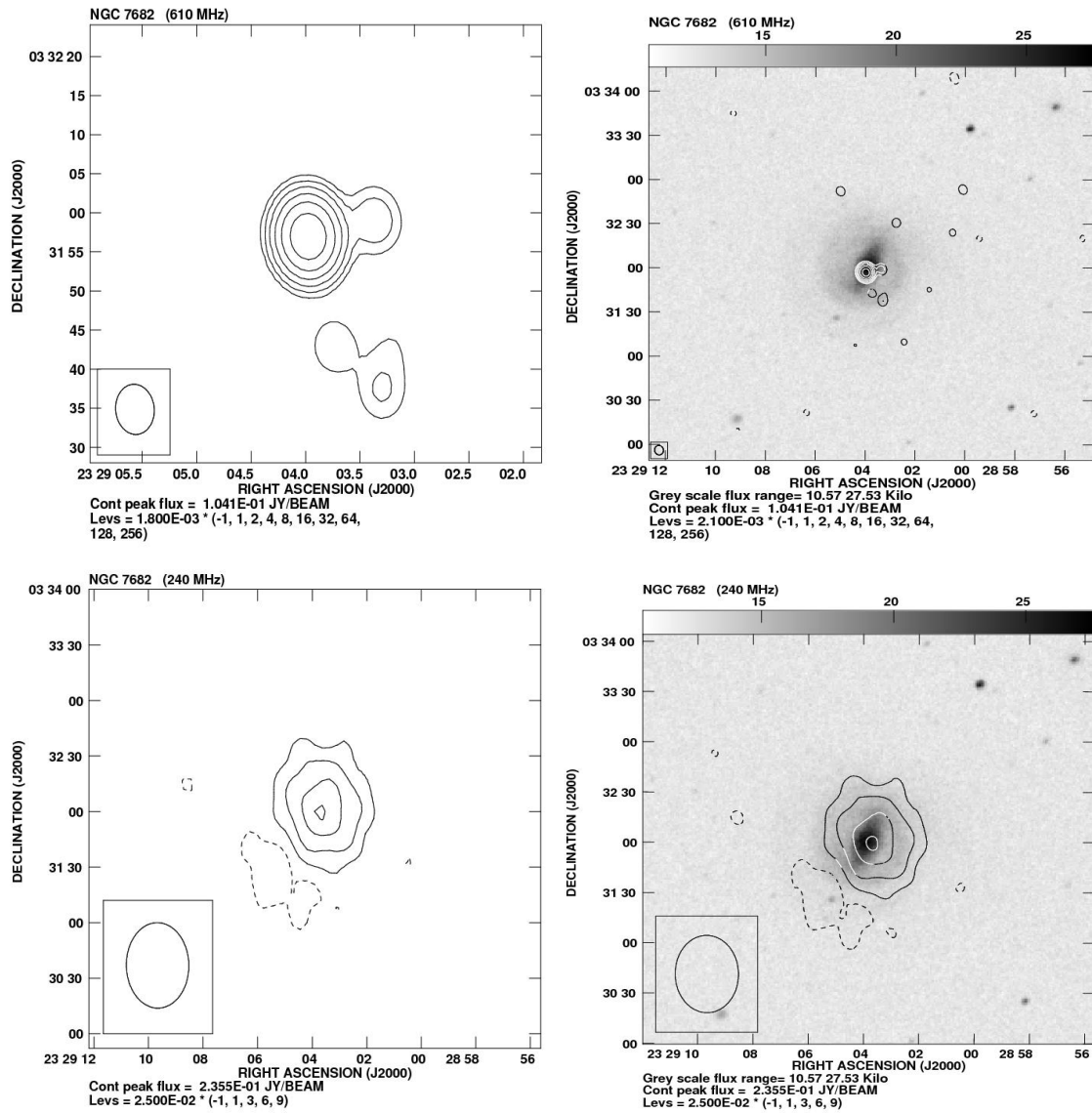
Figure 7.19: 610 MHz, 240 MHz radio contour images of NGC 7682 and radio contours overlaid on its DSS optical image.
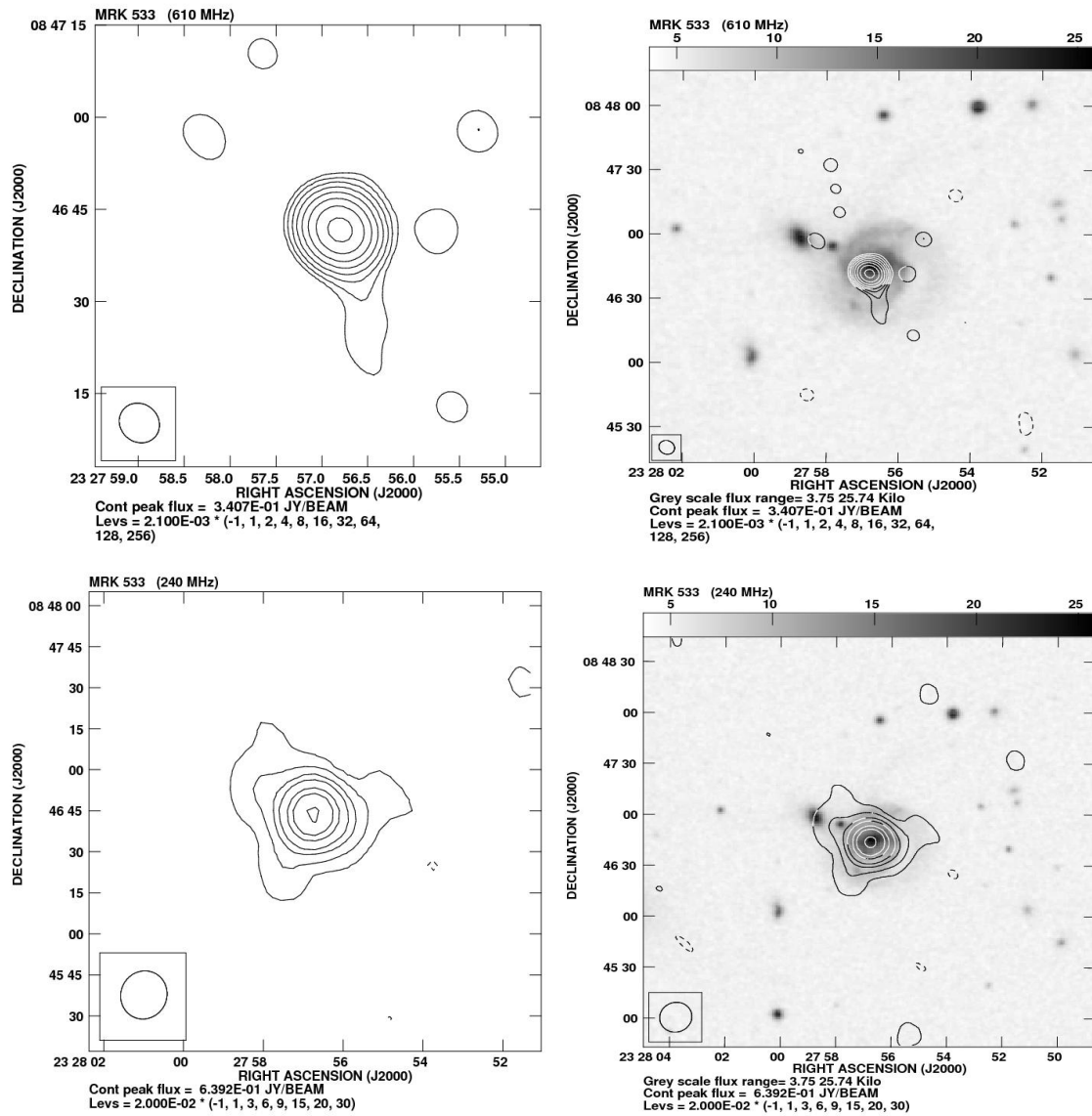
Figure 7.20: 610 MHz, 240 MHz radio contour images of MRK 533 and radio contours overlaid on its DSS optical image.

7.3 Radio emission in Seyfert galaxies

High resolution radio observations, which resolve out the low-surface-brightness extended radio emission, show that the most of Seyfert galaxies possess compact parsec-scale nuclear radio emission which can have multiple aligned components, linear or S-shaped features (*e.g.*, de Bruyn and Wilson (1976); Ulvestad and Wilson (1984); Roy *et al.* (1994); Thean *et al.* (2000); Lal, Shastri, and Gabuzda (2004)). In many Seyfert galaxies the compact core radio emission show elongated structures, similar to the radio jets seen in powerful radio galaxies. The general consensus is that the high-brightness-temperature radio emission arises from the low-power radio jets and outflows, analogous to the larger jets found in radio galaxies but perhaps distorted or stunted by the interaction with the surrounding interstellar medium (ISM) of the host spiral galaxy (Ulvestad, Wilson, and Sramek 1981; Booler, Pedlar, and Davies 1982; Neff and de Bruyn 1983; Pedlar, Unger, and Dyson 1985; Wilson and Ulvestad 1987; Gallimore *et al.* 1996, 1999; Whittle and Wilson 2004). The extended kiloparsec scales radio emission has also been detected in several Seyfert galaxies, however, this kpc-scale emission is, in general, not found to be aligned with the parsec-scale jets (Baum *et al.* 1993; Colbert *et al.* 1996; Gallimore *et al.* 2006) and the origin of it, is debated, *i.e.*, AGN-powered versus starburst-powered. Gallimore *et al.* (2006) reported that a large fraction of Seyfert galaxies exhibit extended radio emission having size of 1 kpc or larger and these do not match the morphology of the disk or its associated star-forming regions. Also the Seyfert galaxies with kpc-scale emission deviate significantly from the FIR-radio correlation for star-forming galaxies, with tendency toward radio excess, and are more likely to have a relatively luminous, compact radio source in the nucleus suggesting that the extended emission in Seyfert galaxies are powered by the AGN rather than starbursts. The kpc-scale extended radio emission plausibly originates from the jet plasma which has been decelerated by the interaction with the nuclear interstellar medium (ISM) and virtually most of the jet power is

lost to the ISM within the inner kiloparsec. The detailed discussions of large-scale radio emission in Seyfert galaxies can be found in Baum *et al.* (1993); Colbert *et al.* (1996); Gallimore *et al.* (2006).

The integrated radio spectral shape of Seyfert galaxies is determined by the combined contributions of all the radio emitting components. In low resolution radio observations, the radio emission from Seyfert galaxies can have contributions from four components, *i.e.*, a partially opaque synchrotron emission from a compact parsec-scale nuclear core, optically thin synchrotron emission from an extended component powered by AGN, optically thin synchrotron emission from star forming regions present in the host galaxy disk and a circumnuclear starburst emission (Wilson 1991). The optically thin synchrotron emission is characterized by straight, steep radio spectrum, while the component from compact core emission is characterized by a flat or inverted spectrum owing to self-absorbed synchrotron or free free emission (Antonucci and Barvainis 1988). The relative fraction of these emitting components may vary from one source to another and in turn, may change the spectral shape. Although total radio emission in Seyfert galaxies may have contributions from host galaxy disk and from starburst regions, the radio emission in most of the Seyfert galaxies is dominated by a compact (≤ 100 pc) nuclear radio emission characterized with high brightness temperature, steep spectrum and non-thermal emission (Kukula *et al.* 1998). The extended emission powered by AGN as well as star formation give rise the straight steep spectrum and therefore it is difficult to conclude whether emission is either powered by AGN or starburst using only spectral shape information. Some Seyfert galaxies also show flat or inverted spectra and in such cases total radio emission is likely to be dominated by the compact nuclear core which is partially opaque to synchrotron emission (Kukula *et al.* 1998). The compact nuclear radio emission characterized with high brightness temperature ($\sim 10^8$ K) and inverted spectrum seen in some of Seyfert galaxies is indicative of the synchrotron self-absorption close to the jet-emanating region (Mundell *et al.* 2000), however, the free-free absorption by thermal, ionized

gas in the vicinity of the nucleus might also be sufficient to flatten the intrinsically steeper synchrotron spectra (Ho and Ulvestad 2001).

7.4 Discussion: radio properties of Seyfert type 1s and 2s

In the following sections I discuss the comparison of radio powers, radio spectra, radio morphologies, radio - IR correlations and IR luminosities for the two Seyfert subtypes in the framework of the Seyfert unification scheme.

7.4.1 Radio powers of Seyfert type 1s and type 2s

The obscuring torus around AGN is optically thin to centimeter radio wavelengths and there is no relativistic beaming effect in Seyfert galaxies (Shastri, Lal, and Gabuzda 2003; Middelberg *et al.* 2004; Ulvestad *et al.* 2005). Therefore the measured radio power is independent to the orientation of the obscuring torus and radio jet axis. And, if unification scheme is valid, both subtypes of Seyfert galaxies are expected to show similar radio powers.

Some of the early studies (de Bruyn and Wilson 1978; Ulvestad and Wilson 1984) reported that Seyfert type 2s are more radio powerful than Seyfert type 1s at centimeter wavelengths, giving results inconsistent with the unification scheme. However, later studies (Ho and Ulvestad 2001) argued that the samples used in earlier studies were biased towards radio powerful Seyfert type 2s. High resolution 3.6 cm VLA observations showed that the two subtypes have similar radio powers in samples based on 12 μm (Thean *et al.* 2001) and 60 μm (Schmitt *et al.* 2001) luminosities. We compare the radio power distributions for the two Seyfert subtypes of our sample at 240 MHz, 610 MHz, 1.4 GHz and 5.0 GHz (*cf.*, Figure 7.21, Table 7.7) and find that the two Seyfert subtypes have similar radio power distributions with similar median values at the respective frequencies. The radio powers at 240

MHz, 610 MHz, 1.4 GHz and 5.0 GHz are in the range of $\sim 10^{28}$ - 10^{31} erg s^{-1} for both the Seyfert types. The two sample Kolmogorov-Smirnov statistical test shows that there is 99% probability that the P$_{610 \text{ MHz}}$ and P$_{1.4 \text{ GHz}}$ distributions of the two Seyfert subtypes are drawn from the same parent population. The probability that the distributions of the two Seyfert subtypes are drawn from the same parent population decreases in the case of P$_{240 \text{ MHz}}$ and P$_{5.0 \text{ GHz}}$ comparison, however, distributions span to similar range with similar median values.

7.4.2   Radio spectra of Seyfert type 1s and type 2s

The previous spectral studies of Seyfert samples are limited mainly to relatively high frequency (≥ 1.4 GHz) and we investigated the nature of Seyferts radio spectra at lower frequencies extending down to 240 MHz. Among the previous studies, Edelson (1987) measured three point (1.4 GHz, 5.0 GHz and 20 GHz) radio spectra of Seyfert galaxies and reported that Seyfert type 1s and 2s show steep ($\alpha \sim -0.7$, $S_\nu \propto \nu^\alpha$) radio spectra with type 1s occasionally tend to show flatter or inverted spectra, however, Rush, Malkan, and Edelson (1996) reported that there is no significant difference between the average 1.4 GHz - 5.0 GHz spectral indices of Seyfert type 1s and type 2s. Antonucci and Barvainis (1988) obtained three point (1.5 GHz, 4.9 GHz and 14.5 GHz) radio spectra of Seyfert galaxies as well as radio-quiet quasars and reported that in a large fraction of sources the two point 4.9 GHz - 14.5 GHz spectral index was flat relative to 1.5 GHz - 4.9 GHz spectral index. The possible flattening might be due to self-absorption of synchrotron emission or free-free emission from AGN or associated nuclear star formation. Barvainis, Lonsdale, and Antonucci (1996) studied four point (1.5 GHz, 4.9 GHz, 8.4 GHz and 14.9 GHz) radio spectra of a sample containing radio-quiet quasars and Seyfert galaxies and found that the radio shapes are quite heterogeneous and similar to radio-loud quasars.

We obtain four point (240 MHz, 610 MHz, 1.4 GHz, 5.0 GHz) integrated radio

spectra of our sample sources using 240 MHz, 610 MHz flux densities from our GMRT observations, 1.4 GHz flux densities from NVSS and 5.0 GHz flux densities from literature (mainly from Gallimore *et al.* (2006); Edelson (1987); Griffith *et al.* (1995)). Since GMRT observations at 240 MHz, 610 MHz and NVSS observations at 1.4 GHz are of low resolution, we considered 5 GHz flux density measured with low resolution observations, *e.g.*, VLA in 'D' configuration (Gallimore *et al.* 2006; Edelson 1987) or observations with single dish Green Bank, and Parkes radio telescopes (Griffith *et al.* 1995; Gregory and Condon 1991). For 7 (4 type 1s and 3 type 2s) of our sample sources, *i.e.*, NGC 3227, NGC 3516, MRK 279, ARK 564, NGC 2273, NGC 5252, NGC 5728, we did not get 240 MHz flux density due to the poor quality of data and therefore, do not have 240 MHz - 610 MHz two point spectral indices ($\alpha_{240\mathrm{MHz}}^{610\mathrm{MHz}}$) for these sources. Also, 5 GHz flux density measured with low resolution observations is unavailable for ARK 564 and NGC 5728 and thus there is no estimation of $\alpha_{1.4\mathrm{GHz}}^{5.0\mathrm{GHz}}$ for these two sources. Thus, we have four point (240 MHz, 610 MHz, 1.4 GHz, 5.0 GHz) integrated radio spectra for 13 (6 type 1s and 7 type 2s) sources, three point (610 MHz, 1.4 GHz, 5.0 GHz) integrated radio spectra for 5 (3 type 1s, 2 type 2s) sources, and two point spectra for 2 (1 type 1, 1 type 2) sources of our sample (*cf.*, Figure 5, Table 7).

We estimated and compared the integrated ($\alpha_{\mathrm{Int.}}$) and two point spectral indices ($\alpha_{240\mathrm{MHz}}^{610\mathrm{MHz}}$, $\alpha_{610\mathrm{MHz}}^{1.4\mathrm{GHz}}$ and $\alpha_{1.4\mathrm{GHz}}^{5.0\mathrm{GHz}}$) for the two Seyfert subtypes. Figure 7.21 shows the integrated radio spectra of our sample sources and we note that most of our sample sources show relatively steep power-law ($\alpha \sim -0.7$, $S_\nu \propto \nu^\alpha$) spectral energy distribution at the low frequency radio regime. We measured the integrated spectral index ($\alpha_{\mathrm{Int.}}$) by fitting the spectral points with a line of the least chi-square fit for the sources, whenever the flux densities are available for atleast three frequencies and seem to follow the single power-law SED (*i.e.*, power-law represented by a straight line in logarithmic scale). There are $\sim 16/20$ sources (8 type 1s and 8 type 2s) for which we could estimate the integrated spectral indices and find that the type 1s and type 2s have similar distributions of integrated spectral indices

with median values ~ 0.75 and ~ 0.72, respectively (*cf.*, Figure 7.23, Table 7.7). The distributions of the two point spectral indices α_{240MHz}^{610MHz}, $\alpha_{610MHz}^{1.4GHz}$ and $\alpha_{1.4GHz}^{5.0GHz}$ for the two subtypes of Seyfert galaxies of our sample are shown in Figure 7.23. While comparing the two point spectral indices of Seyfert type 1s and 2s, we have excluded the sources with inverted spectral indices, *e.g.*, NGC 3516, NGC 5728 in $\alpha_{610MHz}^{1.4GHz}$ distribution and MRK 348, NGC 5252 in $\alpha_{1.4GHz}^{5.0GHz}$ distribution. The positive values of the spectral indices (*i.e.*, inverted spectra) of these sources are considered outliers in the respective distributions and are excluded.

We compared the spectral indices $\alpha_{Int.}$, α_{240MHz}^{610MHz}, $\alpha_{610MHz}^{1.4GHz}$ and $\alpha_{1.4GHz}^{5.0GHz}$ for the two Seyfert subtypes (*cf.*, Figures 7.21, 7.23, Table 7.7) and find that the average spectral indices in the low-frequency radio regime are similar for the two subtypes. The average integrated spectral indices in 240 MHz - 5.0 GHz for Seyfert galaxies in our sample are fairly steep ($\alpha \sim -0.7$), consistent with previous studies (*e.g.*, Morganti *et al.* (1999)) and can be explained as optically thin synchrotron emission. Since the synthesized beam size is different at different frequencies (*e.g.*, $\sim 20''$ - $40''$ at 240 MHz, $\sim 8''$ - $10''$ at 610 MHz, $\sim 45''$ at 1.4 GHz (NVSS) and $\sim 20''$ or larger at 5 GHz), it may result an error in the estimated spectral index values. For example, the larger NVSS synthesized beam ($\sim 45''$) at 1.4 GHz compared to the GMRT synthesized beam ($\sim 8''$ - $10''$) at 610 MHz may result less steep spectrum than actual. We assume a conservative fiducial error values of 15% and 10% at 240 MHz and 610 MHz, respectively and 7% at 1.4 GHz and 5.0 GHz. The assumed errors in flux densities can result $\sim 8\%$, $\sim 5\%$ and $\sim 4\%$ errors in α_{240MHz}^{610MHz}, $\alpha_{610MHz}^{1.4GHz}$ and $\alpha_{1.4GHz}^{5.0GHz}$ respectively. Also, non-simultaneous observations may contribute to error in $\alpha_{610MHz}^{1.4GHz}$ and $\alpha_{1.4GHz}^{5.0GHz}$ estimates, if a source flux varies in between the two observations. However, the estimates of α_{240MHz}^{610MHz} is free from the error due to non-simultaneity since 240 MHz and 610 MHz flux densities are from simultaneous observations carried out with GMRT. In four point radio spectrum of MRK 348, the flux density at 5 GHz is considered as outlier and the integrated spectral index is being estimated using only other three spectral points. The unusual high flux

density at 5 GHz may be attributed to strong variability at 5 GHz as previous observations have shown that the core of MRK 348 is variable at 5 GHz on a scale of months (Neff and de Bruyn 1983; Ulvestad *et al.* 1999). However, it is worth noting that except few peculiar Seyfert galaxies (Neff and de Bruyn 1983; Wrobel 2000; Falcke *et al.* 2000), most of the Seyfert galaxies show little radio variability over the period of few years (Edelson 1987; Mundell *et al.* 2009) and therefore our statistical results are not expected to be affected much by variability.

7.4.3 Radio morphologies of Seyfert type 1s and type 2s

We carried out GMRT observations at 610 MHz and 240 MHz for our sample Seyferts with the primary aim to study the radio spectra at low frequency, however, we also attempt to study the low frequency radio morphologies of our sample Seyfert galaxies. The radio contours maps at 610 MHz (20/20 sample sources), 240 MHz (13/20 sample sources) and radio contours overlaid on optical DSS images for our sample sources are shown in Figures 7.1 to 7.20. In all the radio maps first lowest contour is $\sim 3\sigma$ of the rms of the noise value of the map. Table 7.2 and 7.4 list the image parameters of all the radio maps at 610 MHz and 240 MHz, respectively. In our radio maps typical noise rms and resolution at 610 MHz is ~ 0.8 mJy/beam and $\sim 8''$ - $10''$, respectively, while at 240 MHz the rms is ~ 8.0 mJy/beam and resolution is $\sim 18''$ - $40''$. The radio emission in most of our sample sources is dominated by a central component and in order to estimate the size we fitted the radio emission with an elliptical Gaussian using AIPS task 'JMFIT'. Table 7.3 and 7.5 list the fitted parameters for all the sample sources at 610 MHz and 240 MHz, respectively. The fitted parameters include peak flux density (S_{peak}), integrated flux density ($S_{Int.}$), major axis, minor axis and position angle of the fitted Gaussian and the deconvolved source size. For our results we have used the flux densities obtained from AIPS task 'TVSTAT' than 'JMFIT' since there is a possibility that Gaussian fitted by 'JMFIT' may leave out some extended emission. However,

we find that the flux densities obtained from 'TVSTAT' and 'JMFIT' are similar within the errors. The radio emission at 610 MHz is fitted with a single Gaussian in all of our sample sources except in NGC 4151 and NGC 5728. In NGC 4151 and NGC 5728, the 610 MHz radio emission has two distinct components which are fitted with two elliptical Gaussian components. At 610 MHz, several of our sample sources, *i.e.*, MRK 6, NGC 4151, NGC 7469, MRK 348, MRK 1066 and NGC 5728 have fitted Gaussian size larger than the synthesized beam which suggest the extended nearly kpc-scale emission around the AGN. Indeed, some of our sample sources, *e.g.*, NGC 4151, MRK 766, MRK 348, NGC 5548, NGC 7469 are reported to show kpc-scale extended emission at 5 GHz (Gallimore *et al.* 2006). At 240 MHz, due to rather large synthesized beam and high rms, all of our sample sources are seen as nearly a point source and are fitted with an elliptical Gaussian which has the size similar to the synthesized beam. The radio structure at 240 MHz is mainly dominated by the synthesized beam shape itself. Since the primary aim of our work is to study the radio spectra of two Seyfert subtypes, we observed our sample sources with GMRT at 610/240 MHz in snapshot mode and therefore our radio images are not very deep and are likely to miss very faint extended emission. Indeed, more sensitive radio imaging is required in order to see the faint low-surface-brightness emission and to understand their origin, *i.e.*, AGN versus starburst.

Early studies suggested that Seyfert 2 galaxies are larger in radio than type 1s (*e.g.*, Ulvestad and Wilson (1984)), however, after controlling for the strengths of the radio sources Ulvestad and Wilson (1989) found that the differences in radio sizes of two types are not statistically significant. If unification scheme holds true, Seyfert type 1s are expected to show smaller radio source sizes than 2s, since Seyfert type 1s have nearly face-on tori and their radio jets would be expected to lie along the line of sight to the observer, and hence to be foreshortened. Indeed, Schmitt *et al.* (2001) reported this effect using a sample of Seyfert galaxies selected at 60 μm, while, Ulvestad and Ho (2001) reported that type 1s appears to be larger than

type 2s, which is against the unification scheme. Contradictory results by Ulvestad and Ho (2001) may arise due to the fact that Ulvestad and Ho (2001) observations had larger beam size and therefore sensitive to low-surface-brightness emission that may not necessarily be jet-related. We could not make any definite conclusions about the comparison of radio sizes of the two Seyfert subtypes in our sample, since several of our sources are marginally resolved at 610 MHz and unresolved at 240 MHz due to rather large synthesized beam. Also at low-frequency disk or starburst emission may have significant contribution and emission may not be solely AGN jet-related. Furthermore, it may be that the weaker radio emitting features may have definite morphology, but are so weak that the extended emission has not been detected in our snapshot observations.
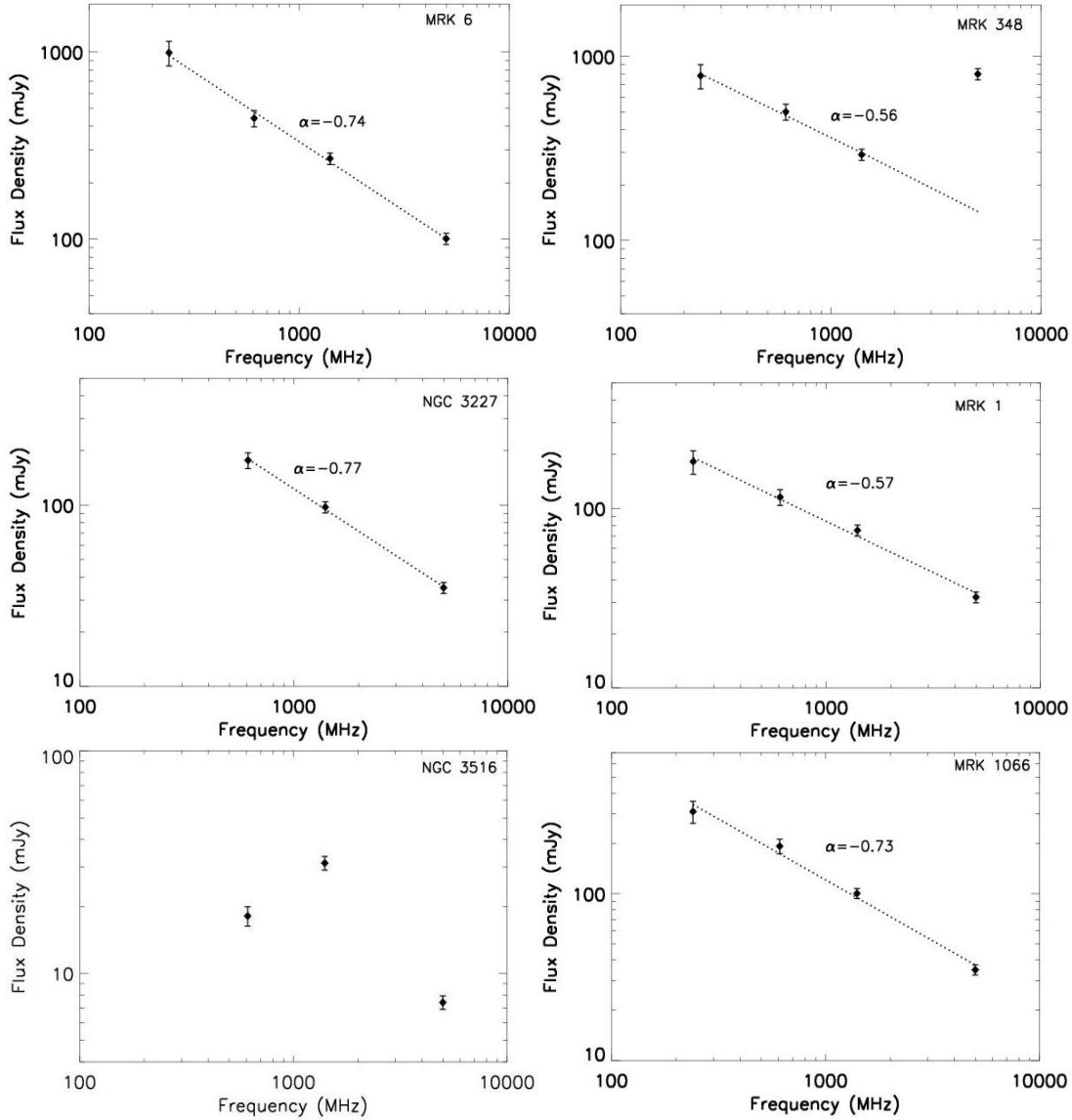
Figure 7.21: Four point (240 MHz, 610 MHz, 1.4 GHz and 5.0 GHz) radio spectra of Seyfert galaxies of our sample. The dotted line shows the least chi-square line fit to the spectral points for the sources wherein atleast three spectral points follow $S_\nu \propto \nu^\alpha$ with similar index. Seyfert type 1s and type 2s are shown in left and right panel, respectively.

Figure 7.21: *-continued*

168
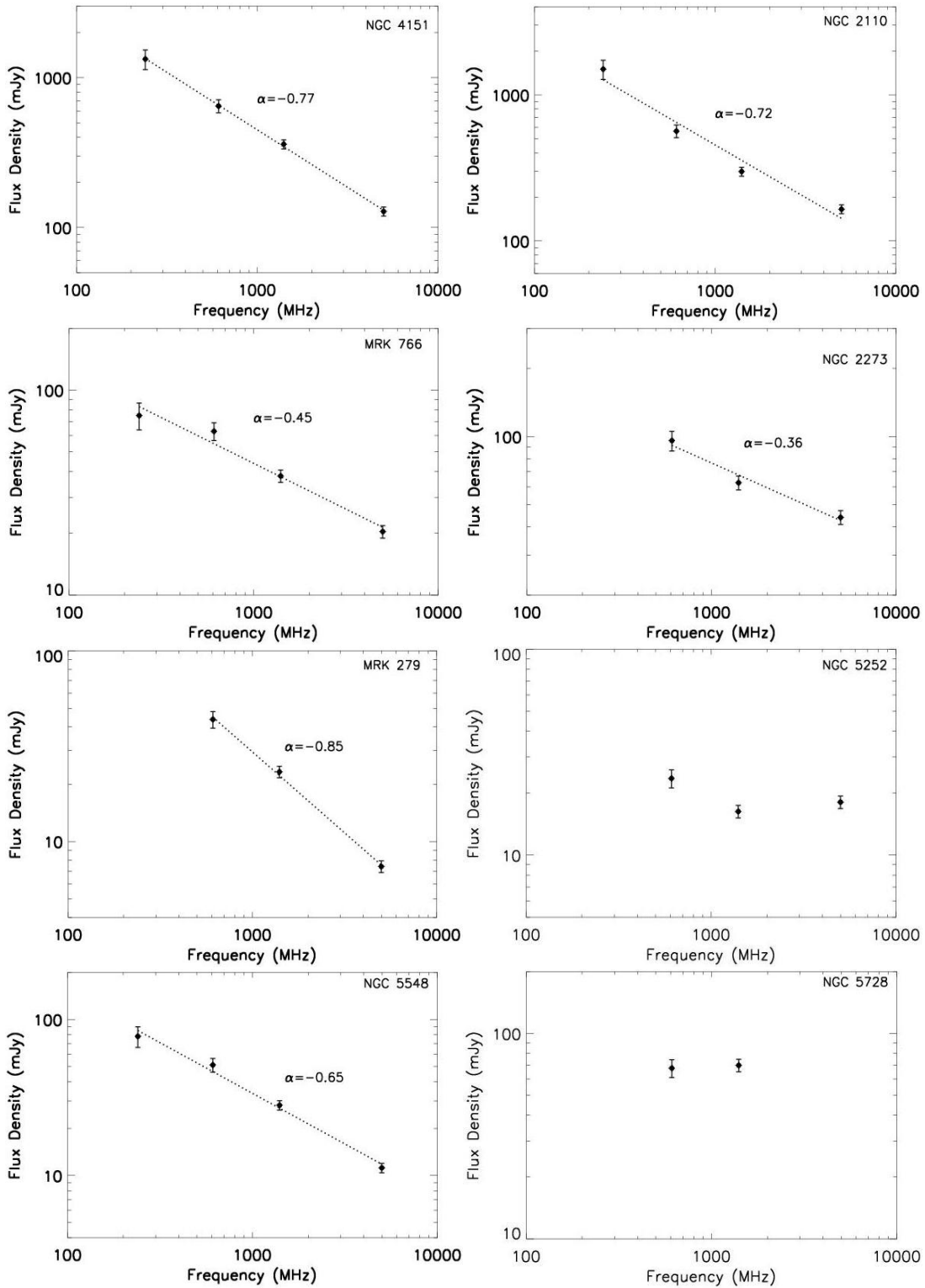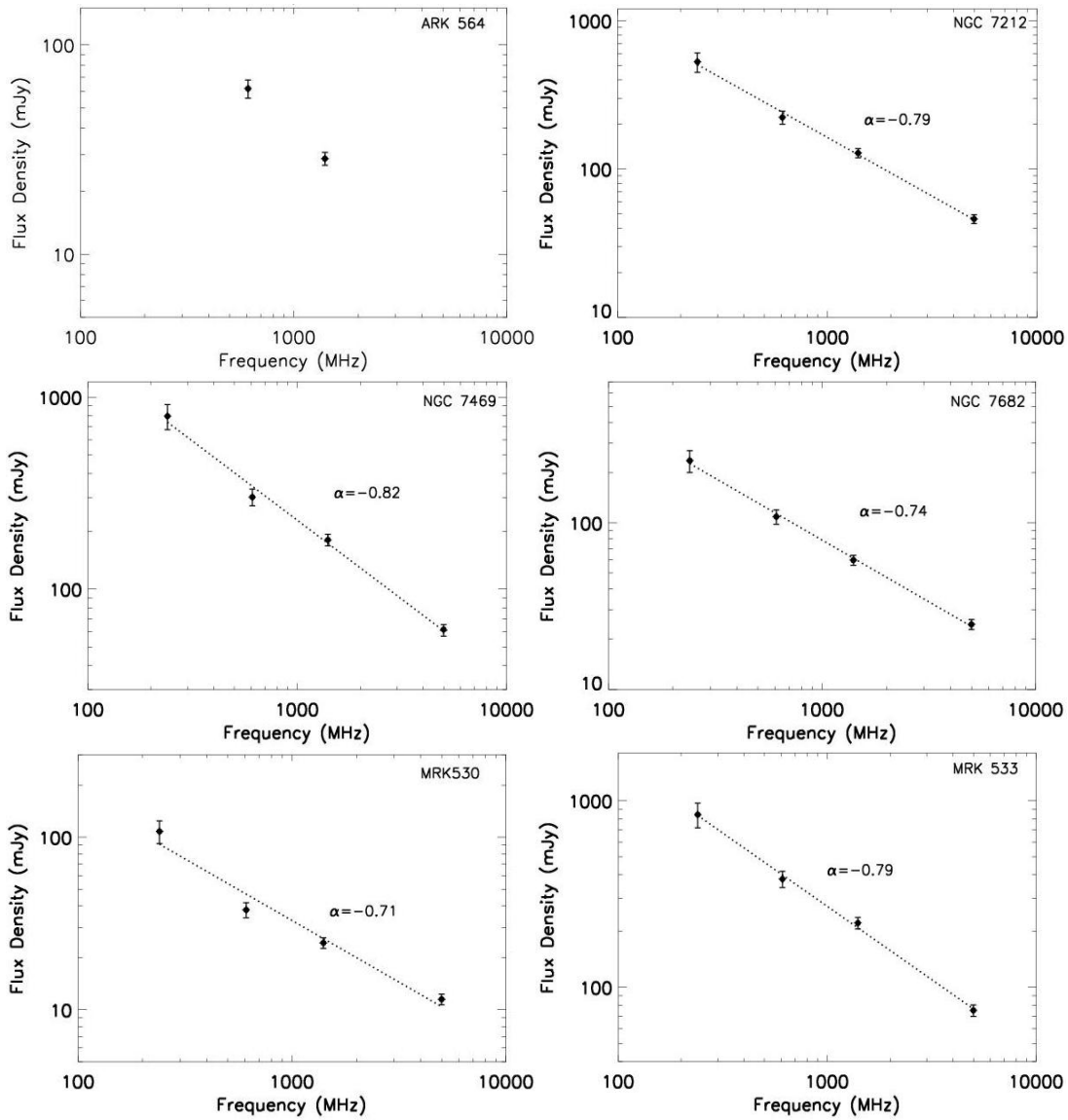
Figure 7.21: *- continued*
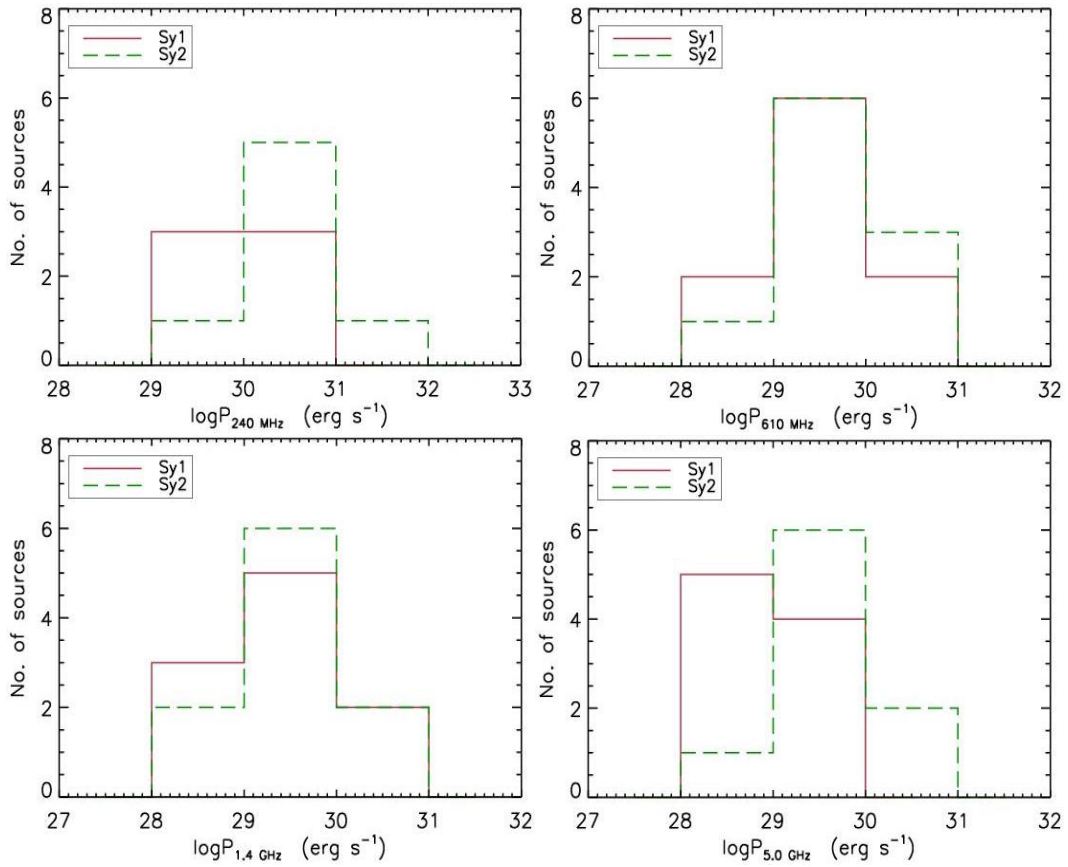
Figure 7.22: Histograms of radio powers at 240 MHz, 610 MHz, 1.4 GHz and 5.0 GHz for the two subtypes of our sample Seyfert galaxies.
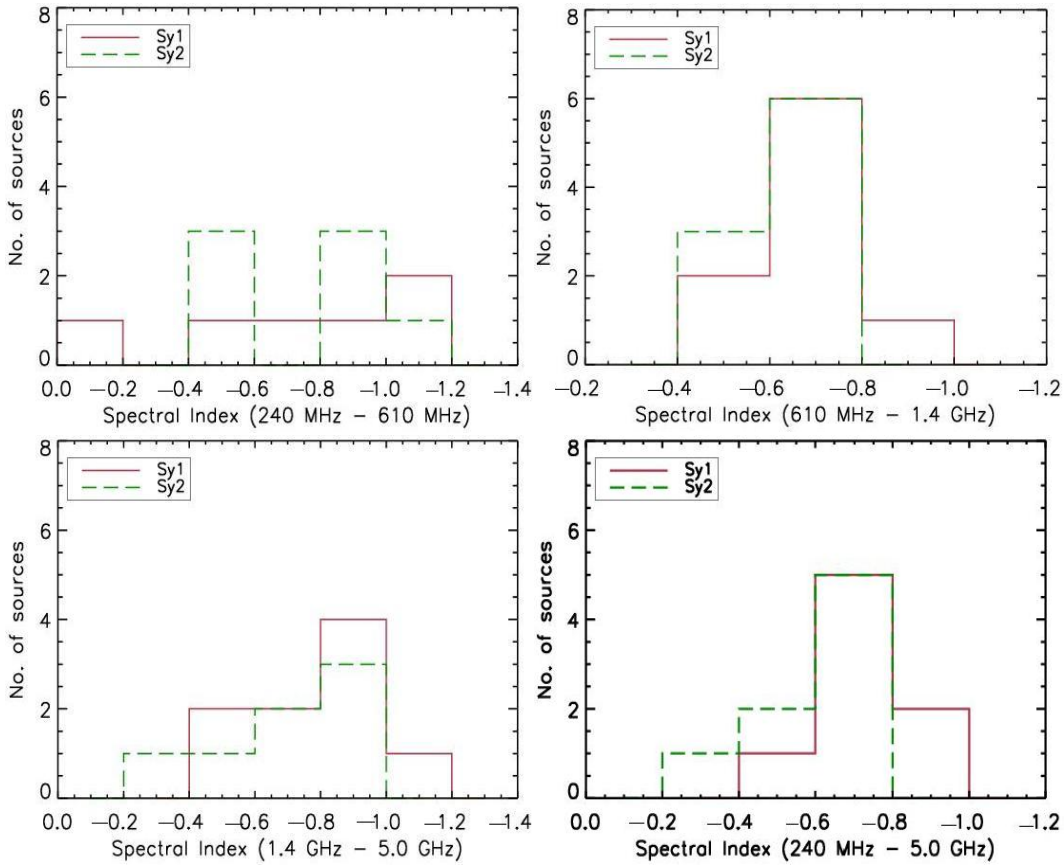
Figure 7.23: Histograms of spectral indices $\alpha_{240\text{MHz}}^{610\text{MHz}}$, $\alpha_{610\text{MHz}}^{1.4\text{GHz}}$, $\alpha_{1.4\text{GHz}}^{5.0\text{GHz}}$, and integrated spectral index $\alpha_{\text{Int.}}$ for the two subtypes of our sample Seyfert galaxies. Spectral index distributions does not include spectral indices of NGC 3516 (type 1) and NGC 5728 (type 2), which are showing inverted and flat two-point spectra, respectively, and are considered as outliers.

7.4.4 Radio and IR correlation

The normal spiral galaxies are reported to exhibit a strong correlation between the radio and infrared (IR) emission (Wunderlich, Wielebinski, and Klein 1987; Sopp and Alexander 1991) that is thought to be a signature of star formation activity. Seyfert galaxies are also reported to show a radio - IR correlation with greater scatter than normal spirals and Seyferts tend to exhibit radio excess than normal spirals with the same IR emission (Sanders and Mirabel 1985; Norris, Allen, and Roche 1988; Wilson 1988; Baum *et al.* 1993; Rush, Malkan, and Edelson 1996). It has been suggested that the radio excess that often disturbs the radio - IR correlation in Seyfert galaxies possibly due to the dominant contribution from AGN core (Sanders and Mirabel 1985; Wilson 1988; Baum *et al.* 1993). Moreover, the radio emission in Seyfert galaxies is likely to have contributions from both the AGN core as well as from the host galaxy disk (Wilson 1988). The IR emission in Seyfert galaxies is believed to be mostly thermal emission from the dust present in the torus that is heated by the optical, ultraviolet (UV) photons from AGN continuum, however, in several Seyferts the far-IR emission may have substantial contribution from star formation activities (Rodriguez Espinosa, Rudy, and Jones 1987). Therefore, one may expect change in the radio - IR correlation for Seyferts depending upon whether and how much nuclear emission is being included. In other words, the deviation of radio - IR correlation in Seyfert galaxies from that of the normal spiral galaxies may depend upon the radio morphologies of Seyfert galaxies. Indeed, Baum *et al.* (1993) found that Seyferts return to the normal galaxies correlation after subtracting radio emission from the central kpc region. Also, there are suggestions that the Seyferts which harbor compact radio cores depart dramatically from the normal galaxies radio - IR correlation in comparison to the Seyferts which lack compact radio cores. Roy *et al.* (1998) reported that the Seyfert galaxies which lack compact radio cores display the radio - IR correlation similar to normal spirals, although with a little more scatter than for normal spirals.

Therefore the study of the radio - IR correlation for Seyfert galaxies may provide a useful diagnostic for investigating the properties of radio and IR emission. Here we investigate the radio - IR correlations for the Seyfert type 1s and type 2s in the framework of the unification scheme.

We study the radio - IR correlations in the Seyfert galaxies of our sample using GMRT radio observations at 610 MHz and 240 MHz and IR measurements from the IRAS Point Source Catalog[2]. The low resolution and low frequency GMRT radio observations at 610 MHz and 240 MHz are likely to account for the sum of the emission from the AGN and the host galaxy disk. Also, IRAS measurements are of low resolution and therefore include both the AGN as well as the host galaxy disk emission. IR flux densities at 12 μm, 25 μm, 60 μm and 100 μm are available from the IRAS Point Source Catalog for 18 (9 type 1s and 9 type 2s) out of 20 Seyfert galaxies of our sample and for NGC 4151, the IRAS measurements are taken from Sanders *et al.* (2003). There are no IRAS measurements available for NGC 5252 and thus in total we have IRAS measurements for 19/20 Seyfert galaxies of our sample (*cf.*, Table 7.7).

Figure 7.24 shows the IR - radio correlation plots for 12 μm, 25 μm, 60 μm and 100 μm luminosities each against the 610 MHz luminosity. Figure 7.25 shows the IR - radio correlation plots for 12 μm, 25 μm, 60 μm and 100 μm luminosities each against the 240 MHz radio luminosity. Tables 7.9 and 7.10 list the Spearman rank correlation coefficients and p-values of the IR - radio correlations for the two Seyfert subtypes as well as for the Seyfert type 1s and type 2s taken together. We find that in our sample both of the two subtypes show a general trend of increasing radio luminosity at 610 MHz and 240 MHz with the increase in IR luminosity at each of the four IRAS bands. The radio luminosities at 610 MHz and 240 MHz appear to be moderately correlated with IR luminosities at 12 μm, 25 μm, 60 μm and 100 μm. The 12 μm and 25 μm luminosities are better correlated to radio

---

[2]http://heasarc.gsfc.nasa.gov/W3Browse/iras/iraspsc.html

luminosities than 60 μm and 100 μm luminosities possibly because most of the near-IR as well as mid-IR emission is thought to be due to thermally radiating dusty torus heated by AGN continuum, while 60 μm and 100 μm flux emission are likely to have larger contribution from star forming region present in the host galaxy disk. The large scatter present in the (100 μm) FIR - radio correlation plots indicates the possible different and uncorrelated origin of the FIR and (610 MHz, 240 MHz) radio emission. Moreover, we do not rule out the possibility of change in the correlation strength with a larger sample, particularly at 240 MHz where the number of sources are quite low. We find that the two Seyfert subtypes follow substantially similar radio - IR correlations which is consistent with the unification scheme.
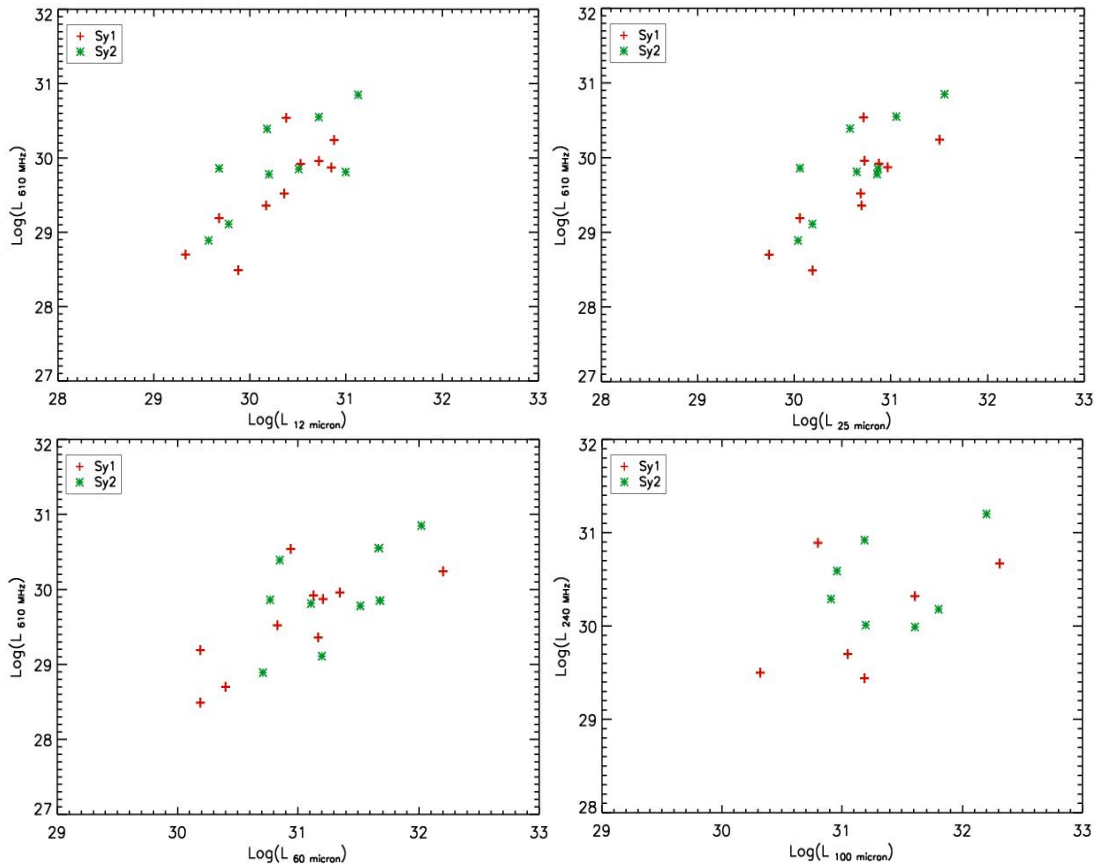
Figure 7.24: 12 μm, 25 μm, 60 μm and 100 μm luminosities each versus 610 MHz luminosities for the two Seyfert subtypes of our sample.

Table 7.7: IRAS fluxes and luminosities at 12 μm, 25 μm, 60 μm and 100 μm of our sample sources

Source name	$F_{12\ \mu m}$ (Jy)	$logL_{12\ \mu m}$ (erg s^{-1})	$F_{25\ \mu m}$ (Jy)	$logL_{25\ \mu m}$ (erg s^{-1})	$F_{60\ \mu m}$ (Jy)	$logL_{60\ \mu m}$ (erg s^{-1})	$logF_{100\ \mu m}$ (Jy)	$logL_{100\ \mu m}$ (erg s^{-1})	q
				Seyfert type 1s					
MRK 6	0.31	30.38	0.68	30.72	1.12	30.94	0.82	30.80	0.66
NGC 3227	0.67	29.33	1.74	29.74	7.89	30.40	17.46	30.74	2.12
NGC 3516	0.45	29.88	0.92	30.19	1.74	30.19	2.17	30.56	1.85
NGC 4151	2.01	29.68	4.87	30.06	6.46	30.19	8.89	30.32	1.38
MRK 766	0.41	30.17	1.38	30.70	4.06	31.17	4.25	31.19	2.11
MRK 279	0.25	30.72	0.26	30.73	1.08	31.35	2.28	31.67	1.87
NGC 5548	0.36	30.36	0.76	30.69	1.04	30.83	1.73	31.05	1.72
ARK 564	0.25	30.53	0.57	30.88	1.00	31.13	1.04	31.15	1.63
NGC 7469	1.30	30.88	5.48	31.50	26.95	32.20	35.22	32.31	2.29
MRK 530	0.36	30.85	0.48	30.97	0.83	31.21	2.12	31.61	1.77
				Seyfert type 2s					
MRK 348	0.31	30.18	0.77	30.58	1.44	30.85	1.83	30.96	0.80
MRK 1	1.79	31.00	0.80	30.65	2.30	31.11	2.85	31.20	1.59
MRK 1066	0.50	30.20	2.31	30.86	10.45	31.52	13.10	31.61	2.13
NGC 2110	0.37	29.68	0.88	30.06	4.46	30.77	6.26	30.91	1.20
NGC 2273	0.46	29.57	1.36	30.04	6.33	30.71	10.27	30.92	2.15
NGC 5252	....	....	....	....	....	....	....	....	....
NGC 5728	0.32	29.78	0.81	30.19	8.40	31.20	15.17	31.46	2.25
NGC 7212	0.34	30.72	0.73	31.06	2.98	31.67	5.16	31.19	1.53
NGC 7682	0.50	30.51	1.15	30.87	7.41	31.68	9.86	31.80	2.21
MRK 533	0.72	31.13	1.92	31.55	5.57	32.02	8.48	32.20	1.54
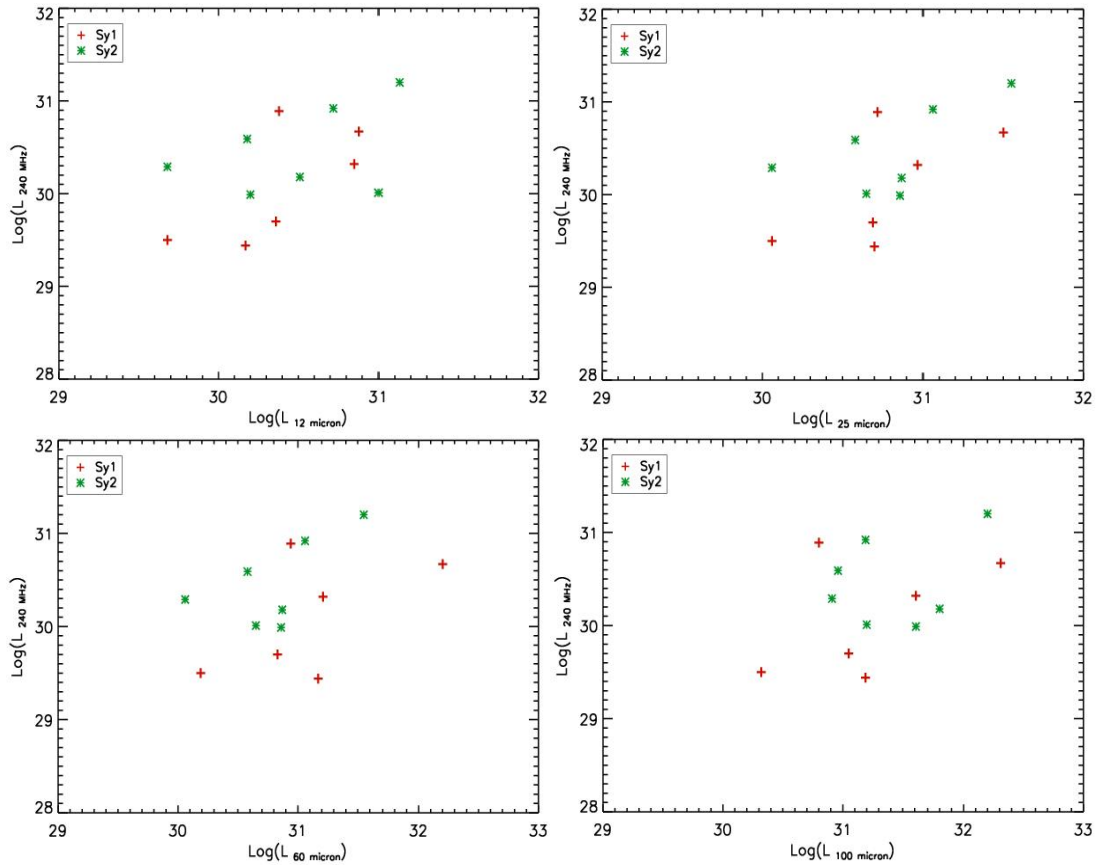
Figure 7.25: 12 μm, 25 μm, 60 μm and 100 μm luminosities each versus 240 MHz luminosities for the two Seyfert subtypes of our sample.

Table 7.8: Medians and Kolmogorov - Smirnov two sample statistical tests for the comparison of radio powers, spectral indices and IR luminosities of Seyfert type 1s and 2s of our sample

Distribution	Median		D	p-value
	Type 1	Type 2		
$\log P_{240\ \mathrm{MHz}}$	30.0	30.3	0.43	0.58
$\log P_{610\ \mathrm{MHz}}$	29.6	29.9	0.20	0.99
$\log P_{1.4\ \mathrm{GHz}}$	29.4	29.5	0.20	0.99
$\log P_{5.0\ \mathrm{GHz}}$	28.9	29.3	0.44	0.35
$\alpha_{240\mathrm{MHz}}^{610\mathrm{MHz}}$	0.81	0.83	0.29	0.96
$\alpha_{610\mathrm{MHz}}^{1.4\mathrm{GHz}}$	0.62	0.65	0.56	0.12
$\alpha_{1.4\mathrm{GHz}}^{5.0\mathrm{GHz}}$	0.80	0.67	0.44	0.34
$\alpha_{\mathrm{Int.}}$	0.75	0.72	0.36	0.63
$\log L_{12\ \mu\mathrm{m}}$	30.37	30.20	0.20	0.98
$\log L_{25\ \mu\mathrm{m}}$	30.71	30.65	0.30	0.76
$\log L_{60\ \mu\mathrm{m}}$	31.04	31.20	0.30	0.76
$\log L_{100\ \mu\mathrm{m}}$	31.10	31.20	0.40	0.40
q	1.81	1.59	0.40	0.40

Notes: Kolmogorov - Smirnov two sample test examines the hypothesis that two samples comes from same distribution. D = Sup x |S1(x) - S2(x)| is the maximum difference between the cumulative distributions of two samples S1(x) and S2(x), respectively.

Table 7.9: Results on the correlation between IR (12 μm, 25 μm, 60 μm and 100 μm) luminosities and 610 MHz radio luminosities

Seyfert	Spearman rank correlation test							
sample	$L_{12\mu m}$ - P_{610MHz}		$L_{25\mu m}$ - P_{610MHz}		$L_{60\mu m}$ - P_{610MHz}		$L_{100\mu m}$ - P_{610MHz}	
	ρ	p-value	ρ	p-value	ρ	p-value	ρ	p-value
Type 1s	0.81	7.5×10^{-3}	0.78	1.1×10^{-2}	0.72	1.8×10^{-2}	0.65	4.6×10^{-2}
Type 2s	0.53	1.12×10^{-1}	0.59	5.8×10^{-2}	0.44	2.0×10^{-1}	0.08	8.3×10^{-1}
All (1s + 2s)	0.72	4.6×10^{-4}	0.74	2.9×10^{-4}	0.62	4.5×10^{-3}	0.46	4.7×10^{-2}

Notes: The p-value is the probability of rejecting the null hypothesis that the two quantities are correlated.

Table 7.10: Results on the correlation between IR (12 μm, 25 μm, 60 μm and 100 μm) luminosities and 240 MHz radio luminosities

Seyfert	Spearman rank correlation test							
sample	$L_{12\mu m}$ - P_{240MHz}		$L_{25\mu m}$ - P_{240MHz}		$L_{60\mu m}$ - P_{240MHz}		$L_{100\mu m}$ - P_{240MHz}	
	ρ	p-value	ρ	p-value	ρ	p-value	ρ	p-value
Type 1s	0.86	2.4×10^{-2}	0.79	4.8×10^{-2}	0.36	4.4×10^{-1}	0.21	6.6×10^{-1}
Type 2s	0.29	5.6×10^{-1}	0.43	3.5×10^{-1}	0.32	5.0×10^{-1}	0.0	1.0
All (1s + 2s)	0.58	3.8×10^{-2}	0.60	3.1×10^{-2}	0.48	9.5×10^{-2}	0.27	3.7×10^{-1}

Notes: The p-value is the probability of rejecting the null hypothesis that the two quantities are correlated.

7.4.5   IR luminosities of the two Seyfert subtypes

The high energy UV and optical photons emanating from AGN heat the surrounding dusty environment which re-radiates in the IR wavelengths over $\sim$ 2.5 - 200 μm range (Pier and Krolik 1992; Granato and Danese 1994). The infrared continua of Seyfert galaxies can be approximated by a series of superposed black-bodies, each originating from a body of dust heated to a characteristic temperature (Haas *et al.* 1998; Klaas *et al.* 2001; Bendo *et al.* 2003; Stevens, Amure, and Gear 2005). In general, the Seyfert galaxies IR spectral energy distribution may primarily be best fitted by two black-body components wherein the warmer component represents the emission associated to the dusty torus around the AGN and the colder component is likely to come from star-forming or extended regions (Rodriguez Espinosa *et al.* 1996; Antón *et al.* 2002). This implies that the mid-IR emission is largely dominated by dust heated by AGN continua whereas the far-IR is a different component probably unrelated with the nuclear activity and is due to dust heated by the stellar population in the disks of host galaxies (Prieto, Pérez García, and Rodríguez Espinosa 2001). It has been suggested that the bulk of the near-IR and mid-IR emission in Seyfert galaxies predominantly comes from the heated dusty torus around AGN (Barvainis 1992). The radiative transfer calculations for the IR emission from a dusty axi-symmetric torus around AGN suggest that the Seyfert type 1s should be, on average, stronger near-IR and mid-IR emitters than the type 2s, while at far-IR wavelengths the two subtypes should appear to be similar (Pier and Krolik 1992, 1993; Granato and Danese 1994; Efstathiou and Rowan-Robinson 1995). However, the predicted IR emission and degree of IR anisotropy depend on geometry and optical depth of the torus. Spinoglio and Malkan (1989) suggested that the 12 μm IR luminosity of Seyfert galaxies can be used as an indicator of AGN bolometric luminosity following the explanation that at 12 μm the absorption of AGN continuum is balanced by the thermal re-emission. If this is the case then the Seyfert unification scheme would predict that the two Seyfert subtypes

should show similar 12 μm luminosity distributions.

We compare the IR luminosity distributions for the two Seyfert subtypes of our sample in the framework of the unification scheme. We plot 12 μm, 25 μm, 60 μm and 100 μm IR luminosity distributions (*cf.*, Figure 7.26) and perform the two sample Kolmogorov - Smirnov test to compare the luminosity distributions of the two Seyfert subtypes at all the four IR bands (*cf.*, Table 7.8). Statistical tests show that the two Seyfert subtypes have similar IR luminosity distributions at 12 μm, 25 μm, 60 μm and 100 μm, which is consistent with the Seyfert unification scheme. We also compare the global ratio of FIR to radio (q) for the two Seyfert subtypes. The global ratio of FIR to radio (q) is defined as q = $\log\left[\frac{\text{FIR}/3.75 \times 10^{12} \text{ Hz}}{\text{S}_\nu(1.4\text{GHz})}\right]$, where FIR = 1.26×10^{-14} [2.58 S$_\nu$(60 μm) + S$_\nu$(100 μm)] W m^{-2}, *i.e.*, the rest-frame far-IR flux computed as a linear combination of measurements in the IRAS 60 μm and 100 μm bands with the assumption of a typical dust temperature of $\sim$ 30 K and 3.75×10^{12} Hz is the central frequency of the FIR (42.5 - 122.5 μm) window (Helou, Soifer, and Rowan-Robinson 1985). The q parameter can also be considered as the quantitative measure of the FIR - radio correlation. The two Seyfert subtypes show similar distributions of the global ratio of FIR to radio (q) (*cf.*, Figure 7.25, Table 7.8) which is consistent with the unification scheme as both the FIR and radio fluxes are mostly unobscured and orientation-independent.
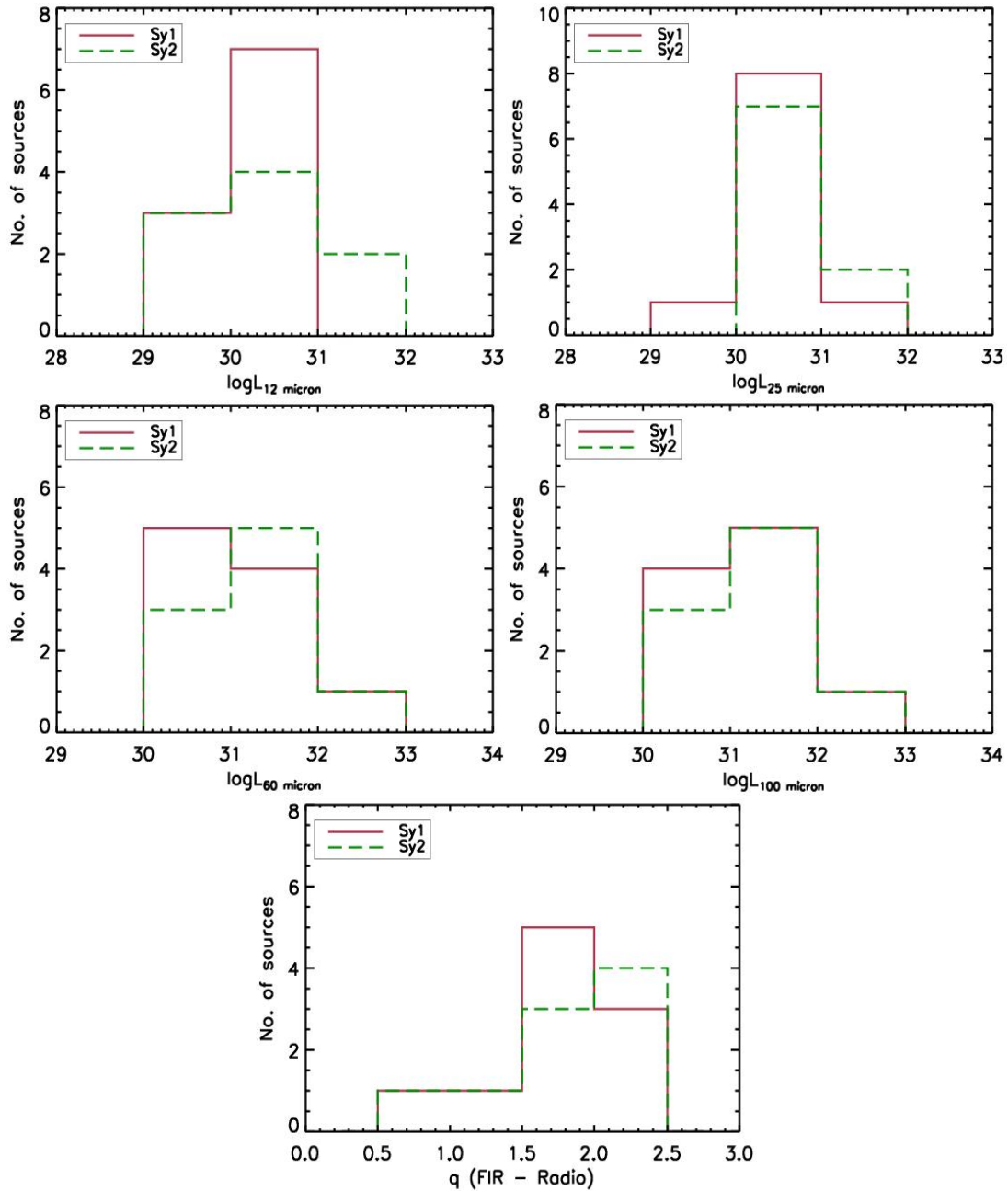
Figure 7.26: 12 μm, 25 μm, 60 μm, 100 μm luminosity distributions and the distribution of global FIR to radio ratio (q) of the two Seyfert subtypes of our sample.

7.5 Notes on individual sources

In this section I present the description of radio properties of individual sources of our sample and the comparison of our low-frequency observations with previous observations. In addition to make a note on high resolution observations, I also make a morphological comparison whenever a source has been observed in FIRST (Faint Images of the Radio Sky at Twenty-cm) survey or with observations which have resolution similar to our observations at 610 MHz. At 240 MHz, nearly all of our sample sources show point source emission which prevent us to make any detailed comparison of 240 MHz radio structures with previous observations.

7.5.1 MRK 6

High resolution radio observations of MRK 6 revealed a well-defined jet extending in the north-south direction nearly aligned with the ionization cone (Kukula *et al.* 1996). A pair of lobes on the sides of the jet along the east-west direction were also seen (Baum *et al.* (1993); Nagar *et al.* (1999)). Kharb *et al.* (2006) made a detailed study of MRK 6 and reported radio emission on three different spatial scales, *i.e.*, ~ 7.5 kpc bubbles, ~ 1.5 kpc bubbles lying nearly orthogonal to each other, and a ~ 1 kpc radio jet lying orthogonal to the 1.5 kpc bubble. The existence of kpc scale radio bubbles/lobes has been attributed to the radio relics related to past episodic nuclear activity. Our less sensitive and low resolution GMRT snapshot observations are not good enough to detect and resolve the radio emission in different spatial scales as reported by Kharb *et al.* (2006), however, we noticed the presence of faint extended emission other than a central core component. The core emission at 610 MHz can be fitted with an elliptical Gaussian of $10''.67 \times 4''.98$ with P.A. $\sim 155°.8$ and the faint extended emission is seen in the residual map.

7.5.2   NGC 3227

High resolution VLA observations at 8.4 GHz showed north-south elongated emission from the nucleus. At sub-arcsec resolution, the core is resolved into $0''.4$ double sources at P.A. $\sim 170°$ (Mundell *et al.* 1995). Gallimore *et al.* (2006) presented 5 GHz radio continuum image of NGC 3227 suggesting an extended radio emission, however, our GMRT observations at 610 MHz showed the radio emission as nearly a point source which can be fitted with an elliptical Gaussian of $8''.85 \times 6''.69$ with P.A. $\sim 120°$. There seems to be a slight extension in radio emission along the P.A. $\sim 130°$.

7.5.3   NGC 3516

High resolution VLA observations of NGC 3516 showed a compact flat-spectrum core with a $\sim 0''.7$ (~ 120 pc) one-sided northern extension along P.A. $\simeq 8°$ (Nagar *et al.* 1999). At arcsec resolution, VLA detected additional components extending out to $\sim 4''$ (~ 740 pc) with P.A. rotated to $\sim 20°$ and aligned with a co-spatial S-shaped optical emission-line structure (Miyaji, Wilson, and Perez-Fournon 1992; Ferruit, Wilson, and Mulchaey 1998). At coarser resolution, a linear radio structure spanning $\sim 45''$ (~ 8.3 kpc), oriented along P.A. $\sim 44°$, across the nucleus is also seen (Baum *et al.* 1993). In our GMRT observations at 610 MHz the radio emission is fitted with an elliptical Gaussian of $10''.44 \times 7''.38$ with P.A. $\sim 4°$. The integrated flux density at 610 MHz is substantially larger than the peak flux density and the fitted Gaussian size is also larger than the synthesized beam size which suggest the presence of extended emission. NGC 3516 shows inverted spectrum between 610 MHz, 1.4 GHz which is generally a signature of opaque synchrotron emission or starburst contamination to AGN emission.

7.5.4   NGC 4151

NGC 4151 is one of the most widely studied Seyfert galaxies in nearly all the wavelengths. The nuclear radio source in NGC 4151 resolves into compact knots aligned in a slightly curved jet structure spanning $\sim 5''$ (~ 340 parsec) across the nucleus and oriented along P.A. $\sim 80°$ (Ulvestad, Wilson, and Sramek 1981; Booler, Pedlar, and Davies 1982; Wilson and Ulvestad 1982; Pedlar *et al.* 1993; Mundell *et al.* 2003). The WSRT observations of NGC 4151 revealed a $\sim 15''$ (~ 1 kpc) linear structure, roughly aligned with the inner jet, and a bracketing pair of radio continuum arcs located at $\sim 45''$ (~ 3 kpc) from the radio nucleus (Baum *et al.* 1993). In our GMRT observations at 610 MHz, the radio emission is double peaked with less stronger peak residing at a distance of $\sim 8''.54$ along the P.A. $\sim 65°.2$ from the central component. The 610 MHz radio emission can be best fitted with two elliptical Gaussian components with central component having peak flux density ~ 323.6 mJy/beam and convolved size $\sim 7''.38 \times 4''.99$ with P.A. $\sim 160°.4$, while the second Gaussian component has peak flux density ~ 212.4 mJy/beam and convolved size $\sim 10''.26 \times 5''.23$ with P.A. $139°.9$. The total radio emission at 610 MHz extends larger than the synthesized beam size which infers the presence of kpc-scale extended emission. However, the FIRST survey at 1.4 GHz shows nearly a point source emission which is fitted with a single elliptical Gaussian of $\sim 6''.07 \times 5''.47$ with P.A. $\sim 77°.6$.

7.5.5   MRK 766

The high resolution observations of MRK 766 at 8.4 GHz showed an unresolved point source emission and no evidence for emission at intermediate scale (Kukula *et al.* 1995). In our GMRT observations at 610 MHz and 240 MHz we see nearly a point source radio emission wherein the shape is determined by synthesized beam itself. At 610 MHz radio emission is fitted with an elliptical Gaussian of $\sim 7''.92 \times 4''.81$ with P.A. $\sim 150°$.

7.5.6 MRK 279

The high resolution VLA observations of MRK 279 at 8.4 GHz showed an unresolved point source emission in both 'A' and 'C' array configurations and no evidence for emission at intermediate scale (Kukula *et al.* 1995). Our GMRT observations at 610 MHz showed nearly a point source emission which is fitted with an elliptical Gaussian of $\sim 7''.86 \times 5''.54$ with P.A. $\sim 19°$.

7.5.7 NGC 5548

The high resolution VLA observations of NGC 5548 revealed a compact core between two diffuse lobes separated by $\sim 15''$ (Wilson and Ulvestad 1982). Gallimore *et al.* (2006) reported marginally resolved lobes after the subtraction of the nuclear point source emission. There are also two radio sources lying $\sim 50''$ and $\sim 100''$ west of the nuclear radio source (Wilson and Ulvestad 1982) and the rough alignment of the sources suggests an origin in NGC 5548, but one cannot rule out the possibility that these radio sources are background objects. No counterparts are apparent either on the DSS image or on 2 MASS images (*e.g.*, Wilson and Ulvestad (1982)). In our GMRT observations, the radio emission at 610 MHz can be fitted with an elliptical Gaussian of $\sim 14''.33 \times 7''.12$ with P.A. $\sim 158°$. The integrated flux density is significantly larger than the peak flux density and the fitted Gaussian size is also much larger than the synthesized beam size which indicate the presence of extended and diffuse emission. NGC 5548 shows elongation along position angle $\sim 160°$ in FIRST as well as in our GMRT observations at 610 MHz which may possibly be due to the lobe emission which is unresolved in our low sensitivity GMRT observations.

7.5.8 ARK 564

The high resolution VLA observations of ARK 564 at 8.4 GHz showed a triple radio source along the north-south direction (P.A. $\sim 6°$), extended to ~ 320 pc (Moran

2000). Our GMRT observations at 610 MHz showed a point source emission with the shape dominated by beam size itself. The radio emission can be fitted with an elliptical Gaussian of $\sim 7''.62 \times 4''.91$ with P.A. $\sim 132°$.

7.5.9   NGC 7469

The VLA 'A' observations of NGC 7469 showed a point source surrounded by a faint emission and the large flux density discrepancy between VLA 'A' and the 'C' array observations indicates that ~ 30 mJy of extended flux has been resolved (Kukula *et al.* 1995). A variety of observations at high spatial resolution indicate that the AGN in NGC 7469 is surrounded by a more or less complete ring of starburst activity (Mauder *et al.* 1994; Genzel *et al.* 1995; Wilson 1991). The radio observations have shown an unresolved central component surrounded by a ring of star-forming regions (Wilson 1991). The VLBI observations at 1.6 GHz resolved the core-jet structure into five different components, lying in an east-west line which extends up to ~ 55 pc (Lonsdale *et al.* 2003). Our GMRT observations at 610 MHz can be fitted with an elliptical Gaussian of $\sim 10''.4 \times 6''.7$ with P.A. $\sim 154°.7$. Since the integrated flux density is substantially larger than the peak flux density and also the fitted Gaussian size is larger than the synthesized beam size, a kpc-scale extended emission is likely to be present in this source.

7.5.10   MRK 530

The VLA observations of MRK 530 at 8.4 GHz showed a compact point source emission with a slight extension (Kukula *et al.* 1995). The milli-arcsec resolution VLBI observations showed a compact core emission with extension along east-west direction at fainter levels (Lal, Shastri, and Gabuzda 2004). Our GMRT observations of MRK 530 at 610 MHz showed nearly a point source emission which is fitted with an elliptical Gaussian of $\sim 7''.28 \times 7''.18$ with P.A. $\sim 97°$. In FIRST survey too radio emission in MRK 530 is seen as a point source.

7.5.11   MRK 348

In MRK 348, the radio continuum emission is dominated by a variable, subparsec-scale (~ 0.5 pc) jet that feeds into a larger (~ 60 pc) linear radio structure oriented roughly north-south (Neff and de Bruyn 1983; Ulvestad *et al.* 1999; Antón *et al.* 2002). Baum *et al.* (1993) observed large-scale radio lobes (~ 6 kpc extent) that roughly align with the small-scale jet structure. Using VLA-D observations at 5 GHz, Gallimore *et al.* (2006) reported the presence of extended emission such that the large-scale lobes are marginally resolved after the nuclear point source subtraction. In our GMRT observations at 610 MHz the radio emission is nearly a point source which can be fitted with an elliptical Gaussian of $\sim 6''.34 \times 5''.8$ with the P.A. $\sim 157°$.

7.5.12   MRK 1

High resolution VLA observations of MRK 1 at 8.4 GHz showed an unresolved point source radio emission from AGN (Kinney *et al.* 2000). Our GMRT observations at 610 MHz and 240 MHz showed nearly a point source emission in this source. The 610 MHz radio emission can be fitted with an elliptical Gaussian of $\sim 6''.31 \times 5''.33$ with P.A. $\sim 177°$ which is similar to the synthesized beam size.

7.5.13   MRK 1066

The high resolution VLA observations of MRK 1066 at 4.9 GHz showed a linear, probably triple, source extending $\sim 2''.8$ along P.A. $\sim 134°$ (Ulvestad and Wilson 1989). A direct relationship seems to exist between the radio structure and the optical line emission region in Mrk 1066 (Haniff, Wilson, and Ward 1988; Veilleux 1991). Nagar *et al.* (1999) made high resolution VLA observations at 8.4 GHz and 1.4 GHz and reported that a single Gaussian model can be fitted to the 1.4 GHz source with position angle of $\sim 137°$ and at 8.4 GHz the central source shows the northwest extension along the position angle $\sim 305°$ with respect to the core. A

more diffuse southeast extension along the position angle $\sim 140°$ with respect to the core also seems to be present. Our GMRT observations of MRK 1066 at 610 MHz can be fitted with an elliptical Gaussian of $\sim 6''.69 \times 5''.63$ with P.A. $\sim 19°$. The radio emission at 610 MHz seems to have extension towards west from the central component but we caution about its fidelity.

7.5.14   NGC 2110

The VLA observations of NGC 2110 showed a symmetrical, jet-like radio emission, extending $\sim 4''$ in the north-south direction and straddling a central compact core (Ulvestad and Wilson 1984). Nagar *et al.* (1999) made high resolution VLA (A and AnB hybrid array configuration) observations of NGC 2110 at 8.4 GHz and 1.4 GHz and reported a point source emission at 1.4 GHz, while at 8.4 GHz a linear jet-like structure was noticed along the position angle $\sim 9°$. In our GMRT observations of NGC 2110 at 610 MHz the radio emission can be fitted with an elliptical Gaussian of $\sim 7''.68 \times 5''.11$ with P.A. $\sim 9°$. We note that the integrated flux density is substantially higher than peak flux density and also the fitted Gaussian size is larger than the synthesized beam size which suggest the presence of an extended and possibly diffuse emission in this source.

7.5.15   NGC 2273

The sub-arcsec VLA observations of NGC 2273 at 5 GHz showed an unequal double with a separation of $\sim 1''.2$ (~ 145 pc) at P.A. 90°, while observations at 1.4 GHz showed the double structure embedded in a more amorphous structure with an extent of $2''.5$ (~ 300 pc) along P.A. 20° (Ulvestad and Wilson 1984). The 5 GHz WSRT observations showed an additional amorphous structure on lager scale and the nuclear point source subtraction suggested an extended emission with a total extent of $\sim 9''$ (~ 1 kpc) along P.A. 160° (Baum *et al.* 1993). Our GMRT

observations of NGC 2273 at 610 MHz showed nearly a point source emission which can be fitted with an elliptical Gaussian of $\sim 8''.34 \times 5''.19$ with P.A. $\sim 152°$.

7.5.16   NGC 5252

The VLA high resolution observations of NGC 5252 at 5 GHz and 1.4 GHz showed a radio structure consisting of a central, compact core, with a relatively flat spectrum and a weaker emission extending $\sim 2''$ north (P.A. $\simeq 345°$) and south (P.A. $\simeq 175°$) of the core (Wilson and Tsvetanov 1994). A second compact radio component is seen $\sim 22''$ north (P.A. $\sim -8°.9$) of the nucleus which may be associated with NGC 5252, lying close to the P.A. of the extended core emission and coinciding with a region of high-excitation ionized gas (Wilson and Tsvetanov 1994), or may be a background source (Morse *et al.* 1998). The radio observations by Nagar *et al.* (1999) at 1.4 GHz and 5 GHz confirm the overall flatter spectrum of the core ($\alpha_{5.0GHz}^{1.4GHz} \sim 0.32$) and the radio continuum features seen in the earlier observations. Our GMRT observations at 610 MHz showed nearly an unresolved point source emission which can be fitted with an elliptical Gaussian of $\sim 10''.56 \times 5''.66$ with position angle $\sim 157°$. The FIRST image also show nearly a point source emission. In our GMRT 610 MHz image of NGC 5252, we also noticed a feeble emission at $\sim 22''$ north of the nucleus, the deeper image of FIRST has made a clear detection of it. We found that the radio spectrum of NGC 5252 is nearly flat in 610 MHz - 1.4 GHz - 5.0 GHz regime which is indicative of the AGN core dominated emission.

7.5.17   NGC 5728

The high resolution VLA observations of NGC 5728 at 5 GHz and 14.9 GHz showed a compact core and a faint radial feature extending to north-east (Schommer *et al.* 1988). The later radio continuum observations of NGC 5728 at 5 GHz and 1.4 GHz revealed that the nuclear emission is fairly co-spatial with the bi-conical ionization cone (Wilson *et al.* 1993). In our 610 MHz GMRT image we noticed a

double peaked emission in NGC 5728 wherein the second off-nuclear component may correspond to the near nuclear star-forming region reported in previous studies (*e.g.*, Schommer *et al.* (1988); Mazzuca *et al.* (2008)). The peaks of the two emitting components are separated by $\sim 10''.7$ (~ 2.0 kpc) with less stronger one residing along P.A. $\sim 67°$ from the stronger component. The two components have peak flux densities ~ 25 mJy/beam and 17.5 mJy/beam and are fitted with two elliptical Gaussian of $\sim 12''.6 \times 7''.47$ with P.A. $\sim 154°$ and $\sim 16''.1 \times 9''.4$ with P.A. $\sim 163°$, respectively.

7.5.18 NGC 7212

The high resolution VLA observations of NGC 7212 showed a compact double source separated by $\sim 0''.7$ in the north-south direction, the northern blob being slightly elongated (Falcke, Wilson, and Simpson 1998). Our GMRT observations at 610 MHz showed nearly a point source emission which can be fitted with an elliptical Gaussian of $\sim 6''.44 \times 4''.88$ with P.A. $\sim 174°.4$. Another nearly compact radio emission is seen at the distance of $\sim 15''.4$ (~ 8 kpc) along P.A. $\sim 20°.8$ from the nucleus of NGC 7212.

7.5.19 NGC 7682

The high resolution VLA observations of NGC 7682 at 8.4 GHz showed an unresolved point source nuclear emission (Kukula *et al.* 1995), however, the milliarcsec 5 GHz VLBI observations showed a point source with extension along the south (P.A. $\sim 180°$) and the south-east (P.A. $\sim 120°$) direction (Lal, Shastri, and Gabuzda 2004). Our GMRT observations at 610 MHz showed the radio emission as nearly a point source which can be fitted with an elliptical Gaussian of $\sim 6''.46 \times 5''.35$ with P.A. $\sim 6°$. A faint radio emission seems to present towards the west of the central component.

7.5.20 MRK 533

The high resolution VLA 'C' array observations of MRK 533 at 8.4 GHz showed a slightly extended emission from nucleus which is resolved into 0.5 arcsec double structure in VLA 'A' array observations (Kukula *et al.* 1995). The observations with VLA and EVN revealed a linear triple radio source of $\sim 0''.7$ angular extent with the components at $\sim 0''.5$ west and $\sim 0''.15$ east of the main peak (Unger *et al.* 1988). Momjian *et al.* (2003) made more sensitive observations of MRK 533 using VLBA, phased VLA and Arecibo at 1.4 GHz and reported the triple source and additional low-surface-brightness emission forming an S-shaped structure. Our GMRT observations at 610 MHz showed a point sources radio emission which can be fitted with an elliptical Gaussian of $\sim 6''.98 \times 6''.26$ with P.A. $\sim 44°$.

7.6   Conclusions

Here I summarize the conclusions drawn from our study on the multi-frequency radio properties of our rigorously selected sample of 20 Seyfert galaxies.

- The radio powers at 240 MHz, 610 MHz, 1.4 GHz and 5.0 GHz are in the range of $\sim 10^{28}$ - 10^{31} erg s^{-1} for both the Seyfert subtypes. The two Seyfert subtypes have similar radio power distributions with similar median values respectively at 240 MHz, 610 MHz, 1.4 GHz and 5.0 GHz.

- The average integrated radio spectral indices for the Seyfert galaxies of our sample is fairly steep (~ -0.7), consistent with the previous studies and can be explained as optically thin synchrotron emission.

- The average spectral curvature in 240 MHz - 5.0 GHz range is similar for the two Seyfert subtypes. A few sample sources show inverted or flat spectrum which may be due to significant contamination from starburst or self-absorption of synchrotron emission.

- At 610 MHz, several of both the Seyfert subtypes of our sample sources show the existence of kpc scale extended emission. While at 240 MHz, due to rather large synthesized beam and high rms, most of the sources are unresolved. Due to coarser resolution and lower sensitivity of our images at 240 MHZ and 610 MHz, we are unable to compare the radio sizes of the two subtypes.

- In our sample Seyfert type 1s and type 2s show similar trend of increasing radio luminosity at 610 MHz and 240 MHz with the increase in IR luminosity at respective bands. In both the Seyfert subtypes the 610 MHz and 240 MHz radio luminosities appear to be moderately correlated with IR luminosities at 12 μm, 25 μm, 60 μm and 100 μm.

– The IR luminosity distributions at 12 μm, 25 μm, 60 μm, 100 μm and the global FIR to radio ratio (q) distributions are similar for the two Seyfert subtypes.

– We conclude that the comparison of low-frequency radio properties (*i.e.*, radio spectra, radio powers), radio - IR correlations and IR luminosities of the two Seyfert subtypes are consistent with the predictions of the Seyfert unification scheme.

Chapter 8

Summary, conclusions and future work

8.1 Summary of the thesis work

Primary objective of this thesis work is to examine the validity of orientation and obscuration based Seyfert unification scheme using multiwavelength (mainly X-ray and radio) observations. The Seyfert unification scheme hypothesizes that Seyfert type 1s and type 2s belong to same parent population and appear different solely due to the differing orientations of the obscuring material having a torus-like geometry around AGN. There have been various attempts to examine the validity of Seyfert unification scheme, giving results consistent as well as inconsistent to the scheme, however, the key issue of using an unbiased and well defined sample still remains. In order to rigorously test the predictions of the Seyfert unification, it is essential that the two Seyfert subtypes being compared should be intrinsically similar within the framework of the scheme. This can be achieved by matching the two Seyfert subtypes in the properties of AGN and host galaxy which are independent of the orientation of the AGN and host galaxy (Lal 2002). We used two rigorously selected samples each consist of 20 Seyfert galaxies. In each sample, the two Seyfert subtypes, *i.e.*, type 1s and type 2s have matched distributions of the orientation-independent properties of AGN as well as host galaxy, *i.e.*, cosmological redshift, [OIII] $\lambda5007$Å luminosity, absolute bulge magnitude, absolute stellar magnitude of

the host galaxy and Hubble stage of the host galaxy. Our sample selection based on the orientation-independent parameters ensures the intrinsic similarity of the two Seyfert subtypes in the framework of the unification scheme and mitigates the biases generally inherent in the samples derived from the flux limited surveys.

The obscuring material supposedly having a torus-like geometry around AGN is optically thick for optical, UV and soft X-ray photons. However, X-ray and radio studies are advantageous since X-ray spectral analysis enables to estimate the absorbing column density and radio emission is optically thin to torus obscuration. We modeled the *XMM-Newton* pn 0.5 - 10.0 keV X-ray spectra of 17 (10 type 1 and 7 type 2) out of 20 Seyfert galaxies of our sample. For 6 Seyfert galaxies, *i.e.*, MRK 1218, NGC 2639, MRK 530, MRK 78, MRK 533 and NGC 7682, of our sample *XMM-Newton* X-ray spectra are being presented for the first time. We find that 0.5 - 10.0 keV X-ray spectra of Seyfert galaxies are generally best fitted with a model consists of: an absorbed power-law with exponential cutoff which contains cold absorption from the Galactic hydrogen column density together with absorption from neutral gas at the redshift of the source; a narrow Gaussian line to fit the iron Kα fluorescent line at 6.4 keV; soft excess component characterized by either a steep power-law and/or a thermal plasma model with temperature kT and in some cases reflection component characterized by reflection from an isotropically illuminated cold slab, (model 'pexrav' in XSPEC) is required for the best fit. The partial covering of the primary power-law component is also required for obtaining the best fit in some sources. There are several type 2 sources in our sample in which the hard (2.0 - 10.0 keV) part of the X-ray spectrum is best fitted with a reflection component alone ('pexrav' model). We performed the statistical comparison of the X-ray spectral properties of the two Seyfert subtypes and find that in comparison to Seyfert type 1s, the Seyfert type 2s show lower X-ray luminosities in soft (0.5 - 2.0 keV) and hard (2.0 - 10.0) X-ray bands, higher X-ray absorbing column densities, higher EWs of Fe Kα line, lower flux ratios of hard X-ray (2.0 - 10.0 keV) to [OIII]. In both the Seyfert subtypes the X-ray luminosity is moderately correlated with

the pc-scale, kpc-scale radio luminosities and [OIII] $\lambda5007\text{Å}$ luminosity in a similar fashion. All these results are consistent with the obscuration and orientation based Seyfert unification scheme.

We noted a significant large fraction of Compton-thick type 2 sources in our sample and as a case study of a Compton-thick AGN, we studied the broad-band 0.5 - 50 keV X-ray spectral properties of NGC 5135 using *Suzaku* (XIS and HID) data to unveil the nature and geometry of obscuring torus. We modeled the broad-band 0.5 - 50 keV *Suzaku* X-ray spectrum of NGC 5135 by a soft component fitted with two thermal plasma models with sub-keV temperatures plus a steep power-law and a hard component reproduced by a heavily absorbed power-law ($N_H \sim$ $2.77^{+1.84}_{-1.07} \times 10^{24}$ cm^{-2}, $\Gamma \sim 1.7$) plus a reflection component and a prominent Fe Kα line of EW ~ 1.8 keV. Our spectral analysis provides the first accurate measurements of the absorbing column density and the strength of the reflection component for this source, which are the key ingredients in understanding the nature of Compton-thick obscuring material around AGN.

We studied the radio properties of our sample of 20 Seyfert galaxies using GMRT observations carried out at 240 MHz, 610 MHz and NRAO VLA Sky survey observations at 1.4 GHz and VLA observations at 5 GHz present in the literature. The four point (240 MHz, 610 MHz, 1.4 GHz, 5.0 GHz) integrated radio spectra of the two Seyfert subtypes are similar and fairly steep (*i.e.*, spectral index ~ -0.7). However, a few sources, *e.g.*, NGC 3516, NGC 5728 show inverted or flat spectra possibly due to starburst contamination or self-absorption of synchrotron emission. In several of our sample sources (*e.g.*, MRK 6, NGC 4151, NGC 7469, MRK 348, MRK 1066, NGC 5728 and NGC 7682) extended kpc-scale radio emission at 610 MHz is noticeable, however, at 240 MHz due to rather large synthesized beam size, most of our sample sources are seen as unresolved point sources. We could not compare the radio sizes of the two subtypes at 610 MHz and 240 MHz as many of our sample sources are either marginally resolved or unresolved. We investigated the radio - IR correlations and found that the near-IR, mid-IR luminosities are

moderately correlated with 610 MHz and 240 MHz radio luminosities for both the Seyfert subtypes while at far-IR the radio - IR correlation becomes poorer. The two Seyfert subtypes show similar IR luminosity distributions at each of the four IRAS bands (*i.e.*, 12 μm, 25 μm, 60 μm and 100 μm), consistent with the unification scheme. I conclude that the results on the study of X-ray, radio and IR properties of Seyfert galaxies are consistent with the orientation and obscuration based Seyfert unification scheme.

8.2   Conclusions of the thesis work

– 0.5 - 10.0 keV X-ray spectra of Seyfert galaxies can approximately be modeled as "exp(-N_{H_0} σ_{abs}) × [soft component + exp(-N_{H_1} σ_{abs}) ($AE^{-\Gamma}$ + emission lines)]", where, σ_{abs} is the photoelectric absorption cross-section, N_{H_0} and N_{H_1} are the equivalent hydrogen absorbing column densities, soft component is characterized by either thermal plasma model(s) with sub-keV temperature(s) and/or a steep power-law, $AE^{-\Gamma}$ is the primary power-law component and Fe Kα is the prominent emission line.

– The observed soft X-ray (0.5 - 2.0 keV) luminosities of Seyfert 1s of our sample range from $\sim 10^{40}$ erg s^{-1} to $\sim 10^{44}$ erg s^{-1} with the median value of $\sim 6.6 \times 10^{42}$ erg s^{-1}, while for Seyfert 2s, it range from $\sim 10^{38}$ erg s^{-1} to $\sim 10^{42}$ erg s^{-1} with the median value of $\sim 6.9 \times 10^{40}$ erg s^{-1}. The nearly 2 dex difference in the medians of the observed soft X-ray luminosities of the two Seyfert subtypes can be explained as the presence of more line-of-sight absorption in type 2s than that in type 1s, which is expected since in type 2s, the obscuring torus intercepts observer's line-of-sight, according to the orientation based Seyfert unification.

– In hard X-ray (2.0 - 10.0 keV) band, Seyfert 1s of our sample have observed luminosities ranging from $\sim 10^{40}$ erg s^{-1} to $\sim 10^{45}$ erg s^{-1} with the median

value $\sim 1 \times 10^{43}$ erg s^{-1}, while for Seyfert 2s, it range from $\sim 10^{40}$ erg s^{-1} to $\sim 10^{44}$ erg s^{-1} with the median value $\sim 6.8 \times 10^{41}$ erg s^{-1}. The difference between the observed hard (2.0 - 10.0 keV) X-ray luminosity distributions for the two Seyfert types is lower in comparison to that in the soft X-ray (0.5 - 2.0 keV) band and can be understood as the hard X-ray (2.0 - 10.0 keV) photons have higher probability of transmission through the same torus as photoelectric absorption cross-section decreases with the increase in photon energy.

– The estimated absorbing column density in Seyfert galaxies of our sample varies from the Galactic value to as high as $N_H \geq 1.5 \times 10^{24}$ cm^{-2} (*i.e.*, Compton-thick obscuration). For type 1 sources, the equivalent N_H ranges from $\sim 10^{20}$ cm^{-2} (Galactic value) to $\sim 10^{22}$ cm^{-2}, while for type 2s, it ranges from $\sim 10^{22}$ cm^{-2} to $> 1.5 \times 10^{24}$ cm^{-2}. As expected from the unification scheme, Seyfert type 1s of our sample have systematically lower X-ray absorbing column densities than Seyfert type 2s.

– Several Seyfert type 2s of our sample, *e.g.*, MRK 1, NGC 2273, MRK 78, NGC 5135, NGC 7212, MRK 533 and NGC 7682 are heavily obscured and the 2.0 - 10.0 keV spectral part is dominated by the reflection component. These sources are identified as Compton-thick AGNs in which the obscuring material becomes optically thick to Compton scattering and the transmitted component of the primary X-ray radiation is completely suppressed at energies < 10 keV, resulting the spectra in 2.0 - 10.0 keV energy range flat and dominated by the reprocessed emission from a cold and/or warm scatterer.

– For both the Seyfert subtypes the 2.0 - 10.0 keV X-ray luminosities are found to be correlated with the pc-scale and kpc-scale radio luminosities. In Seyfert galaxies, the nuclear X-ray emission is believed to originate from the accretion disk - corona system and the radio emission is primarily attributed

to the synchrotron emission from the jet/outflow. Therefore, the correlation between the nuclear hard X-ray and radio luminosity in Seyfert galaxies indicates the coupling between accretion disk and jet.

– Both the Seyfert subtypes also show a similar and significant correlation between the 2.0 - 10.0 keV luminosity ($L_{2.0-10.0\ keV}$) and [OIII] λ5007Å line luminosity ($L_{[OIII]\ \lambda5007Å}$) which can understood as both $L_{2.0-10.0\ keV}$ and $L_{[OIII]\ \lambda5007Å}$ are considered to be related to the AGN power.

– We detected the fluorescent Fe Kα emission line at 6.4 keV in all except NGC 2639 of our sample sources suggesting the ubiquitous presence of the Fe Kα line in the X-ray spectra of Seyfert galaxies. In all sources, the Fe Kα line is modeled as a narrow Gaussian line with the centroid energy $\sim$ 6.4 keV, which suggests the line emission from neutral or mildly ionized Fe.

– Seyfert type 2s have systematically larger equivalent widths of Fe Kα line (ranges from $\sim$ 350 eV to 2.2 keV, except for MRK 348) than that in type 1s ($\sim$ 20 - 200 eV). This is consistent with the unification scheme, as in type 2s, due to high absorption, EW of Fe Kα line is measured against much suppressed continuum.

– X-ray spectral properties, *e.g.*, reflection dominated hard X-ray component, low flux ratio of hard X-ray (2.0 - 10.0 keV) to [OIII] and the high EW of Fe Kα line implies that $\sim$ 7 - 8 out of 10 type 2 sources of our sample are Compton-thick ($N_H > 1.5 \times 10^{24}$ cm^{-2}). The high fraction of Compton-thick type 2s is in agreement with previous studies (*e.g.*, Risaliti, Maiolino, and Salvati (1999)) and may account for the missing fraction of heavily obscured AGNs in X-ray background emission models.

– The fraction of Compton-thick AGNs in the local universe is poorly known and our results suggest a large fraction of Compton-thick sources, *i.e.*, $\sim$ 60 - 70% of the Seyfert type 2 population and $\sim$ 30 - 35% of the entire Seyfert

population. Indeed, a large fraction of Compton-thick AGNs is required by the X-ray background synthesis models to explain the peak of the X-ray background emission at 30 - 40 keV (Gilli, Comastri, and Hasinger 2007). The presence of a large fraction of Compton-thick AGNs is also evident from the fact that the measured space density of black holes in the local Universe is a factor of two higher than that predicted from the X-ray luminosity function (Marconi *et al.* 2004).

— Using *Suzaku* 0.5 - 50 keV broad-band X-ray spectral modeling of NGC 5135 we showed that the AGN in NGC 5135 is obscured by the Compton-thick obscuring material with absorbing column density $N_H \sim 2.9 \times 10^{24}$ cm^{-2}. The 0.5 - 50 keV broad band X-ray continuum spectrum of heavily obscured AGN in NGC 5135 is much more complex than a single absorbed power-law and additional components *i.e.*, thermal soft X-ray emission and a fairly strong reflection component above 10 keV, are required. Our *Suzaku* X-ray spectral study of NGC 5135 can represent a case study of some of the complex realities in Compton-thick AGNs.

— The radio powers at 240 MHz, 610 MHz, 1.4 GHz and 5.0 GHz are in the range of $\sim 10^{28}$ - 10^{31} erg s^{-1}, respectively, for both the Seyfert subtypes. The two Seyfert subtypes have similar radio power distributions with similar median values, respectively, at 240 MHz, 610 MHz, 1.4 GHz and 5.0 GHz.

— The distributions of 240 MHz - 5.0 GHz radio spectral indices are similar for the two Seyfert subtypes and the typical values of the radio spectral index for both the Seyfert subtypes are fairly steep ($\alpha \sim -0.7$; $S_\nu \propto \nu^\alpha$), consistent with the optically thin synchrotron emission. A few sample sources show inverted or flat spectrum which may be due to the significant contamination from starburst or self-absorption of synchrotron emission.

— At 610 MHz, several of both the Seyfert subtypes of our sample sources

show the existence of kpc-scale extended emission. While at 240 MHz, due
to rather large synthesized beam and high rms of noise, most of the sources
are unresolved. Due to coarse resolution and low sensitivity of our images at
240 MHZ and 610 MHz, we are unable to compare the radio sizes of the two
subtypes.

– In both the Seyfert subtypes the 610 MHz and 240 MHz radio luminosities
  appear to be moderately correlated with IR luminosities at 12 μm, 25 μm,
  60 μm and 100 μm. The IR luminosity distributions at 12 μm, 25 μm, 60
  μm, 100 μm and the distributions of the global ratio of far-IR to radio (q)
  are similar for the Seyfert type 1s and type 2s.

– Our results on the study of X-ray spectral properties, X-ray - radio correla-
  tion, radio properties (*i.e.*, radio spectra, radio powers), radio - IR correla-
  tions and IR luminosities of the Seyfert galaxies of our samples are consistent
  with the predictions of the Seyfert unification scheme.

8.3 Limitations of torus-based Seyfert unification scheme

Our results on the study of X-ray and radio properties of the rigorously selected
samples of Seyfert galaxies are consistent with the orientation-based Seyfert uni-
fication scheme. However, considering the recent studies in literature we note
that in order to explain the subtle differences between the two Seyfert subtypes it
seems essential to account for the fundamental parameters of AGN - host galaxy
system, such as mass of the SMBH, accretion rate/mode, effect of nuclear activity
(*e.g.*, AGN luminosity) on the evolution of BLR, NLR and the properties of the
obscuring torus, etc. In the following sections I discuss some of the issues which

emphasize the importance of fundamental parameters of the AGN - host galaxy system.

8.3.1 Role of AGN fueling

In accordance to unification scheme, type 1s and type 2s must have similar accretion and ejection properties around SMBH. However, recent studies have shown that Seyfert type 2 galaxies are accreting at lower Eddington ratios than type 1 Seyfert galaxies, although black hole mass distributions for two subtypes are similar (Panessa and Bassani 2002; Ho 2008). These results are inconsistent with the unification scheme and likely to strengthen the notions that the formation of BLR is related to accretion rate (*i.e.*, for very low accretion rates the BLR may no longer exist (*e.g.*, Nicastro, Martocchia, and Matt (2003)). Furthermore, it is debated whether obscuration based unification scheme remains valid at the very low luminosity end of the AGNs (*e.g.*, Panessa and Bassani (2002); Ho and Ulvestad (2001); Ho (2008)). Comprehensively, AGN phenomenons reside on the combination of unification scheme and the fundamental parameters such as mass of SMBH, mass accretion rate, etc.

8.3.2 Diversity among the two Seyfert subtypes

For Seyfert type 1s galaxies typical FWHM of the Balmer lines lie in the range 2000 - 6000 km s^{-1}, however, there is a group of Seyfert type 1s which show narrow Balmer lines (*i.e.*, FWHM < 2000 km s^{-1}), although, all other properties are similar to Seyfert type 1s and these are named as 'narrow line Seyfert type 1 galaxies (NLS1)' (Osterbrock and Pogge 1985, 1987; Goodrich 1989). NLS1s also show weak [OIII] and strong FeII emission lines (Osterbrock and Pogge 1985), strong variability, and a softer than usual X-ray continuum (Boller, Brandt, and Fink 1996; Grupe *et al.* 1999). SDSS optical spectroscopic studies show that NLS1s are a minority, *i.e.*, 15 % of all the Seyfert type 1s, (Williams, Pogge, and Mathur

2002) and the fraction of NLS1 population can depend on the AGN luminosity (Sulentic *et al.* 2007). Grupe and Mathur (2004) found that NLS1s have, on average, lower M_{BH} than expected from M_{BH}-σ scaling relation (Tremaine *et al.* 2002), while in broad line Seyfert type 1s (BLS1) the M_{BH} is in fairly good agreement to the same scaling relation. The estimated low values of M_{BH} result in to almost an order of magnitude higher average Eddington ratios (L/L_{Edd}) for the NLS1 population than the average values for BLS1s (Grupe and Mathur 2004)). Therefore, NLS1s appear as a different subclass, containing less massive SMBH and having higher Eddington ratios (Boller, Brandt, and Fink 1996; Mineshige *et al.* 2000; Wang and Netzer 2003). However, there are studies which suggest that the lack of broad permitted Balmer lines in NLS1 can be explained by considering small viewing angle to BLR which has disk-like geometry. Decarli *et al.* (2008) assumed the disk-like geometry for the BLR of Seyfert galaxies and used the observed frequency of NLS1s to estimate their typical viewing angle and showed that the estimates of M_{BH} for NLS1s agree with the standard M_{BH}-σ scaling relation and as a result the average accretion rate in NLS1 is found to be similar to that of BLS1s. It is noted that a disc-like geometry for the BLR has been suggested by several authors in the past (*e.g.*, Wills and Browne (1986); Vestergaard, Wilkes, and Barthel (2000); Bian and Zhao (2004); Labita *et al.* (2006). Therefore, the differences between NLS1s and BLS1s can be explained on the basis of the differing orientations of the disk-like BLR.

Tran (2001) presented a spectropolarimetric survey of Seyfert type 2 galaxies and reported a large fraction ($\sim$ 50 %) of type 2 Seyferts which do not show any broad component of emission line in polarized light and presumably lack hidden broad line region (named as non-Hidden Broad Line Region type 2s, *i.e.*, non-HBLR type 2s). Tran (2001) also showed that in comparison to the non-HBLR Type 2s, the HBLR type 2s display distinctly higher radio power relative to their far-infrared output and hotter dust temperature as indicated by the $f_{25\mu m}/f_{60\mu m}$ color. However, the level of obscuration is indistinguishable between the two types

of Seyfert galaxies. Tran (2001) proposed the existence of two intrinsically different populations of Seyfert type 2 galaxies: one harboring an energetic, hidden type 1 nucleus with a broad-line region (*i.e.*, HBLR Seyfert type 2s) and the other a 'pure' Seyfert type 2 galaxy, with a weak or absent Seyfert type 1 nuclei and a strong, perhaps dominating starburst component (*i.e.*, non-HBLR Seyfert type 2). Moreover, Tran (2003) show that the levels of obscuration and circumnuclear star formation, appear to be similar in HBLR and non-HBLR Seyfert type 2 galaxies. There have been suggestions that orientation alone may not be sufficient to explain the observed differences between Seyfert type 1s and type 2s, given the diversity amongst type 1s and type 2s itself (Tran 1995, 2001, 2003; Wang and Zhang 2007).

8.3.3   Role of the geometry and structure of torus

The geometry and structure of the torus remains poorly understood and is limited to few Seyfert galaxies. The torus could be clumpy or mixed with a star formation region and the medium which scatters BLR photons seems to have complicated structure and composition (hot electrons and various sizes of dust grains) (*e.g.*, Elitzur (2006)). A fast transition from Compton-thick to Compton-thin in the Seyfert 1.8 galaxy NGC 1365 implies that there are random motions of dusty clouds inside the torus (Risaliti *et al.* 2005). Infrared detection of dusty cloud distribution shows clear structure within $\sim$ 20 - 50 pc around the central engine in NGC 1068 (Tomono, Terada, and Kobayashi 2006). These studies favor clumpy torus scenario (*i.e.*, consist of smaller clouds) over smooth distribution of matter in torus. The opening angle of the dusty torus is an important ingredient in the unification scheme and there are evidence for the evolution of the opening angle of the torus with hard X-ray luminosity, displaying a receding torus (Steffen *et al.* 2004; Barger *et al.* 2005). Also, the ratio (R) of number of type 2s to type 1s Seyferts decreases with hard X-ray luminosity (L_{HX}) indicating that the opening

angle of the dusty torus is changing with AGN luminosity (*e.g.*, Ueda *et al.* (2003); Hasinger (2008)). The appearance of type 2s, not only depends on the orientation of the dusty torus, but also strongly depends on its opening angle. Clearly, the unification scheme should include the evolution of the opening angle of the torus.

8.3.4   Role of gas-to-dust ratio in the torus

Panessa and Bassani (2002) noted significant fraction ($\sim 10\%$ - 30%) of unabsorbed or low-absorption ($N_H < 10^{22}$ cm^{-2}) Seyfert type 2s and Gallo *et al.* (2006) found that $\sim 50\%$ of the soft X-ray ROSAT-selected AGNs are type 2 Seyfert galaxies, which can be due to large fraction of low absorption Seyfert type 2s. The X-ray unabsorbed Seyfert type 2 galaxies cannot be explained by the unification scheme in its simple formulation. The BLRs of these unabsorbed Seyfert type 2s are either obscured by non-standard torus or BLR is weak, absent or has just faded away. One possibility is that the unabsorbed Seyfert type 2s could be "true" Seyfert 2s and lack broad-line region, due to lower accretion rate onto SMBH than a critical value of accretion rate (Laor 2003; Nicastro, Martocchia, and Matt 2003). The other possibility is that there is low-absorbing material along the observer's line-of-sight which has different gas-to-dust ratio than Galactic one. A higher dust-to-gas ratio (*i.e.*, $A_V/N_H \sim 10$ - 50 higher than the Galactic value) is required to hide the BLR and to show low X-ray absorbing column density (N_H) in X-ray unabsorbed or low-absorption Seyfert type 2s (Panessa and Bassani 2002). Indeed, few LLAGNs are characterized by an A_V/N_H ratio consistent with higher than the Galactic value (Maiolino *et al.* 2001). Star formation/bursts inside the torus (Collin and Zahn 1999) produces large amount of dust and can change the gas-to-dust ratio. Therefore, gas-to-dust ratio seems to be an important parameter in determining whether an optically defined Seyfert type 2 galaxy will show high or low X-ray absorption (Maiolino *et al.* 2001; Gallo *et al.* 2006).

8.3.5 Unification scheme with evolutionary scenario

Wang and Zhang (2007) studied a large sample (243 Seyferts) of nearby Seyfert galaxies to test the Seyfert unification scheme. The sample includes 94 broad emission line Seyfert type 1 galaxies (BLS1s), 44 narrow emission line Seyfert type 1s (NLS1s), 36 X-ray-absorbed hidden broad line region Seyfert type 2s (HBLR S2s), 42 X-ray-absorbed non-HBLR S2s, and 27 X-ray-unabsorbed Seyfert 2s (unabsorbed non-HBLR S2s and HBLR S2s). They reported that: NLS1s have less massive SMBH than BLS1s, HBLR Seyfert 2s have the same mass distribution of SMBH as BLS1s, absorbed non-HBLR Seyfert 2s have less massive SMBH than HBLR Seyfert 2s, and unabsorbed non-HBLR S2s have the most massive SMBH. Wang and Zhang (2007) noted a sequence of SMBH masses from small to large in narrow to broad-line Seyfert galaxies and suggest evidence for the evolutionary sequence. They also reported that the opening angles of the torus in NLS1s and absorbed non-HBLR S2s are significantly smaller than those in BLS1s and HBLR S2s and the unabsorbed Seyfert 2 galaxies could be caused by low gas-to-dust ratios. The evolutionary scenario may be at work by which Seyfert galaxies tend to finally evolve to unabsorbed non-HBLR Seyfert 2 galaxies, wherein, SMBHs accrete with low accretion rates and both the broad-line region and dusty torus disappear.

8.4 Future work

8.4.1 IR spectral properties of our Seyfert sample: testing unification scheme

Obscuring material having toroidal geometry around AGN is optically-thick for optical to soft X-ray emission, however, optical-thickness decreases at IR wavelengths and hence IR emission does not suffer high obscuration. The dusty torus

absorbs the shorter wavelength emission *e.g.*, optical, UV emission from AGN and re-radiates in IR wavelengths a substantial fraction of the bolometric flux of the AGN. Therefore, detailed IR spectral energy distribution (SED) of Seyfert galaxies can reveal the properties of the dust in the nuclear region, as well as place constraints on the optical to soft X-ray spectrum (*i.e.*, starburst and AGN spectrum) that heats the dust. The geometry and opacity of the obscuring torus is expected to have an observable impact on the shape of the IR SED (Pier and Krolik 1992; Granato and Danese 1994; Ivezic and Elitzur 1997; Nenkova, Ivezić, and Elitzur 2002). Thus, Seyfert unification can be tested by comparing the properties of IR spectra of type 1 and 2 Seyfert galaxies.

IR spectral studies of 12 μm Seyfert sample by Buchanan *et al.* (2006) reported that the Seyfert type 2s tend to show stronger starburst contributions than the Seyfert type 1s, contrary to similar content of starburst expected from Seyfert unification scheme. However, this may be due to the selection effect that only those Seyfert 2 galaxies with strong starburst contributions had high enough integrated 12 μm flux densities to fall above the flux limit of the selected sample. Seyfert 2s with intrinsically faint AGN could be chosen in the sample if they have an additional starburst contribution to the 12 μm flux density. This would result in the sample being biased towards Seyfert 2 galaxies with a greater relative and absolute starburst contribution than the Seyfert 1 galaxies in the sample. Also, obscuring torus may not be completely optically thin for 12μm emission (*i.e.*, which is criteria of 12 μm sample selection) and this will bias the sample against Seyfert type 2s. The selection of Seyfert samples based on the orientation-independent and isotropic properties is essential to test the predictions of Seyfert unification at IR wavelengths. We plan to study Spitzer IR (5 μm - 38 μm) spectra of our sample to test the predictions of Seyfert unification at IR regime.

8.4.2 Census of Compton-thick AGNs

There are evidence that the obscured AGNs are much more numerous than un-obscured AGNs, both in the local universe and at intermediate-to-high redshifts (*e.g.*, Maiolino and Rieke (1995); Risaliti, Maiolino, and Salvati (1999); Matt *et al.* (2000); Hasinger (2008)), however, the relative space density of the obscured AGNs is not well known. Furthermore, mildly Compton-thick AGNs are the promising candidates to explain the residual spectrum of the X-ray background around its 30 keV peak (Comastri 2004; Worsley *et al.* 2005) but only a handful of Compton-thick AGNs are known beyond the local Universe. The unknown fraction of mildly, heavily Compton-thick AGNs, in turn, also, indicate the missing of a substantial fraction of the accretion power in the universe and of the baryonic matter locked in SMBH (Marconi *et al.* 2004). Therefore, the census of the obscured AGNs is necessary to understand the co-evolution of AGN and host galaxy.

In X-ray spectral study of our rigorously selected Seyfert galaxies sample we noted a substantially large fraction of Compton-thick type 2 AGNs (Singh V., Shastri P. & Risaliti G., 2011, A&A). Further on, I am interested to study the Compton-thick AGN population and its dependence on AGN luminosity and redshift. Hard X-ray (E > 10 keV) observations from *Suzaku*, Integral/IBIS, Swift/BAT are useful to study the Compton-thick AGN population. To infer the fraction of Compton-thick sources at high redshift, we can use *Chandra* and *XMM-Newton* deep surveys (*e.g.*, XDEEP2) as well as indirect indicators such as mid-IR AGN-like excess in deep Spitzer observations (*i.e.*, heavily Compton-thick AGNs may not have hard X-ray counterpart even in deep X-ray observations (*e.g.*, Alonso-Herrero *et al.* (2006); Polletta *et al.* (2006); Fiore *et al.* (2008)).

Bibliography

Akylas, A., Georgantopoulos, I.: 2009, XMM-Newton observations of Seyfert galaxies from the Palomar spectroscopic survey: the X-ray absorption distribution. *A&A* **500**, 999–1012.

Alonso-Herrero, A., Pérez-González, P.G., Alexander, D.M., Rieke, G.H., Rigopoulou, D., Le Floc'h, E., Barmby, P., Papovich, C., Rigby, J.R., Bauer, F.E., Brandt, W.N., Egami, E., Willner, S.P., Dole, H., Huang, J.: 2006, Infrared Power-Law Galaxies in the Chandra Deep Field-South: Active Galactic Nuclei and Ultraluminous Infrared Galaxies. *Astrophys. J.* **640**, 167–184.

Anders, E., Grevesse, N.: 1989, Abundances of the elements - Meteoritic and solar. *Geochimica et Cosmochimica Acta* **53**, 197–214.

Antón, S., Thean, A.H.C., Pedlar, A., Browne, I.W.A.: 2002, The orientation of the Seyfert nucleus in Markarian 348. *MNRAS* **336**, 319–327.

Antonucci, R.: 1993, Unified models for active galactic nuclei and quasars. *Annual review of Asto & Asphy* **31**, 473–521.

Antonucci, R., Barvainis, R.: 1988, Excess 2 centimeter emission - A new continuum component in the spectra of radio-quiet quasars. *ApJL* **332**, L13–L17.

Antonucci, R.R.J., Miller, J.S.: 1985, Spectropolarimetry and the nature of NGC 1068. *Astrophys. J.* **297**, 621–632.

Arnaud, K.A.: 1996, XSPEC: The First Ten Years. In: Jacoby, G.H., Barnes, J. (eds.) *Astronomical Data Analysis Software and Systems V*, *Astronomical Society of the Pacific Conference Series*, **101**, 17.

Awaki, H., Anabuki, N., Fukazawa, Y., Gallo, L.C., Ikeda, S., Isobe, N., Itoh, T., Kunieda, H., Makishima, K., Markowitz, A., Miniutti, G., Mizuno, T., Okajima, T., Ptak, A., Reeves, J.N., Takahashi, T., Terashima, Y., Yaqoob, T.: 2008, Wide-Band Spectroscopy of the Compton Thick Seyfert2 Galaxy Markarian 3 with Suzaku. *Publ. Astron. Soc. Japan* **60**, 293.

Awaki, H., Koyama, K., Inoue, H., Halpern, J.P.: 1991, X-ray implications of a unified model of Seyfert galaxies. *Publ. Astron. Soc. Japan* **43**, 195–212.

Awaki, H., Murakami, H., Ogawa, Y., Leighly, K.M.: 2006, Variability Study of Seyfert 2 Galaxies with XMM-Newton. *Astrophys. J.* **645**, 928–939.

Awaki, H., Terashima, Y., Higaki, Y., Fukazawa, Y.: 2009, Detection of Hard X-Rays from the Compton-Thick Seyfert 2 Galaxy NGC 2273 with Suzaku. *Publ. Astron. Soc. Japan* **61**, 317.

Awaki, H., Ueno, S., Taniguchi, Y., Weaver, K.A.: 2000, X-Ray Emission from Seyfert 2 Galaxies with Optical Polarized Broad Lines. *Astrophys. J.* **542**, 175–185.

Baldwin, J., Ferland, G., Korista, K., Verner, D.: 1995, Locally Optimally Emitting Clouds and the Origin of Quasar Emission Lines. *ApJL* **455**, L119.

Baldwin, J.A., Ferland, G.J., Korista, K.T., Carswell, R.F., Hamann, F., Phillips, M.M., Verner, D., Wilkes, B.J., Williams, R.E.: 1996, Very High Density Clumps and Outflowing Winds in QSO Broad-Line Regions. *Astrophys. J.* **461**, 664.

Barcons, X., Carrera, F.J., Ceballos, M.T.: 2003, H1320+551: a type 1.8/1.9 Seyfert galaxy with an unabsorbed X-ray spectrum. *MNRAS* **339**, 757–764.

Barger, A.J., Cowie, L.L., Mushotzky, R.F., Yang, Y., Wang, W., Steffen, A.T., Capak, P.: 2005, The Cosmic Evolution of Hard X-Ray-selected Active Galactic Nuclei. *AJ* **129**, 578 – 609.

Barvainis, R.: 1992, Dust reverberation - A model for the infrared variations of Fairall 9. *Astrophys. J.* **400**, 502 – 509.

Barvainis, R., Lonsdale, C., Antonucci, R.: 1996, Radio Spectra of Radio Quiet Quasars. *AJ* **111**, 1431.

Bassani, L., Dadina, M., Maiolino, R., Salvati, M., Risaliti, G., della Ceca, R., Matt, G., Zamorani, G.: 1999, A Three-dimensional Diagnostic Diagram for Seyfert 2 Galaxies: Probing X-Ray Absorption and Compton Thickness. *ApJS* **121**, 473 – 482.

Baum, S.A., O'Dea, C.P., Dallacassa, D., de Bruyn, A.G., Pedlar, A.: 1993, Kiloparsec-Scale Radio Emission in Seyfert Galaxies: Evidence for Starburst-driven Superwinds? *Astrophys. J.* **419**, 553.

Beckmann, V., Soldi, S., Ricci, C., Alfonso-Garzón, J., Courvoisier, T., Domingo, A., Gehrels, N., Lubiński, P., Mas-Hesse, J.M., Zdziarski, A.A.: 2009, The second INTEGRAL AGN catalogue. *A&A* **505**, 417 – 439.

Begelman, M.C.: 1995, The Acceleration and Collimation of Jets. *Proceedings of the National Academy of Science* **92**, 11442 – 11446.

Begelman, M.C., Blandford, R.D., Rees, M.J.: 1984, Theory of extragalactic radio sources. *Reviews of Modern Physics* **56**, 255 – 351.

Bendo, G.J., Joseph, R.D., Wells, M., Gallais, P., Haas, M., Heras, A.M., Klaas, U., Laureijs, R.J., Leech, K., Lemke, D., Metcalfe, L., Rowan-Robinson, M., Schulz, B., Telesco, C.: 2003, Dust Temperatures in the Infrared Space Observatory Atlas of Bright Spiral Galaxies. *AJ* **125**, 2361 – 2372.

Bian, W., Zhao, Y.: 2004, The black hole-bulge relation in active galactic nuclei. *MNRAS* **347**, 607 – 612.

Bianchi, S., Guainazzi, M., Matt, G., Chiaberge, M., Iwasawa, K., Fiore, F., Maiolino, R.: 2005, A search for changing-look AGN in the Grossan catalog. *A&A* **442**, 185 – 194.

Bianchi, S., Guainazzi, M., Matt, G., Fonseca Bonilla, N., Ponti, G.: 2009, CAIXA: a catalogue of AGN in the XMM-Newton archive. I. Spectral analysis. *A&A* **495**, 421 – 430. doi:10.1051/0004-6361:200810620.

Bianchi, S., Matt, G., Balestra, I., Guainazzi, M., Perola, G.C.: 2004, X-ray reprocessing in Seyfert galaxies: Simultaneous XMM-Newton/BeppoSAX observations. *A&A* **422**, 65 – 76.

Bianchi, S., Matt, G., Balestra, I., Perola, G.C.: 2003, The origin of the iron lines in NGC 7213. *A&A* **407**, L21 – L24. doi:10.1051/0004-6361:20031054.

Bianchi, S., Miniutti, G., Fabian, A.C., Iwasawa, K.: 2005, The XMM-Newton view of Mrk 3 and IXO 30. *MNRAS* **360**, 380 – 389.

Blandford, R.D., Begelman, M.C.: 1999, On the fate of gas accreting at a low rate on to a black hole. *MNRAS* **303**, L1 – L5.

Blandford, R.D., Payne, D.G.: 1982, Hydromagnetic flows from accretion discs and the production of radio jets. *MNRAS* **199**, 883 – 903.

Blandford, R.D., Znajek, R.L.: 1977, Electromagnetic extraction of energy from Kerr black holes. *MNRAS* **179**, 433 – 456.

Blissett, R.J., Cruise, A.M.: 1979, The restoration of astronomical X-ray spectra. *MNRAS* **186**, 45 – 57.

Blustin, A.J., Branduardi-Raymont, G., Behar, E., Kaastra, J.S., Kriss, G.A., Page, M.J., Kahn, S.M., Sako, M., Steenbrugge, K.C.: 2003, Multiwavelength

studies of the Seyfert 1 galaxy NGC 7469 II. X-ray and UV observations with XMM-Newton. *A&A* **403**, 481 – 492.

Blustin, A.J., Kriss, G.A., Holczer, T., Behar, E., Kaastra, J.S., Page, M.J., Kaspi, S., Branduardi-Raymont, G., Steenbrugge, K.C.: 2007, The mass-energy budget of the ionised outflow in NGC 7469. *A&A* **466**, 107 – 118.

Boldt, E.: 1987, The cosmic X-ray background. *Phys. Rep.* **146**, 215 – 257.

Boller, T., Brandt, W.N., Fink, H.: 1996, Soft X-ray properties of narrow-line Seyfert 1 galaxies. *A&A* **305**, 53.

Booler, R.V., Pedlar, A., Davies, R.D.: 1982, High-resolution 1666-MHz observations of the nucleus of NGC 4151. *MNRAS* **199**, 229 – 237.

Braito, V., Della Ceca, R., Piconcelli, E., Severgnini, P., Bassani, L., Cappi, M., Franceschini, A., Iwasawa, K., Malaguti, G., Marziani, P., Palumbo, G.G.C., Persic, M., Risaliti, G., Salvati, M.: 2004, The XMM-Newton and BeppoSAX view of the Ultra Luminous Infrared Galaxy MKN 231. *A&A* **420**, 79 – 88.

Braito, V., Reeves, J.N., Della Ceca, R., Ptak, A., Risaliti, G., Yaqoob, T.: 2009, A Suzaku observation of the ULIRG IRAS19254-7245: discerning the AGN component. *A&A* **504**, 53 – 59. doi:10.1051/0004-6361/200811516.

Brinkmann, W., Laurent-Muehleisen, S.A., Voges, W., Siebert, J., Becker, R.H., Brotherton, M.S., White, R.L., Gregg, M.D.: 2000, Radio and X-ray bright AGN: the ROSAT - FIRST correlation. *A&A* **356**, 445 – 462.

Buchanan, C.L., Gallimore, J.F., O'Dea, C.P., Baum, S.A., Axon, D.J., Robinson, A., Elitzur, M., Elvis, M.: 2006, Spitzer IRS Spectra of a Large Sample of Seyfert Galaxies: A Variety of Infrared Spectral Energy Distributions in the Local Active Galactic Nucleus Population. *AJ* **132**, 401 – 419.

Caccianiga, A., Severgnini, P., Braito, V., Della Ceca, R., Maccacaro, T., Wolter, A., Barcons, X., Carrera, F.J., Lehmann, I., Page, M.J., Saxton, R., Webb, N.A.: 2004, The XMM-Newton HBS28 sample: Studying the obscuration in hard X-ray selected AGNs. *A&A* **416**, 901–915.

Canosa, C.M., Worrall, D.M., Hardcastle, M.J., Birkinshaw, M.: 1999, X-ray observations of low-power radio galaxies from the B2 catalogue. *MNRAS* **310**, 30–38.

Cappi, M., Bassani, L., Comastri, A., Guainazzi, M., Maccacaro, T., Malaguti, G., Matt, G., Palumbo, G.G.C., Blanco, P., Dadina, M., dal Fiume, D., di Cocco, G., Fabian, A.C., Frontera, F., Maiolino, R., Piro, L., Trifoglio, M., Zhang, N.: 1999, BeppoSAX observations of MKN 3: Piercing through the torus of a Seyfert 2 galaxy. *A&A* **344**, 857–867.

Cappi, M., Panessa, F., Bassani, L., Dadina, M., Dicocco, G., Comastri, A., della Ceca, R., Filippenko, A.V., Gianotti, F., Ho, L.C., Malaguti, G., Mulchaey, J.S., Palumbo, G.G.C., Piconcelli, E., Sargent, W.L.W., Stephen, J., Trifoglio, M.: 2006, X-ray spectral survey with XMM-Newton of a complete sample of nearby Seyfert galaxies. *A&A* **446**, 459–470.

Cardamone, C.N., Moran, E.C., Kay, L.E.: 2007, "Hidden" Seyfert 2 Galaxies in the Chandra Deep Field North. *AJ* **134**, 1263–1275.

Cecil, G., Wilson, A.S., Tully, R.B.: 1992, The braided jets in the spiral galaxy NGC 4258. *Astrophys. J.* **390**, 365–377.

Chen, X.: 1995, Hot accretion discs with advection. *MNRAS* **275**, 641–648.

Cid Fernandes, R.J., Storchi-Bergmann, T., Schmitt, H.R.: 1998, The Stellar Content of Active Galaxies. *MNRAS* **297**, 579–616.

Colbert, E.J.M., Baum, S.A., Gallimore, J.F., O'Dea, C.P., Christensen, J.A.: 1996, Large-Scale Outflows in Edge-on Seyfert Galaxies. II. Kiloparsec-Scale Radio Continuum Emission. *Astrophys. J.* **467**, 551.

Colina, L., Garcia Vargas, M.L., Gonzalez Delgado, R.M., Mas-Hesse, J.M., Perez, E., Alberdi, A., Krabbe, A.: 1997, On the Origin of the Ultraviolet Continuum in Seyfert 2 Galaxies. *ApJL* **488**, L71.

Collin, S., Zahn, J.: 1999, Star formation and evolution in accretion disks around massive black holes. *A&A* **344**, 433–449.

Comastri, A.: 2004, Compton-Thick AGN: The Dark Side of the X-Ray Background. In: A. J. Barger (ed.) *Supermassive Black Holes in the Distant Universe*, *Astrophysics and Space Science Library*, **308**, 245.

Cornwell, T.J., Evans, K.F.: 1985, A simple maximum entropy deconvolution algorithm. *A&A* **143**, 77–83.

Corral, A., Barcons, X., Carrera, F.J., Ceballos, M.T., Mateos, S.: 2005, Simultaneous X-ray and optical spectroscopy of the Seyfert galaxy Mrk 993. *A&A* **431**, 97–102.

Dadina, M.: 2008, Seyfert galaxies in the local Universe (z ≤ 0.1): the average X-ray spectrum as seen by BeppoSAX. *A&A* **485**, 417–424.

Dahari, O., De Robertis, M.M.: 1988, Extinction, profile asymmetry, and tidal effects in Seyfert and starburst galaxies. *Astrophys. J.* **331**, 727–745.

de Bruyn, A.G., Wilson, A.S.: 1976, A 1415 MHz Survey of Seyfert and Related Galaxies. *A&A* **53**, 93.

de Bruyn, A.G., Wilson, A.S.: 1978, The radio properties of Seyfert galaxies. *A&A* **64**, 433–444.

de Grijp, M.H.K., Lub, J., Miley, G.K.: 1987, Warm IRAS sources. I. A. Catalogue of AGN candidates from the point source catalog. *A&AS* **70**, 95 – 114.

de Grijp, M.H.K., Miley, G.K., Lub, J., de Jong, T.: 1985, Infrared Seyferts - A new population of active galaxies? *Nature* **314**, 240 – 242.

De Robertis, M.M., Yee, H.K.C., Hayhoe, K.: 1998, A CCD Study of the Environment of Seyfert Galaxies. II. Testing the Interaction Hypothesis. *Astrophys. J.* **496**, 93.

De Rosa, A., Fabian, A.C., Piro, L.: 2002, The complex iron line in NGC 7469 observed by BeppoSAX. *MNRAS* **334**, L21 – L25.

de Vaucouleurs, G., de Vaucouleurs, A., Corwin, H.G. Jr., Buta, R.J., Paturel, G., Fouque, P.: 1991, Third Reference Catalogue of Bright Galaxies. Volume 1-3, XII, 2069 pp. 7 figs.. Springer-Verlag Berlin Heidelberg New York.

Decarli, R., Dotti, M., Fontana, M., Haardt, F.: 2008, Are the black hole masses in narrow-line Seyfert 1 galaxies actually small? *MNRAS* **386**, L15 – L19.

Della Ceca, R., Severgnini, P., Caccianiga, A., Comastri, A., Gilli, R., Fiore, F., Piconcelli, E., Malaguti, P., Vignali, C.: 2008, Heavily obscured AGN with BeppoSAX, INTEGRAL, SWIFT, XMM and Chandra: prospects for Simbol-X . *Memorie della Societa Astronomica Italiana* **79**, 65.

Dopita, M.A., Sutherland, R.S.: 1995, Spectral Signatures of Fast Shocks. II. Optical Diagnostic Diagrams. *Astrophys. J.* **455**, 468.

Dultzin-Hacyan, D., Krongold, Y., Fuentes-Guridi, I., Marziani, P.: 1999, The Close Environment of Seyfert Galaxies and Its Implication for Unification Models. *ApJL* **513**, L111 – L114.

Edelson, R.A.: 1987, Broad-band properties of the CfA Seyfert galaxies. I - Radio properties. *Astrophys. J.* **313**, 651 – 661.

Efstathiou, A., Rowan-Robinson, M.: 1995, Dusty discs in active galactic nuclei. *MNRAS* **273**, 649 – 661.

Elitzur, M.: 2006, The obscuring torus in AGN. *New Astronomy Review* **50**, 728 – 731.

Evans, I.N., Ford, H.C., Kinney, A.L., Antonucci, R.R.J., Armus, L., Caganoff, S.: 1991, HST imaging of the inner 3 arcseconds of NGC 1068 in the light of forbidden O III 5007 A. *ApJL* **369**, L27 – L30.

Falcke, H., Henkel, C., Peck, A.B., Hagiwara, Y., Prieto, M.A., Gallimore, J.F.: 2000, Discovery of a very luminous megamaser during a radio flare in the Seyfert 2 galaxy Mrk 348. *A&A* **358**, L17 – L20.

Falcke, H., Körding, E., Markoff, S.: 2004, A scheme to unify low-power accreting black holes. Jet-dominated accretion flows and the radio/X-ray correlation. *A&A* **414**, 895 – 903.

Falcke, H., Wilson, A.S., Simpson, C.: 1998, HST and VLA Observations of Seyfert 2 Galaxies: The Relationship between Radio Ejecta and the Narrow-Line Region. *Astrophys. J.* **502**, 199.

Fanaroff, B.L., Riley, J.M.: 1974, The morphology of extragalactic radio sources of high and low luminosity. *MNRAS* **167**, 31P – 36P.

Ferland, G.J., Netzer, H.: 1983, Are there any shock-heated galaxies. *Astrophys. J.* **264**, 105 – 113.

Ferrarese, L., Merritt, D.: 2000, A Fundamental Relation between Supermassive Black Holes and Their Host Galaxies. *ApJL* **539**, L9 – L12.

Ferruit, P., Wilson, A.S., Mulchaey, J.: 2000, Hubble Space Telescope WFPC2 Imaging of a Sample of Early-Type Seyfert Galaxies. *ApJS* **128**, 139 – 169.

Ferruit, P., Wilson, A.S., Mulchaey, J.S.: 1998, Hubble Space Telescope WFPC2 Imaging of the Seyfert Galaxy NGC 3516. *Astrophys. J.* **509**, 646 – 652.

Fiore, F., Grazian, A., Santini, P., Puccetti, S., Brusa, M., Feruglio, C., Fontana, A., Giallongo, E., Comastri, A., Gruppioni, C., Pozzi, F., Zamorani, G., Vignali, C.: 2008, Unveiling Obscured Accretion in the Chandra Deep Field-South. *Astrophys. J.* **672**, 94 – 101.

Fomalont, E.B., Perley, R.A.: 1999, Calibration and Editing. In: G. B. Taylor, C. L. Carilli, & R. A. Perley (ed.) *Synthesis Imaging in Radio Astronomy II*, *Astronomical Society of the Pacific Conference Series*, **180**, 79.

Friedli, D., Martinet, L.: 1993, Bars Within Bars in Lenticular and Spiral Galaxies - a Step in Secular Evolution. *A&A* **277**, 27.

Fukazawa, Y., Mizuno, T., Watanabe, S., Kokubun, M., Takahashi, H., Kawano, N., Nishino, S., Sasada, M., Shirai, H., Takahashi, T., Umeki, Y., 20 coauthors, : 2009, Modeling and Reproducibility of Suzaku HXD PIN/GSO Background. *Publ. Astron. Soc. Japan* **61**, 17.

Gallagher, S.C., Brandt, W.N., Chartas, G., Garmire, G.P., Sambruna, R.M.: 2002, X-Raying the Ultraluminous Infrared Starburst Galaxy and Broad Absorption Line QSO Markarian 231 with Chandra. *Astrophys. J.* **569**, 655 – 670.

Gallimore, J.F., Axon, D.J., O'Dea, C.P., Baum, S.A., Pedlar, A.: 2006, A Survey of Kiloparsec-Scale Radio Outflows in Radio-Quiet Active Galactic Nuclei. *AJ* **132**, 546 – 569.

Gallimore, J.F., Baum, S.A., O'Dea, C.P., Pedlar, A.: 1996, The Subarcsecond Radio Structure in NGC 1068. I. Observations and Results. *Astrophys. J.* **458**, 136.

Gallimore, J.F., Baum, S.A., O'Dea, C.P., Pedlar, A., Brinks, E.: 1999, Neutral Hydrogen (21 Centimeter) Absorption in Seyfert Galaxies: Evidence for Free-Free Absorption and Subkiloparsec Gaseous Disks. *Astrophys. J.* **524**, 684 – 706.

Gallo, L.C., Lehmann, I., Pietsch, W., Boller, T., Brinkmann, W., Friedrich, P., Grupe, D.: 2006, XMM-Newton observations of bright ROSAT selected active galactic nuclei with low intrinsic absorption. *MNRAS* **365**, 688 – 698.

Garcet, O., Gandhi, P., Gosset, E., Sprimont, P.G., Surdej, J., Borkowski, V., Tajer, M., Pacaud, F., Pierre, M., Chiappetti, L., Maccagni, D., Page, M.J., Carrera, F.J., Tedds, J.A., Mateos, S., Krumpe, M., Contini, T., Corral, A., Ebrero, J., Gavignaud, I., Schwope, A., Le Fèvre, O., Polletta, M., Rosen, S., Lonsdale, C., Watson, M., Borczyk, W., Vaisanen, P.: 2007, The XMM large scale structure survey: optical vs. X-ray classifications of active galactic nuclei and the unified scheme. *A&A* **474**, 473 – 489.

Gebhardt, K., Bender, R., Bower, G., Dressler, A., Faber, S.M., Filippenko, A.V., Green, R., Grillmair, C., Ho, L.C., Kormendy, J., Lauer, T.R., Magorrian, J., Pinkney, J., Richstone, D., Tremaine, S.: 2000, A Relationship between Nuclear Black Hole Mass and Galaxy Velocity Dispersion. *ApJL* **539**, L13 – L16.

Genzel, R., Weitzel, L., Tacconi-Garman, L.E., Blietz, M., Cameron, M., Krabbe, A., Lutz, D., Sternberg, A.: 1995, Infrared imaging and spectroscopy of NGC 7469. *Astrophys. J.* **444**, 129 – 145.

George, I.M., Fabian, A.C.: 1991, X-ray reflection from cold matter in active galactic nuclei and X-ray binaries. *MNRAS* **249**, 352 – 367.

Ghisellini, G., George, I.M., Fabian, A.C., Done, C.: 1991, Anisotropic inverse Compton emission. *MNRAS* **248**, 14 – 19.

Ghisellini, G., Haardt, F., Matt, G.: 1994, The Contribution of the Obscuring Torus to the X-Ray Spectrum of Seyfert Galaxies - a Test for the Unification Model. *MNRAS* **267**, 743.

Ghisellini, G., Haardt, F., Matt, G.: 2004, Aborted jets and the X-ray emission of radio-quiet AGNs. *A&A* **413**, 535−545.

Gilli, R., Comastri, A., Hasinger, G.: 2007, The synthesis of the cosmic X-ray background in the Chandra and XMM-Newton era. *A&A* **463**, 79−96.

Giovannini, G., Taylor, G.B., Arbizzani, E., Bondi, M., Cotton, W.D., Feretti, L., Lara, L., Venturi, T.: 1999, B2 1144+35: A Giant Low-Power Radio Galaxy with Superluminal Motion. *Astrophys. J.* **522**, 101−112.

González Delgado, R.M., Heckman, T., Leitherer, C.: 2001, The Nuclear and Circumnuclear Stellar Population in Seyfert 2 Galaxies: Implications for the Starburst-Active Galactic Nucleus Connection. *Astrophys. J.* **546**, 845−865.

González Delgado, R.M., Heckman, T., Leitherer, C., Meurer, G., Krolik, J., Wilson, A.S., Kinney, A., Koratkar, A.: 1998, Ultraviolet-Optical Observations of the Seyfert 2 Galaxies NGC 7130, NGC 5135, and IC 3639: Implications for the Starburst-Active Galactic Nucleus Connection. *Astrophys. J.* **505**, 174−198.

Goodrich, R.W.: 1989, Spectropolarimetry of 'narrow-line' Seyfert 1 galaxies. *Astrophys. J.* **342**, 224−234.

Goodrich, R.W., Veilleux, S., Hill, G.J.: 1994, Infrared spectroscopy of Seyfert 2 galaxies: A look through the obscuring Torus? *Astrophys. J.* **422**, 521−536.

Granato, G.L., Danese, L.: 1994, Thick Tori around Active Galactic Nuclei - a Comparison of Model Predictions with Observations of the Infrared Continuum and Silicate Features. *MNRAS* **268**, 235.

Grandi, P., Haardt, F., Ghisellini, G., Grove, E.J., Maraschi, L., Urry, C.M.: 1998, High-Energy Break and Reflection Features in the Seyfert Galaxy MCG+8-11-11. *Astrophys. J.* **498**, 220.

Gregory, P.C., Condon, J.J.: 1991, The 87GB catalog of radio sources covering delta between O and + 75 deg at 4.85 GHz. *ApJS* **75**, 1011–1291.

Griffith, M.R., Wright, A.E., Burke, B.F., Ekers, R.D.: 1995, The Parkes-MIT-NRAO (PMN) surveys. 6: Source catalog for the equatorial survey (-9.5 deg less than delta less than +10.0 deg). *ApJS* **97**, 347–453.

Griffiths, R.G., Warwick, R.S., Georgantopoulos, I., Done, C., Smith, D.A.: 1998, The broad-band X-ray spectrum of MRK 3. *MNRAS* **298**, 1159–1168.

Gruber, D.E., Matteson, J.L., Peterson, L.E., Jung, G.V.: 1999, The Spectrum of Diffuse Cosmic Hard X-Rays Measured with HEAO 1. *Astrophys. J.* **520**, 124–129.

Grupe, D., Beuermann, K., Mannheim, K., Thomas, H.: 1999, New bright soft X-ray selected ROSAT AGN. II. Optical emission line properties. *A&A* **350**, 805–815.

Grupe, D., Mathur, S.: 2004, M_{BH} - σ Relation for a Complete Sample of Soft X-Ray-selected Active Galactic Nuclei. *ApJL* **606**, L41–L44.

Guainazzi, M., Bianchi, S.: 2007, On the origin of soft X-rays in obscured AGN: answers from high-resolution spectroscopy with XMM-Newton. *MNRAS* **374**, 1290–1302.

Guainazzi, M., Fabian, A.C., Iwasawa, K., Matt, G., Fiore, F.: 2005, On the transmission-dominated to reprocessing-dominated spectral state transitions in Seyfert 2 galaxies. *MNRAS* **356**, 295–308.

Guainazzi, M., Matt, G., Brandt, W.N., Antonelli, L.A., Barr, P., Bassani, L.: 2000, A broad-band X-ray view of NGC 4945. *A&A* **356**, 463–474.

Guainazzi, M., Matt, G., Perola, G.C.: 2005, X-ray obscuration and obscured AGN in the local universe. *A&A* **444**, 119–132.

Haardt, F., Maraschi, L.: 1991, A two-phase model for the X-ray emission from Seyfert galaxies. *ApJL* **380**, L51–L54.

Haas, M., Chini, R., Meisenheimer, K., Stickel, M., Lemke, D., Klaas, U., Kreysa, E.: 1998, On the Far-Infrared Emission of Quasars. *ApJL* **503**, L109+.

Haniff, C.A., Wilson, A.S., Ward, M.J.: 1988, High-resolution emission-line imaging of Seyfert galaxies. I - Observations. II - Evidence for anisotropic ionizing radiation. *Astrophys. J.* **334**, 104–119.

Hasinger, G.: 2008, Absorption properties and evolution of active galactic nuclei. *A&A* **490**, 905–922.

Heckman, T.M., Blitz, L., Wilson, A.S., Armus, L., Miley, G.K.: 1989, A millimeter-wave survey of CO emission in Seyfert galaxies. *Astrophys. J.* **342**, 735–758.

Heckman, T.M., Gonzalez-Delgado, R., Leitherer, C., Meurer, G.R., Krolik, J., Wilson, A.S., Koratkar, A., Kinney, A.: 1997, A Powerful Nuclear Starburst in the Seyfert Galaxy Markarian 477: Implications for the Starburst–Active Galactic Nucleus Connection. *Astrophys. J.* **482**, 114.

Heckman, T.M., Ptak, A., Hornschemeier, A., Kauffmann, G.: 2005, The Relationship of Hard X-Ray and Optical Line Emission in Low-Redshift Active Galactic Nuclei. *Astrophys. J.* **634**, 161–168.

Heisler, C.A., Lumsden, S.L., Bailey, J.A.: 1997, Visibility of scattered broad-line emission in Seyfert 2 galaxies. *Nature* **385**, 700–702.

Helou, G., Soifer, B.T., Rowan-Robinson, M.: 1985, Thermal infrared and non-thermal radio - Remarkable correlation in disks of galaxies. *ApJL* **298**, L7−L11.

Ho, L.: 1999, Supermassive Black Holes in Galactic Nuclei: Observational Evidence and Astrophysical Consequences. In: S. K. Chakrabarti (ed.) *Observational Evidence for the Black Holes in the Universe*, Astrophysics and Space Science Library, **234**, 157.

Ho, L.C.: 2008, Nuclear Activity in Nearby Galaxies. *ARAA* **46**, 475−539.

Ho, L.C., Filippenko, A.V., Sargent, W.L.: 1995, A search for 'dwarf' Seyfert nuclei. 2: an optical spectral atlas of the nuclei of nearby galaxies. *ApJS* **98**, 477−593.

Ho, L.C., Filippenko, A.V., Sargent, W.L.: 1997, Optical spectral atlas of Seyfert nuclei (Ho+ 1995). *VizieR Online Data Catalog* **209**, 80477.

Ho, L.C., Filippenko, A.V., Sargent, W.L.W.: 1997, A Search for "Dwarf" Seyfert Nuclei. V. Demographics of Nuclear Activity in Nearby Galaxies. *Astrophys. J.* **487**, 568.

Ho, L.C., Ulvestad, J.S.: 2001, Radio Continuum Survey of an Optically Selected Sample of Nearby Seyfert Galaxies. *ApJS* **133**, 77−118.

Högbom, J.A.: 1974, Aperture Synthesis with a Non-Regular Distribution of Interferometer Baselines. *A&AS* **15**, 417.

Huchra, J., Burg, R.: 1992, The spatial distribution of active galactic nuclei. I - The density of Seyfert galaxies and liners. *Astrophys. J.* **393**, 90−97.

Ikeda, S., Awaki, H., Terashima, Y.: 2009, Study on X-Ray Spectra of Obscured Active Galactic Nuclei Based on Monte Carlo Simulation − An Interpretation of Observed Wide-Band Spectra. *Astrophys. J.* **692**, 608−617.

Itoh, T., Done, C., Makishima, K., Madejski, G., Awaki, H., Gandhi, P., Isobe, N., Dewangan, G.C., Griffthis, R.E., Anabuki, N., Okajima, T., Reeves, J.N., Takahashi, T., Ueda, Y., Eguchi, S., Yaqoob, T.: 2008, Suzaku Wide-Band X-Ray Spectroscopy of the Seyfert2 AGN in NGC 4945. *Publ. Astron. Soc. Japan* **60**, 251.

Ivezic, Z., Elitzur, M.: 1997, Self-similarity and scaling behaviour of infrared emission from radiatively heated dust - I. Theory. *MNRAS* **287**, 799 – 811.

Jaffe, W., Meisenheimer, K., Röttgering, H.J.A., Leinert, C., Richichi, A., Chesneau, O., Fraix-Burnet, D., Glazenborg-Kluttig, A., Granato, G., Graser, U., Heijligers, B., Köhler, R., Malbet, F., Miley, G.K., Paresce, F., Pel, J., Perrin, G., Przygodda, F., Schoeller, M., Sol, H., Waters, L.B.F.M., Weigelt, G., Woillez, J., de Zeeuw, P.T.: 2004, The central dusty torus in the active nucleus of NGC 1068. *Nature* **429**, 47 – 49.

Kaastra, J.S., Mewe, R., Liedahl, D.A., Komossa, S., Brinkman, A.C.: 2000, X-ray absorption lines in the Seyfert 1 galaxy NGC 5548 discovered with Chandra-LETGS. *A&A* **354**, L83 – L86.

Kaspi, S., Brandt, W.N., Netzer, H., Sambruna, R., Chartas, G., Garmire, G.P., Nousek, J.A.: 2000, Discovery of Narrow X-Ray Absorption Lines from NGC 3783 with the Chandra High Energy Transmission Grating Spectrometer. *ApJL* **535**, L17 – L20.

Keel, W.C., de Grijp, M.H.K., Miley, G.K.: 1988, New active galactic nuclei from the IRAS deep fields. *A&A* **203**, 250 – 254.

Keel, W.C., de Grijp, M.H.K., Miley, G.K., Zheng, W.: 1994, Warm IRAS Sources from the Point Source Catalog - Part Three - Emission Line Properties Correlations and AGN / Active Galactic Nuclei / Unified Models. *A&A* **283**, 791.

Kellermann, K.I., Sramek, R., Schmidt, M., Shaffer, D.B., Green, R.: 1989, VLA observations of objects in the Palomar Bright Quasar Survey. *AJ* **98**, 1195 – 1207.

Khachikian, E.Y., Weedman, D.W.: 1974, An atlas of Seyfert galaxies. *Astrophys. J.* **192**, 581 – 589.

Kharb, P., O'Dea, C.P., Baum, S.A., Colbert, E.J.M., Xu, C.: 2006, A Radio Study of the Seyfert Galaxy Markarian 6: Implications for Seyfert Life Cycles. *Astrophys. J.* **652**, 177 – 188.

King, A.: 2005, The AGN-Starburst Connection, Galactic Superwinds, and M_{BH}-σ. *ApJL* **635**, L121 – L123.

Kinkhabwala, A., Sako, M., Behar, E., Kahn, S.M., Paerels, F., Brinkman, A.C., Kaastra, J.S., Gu, M.F., Liedahl, D.A.: 2002, XMM-Newton Reflection Grating Spectrometer Observations of Discrete Soft X-Ray Emission Features from NGC 1068. *Astrophys. J.* **575**, 732 – 746.

Kinney, A.L., Schmitt, H.R., Clarke, C.J., Pringle, J.E., Ulvestad, J.S., Antonucci, R.R.J.: 2000, Jet Directions in Seyfert Galaxies. *Astrophys. J.* **537**, 152 – 177.

Klaas, U., Haas, M., Müller, S.A.H., Chini, R., Schulz, B., Coulson, I., Hippelein, H., Wilke, K., Albrecht, M., Lemke, D.: 2001, Infrared to millimetre photometry of ultra-luminous IR galaxies: New evidence favouring a 3-stage dust model. *A&A* **379**, 823 – 844.

Koide, S., Shibata, K., Kudoh, T.: 1999, Relativistic Jet Formation from Black Hole Magnetized Accretion Disks: Method, Tests, and Applications of a General RelativisticMagnetohydrodynamic Numerical Code. *Astrophys. J.* **522**, 727 – 752.

Kokubun, M., Makishima, K., Takahashi, T., Murakami, T., Tashiro, M., Fukazawa, Y., Kamae, T., Madejski, G.M., Nakazawa, K., Yamaoka, K., 48 coauthors, : 2007, In-Orbit Performance of the Hard X-Ray Detector on Board Suzaku. *Publ. Astron. Soc. Japan* **59**, 53 – 76.

Kormendy, J.: 2001, Supermassive Black Holes in Disk Galaxies. In: J. G. Funes & E. M. Corsini (ed.) *Galaxy Disks and Disk Galaxies*, *Astronomical Society of the Pacific Conference Series*, **230**, 247 – 256.

Kormendy, J., Richstone, D.: 1995, Inward Bound—The Search For Supermassive Black Holes In Galactic Nuclei. *ARAA* **33**, 581.

Koski, A.T.: 1978, Spectrophotometry of Seyfert 2 galaxies and narrow-line radio galaxies. *Astrophys. J.* **223**, 56 – 73.

Koyama, K., Tsunemi, H., Dotani, T., Bautz, M.W., Hayashida, K., Tsuru, T.G., Matsumoto, H., Ogawara, Y., Ricker, G.R., Doty, J., coauthers, .: 2007, X-Ray Imaging Spectrometer (XIS) on Board Suzaku. *Publ. Astron. Soc. Japan* **59**, 23 – 33.

Krolik, J.H.: 1999, Active galactic nuclei : from the central black hole to the galactic environment. Active galactic nuclei : from the central black hole to the galactic environment /Julian H. Krolik. Princeton, N. J. : Princeton University Press, c1999..

Krolik, J.H., Begelman, M.C.: 1988, Molecular tori in Seyfert galaxies - Feeding the monster and hiding it. *ApJ* **329**, 702 – 711.

Krolik, J.H., Madau, P., Zycki, P.T.: 1994, X-ray bumps, iron K-alpha lines, and X-ray suppression by obscuring tori in Seyfert galaxies. *ApJL* **420**, L57 – L61.

Kukula, M.J., Dunlop, J.S., Hughes, D.H., Rawlings, S.: 1998, The radio properties of radio-quiet quasars. *MNRAS* **297**, 366 – 382.

Kukula, M.J., Holloway, A.J., Pedlar, A., Meaburn, J., Lopez, J.A., Axon, D.J., Schilizzi, R.T., Baum, S.A.: 1996, Unusual radio and optical structures in the Seyfert galaxy Markarian 6. *MNRAS* **280**, 1283 – 1292.

Kukula, M.J., Pedlar, A., Baum, S.A., O'Dea, C.P.: 1995, High-resolution radio observations of the CfA Seyfert Sample -I. The observations. *MNRAS* **276**, 1262 – 1280.

Kwan, J., Krolik, J.H.: 1981, The formation of emission lines in quasars and Seyfert nuclei. *Astrophys. J.* **250**, 478 – 507.

Labita, M., Treves, A., Falomo, R., Uslenghi, M.: 2006, The BH mass of nearby QSOs: a comparison of the bulge luminosity and virial methods. *MNRAS* **373**, 551 – 560.

Lal, D.V.: 2002, Seyfert Galaxies: Nuclear Radio Structure and Unification. PhD thesis, Joint Astronomy Programme, Department of Physics, Indian Institute of Science, Bangalore 560 012, India. Indian Institute of Astrophysics, Bangalore 560 034, India.

Lal, D.V., Shastri, P., Gabuzda, D.C.: 2001, Seyfert Galaxies on milliarcsecond scales. *Astronomical and Astrophysical Transactions* **20**, 311 – 313.

Lal, D.V., Shastri, P., Gabuzda, D.C.: 2004, Milliarcsec-scale radio structure of a matched sample of Seyfert 1 and Seyfert 2 galaxies. *A&A* **425**, 99 – 108.

LaMassa, S.M., Heckman, T.M., Ptak, A., Hornschemeier, A., Martins, L., Sonnentrucker, P., Tremonti, C.: 2009, XMM-Newton Observations of a Complete Sample of Optically Selected Type 2 Seyfert Galaxies. *Astrophys. J.* **705**, 568 – 586. doi:10.1088/0004-637X/705/1/568.

Laor, A.: 2003, On the Nature of Low-Luminosity Narrow-Line Active Galactic Nuclei. *Astrophys. J.* **590**, 86 – 94.

Laurikainen, E., Salo, H., Teerikorpi, P., Petrov, G.: 1994, Environments of Seyfert galaxies. I. Construction of the sample and selection effects. *A&AS* **108**, 491–508.

Lawrence, A., Elvis, M.: 1982, Obscuration and the various kinds of Seyfert galaxies. *Astrophys. J.* **256**, 410–426.

Leahy, D.A., Creighton, J.: 1993, Montecarlo Simulations of X-Ray Spectra for Internally Illuminated Spherical Matter Distributions. *MNRAS* **263**, 314.

Leighly, K.M., Mushotzky, R.F., Yaqoob, T., Kunieda, H., Edelson, R.: 1996, The X-Ray Spectral Variability of Markarian 766. *Astrophys. J.* **469**, 147.

Levenson, N.A., Heckman, T.M., Krolik, J.H., Weaver, K.A., Życki, P.T.: 2006, Penetrating the Deep Cover of Compton-thick Active Galactic Nuclei. *Astrophys. J.* **648**, 111–127.

Levenson, N.A., Krolik, J.H., Życki, P.T., Heckman, T.M., Weaver, K.A., Awaki, H., Terashima, Y.: 2002, Extreme X-Ray Iron Lines in Active Galactic Nuclei. *ApJL* **573**, L81–L84.

Levenson, N.A., Weaver, K.A., Heckman, T.M.: 2001, The Seyfert-Starburst Connection in X-Rays. II. Results and Implications. *Astrophys. J.* **550**, 230–242.

Levenson, N.A., Weaver, K.A., Heckman, T.M., Awaki, H., Terashima, Y.: 2004, Accretion and Outflow in the Active Galactic Nucleus and Starburst of NGC 5135. *Astrophys. J.* **602**, 135–147.

Liedahl, D.A., Osterheld, A.L., Goldstein, W.H.: 1995, New calculations of Fe L-shell X-ray spectra in high-temperature plasmas. *ApJL* **438**, L115–L118.

Lonsdale, C.J., Lonsdale, C.J., Smith, H.E., Diamond, P.J.: 2003, VLBI Imaging of Luminous Infrared Galaxies: Active Galactic Nucleus Cores in Markarian 231, UGC 5101, and NGC 7469. *Astrophys. J.* **592**, 804–818.

Loredo, T.J., Epstein, R.I.: 1989, Analyzing gamma-ray burst spectral data. *Astrophys. J.* **336**, 896 – 919.

Magdziarz, P., Zdziarski, A.A.: 1995, Angle-dependent Compton reflection of X-rays and gamma-rays. *MNRAS* **273**, 837 – 848.

Magorrian, J., Tremaine, S., Richstone, D., Bender, R., Bower, G., Dressler, A., Faber, S.M., Gebhardt, K., Green, R., Grillmair, C., Kormendy, J., Lauer, T.: 1998, The Demography of Massive Dark Objects in Galaxy Centers. *AJ* **115**, 2285 – 2305.

Maiolino, R., Marconi, A., Salvati, M., Risaliti, G., Severgnini, P., Oliva, E., La Franca, F., Vanzi, L.: 2001, Dust in active nuclei. I. Evidence for "anomalous" properties. *A&A* **365**, 28 – 36.

Maiolino, R., Rieke, G.H.: 1995, Low-Luminosity and Obscured Seyfert Nuclei in Nearby Galaxies. *Astrophys. J.* **454**, 95.

Maiolino, R., Ruiz, M., Rieke, G.H., Papadopoulos, P.: 1997, Molecular Gas, Morphology, and Seyfert Galaxy Activity. *Astrophys. J.* **485**, 552.

Maiolino, R., Salvati, M., Bassani, L., Dadina, M., della Ceca, R., Matt, G., Risaliti, G., Zamorani, G.: 1998, Heavy obscuration in X-ray weak AGNs. *A&A* **338**, 781 – 794.

Malkan, M.A., Gorjian, V., Tam, R.: 1998, A Hubble Space Telescope Imaging Survey of Nearby Active Galactic Nuclei. *ApJS* **117**, 25.

Maloney, P.R., Reynolds, C.S.: 2000, ASCA Observation of an X-Ray-luminous Active Nucleus in Markarian 231. *ApJL* **545**, L23 – L26.

Marconi, A., Risaliti, G., Gilli, R., Hunt, L.K., Maiolino, R., Salvati, M.: 2004, Local supermassive black holes, relics of active galactic nuclei and the X-ray background. *MNRAS* **351**, 169 – 185.

Marscher, A.P.: 1995, Probes of the Inner Jets of Blazars. *Proceedings of the National Academy of Science* **92**, 11439 – 11441.

Marscher, A.P.: 2009, Jets in Active Galactic Nuclei. *ArXiv e-prints*, in press.

Mason, K.O., Branduardi-Raymont, G., Ogle, P.M., Page, M.J., Puchnarewicz, E.M., Behar, E., Córdova, F.A., Davis, S., Maraschi, L., McHardy, I.M., O'Brien, P.T., Priedhorsky, W.C., Sasseen, T.P.: 2003, The X-Ray Spectrum of the Seyfert I Galaxy Markarian 766: Dusty Warm Absorber or Relativistic Emission Lines? *Astrophys. J.* **582**, 95 – 104.

Mateos, S., Barcons, X., Carrera, F.J., Ceballos, M.T., Caccianiga, A., Lamer, G., Maccacaro, T., Page, M.J., Schwope, A., Watson, M.G.: 2005, X-ray spectra of XMM-Newton serendipitous medium flux sources. *A&A* **433**, 855 – 873.

Mathur, S., Kuraszkiewicz, J., Czerny, B.: 2001, Evolution of active galaxies: black-hole mass-bulge relations for narrow line objects. *New Astronomy* **6**, 321 – 329.

Matt, G., Bianchi, S., de Rosa, A., Grandi, P., Perola, G.C.: 2006, XMM-Newton observation of the bright Seyfert 1 galaxy, MCG+8-11-11. *A&A* **445**, 451 – 456.

Matt, G., Fabian, A.C., Guainazzi, M., Iwasawa, K., Bassani, L., Malaguti, G.: 2000, The X-ray spectra of Compton-thick Seyfert 2 galaxies as seen by BeppoSAX. *MNRAS* **318**, 173 – 179.

Matt, G., Fiore, F., Perola, G.C., Piro, L., Fink, H.H., Grandi, P., Matsuoka, M., Oliva, E., Salvati, M.: 1996, A reflection-dominated X-ray spectrum discovered by ASCA in the Circinus galaxy. *MNRAS* **281**, L69 – L73.

Matt, G., Guainazzi, M., Frontera, F., Bassani, L., Brandt, W.N., Fabian, A.C., Fiore, F., Haardt, F., Iwasawa, K., Maiolino, R., Malaguti, G., Marconi, A., Matteuzzi, A., Molendi, S., Perola, G.C., Piraino, S., Piro, L.: 1997, Hard X-ray detection of NGC 1068 with BeppoSAX. *A&A* **325**, L13 – L16.

Matt, G., Guainazzi, M., Maiolino, R., Molendi, S., Perola, G.C., Antonelli, L.A., Bassani, L., Brandt, W.N., Fabian, A.C., Fiore, F., Iwasawa, K., Malaguti, G., Marconi, A., Poutanen, J.: 1999, One more surprise from the Circinus Galaxy: BeppoSAX discovery of a transmission component in hard X-rays. *A&A* **341**, L39 – L42.

Matt, G., Perola, G.C., Fiore, F., Guainazzi, M., Nicastro, F., Piro, L.: 2000, The BeppoSAX observation of Mrk 766. *A&A* **363**, 863 – 868.

Matt, G., Perola, G.C., Piro, L.: 1991, The iron line and high energy bump as X-ray signatures of cold matter in Seyfert 1 galaxies. *A&A* **247**, 25 – 34.

Mauder, W., Weigelt, G., Appenzeller, I., Wagner, S.J.: 1994, High resolution optical images of the starburst ring around the Seyfert nucleus of NGC7469. *A&A* **285**, 44 – 50.

Mazzuca, L.M., Knapen, J.H., Veilleux, S., Regan, M.W.: 2008, A Connection between Star Formation in Nuclear Rings and Their Host Galaxies. *ApJS* **174**, 337 – 365.

Merloni, A., Heinz, S., di Matteo, T.: 2003, A Fundamental Plane of black hole activity. *MNRAS* **345**, 1057 – 1076.

Meurs, E.J.A., Wilson, A.S.: 1984, Markarian Seyfert galaxies - Optical and radio luminosity functions and other statistical studies. *A&A* **136**, 206 – 226.

Mewe, R., Gronenschild, E.H.B.M., van den Oord, G.H.J.: 1985, Calculated X-radiation from optically thin plasmas. V. *A&AS* **62**, 197 – 254.

Middelberg, E., Roy, A.L., Nagar, N.M., Krichbaum, T.P., Norris, R.P., Wilson, A.S., Falcke, H., Colbert, E.J.M., Witzel, A., Fricke, K.J.: 2004, Motion and properties of nuclear radio components in Seyfert galaxies seen with VLBI. *A&A* **417**, 925 – 944.

Miller, J.S., Goodrich, R.W.: 1990, Spectropolarimetry of high-polarization Seyfert 2 galaxies and unified Seyfert theories. *Astrophys. J.* **355**, 456 – 467.

Miller, J.S., Goodrich, R.W., Mathews, W.G.: 1991, Multidirectional views of the active nucleus of NGC 1068. *Astrophys. J.* **378**, 47 – 64.

Miller, L., Turner, T.J., Reeves, J.N., George, I.M., Porquet, D., Nandra, K., Dovciak, M.: 2006, Variable iron-line emission near the black hole of Markarian 766. *A&A* **453**, L13 – L16.

Mineshige, S., Kawaguchi, T., Takeuchi, M., Hayashida, K.: 2000, Slim-Disk Model for Soft X-Ray Excess and Variability of Narrow-Line Seyfert 1 Galaxies. *Publ. Astron. Soc. Japan* **52**, 499 – 508.

Miyaji, T., Wilson, A.S., Perez-Fournon, I.: 1992, The radio source and bipolar nebulosity in the Seyfert galaxy NGC 3516. *Astrophys. J.* **385**, 137 – 145.

Momjian, E., Romney, J.D., Carilli, C.L., Troland, T.H.: 2003, Sensitive VLBI Continuum and H I Absorption Observations of NGC 7674: First Scientific Observations with the Combined Array VLBA, VLA, and Arecibo. *Astrophys. J.* **597**, 809 – 822.

Moran, E.C.: 2000, Radio properties of NLS1s. *New Astronomy Review* **44**, 527 – 529.

Morganti, R., Tsvetanov, Z.I., Gallimore, J., Allen, M.G.: 1999, Radio continuum morphology of southern Seyfert galaxies. *A&AS* **137**, 457 – 471.

Morrison, R., McCammon, D.: 1983, Interstellar photoelectric absorption cross sections, 0.03-10 keV. *Astrophys. J.* **270**, 119 – 122.

Morse, J.A., Cecil, G., Wilson, A.S., Tsvetanov, Z.I.: 1998, Inclined Gas Disks in the Lenticular Seyfert Galaxy NGC 5252. *Astrophys. J.* **505**, 159 – 173.

Mulchaey, J.S., Koratkar, A., Ward, M.J., Wilson, A.S., Whittle, M., Antonucci, R.R.J., Kinney, A.L., Hurt, T.: 1994, Multiwavelength tests of the dusty torus model for Seyfert galaxies. *Astrophys. J.* **436**, 586 – 598.

Mundell, C.G., Ferruit, P., Nagar, N., Wilson, A.S.: 2009, Radio Variability in Seyfert Nuclei. *Astrophys. J.* **703**, 802 – 815.

Mundell, C.G., Holloway, A.J., Pedlar, A., Meaburn, J., Kukula, M.J., Axon, D.J.: 1995, Anisotropic radio and optical emission in the Seyfert nucleus of NGC 3227. *MNRAS* **275**, 67 – 75.

Mundell, C.G., Wilson, A.S., Ulvestad, J.S., Roy, A.L.: 2000, Parsec-Scale Images of Flat-Spectrum Radio Sources in Seyfert Galaxies. *Astrophys. J.* **529**, 816 – 831.

Mundell, C.G., Wrobel, J.M., Pedlar, A., Gallimore, J.F.: 2003, The Nuclear Regions of the Seyfert Galaxy NGC 4151: Parsec-Scale H I Absorption and a Remarkable Radio Jet. *Astrophys. J.* **583**, 192 – 204.

Nagar, N.M., Wilson, A.S.: 1999, The Relative Orientation of Nuclear Accretion and Galaxy Stellar Disks in Seyfert Galaxies. *Astrophys. J.* **516**, 97 – 113.

Nagar, N.M., Wilson, A.S., Mulchaey, J.S., Gallimore, J.F.: 1999, Radio Structures of Seyfert Galaxies. VIII. A Distance- and Magnitude-Limited Sample of Early-Type Galaxies. *ApJS* **120**, 209 – 245.

Nandra, K., George, I.M., Mushotzky, R.F., Turner, T.J., Yaqoob, T.: 1997, ASCA Observations of Seyfert 1 Galaxies. II. Relativistic Iron K alpha Emission. *Astrophys. J.* **477**, 602.

Nandra, K., George, I.M., Mushotzky, R.F., Turner, T.J., Yaqoob, T.: 1997, On the Dependence of the Iron K-Line Profiles with Luminosity in Active Galactic Nuclei. *ApJL* **488**, L91.

Nandra, K., Pounds, K.A.: 1994, GINGA Observations of the X-Ray Spectra of Seyfert Galaxies. *MNRAS* **268**, 405.

Narayan, R., Igumenshchev, I.V., Abramowicz, M.A.: 2000, Self-similar Accretion Flows with Convection. *Astrophys. J.* **539**, 798 – 808.

Narayan, R., Nityananda, R.: 1986, Maximum entropy image restoration in astronomy. *ARAA* **24**, 127 – 170.

Narayan, R., Yi, I.: 1994, Advection-dominated accretion: A self-similar solution. *ApJL* **428**, L13 – L16.

Neff, S.G., de Bruyn, A.G.: 1983, The compact radio core of MKN 348 - Evidence for directed outflow in a type 2 Seyfert galaxy. *A&A* **128**, 318 – 324.

Nelson, C.H., Whittle, M.: 1995, Stellar and Gaseous Kinematics of Seyfert Galaxies. I. Spectroscopic Data. *ApJS* **99**, 67.

Nenkova, M., Ivezić, Ž., Elitzur, M.: 2002, Dust Emission from Active Galactic Nuclei. *ApJL* **570**, L9 – L12.

Netzer, H., Maoz, D.: 1990, On the emission-line response to continuum variations in the Seyfert galaxy NGC 5548. *ApJL* **365**, L5 – L7.

Nicastro, F., Martocchia, A., Matt, G.: 2003, The Lack of Broad-Line Regions in Low Accretion Rate Active Galactic Nuclei as Evidence of Their Origin in the Accretion Disk. *ApJL* **589**, L13 – L16.

Norris, R.P., Allen, D.A., Roche, P.F.: 1988, The radio emission from far-infrared galaxies - Seyfert or starburst? *MNRAS* **234**, 773 – 782.

Orienti, M., Prieto, M.A.: 2010, Radio structures of the nuclei of nearby Seyfert galaxies and the nature of the missing diffuse emission. *MNRAS* **401**, 2599 – 2610.

Osterbrock, D.E.: 1981, Seyfert galaxies with weak broad H alpha emission lines. *Astrophys. J.* **249**, 462 – 470.

Osterbrock, D.E.: 1989, Astrophysics of gaseous nebulae and active galactic nuclei.

Osterbrock, D.E., Ferland, G.J.: 2006, Astrophysics of gaseous nebulae and active galactic nuclei.

Osterbrock, D.E., Pogge, R.W.: 1985, The spectra of narrow-line Seyfert 1 galaxies. *Astrophys. J.* **297**, 166 – 176.

Osterbrock, D.E., Pogge, R.W.: 1987, Optical spectra of narrow emission line Palomar-Green galaxies. *Astrophys. J.* **323**, 108 – 117.

Page, M.J., Loaring, N.S., Dwelly, T., Mason, K.O., McHardy, I., Gunn, K., Moss, D., Sasseen, T., Cordova, F., Kennea, J., Seymour, N.: 2006, X-ray spectra of sources in the 13^H XMM-Newton/Chandra deep field. *MNRAS* **369**, 156 – 170.

Panessa, F., Barcons, X., Bassani, L., Cappi, M., Carrera, F.J., Ho, L.C., Pellegrini, S.: 2007, The X-ray and radio connection in low-luminosity active nuclei. *A&A* **467**, 519 – 527.

Panessa, F., Bassani, L.: 2002, Unabsorbed Seyfert 2 galaxies. *A&A* **394**, 435 – 442.

Panessa, F., Bassani, L., Cappi, M., Dadina, M., Barcons, X., Carrera, F.J., Ho, L.C., Iwasawa, K.: 2006, On the X-ray, optical emission line and black hole mass properties of local Seyfert galaxies. *A&A* **455**, 173 – 185.

Pappa, A., Georgantopoulos, I., Stewart, G.C., Zezas, A.L.: 2001, The X-ray spectra of optically selected Seyfert 2 galaxies: are there any Seyfert 2 galaxies with no absorption? *MNRAS* **326**, 995 – 1006.

Pedlar, A., Kukula, M.J., Longley, D.P.T., Muxlow, T.W.B., Axon, D.J., Baum, S., O'Dea, C., Unger, S.W.: 1993, The Radio Nucleus of NGC4151 at 5-GHZ and 8-GHZ. *MNRAS* **263**, 471.

Pedlar, A., Unger, S.W., Dyson, J.E.: 1985, Radio Seyferts and the forbidden-line region. *MNRAS* **214**, 463 – 473.

Perola, G.C., Matt, G., Fiore, F., Grandi, P., Guainazzi, M., Haardt, F., Maraschi, L., Mineo, T., Nicastro, F., Piro, L.: 2000, BeppoSAX observations of Mrk 509 and MCG +8-11-11. *A&A* **358**, 117 – 124.

Peterson, B.M.: 1997, An Introduction to Active Galactic Nuclei. An introduction to active galactic nuclei, Publisher: Cambridge, New York Cambridge University Press, 1997 Physical description xvi, 238 p. ISBN 0521473489.

Peterson, B.M., Ferrarese, L., Gilbert, K.M., Kaspi, S., Malkan, M.A., Maoz, D., Merritt, D., Netzer, H., Onken, C.A., Pogge, R.W., Vestergaard, M., Wandel, A.: 2004, Central Masses and Broad-Line Region Sizes of Active Galactic Nuclei. II. A Homogeneous Analysis of a Large Reverberation-Mapping Database. *Astrophys. J.* **613**, 682 – 699.

Phillips, M.M., Charles, P.A., Baldwin, J.A.: 1983, Nearby galaxies with Seyfert-like nuclei. *Astrophys. J.* **266**, 485 – 501.

Pier, E.A., Krolik, J.H.: 1992, Infrared spectra of obscuring dust tori around active galactic nuclei. I - Calculational method and basic trends. *Astrophys. J.* **401**, 99 – 109.

Pier, E.A., Krolik, J.H.: 1993, Infrared Spectra of Obscuring Dust Tori around Active Galactic Nuclei. II. Comparison with Observations. *Astrophys. J.* **418**, 673 – +.

Piro, L., de Rosa, A., Matt, G., Perola, G.C.: 2005, Clearing up the clouds around NGC 4151: evidence of a highly ionized absorber. *A&A* **441**, L13 – L17.

Pogge, R.W.: 1988, A extended ionizing radiation cone from the nucleus of the Seyfert 2 galaxy NGC 1068. *Astrophys. J.* **328**, 519 – 522.

Pogge, R.W.: 1989, Ionized gas in the nuclear regions of nearby non-Seyfert spiral galaxies. *ApJs* **71**, 433 – 453.

Polletta, M., Bassani, L., Malaguti, G., Palumbo, G.G.C., Caroli, E.: 1996, A Multiwavelength Catalog of Seyfert 2 Galaxies Observed in the 2–10 keV Energy Band. *ApJS* **106**, 399.

Polletta, M., Wilkes, B.J., Siana, B., Lonsdale, C.J., Kilgard, R., Shupe, D.L., Surace, J., Smith, H.E., Owen, F.: 2006, The Most Obscured AGN in the Chandra/SWIRE Survey in the Lockman Hole. In: A. Wilson (ed.) *The X-ray Universe 2005*, *ESA Special Publication*, **604**, 807.

Pounds, K.A., Done, C., Osborne, J.P.: 1995, RE 1034+39: a high-state Seyfert galaxy? *MNRAS* **277**, L5 – L10.

Pounds, K.A., Page, K.L.: 2005, An XMM-Newton observation of Mkn 3 - a Seyfert galaxy just over the edge. *MNRAS* **360**, 1123 – 1131.

Prieto, M.A., Pérez García, A.M., Rodríguez Espinosa, J.M.: 2001, On the relation between the IR continuum and the active galactic nucleus in Seyfert galaxies. *A&A* **377**, 60 – 65.

Pringle, J.E., Antonucci, R.R.J., Clarke, C.J., Kinney, A.L., Schmitt, H.R., Ulvestad, J.S.: 1999, Direct Measurement of the Jet Geometry in Seyfert Galaxies. *ApJL* **526**, L9 – L12.

Ptak, A., Heckman, T., Levenson, N.A., Weaver, K., Strickland, D.: 2003, A Chandra Survey of the Nearest Ultraluminous Infrared Galaxies: Obscured Active Galactic Nuclei or Superstarbursts? *Astrophys. J.* **592**, 782 – 803.

Quataert, E., Gruzinov, A.: 2000, Convection-dominated Accretion Flows. *Astrophys. J.* **539**, 809 – 814.

Rafanelli, P., Violato, M., Baruffolo, A.: 1995, On the excess of physical companions among Seyfert galaxies. *AJ* **109**, 1546 – 1554.

Ranalli, P., Comastri, A., Setti, G.: 2003, The 2-10 keV luminosity as a Star Formation Rate indicator. *A&A* **399**, 39 – 50.

Reynolds, C.S.: 1997, An X-ray spectral study of 24 type 1 active galactic nuclei. *MNRAS* **286**, 513 – 537.

Risaliti, G., Braito, V., Laparola, V., Bianchi, S., Elvis, M., Fabbiano, G., Maiolino, R., Matt, G., Reeves, J., Salvati, M., Wang, J.: 2009, A Strong Excess in the 20-100 keV Emission of NGC 1365. *ApJL* **705**, L1 – L5.

Risaliti, G., Elvis, M., Fabbiano, G., Baldi, A., Zezas, A.: 2005, Rapid Compton-thick/Compton-thin Transitions in the Seyfert 2 Galaxy NGC 1365. *ApJL* **623**, L93 – L96.

Risaliti, G., Maiolino, R., Salvati, M.: 1999, The Distribution of Absorbing Column Densities among Seyfert 2 Galaxies. *Astrophys. J.* **522**, 157 – 164.

Risaliti, G., Salvati, M., Elvis, M., Fabbiano, G., Baldi, A., Bianchi, S., Braito, V., Guainazzi, M., Matt, G., Miniutti, G., Reeves, J., Soria, R., Zezas, A.: 2009, The XMM-Newton long look of NGC 1365: uncovering of the obscured X-ray source. *MNRAS* **393**, L1 – L5.

Rodriguez Espinosa, J.M., Perez Garcia, A.M., Lemke, D., Meisenheimer, K.: 1996, Bimodal dust emission in three classical Seyfert galaxies: NGC 3227, NGC 4051 and NGC 4151. *A&A* **315**, L129 – L132.

Rodriguez Espinosa, J.M., Rudy, R.J., Jones, B.: 1987, Star formation in Seyfert galaxies. *Astrophys. J.* **312**, 555 – 565.

Rowan-Robinson, M.: 1977, On the unity of activity in galaxies. *Astrophys. J.* **213**, 635 – 647.

Roy, A.L., Norris, R.P., Kesteven, M.J., Troup, E.R., Reynolds, J.E.: 1994, Compact radio cores in Seyfert galaxies. *Astrophys. J.* **432**, 496 – 507.

Roy, A.L., Norris, R.P., Kesteven, M.J., Troup, E.R., Reynolds, J.E.: 1998, Seyfert galaxies and the radio-far-infrared correlation. *MNRAS* **301**, 1019 – 1030.

Rush, B., Malkan, M.A., Edelson, R.A.: 1996, The Radio Properties of Seyfert Galaxies in the 12 Micron and CfA Samples. *Astrophys. J.* **473**, 130.

Sadler, E.M., Slee, O.B., Reynolds, J.E., Roy, A.L.: 1995, Parsec-scale radio cores in spiral galaxies. *MNRAS* **276**, 1373 – 1381.

Sako, M., Kahn, S.M., Paerels, F., Liedahl, D.A.: 2000, The Chandra High-Energy Transmission Grating Observation of an X-Ray Ionization Cone in Markarian 3. *ApJL* **543**, L115 – L118.

Salvato, M., Greiner, J., Kuhlbrodt, B.: 2004, Multiwavelength Scaling Relations for Nuclei of Seyfert Galaxies. *ApJL* **600**, L31 – L34.

Sambruna, R.M., Netzer, H., Kaspi, S., Brandt, W.N., Chartas, G., Garmire, G.P., Nousek, J.A., Weaver, K.A.: 2001, High-Resolution X-Ray Spectroscopy of the Seyfert 2 Galaxy Circinus with Chandra. *ApJL* **546**, L13 – L17.

Sandage, A.: Classification and Stellar Content of Galaxies Obtained from Direct Photography 1975, Galaxies and the Universe, 1.

Sanders, D.B., Mazzarella, J.M., Kim, D., Surace, J.A., Soifer, B.T.: 2003, The IRAS Revised Bright Galaxy Sample. *AJ* **126**, 1607 – 1664.

Sanders, D.B., Mirabel, I.F.: 1985, CO detections and IRAS observations of bright radio spiral galaxies at CZ equal or less than 9000 kilometers per second. *ApJL* **298**, L31 – L35.

Sanders, D.B., Mirabel, I.F.: 1996, Luminous Infrared Galaxies. *ARAA* **34**, 749.

Schmidt, M., Green, R.F.: 1983, Quasar evolution derived from the Palomar bright quasar survey and other complete quasar surveys. *Astrophys. J.* **269**, 352 – 374.

Schmitt, H.R., Antonucci, R.R.J., Ulvestad, J.S., Kinney, A.L., Clarke, C.J., Pringle, J.E.: 2001, Testing the Unified Model with an Infrared-selected Sample of Seyfert Galaxies. *Astrophys. J.* **555**, 663 – 672.

Schmitt, H.R., Donley, J.L., Antonucci, R.R.J., Hutchings, J.B., Kinney, A.L.: 2003, A Hubble Space Telescope Survey of Extended [O III] λ5007 Emission in a Far-Infrared Selected Sample of Seyfert Galaxies: Observations. *ApJS* **148**, 327 – 352.

Schmitt, H.R., Donley, J.L., Antonucci, R.R.J., Hutchings, J.B., Kinney, A.L., Pringle, J.E.: 2003, A Hubble Space Telescope Survey of Extended [O III] λ5007 Å Emission in a Far-Infrared-Selected Sample of Seyfert Galaxies: Results. *Astrophys. J.* **597**, 768 – 779.

Schmitt, H.R., Storchi-Bergmann, T., Baldwin, J.A.: 1994, Anisotropic high-excitation emission and chemical abundances in the Seyfert 2 galaxy NGC 5643. *Astrophys. J.* **423**, 237 – 247.

Schommer, R.A., Caldwell, N., Wilson, A.S., Baldwin, J.A., Phillips, M.M., Williams, T.B., Turtle, A.J.: 1988, Ionized gas and radio emission in the barred Seyfert galaxy NGC 5728. *Astrophys. J.* **324**, 154 – 171.

Schurch, N.J., Warwick, R.S.: 2002, Characterizing the complex absorber in NGC 4151. *MNRAS* **334**, 811 – 818.

Schurch, N.J., Warwick, R.S., Griffiths, R.E., Kahn, S.M.: 2004, The complex soft X-ray spectrum of NGC 4151. *MNRAS* **350**, 1 – 9.

Serlemitsos, P.J., Soong, Y., Chan, K.W., Okajima, T., Lehan, J.P., Maeda, Y., Itoh, K., Mori, H., Iizuka, R., Itoh, A., coauthors, .: 2007, The X-Ray Telescope onboard Suzaku. *Publ. Astron. Soc. Japan* **59**, 9 – 21.

Severgnini, P., Caccianiga, A., Braito, V., Della Ceca, R., Maccacaro, T., Wolter, A., Sekiguchi, K., Sasaki, T., Yoshida, M., Akiyama, M., Watson, M.G., Barcons, X., Carrera, F.J., Pietsch, W., Webb, N.A.: 2003, XMM-Newton observations reveal AGN in apparently normal galaxies. *A&A* **406**, 483 – 492.

Seyfert, C.K.: 1943, Nuclear Emission in Spiral Nebulae. *Astrophys. J.* **97**, 28.

Shakura, N.I., Sunyaev, R.A.: 1973, Black holes in binary systems. Observational appearance. *A&A* **24**, 337 – 355.

Shastri, P., Lal, D.V., Gabuzda, D.C.: 2003, Jets in Seyfert Galaxies. In: S. Collin, F. Combes, & I. Shlosman (ed.) *Active Galactic Nuclei: From Central Engine to Host Galaxy, Astronomical Society of the Pacific Conference Series*, **290**, 311.

Shen, Z., Jiang, D.R., Kameno, S., Chen, Y.J.: 2001, Superluminal motion in a compact steep spectrum radio source 3C 138. *A&A* **370**, 65 – 69.

Shlosman, I., Begelman, M.C., Frank, J.: 1990, The fuelling of active galactic nuclei. *Nature* **345**, 679 – 686.

Shu, X.W., Yaqoob, T., Wang, J.X.: 2010, The Cores of the Fe Kα Lines in Active Galactic Nuclei: An Extended Chandra High Energy Grating Sample. *ApJS* **187**, 581 – 606. doi:10.1088/0067-0049/187/2/581.

Silverman, J.D., Green, P.J., Barkhouse, W.A., Kim, D., Aldcroft, T.L., Cameron, R.A., Wilkes, B.J., Mossman, A., Ghosh, H., Tananbaum, H., Smith, M.G., Smith, R.C., Smith, P.S., Foltz, C., Wik, D., Jannuzi, B.T.: 2005, Hard X-Ray-emitting Active Galactic Nuclei Selected by the Chandra Multiwavelength Project. *Astrophys. J.* **618**, 123 – 138.

Simien, F., de Vaucouleurs, G.: 1986, Systematics of bulge-to-disk ratios. *Astrophys. J.* **302**, 564 – 578.

Smith, D.A., Done, C.: 1996, Unified theories of active galactic nuclei: a hard X-ray sample of Seyfert 2 galaxies. *MNRAS* **280**, 355 – 377.

Sopp, H.M., Alexander, P.: 1991, A composite plot of far-infrared versus radio luminosity, and the origin of far-infrared luminosity in quasars. *MNRAS* **251**, 14P – 16P.

Spinoglio, L., Malkan, M.A.: 1989, The 12 micron galaxy sample. I - Luminosity functions and a new complete active galaxy sample. *Astrophys. J.* **342**, 83 – 99.

Stasińska, G.: 1984, Confrontation of a sample of Seyfert 2 galaxies with photoionized models. *A&A* **135**, 341 – 355.

Stawarz, Ł., Sikora, M., Ostrowski, M., Begelman, M.C.: 2004, On Multiwavelength Emission of Large-Scale Quasar Jets. *Astrophys. J.* **608**, 95 – 107.

Steffen, A.T., Barger, A.J., Capak, P., Cowie, L.L., Mushotzky, R.F., Yang, Y.: 2004, An Optical Catalog of the Chandra Large Area Synoptic X-Ray Survey Sources. *AJ* **128**, 1483 – 1500.

Stevens, J.A., Amure, M., Gear, W.K.: 2005, Dust in spiral galaxies: global properties. *MNRAS* **357**, 361 – 380.

Sulentic, J.W., Bachev, R., Marziani, P., Negrete, C.A., Dultzin, D.: 2007, C IV λ1549 as an Eigenvector 1 Parameter for Active Galactic Nuclei. *Astrophys. J.* **666**, 757 – 777.

Swarup, G., Ananthakrishnan, S., Kapahi, V.K., Rao, A.P., Subrahmanya, C.R., Kulkarni, V.K.: 1991, The Giant Metre-Wave Radio Telescope. *CURRENT SCIENCE V.60, NO.2/JAN25, P. 95, 1991* **60**, 95.

Tacconi, L.J., Genzel, R., Blietz, M., Cameron, M., Harris, A.I., Madden, S.: 1994, The nature of the dense obscuring material in the nucleus of NGC 1068. *ApJL* **426**, L77.

Takahashi, T., Abe, K., Endo, M., Endo, Y., Ezoe, Y., Fukazawa, Y., Hamaya, M., Hirakuri, S., Hong, S., Horii, M., coauthers, .: 2007, Hard X-Ray Detector (HXD) on Board Suzaku. *Publ. Astron. Soc. Japan* **59**, 35 – 51.

Terashima, Y., Iyomoto, N., Ho, L.C., Ptak, A.F.: 2002, X-Ray Properties of LIN-ERs and Low-Luminosity Seyfert Galaxies Observed with ASCA. I. Observations and Results. *ApJS* **139**, 1 – 36.

Thean, A., Pedlar, A., Kukula, M.J., Baum, S.A., O'Dea, C.P.: 2000, High-resolution radio observations of Seyfert galaxies in the extended 12-μm sample - I. The observations. *MNRAS* **314**, 573 – 588.

Thean, A., Pedlar, A., Kukula, M.J., Baum, S.A., O'Dea, C.P.: 2001, High-resolution radio observations of Seyfert galaxies in the extended 12-μm sample - II. The properties of compact radio components. *MNRAS* **325**, 737 – 760.

Tomono, D., Terada, H., Kobayashi, N.: 2006, Distribution of Dust Clouds around the Central Engine of NGC 1068. *Astrophys. J.* **646**, 774 – 782.

Tran, H.D.: 1995, The Nature of Seyfert 2 Galaxies with Obscured Broad-Line Regions. I. Observations. *Astrophys. J.* **440**, 565.

Tran, H.D.: 2001, Hidden Broad-Line Seyfert 2 Galaxies in the CFA and 12 μM Samples. *ApJL* **554**, L19 – L23.

Tran, H.D.: 2003, The Unified Model and Evolution of Active Galaxies: Implications from a Spectropolarimetric Study. *Astrophys. J.* **583**, 632 – 648.

Tran, H.D., Miller, J.S., Kay, L.E.: 1992, Detection of obscured broad-line regions in four Seyfert 2 galaxies. *Astrophys. J.* **397**, 452 – 456.

Treister, E., Urry, C.M., Virani, S.: 2009, The Space Density of Compton-Thick Active Galactic Nucleus and the X-Ray Background. *Astrophys. J.* **696**, 110 – 120.

Tremaine, S., Gebhardt, K., Bender, R., Bower, G., Dressler, A., Faber, S.M., Filippenko, A.V., Green, R., Grillmair, C., Ho, L.C., Kormendy, J., Lauer, T.R., Magorrian, J., Pinkney, J., Richstone, D.: 2002, The Slope of the Black Hole Mass versus Velocity Dispersion Correlation. *Astrophys. J.* **574**, 740 – 753.

Tueller, J., Mushotzky, R.F., Barthelmy, S., Cannizzo, J.K., Gehrels, N., Markwardt, C.B., Skinner, G.K., Winter, L.M.: 2008, Swift BAT Survey of AGNs. *Astrophys. J.* **681**, 113 – 127.

Turner, T.J.: 1999, X-Ray Observations of Markarian 231. *Astrophys. J.* **511**, 142 – 148.

Turner, T.J., George, I.M., Nandra, K., Mushotzky, R.F.: 1997, ASCA Observations of Type 2 Seyfert Galaxies. I. Data Analysis Results. *ApJS* **113**, 23.

Turner, T.J., George, I.M., Nandra, K., Mushotzky, R.F.: 1997, ASCA Observations of Type 2 Seyfert Galaxies. I. Data Analysis Results. *ApJS* **113**, 23.

Turner, T.J., George, I.M., Nandra, K., Mushotzky, R.F.: 1997, ASCA Observations of Type 2 Seyfert Galaxies. II. The Importance of X-Ray Scattering and Reflection. *Astrophys. J.* **488**, 164.

Turner, T.J., George, I.M., Nandra, K., Mushotzky, R.F.: 1998, ASCA Observations of Type 2 Seyfert Galaxies. III. Orientation and X-Ray Absorption. *Astrophys. J.* **493**, 91.

Ueda, Y., Akiyama, M., Ohta, K., Miyaji, T.: 2003, Cosmological Evolution of the Hard X-Ray Active Galactic Nucleus Luminosity Function and the Origin of the Hard X-Ray Background. *Astrophys. J.* **598**, 886 – 908.

Ulvestad, J.S., Ho, L.C.: 2001, Statistical Properties of Radio Emission from the Palomar Seyfert Galaxies. *Astrophys. J.* **558**, 561−577.

Ulvestad, J.S., Wilson, A.S.: 1984, Radio structures of Seyfert galaxies. V - A flux-limited sample of Markarian galaxies. *Astrophys. J.* **278**, 544−557.

Ulvestad, J.S., Wilson, A.S.: 1984, Radio structures of Seyfert galaxies. VI - VLA observations of a nearby sample. *Astrophys. J.* **285**, 439−452.

Ulvestad, J.S., Wilson, A.S.: 1989, Radio structures of Seyfert galaxies. VII - Extension of a distance-limited sample. *Astrophys. J.* **343**, 659−671.

Ulvestad, J.S., Wilson, A.S., Sramek, R.A.: 1981, Radio structures of Seyfert galaxies. II. *Astrophys. J.* **247**, 419−442.

Ulvestad, J.S., Wong, D.S., Taylor, G.B., Gallimore, J.F., Mundell, C.G.: 2005, VLBA Identification of the Milliarcsecond Active Nucleus in the Seyfert Galaxy NGC 4151. *AJ* **130**, 936−944.

Ulvestad, J.S., Wrobel, J.M., Roy, A.L., Wilson, A.S., Falcke, H., Krichbaum, T.P.: 1999, Subrelativistic Radio Jets and Parsec-Scale Absorption in Two Seyfert Galaxies. *ApJL* **517**, L81−L84.

Unger, S.W., Pedlar, A., Axon, D.J., Graham, D.A., Harrison, B.A., Saikia, D.J., Whittle, M., Meurs, E.J.A., Dyson, J.E., Taylor, D.: 1988, Radio ejection and broad forbidden emission lines in the Seyfert galaxy NGC 7674. *MNRAS* **234**, 745−754.

Urry, K., Padovanni, G., Wilson, A.S., Yoshida, M.: 1995, Title. *ApJ* **521**, 565−571.

Veilleux, S.: 1991, A study of the structure and kinematics of the narrow-line region in Seyfert galaxies. III - Individual objects. *Astrophys. J.* **369**, 331−363.

Veilleux, S., Sanders, D.B., Kim, D.C.: 1997, A Near-Infrared Search for Hidden Broad-Line Regions in Ultraluminous Infrared Galaxies. *Astrophys. J.* **484**, 92.

Véron-Cetty, M., Véron, P.: 2006, A catalogue of quasars and active nuclei: 12th edition. *A&A* **455**, 773 – 777.

Vestergaard, M., Wilkes, B.J., Barthel, P.D.: 2000, Clues to Quasar Broad-Line Region Geometry and Kinematics. *ApJL* **538**, L103 – L106.

Vignali, C., Brandt, W.N., Boller, T., Fabian, A.C., Vaughan, S.: 2004, Arakelian 564: an XMM-Newton view. *MNRAS* **347**, 854 – 860.

Wandel, A.: 2002, Black Holes of Active and Quiescent Galaxies. I. The Black Hole-Bulge Relation Revisited. *Astrophys. J.* **565**, 762 – 772.

Wang, J., Mao, Y.F., Wei, J.Y.: 2009, Accretion Properties of a Sample of Hard X-Ray (< 60 keV) Selected Seyfert 1 Galaxies. *AJ* **137**, 3388 – 3397.

Wang, J., Netzer, H.: 2003, Extreme slim accretion disks and narrow line Seyfert 1 galaxies: The nature of the soft X-ray hump. *A&A* **398**, 927 – 936.

Wang, J., Zhang, E.: 2007, The Unified Model of Active Galactic Nuclei. II. Evolutionary Connection. *Astrophys. J.* **660**, 1072 – 1092.

Weaver, K.A., Gelbord, J., Yaqoob, T.: 2001, Variable Iron Kα Lines in Seyfert 1 Galaxies. *Astrophys. J.* **550**, 261 – 279.

Weaver, K.A., Nousek, J., Yaqoob, T., Mushotzky, R.F., Makino, F., Otani, C.: 1996, X-Ray Reprocessing by a Molecular Torus in the Seyfert 1.9 Galaxy NGC 2992. *Astrophys. J.* **458**, 160.

Weedman, D.W.: 1977, Seyfert galaxies. *ARAA* **15**, 69 – 95.

Whittle, M.: 1992, Virial and jet-induced velocities in Seyfert galaxies. I - A compilation of narrow line region and host galaxy properties. *ApJS* **79**, 49 – 75.

Whittle, M.: 1992, Virial and jet-induced velocities in Seyfert galaxies. I - A compilation of narrow line region and host galaxy properties. *ApJS* **79**, 49 – 75.

Whittle, M.: 1992, Virial and Jet-induced Velocities in Seyfert Galaxies. III. Galaxy Luminosity as Virial Parameter. *Astrophys. J.* **387**, 121.

Whittle, M., Wilson, A.S.: 2004, Jet-Gas Interactions in Markarian 78. I. Morphology and Kinematics. *AJ* **127**, 606 – 624.

Williams, R.J., Pogge, R.W., Mathur, S.: 2002, Narrow-line Seyfert 1 Galaxies from the Sloan Digital Sky Survey Early Data Release. *AJ* **124**, 3042 – 3049.

Wills, B.J., Browne, I.W.A.: 1986, Relativistic beaming and quasar emission lines. *Astrophys. J.* **302**, 56 – 63.

Wilson, A.S.: 1988, Star formation and nuclear activity in Seyfert galaxies. *A&A* **206**, 41 – 46.

Wilson, A.S.: 1991, The radio emission of Seyfert galaxies. In: N. Duric & P. C. Crane (ed.) *The Interpretation of Modern Synthesis Observations of Spiral Galaxies*, *Astronomical Society of the Pacific Conference Series*, **18**, 227 – 250.

Wilson, A.S., Braatz, J.A., Heckman, T.M., Krolik, J.H., Miley, G.K.: 1993, The Ionization Cones in the Seyfert Galaxy NGC 5728. *ApJL* **419**, L61.

Wilson, A.S., Tsvetanov, Z.I.: 1994, Ionization cones and radio ejecta in active galaxies. *AJ* **107**, 1227 – 1234.

Wilson, A.S., Ulvestad, J.S.: 1982, Radio structures of Seyfert galaxies. III - Radio and optical observations of NGC 5548. *Astrophys. J.* **260**, 56 – 64.

Wilson, A.S., Ulvestad, J.S.: 1982, Radio structures of Seyfert galaxies. IV - Jets in NGC 1068 and NGC 4151. *Astrophys. J.* **263**, 576 – 594.

Wilson, A.S., Ulvestad, J.S.: 1987, A radiative bow shock wave (?) driven by nuclear ejecta in a Seyfert galaxy. *Astrophys. J.* **319**, 105 – 117.

Winkler, H.: 1992, Variability studies of Seyfert galaxies. II - Spectroscopy. *MNRAS* **257**, 677 – 688.

Woltjer, L.: 1959, Emission Nuclei in Galaxies. *Astrophys. J.* **130**, 38.

Worsley, M.A., Fabian, A.C., Bauer, F.E., Alexander, D.M., Hasinger, G., Mateos, S., Brunner, H., Brandt, W.N., Schneider, D.P.: 2005, The unresolved hard X-ray background: the missing source population implied by the Chandra and XMM-Newton deep fields. *MNRAS* **357**, 1281 – 1287.

Wrobel, J.M.: 2000, Photometric Variability and Astrometric Stability of the Radio Continuum Nucleus in the Seyfert Galaxy NGC 5548. *Astrophys. J.* **531**, 716 – 726.

Wunderlich, E., Wielebinski, R., Klein, U.: 1987, A further study of the relation of the radio-far-infrared in galaxies. I - Observations and data processing. *A&AS* **69**, 487 – 504.

Yang, Y., Wilson, A.S., Ferruit, P.: 2001, Chandra X-Ray Observations of NGC 4151. *Astrophys. J.* **563**, 124 – 134.

Yang, Y., Wilson, A.S., Matt, G., Terashima, Y., Greenhill, L.J.: 2009, Suzaku Observations of the Circinus Galaxy. *Astrophys. J.* **691**, 131 – 139.

Yaqoob, T.: 1997, X-Ray Transmission in Cold Matter: Nonrelativistic Corrections for Compton Scattering. *Astrophys. J.* **479**, 184.

Yaqoob, T., George, I.M., Nandra, K., Turner, T.J., Serlemitsos, P.J., Mushotzky, R.F.: 2001, Physical Diagnostics from a Narrow Fe Kα Emission Line Detected by Chandra in the Seyfert 1 Galaxy NGC 5548. *Astrophys. J.* **546**, 759 – 768. doi:10.1086/318315.

Yee, H.K.C., Stockman, H.S., Green, R.F.: 1981, Imaging of the Resolved Component of Quasars. In: *Bulletin of the American Astronomical Society*, *Bulletin of the American Astronomical Society*, **13**, 806.

Young, A.J., Wilson, A.S., Shopbell, P.L.: 2001, A Chandra X-Ray Study of NGC 1068. I. Observations of Extended Emission. *Astrophys. J.* **556**, $6-23$.

Young, S., Packham, C., Hough, J.H., Efstathiou, A.: 1996, The nuclear torus in the active galaxy NGC 1068. *MNRAS* **283**, $L1-L5$.